

ONSET OF FLOW INSTABILITY AND CRITICAL HEAT FLUX IN HORIZONTAL, THIN,
UNIFORMLY-HEATED ANNULI

A THESIS

Presented to

The Academic Faculty

by

Ryan Manse Stoddard

In Partial Fulfillment

of the Requirements for the Degree

Master of Science in Mechanical Engineering

Georgia Institute of Technology

April 2000

DISTRIBUTION STATEMENT A
Approved for Public Release
Distribution Unlimited

20000710 055

DMO QUALITY INSPECTED 4

AD NUMBER	DATE 15 JUNE 2000	DTIC ACCESSION NOTICE
1. REPORT IDENTIFYING INFORMATION		REQUESTER: 1. Put your mailing address on reverse of form. 2. Complete items 1 and 2. 3. Attach form to reports ... mailed to DTIC. 4. Use unclassified technology 5. Do not order document for 6 to 8 weeks.
A. ORIGINATING AGENCY Naval Postgraduate School, Monterey, CA 93943		
B. REPORT TITLE AND/OR NUMBER Onset of Flow Instability & Critical Heat Flux in Horizontal, Thin, Uniformly-Heated		
C. MONITOR REPORT NUMBER By: Ryan M. Stoddard, Thesis, Georgia Institute of Technology April 2000		
D. PREPARED UNDER CONTRACT NUMBER N62271-97-G-0021		
2. DISTRIBUTION STATEMENT		DTIC: 1. Assign AD Number.

APPROVED FOR PUBLIC RELEASE
DISTRIBUTION UNLIMITED

DTIC Form 50
JUL 96

20000710 055

**ONSET OF FLOW INSTABILITY AND CRITICAL HEAT FLUX IN HORIZONTAL, THIN,
UNIFORMLY-HEATED ANNULI**

A THESIS

Presented to

The Academic Faculty

by

Ryan Manse Stoddard

In Partial Fulfillment

of the Requirements for the Degree


Master of Science in Mechanical Engineering

Georgia Institute of Technology

April 2000

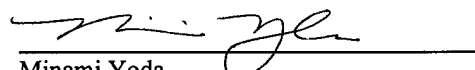
ONSET OF FLOW INSTABILITY AND CRITICAL HEAT FLUX IN HORIZONTAL, THIN,
UNIFORMLY-HEATED ANNULI

APPROVED:


Said I. Abdel-Khalik, Co-Advisor


Sheldon M. Jeter, Co-Advisor


S. Mostafa Ghiaasiaan


Minami Yoda

Date Approved by Chairman 4/10/00

ACKNOWLEDGMENTS

The successful completion of this investigation and subsequent thesis would not have been possible without the continuous support and guidance of several people. First, I would like to thank my co-advisor Dr. S.I Abdel-Khalik for his constant interest and guidance during my studies at Georgia Tech. I would also like to thank my co-advisor, Dr. Sheldon Jeter and the rest of my committee, Dr. S. Mostafa Ghiaasiaan, and Dr. Minami Yoda.

Special thanks go to Mr. Michael Dowling and Mr. Dennis Sadowski for their limitless patience and daily assistance. Without them the entire lab, much less this project, would cease to function and I would never have finished.

I would also like to thank all of my graduate student colleagues for keeping me sane during my long days of captivity in the basement of ESM: Dr. Thomas Adams, Dr. Chris Pascual, Joerg Stromberger, Zhaiwen Ma, Jianwei Wang, Tim Remley, Ann Blasick, Nate Ekberg, Matthew Rhodes, Justin Collins, Lance Elwell, Blace Albert, Joe Root, Terrell Finch, Sam Durbin, Henry Edwards, and Matt Casiano.

Finally, and most importantly, I am thankful to my wife Michelle Stoddard for her never-ending love, encouragement, and patience over the past two years, and to my parents, brothers, and parents-in-law for their constant support.

TABLE OF CONTENTS

ACKNOWLEDGMENTS	iii
LIST OF FIGURES	viii
LIST OF TABLES.....	xii
NOMENCLATURE	xv
SUMMARY	xvii
CHAPTER I: INTRODUCTION.....	1
I.1 Onset of Flow Instability (OFI).....	1
I.2 Critical Heat Flux	5
I.3 Accelerator Production of Tritium (APT) Project.....	7
I.4 Motivation and Objectives.....	12
CHAPTER II: LITERATURE REVIEW	14
II.1 Introduction.....	14
II.2 Onset of Flow Instability.....	14
II.2.1 Flow Instability Initiation.....	17
II.2.2 Onset of Significant Void.....	18
II.3 Review of OSV Models	19
II.3.1 Theoretical OSV Models.....	19
II.3.2 Empirical OSV Models	21
II.4 Critical Heat Flux	39
II.5 Review of CHF Models.....	41
II.5.1 Empirical CHF Correlations.....	41
II.5.2 Tabular CHF Correlation	42
CHAPTER III: INSTRUMENTATION AND EQUIPMENT	48
III.1 Experimental Test Facility Overview	48
III.2 Experimental Setups	50
III.3 Flow Loop Configuration	51
III.3.1 System Instrumentation	51
III.3.1.1 Absolute Pressure Transducers.....	51
III.3.1.2 Differential Pressure Transducer	55
III.3.1.3 Turbine Flowmeters	55
III.3.1.4 Rotameters	55
III.3.1.5 Thermocouples.....	56
III.3.1.6 Pressure Gauges.....	57
III.3.1.7 Data Acquisition System (DAS).....	58

TABLE OF CONTENTS (continued)

III.3.1.8: Hewlett Packard Data Acquisition / Switch Unit	58
III.3.2 Flow Loop Configuration One	59
III.3.3 Flow Loop Configuration Two	61
III.3.4 Flow Loop Configuration Three	63
III.3.5 Flow Loop Configuration Four	65
III.3.6 Control of Flow Parameters	67
III.3.6.1 Test Section Inlet Temperature Preparation	67
III.3.6.2 Working Fluid Gas Saturation and System Pressurization	69
III.3.6.3 Minimization of Oxidation / Clarification of Setup 7	71
III.4 Inner Heater Configuration	71
III.4.1 Inner Heater D	74
III.4.2 Inner Heaters E, F, and G	75
III.4.3 Inner Heater H	76
III.4.4 Inner Heaters I, J, K, and L	77
III.4.5 Inner Heater M	78
III.4.6 Inner Heaters N and O	79
III.5 Outer Heater Configuration	81
III.5.1 Outer Heater E	83
III.5.2 Outer Heater H	84
III.5.3 Wire Wrapping Style	85
III.5.4 Outer Heater I and J	91
III.5.5 Outer Heater K	92
III.5.6 Outer Heater L	93
III.6 Power Supply Configuration	94
III.6.1 Power Supply Configuration One	95
III.6.2 Power Supply Configuration Two	96
III.6.3 Power Supply Configuration Three	99
III.6.4 Power Supply Configuration Four	104
III.7 Mounting Configuration	107
III.7.1 Mounting Configuration One	110
III.7.2 Mounting Configuration Two	113
III.8 Insulation Configuration	116
III.9 Non-Condensable Gas Status	117
CHAPTER IV: EXPERIMENTAL PROCEDURES	119
IV.1 Initial System Preparation	119
IV.2 System Filling Procedure	120
IV.3 Working Fluid Gas Saturation and System Pressurization	125
IV.4 OFI Primary Flow Loop Preparation	127
IV.4.1 Flow Loop Configuration One	127
IV.4.2 Flow Loop Configuration Two	129

TABLE OF CONTENTS (continued)

IV.4.3 Flow Loop Configuration Three.....	132
IV.5 CHF Primary Flow Loop Preparation.....	134
IV.6 Test Section Inlet Temperature Control	137
IV.7 OFI Experimental Procedure and Analysis Techniques.....	138
IV.7.1 OFI Experimental Procedure	138
IV.7.2 OFI Experimental Analysis Techniques.....	139
IV.8 CHF Experimental Procedure and Analysis Techniques.....	149
IV.8.1 CHF Experimental Procedure.....	149
IV.8.2 CHF Experimental Analysis Techniques.....	150
CHAPTER V: RESULTS AND DISCUSSION.....	158
V.1 Onset of Flow Instability.....	158
V.1.1 Brief Discussion of the Findings of Blasick (1999).....	159
V.1.2 Effect of Annular Gap Width on OFI	163
V.1.3 Effect of Inner-to-Outer Heat Flux Ratio and Heated Length on OFI.....	164
V.1.4 Effect of Surface Heat Flux on OFI.....	167
V.1.5 Effect of Test Section Inlet Temperature on OFI	168
V.1.6 Effect of Test Section Exit Pressure on OFI.....	168
V.1.7 Comparison with Kennedy's OFI Model.....	169
V.1.8 Comparison with Roach (1998) OFI Model	171
V.1.9 Comparison with the Saha and Zuber (1974) OSV Model.....	173
V.1.10 Comparison with the Unal (1975) IPNVG Model.....	175
V.1.11 Development of OFI Correlation	177
V.2 Critical Heat Flux (CHF)	180
V.2.1 Effect of Coolant Mass Flux on CHF	181
V.2.2 Effect of Test Section Inlet Temperature on CHF	182
V.2.3 Effect of Test Section Exit Pressure on CHF.....	182
V.2.4 Comparison with the Caira, et al. (1993) Empirical CHF Correlation	183
V.2.5 Comparison with the Bowring (1972) Empirical CHF Correlation.....	185
V.2.6 Comparison with Predicted OFI Correlation	186
CHAPTER VI: CONCLUSIONS.....	189
VI.1 OFI Conclusions	189
VI.2 CHF Conclusions.....	191
APPENDIX A: EES PROPERTIES ALGORITHM	193
APPENDIX B: SUMMARY OF OFI EXPERIMENTAL DATA	195
APPENDIX C: SUMMARY OF CHF EXPERIMENTAL DATA.....	200

TABLE OF CONTENTS (continued)

APPENDIX D: OFI ERROR ANALYSIS	202
D.1 Mass Flux Error Analysis	202
D.2 Heat Flux Error Analysis	213
APPENDIX E: CHF ERROR ANALYSIS	224
E.1 Mass Flux Error Analysis	224
E.2 Heat Flux Error Analysis	233
BIBLIOGRAPHY	240

LIST OF FIGURES

<u>FIGURE</u>	<u>PAGE</u>
1.1 Schematic Diagram of the Demand Curve for a Heated Channel	2
1.2 Excursive Instability (from Lahey and Moody, 1979).....	4
1.3 Typical Temperature and Flow Regime Variation in a Heated Tube	6
1.4 Schematic of APT Target Assembly (from Pasamehmetoglu, et al., 1998)	9
1.5 Scale Cross-Sectional View of a TNS Rung for Ladder Levels One or Two.....	10
1.6 Simplified View of the Innermost Annular Coolant Channel	11
2.1 CHF Mechanisms for Various Flow Regimes in Upward Flow	40
3.1 Schematic Diagram of the Georgia Tech Microchannel Test Facility	52
3.2 Schematic Diagram of Flow Loop Configuration One.....	60
3.3 Schematic Diagram of Flow Loop Configuration Two	62
3.4 Schematic Diagram of Flow Loop Configuration Three	64
3.5 Schematic Diagram of Flow Loop Configuration Four	66
3.6 Diagram of Inner Heater D	75
3.7 Diagram of Inner Heaters E, F, and G	76
3.8 Diagram of Inner Heater H	77
3.9 Diagram of Inner Heaters I, J, K, and L.....	78
3.10 Diagram of Inner Heater M.....	79
3.11 Diagram of Inner Heaters N and O	81
3.12 Diagram of Outer Heater E	84

LIST OF FIGURES (continued)

<u>FIGURE</u>	<u>PAGE</u>
3.13 Diagram of Outer Heater H.....	85
3.14 Diagram of Heater Wire Clamp.....	87
3.15 Diagram of Outer Heater Electrode Ring	89
3.16 Diagram of Outer Heaters I and J	92
3.17 Diagram of Outer Heater K.....	93
3.18 Diagram of Outer Heater L	94
3.19 Electrical Diagram of Power Supply Configuration One	96
3.20 Electrical Diagram of Power Supply Configuration Two.....	98
3.21 Diagram of Outer Heater DC Electrode Plate.....	98
3.22 Electrical Diagram of Power Supply Configuration Three.....	100
3.23 Component Diagram of Power Supply Configuration Three	100
3.24 Diagram of Inner Heater DC Electrode Plate	103
3.25 Electrical Diagram of Power Supply Configuration Four	106
3.26 Component Diagram of Power Supply Configuration Four	107
3.27 Diagram of Triangular Optical Mounting Rail	108
3.28 Diagram of Custom Made Swagelok T-Fitting Mount.....	109
3.29 Diagram of Teflon and Rubber Inserts for Swagelok T-Fitting	111
3.30 Diagram of Mounting Configuration One	112
3.31 Diagram of Teflon and Rubber Inserts for Swagelok T-Fitting	114
3.32 Diagram of Mounting Configuration Two.....	115

LIST OF FIGURES (continued)

<u>FIGURE</u>	<u>PAGE</u>
3.33 Diagram of Insulation Configuration One	117
4.1 Schematic Diagram of the Georgia Tech Microchannel Test Facility	122
4.2 Schematic Diagram of Flow Loop Configuration One.....	128
4.3 Schematic Diagram of Flow Loop Configuration Two	130
4.4 Schematic Diagram of Flow Loop Configuration Three	133
4.5 Schematic Diagram of Flow Loop Configuration Four	136
4.6 Typical Experimental OFI Demand Curve	140
4.7 Typical Experimental Plot of Heater Wall Temperature Versus Time.....	154
4.8 Typical Experimental Plot of Coolant Mass Flux Versus Time	156
4.9 Typical Experimental Plot of Test Section Inlet Temperature Versus Time.....	156
4.10 Typical Experimental Plot of Test Section Exit Pressure Versus Time	157
5.1 Effect of Non-Condensable Gas Content on OFI (from Blasick, 1999).....	161
5.2 Effect of Inner-to-Outer Surface Heat Flux Ratio on OFI.....	162
5.3 Effect of Annular Gap Width on OFI	164
5.4 Comparison of Zero Heat Flux Ratio Data to OFI Heat Flux Correlation	166
5.5 Comparison of Zero Heat Flux Ratio Data to OFI Mass Flux Correlation	166
5.6 Effect of Surface Heat Flux on OFI.....	167
5.7 Effect of Test Section Inlet Temperature on OFI	168
5.8 Effect of Test Section Exit Pressure on OFI.....	169
5.9 Comparison of OFI Heat Flux Data with Kennedy, et al. (1997) OFI Model.....	170

LIST OF FIGURES (continued)

<u>FIGURE</u>	<u>PAGE</u>
5.10 Comparison of OFI Mass Flux Data with Kennedy, et al. (1997) OFI Model	171
5.11 Comparison of OFI Heat Flux Data with Roach (1998) Low-Flow, Air-Saturated OFI Model.....	172
5.12 Comparison of OFI Mass Flux Data with Roach (1998) Low-Flow, Air-Saturated OFI Model.....	173
5.13 Correlation of OFI Heat Flux Data Against Saha & Zuber OSV Model.....	174
5.14 Correlation of OFI Mass Flux Against Saha & Zuber OSV Model	175
5.15 Correlation of OFI Heat Flux Data Against Unal (1975) IPNVG Model.....	176
5.16 Correlation of OFI Mass Flux Data Against Unal (1975) IPNVG Model.....	177
5.17 OFI Heat Flux Correlation	179
5.18 OFI Mass Flux Correlation	180
5.19 Effect of Coolant Mass Flux on CHF	181
5.20 Effect of Test Section Inlet Temperature on CHF	182
5.21 Effect of Test Section Exit Pressure on CHF.....	183
5.22 Correlation of Experimental CHF Data Against Caira, et al. (1993) CHF Model	184
5.23 Correlation of Experimental CHF Data Against Bowring (1972) CHF Model....	186
5.24 Experimental CHF Data Versus Predicted OFI Heat Flux	187
5.25 Experimental CHF Data Versus 3.047 Times Predicted OFI Heat Flux	188
D.1 OFI Plot with Fourth and Fifth Order Quadratic Fits	206

LIST OF TABLES

<u>TABLE</u>	<u>PAGE</u>
1.1 Summary of Geometric Data for Ladders and Rungs in APT Target.....	9
2.1 Levy's Theoretical OSV Model (1967).....	23
2.2 Staub's Theoretical OSV Model (1968).....	25
2.3 Rogers, et al. Theoretical OSV Model (1987).....	27
2.4 Bowring's Empirical OSV Correlation (1962).....	29
2.5 Thom, et al. Empirical OSV Correlation (1966).....	30
2.6 Ahmad's Empirical OSV Correlation (1970)	31
2.7 Dix's Empirical OSV Correlation (1971).....	32
2.8 Saha and Zuber Empirical OSV Correlation (1974).....	33
2.9 Sekoguchi, et al. Empirical OSV Correlation (1974)	34
2.10 Unal's Empirical OSV Correlation (1975)	35
2.11 Kennedy, et al. Empirical OFI Correlation (1997)	36
2.12 Roach Empirical OFI Correlation (1998)	37
2.13 Blasick, Empirical OFI Correlation (1999)	38
2.14 Bowring's Empirical CHF Correlation (1972)	43
2.15 Caira, et al. Empirical CHF Correlation (1993).....	44
2.16 McBeth, et al. Empirical CHF Correlation (1964)	45
2.17 CISE-4 CHF Correlation (1975).....	46
2.18 Groeneveld, et al. Tabular CHF Correlation (1986).....	47

LIST OF TABLES (continued)

<u>TABLE</u>	<u>PAGE</u>
3.1 Summary of Experimental Setups	50
3.2 Listing of GTMTF Hardware Components	53
3.3 Listing of GTMTF Instrumentation	54
3.4 Summary of Inner Heater Configurations.....	72
3.5 Summary of Outer Heater Configurations.....	82
3.6 Summary of Wire Wrapping Styles.....	85
4.1 Effect of Heat Loss Estimation on OFI Calculations.....	143
4.2 Effect of Heat Loss Estimation on OFI Calculations.....	145
B.1 OFI Experimental Data from Blasick (1999).....	195
B.2 OFI Experimental Data (Stoddard).....	198
C.1 CHF Experimental Data (Stoddard).....	200
D.1 Summary of Volumetric Flowrate Uncertainties at OFI.....	207
D.2 Summary of Coolant Mass Flux Error Sources at OFI.....	210
D.3 OFI Coolant Mass Flux Error Analysis Results	211
D.4 Summary of Outer Heater Power Uncertainties at OFI (first 61 experiments)	215
D.5 Summary of Inner Heater Power Uncertainties at OFI (first 61 experiments)	216
D.6 Summary of Total Power Level Uncertainties at OFI (last five experiments)	218
D.7 Summary of Heat Flux Uncertainties at OFI	220
D.8 OFI Surface Heat Flux Error Analysis Results.....	222
E.1 Summary of Volumetric Flowrate Uncertainties at CHF	227

LIST OF TABLES (continued)

TABLE	<u>PAGE</u>
E.2 Summary of Coolant Mass Flux Error Sources at CHF	230
E.3 CHF Coolant Mass Flux Error Analysis Results	231
E.4 Summary of Total Power Level Uncertainties at CHF	235
E.5 Summary of Heat Flux Uncertainties at CHF	237
E.6 CHF Surface Heat Flux Error Analysis Results	238

NOMENCLATURE

α	void fraction
A_{cs}	cross sectional area
A_s	surface area
AC	alternating current
APT	Accelerator Production of Tritium
CHF	Critical Heat Flux
D	diameter
D_h	hydraulic diameter
DAS	Data Acquisition System
DC	direct current
DOE	Department of Energy
EES	Engineering Equation Solver
G	mass flux
GPH	gallons per hour
GTMTF	Georgia Tech Microchannel Test Facility
h	heat transfer coefficient
L	length
L_h	heated length
\dot{m}	mass flowrate
Nu	Nusselt number

OFI	Onset of Flow Instability
OSV	Onset of Significant Void
P	pressure
ΔP	differential pressure
Pe	Peclet number
Pr	Prandtl number
q''	heat flux
ρ	density
Re	Reynolds number
RPM	revolutions per minute
σ	standard deviation
SI	Standard International
SS	stainless steel
T	temperature
TNS	Tungsten Neutron Source
TPI	turns per inch
\dot{V}	volumetric flowrate

SUMMARY

Two-phase flow instability (Ledinegg Excursion) and critical heat flux in heated microchannels are of great concern in the design and operation of numerous practical systems. In order to prevent Ledinegg flow excursion and eventual burnout of the heated channel, limits are typically imposed on the channel power and coolant mass flux to avoid the possibility of operation within the negatively-sloped region of the coolant channel demand curve.

The primary purpose of this investigation was to experimentally determine the effect of design and operational parameters on the onset of flow instability (OFI) and critical heat flux (CHF) in thin, horizontal, uniformly-heated annuli. The work was motivated by the need for such data for the design and safety analysis of the Accelerator Production of Tritium (APT) project under development at Los Alamos National Laboratory. To this end, thirteen different experimental setups were employed to determine the OFI and CHF behavior of annular channels with hydraulic diameters on the order of two millimeters (annular gap widths of approximately 1.0 mm). The OFI data were then compiled and used to create two correlations; one comparing OFI heat flux to saturation heat flux and the other comparing OFI mass flux to saturation mass flux. The CHF data acquired in this investigation were compared with several empirical CHF correlations available in the literature and used to demonstrate that OFI, rather than CHF, is the limiting phenomenon in microchannel heat transfer.

All OFI experiments were conducted in the Georgia Tech Microchannel Test

Facility (GTMTF) with test section inlet temperatures ranging from 30 to 70°C, exit pressures from 0.345 to 1.034 MPa, surface heat fluxes from 0.45 to 2.5 MW/m², inner-to-outer surface heat flux ratios from 0:1 to 1:0, and fully saturated non-condensable gas concentrations. The corresponding range of coolant mass flux was 85 to 2900 kg/m² s. A total of 66 OFI experiments were conducted in this investigation; together with the OFI data (129 experiments) of Blasick (1999), these data were used to develop the following correlations.

$$q''_{OFI} = 0.942 * q''_{sat} \pm 9.80\% \quad (S.1)$$

$$G_{OFI} = 1.064 * G_{sat} \pm 11.55\% \quad (S.2)$$

The above correlations mean that for a specified mass flux, the heat flux necessary to cause OFI equals 94.2% of the heat flux required to cause bulk exit saturation of the working fluid. Alternatively, for a specified heat flux, the mass flux corresponding to OFI equals 1.064 times the mass flux required to cause bulk exit saturation of the working fluid. The test section heated length and inner-to-outer heat flux ratio were found to have insignificant effects on OFI.

All CHF experiments were also conducted in the Georgia Tech Microchannel Test Facility (GTMTF) with test section inlet temperatures ranging from 30 to 65°C, exit pressures from 0.345 to 1.034 MPa, coolant mass fluxes from 100 to 400 kg/m² s, an inner-to-outer surface heat flux ratio of 1:1, and fully saturated non-condensable gas

concentrations. The corresponding range of surface heat flux was 0.2309 to 1.0686 MW/m². A total of 35 CHF experiments were conducted in this investigation and compared with several CHF correlations available in the literature. In addition, the CHF data were compared with the OFI correlation developed during this investigation; the following relation was obtained.

$$q''_{CHF} = 3.047 * q''_{OFI} \pm 12.63\% \quad (S.3)$$

Given a specified mass flux, the heat flux necessary to cause CHF was found to be 3.047 times the heat flux required to cause OFI. This effectively demonstrates that OFI, rather than CHF, is the limiting phenomenon in microchannel heat transfer. The data obtained in this investigation provided the basis for quantifying the thermal margins for the proposed Accelerator Production of Tritium (APT) target bundle geometry under both normal operation and accident conditions.

CHAPTER I

INTRODUCTION

Forced convection using single-phase liquid water is a common cooling mechanism used in several high power density engineering applications. Typically, design specifications require coolant channels to remain completely filled with sub-cooled liquid water to ensure adequate cooling of heated surfaces. Despite these planned steady state parameters, accident or transient conditions can cause boiling to take place. For this reason, it is important in the design and operation of heated channels to understand and predict the onset of boiling and two-phase flow instabilities that can lead to channel dry-out and potential overheating of the system. The present work describes experiments that examine the onset of Ledinegg flow instability and critical heat flux caused by significant voiding in an annular channel.

I.1 Onset of Flow Instability (OFI)

Figure 1.1 shows a typical demand curve for a uniformly heated channel. In the high mass flux regime, sub-cooled single-phase conditions exist throughout the channel. Consequently, all heat transfer is accomplished through single-phase forced convection. As the mass flux through the channel is decreased, sub-cooled boiling followed by

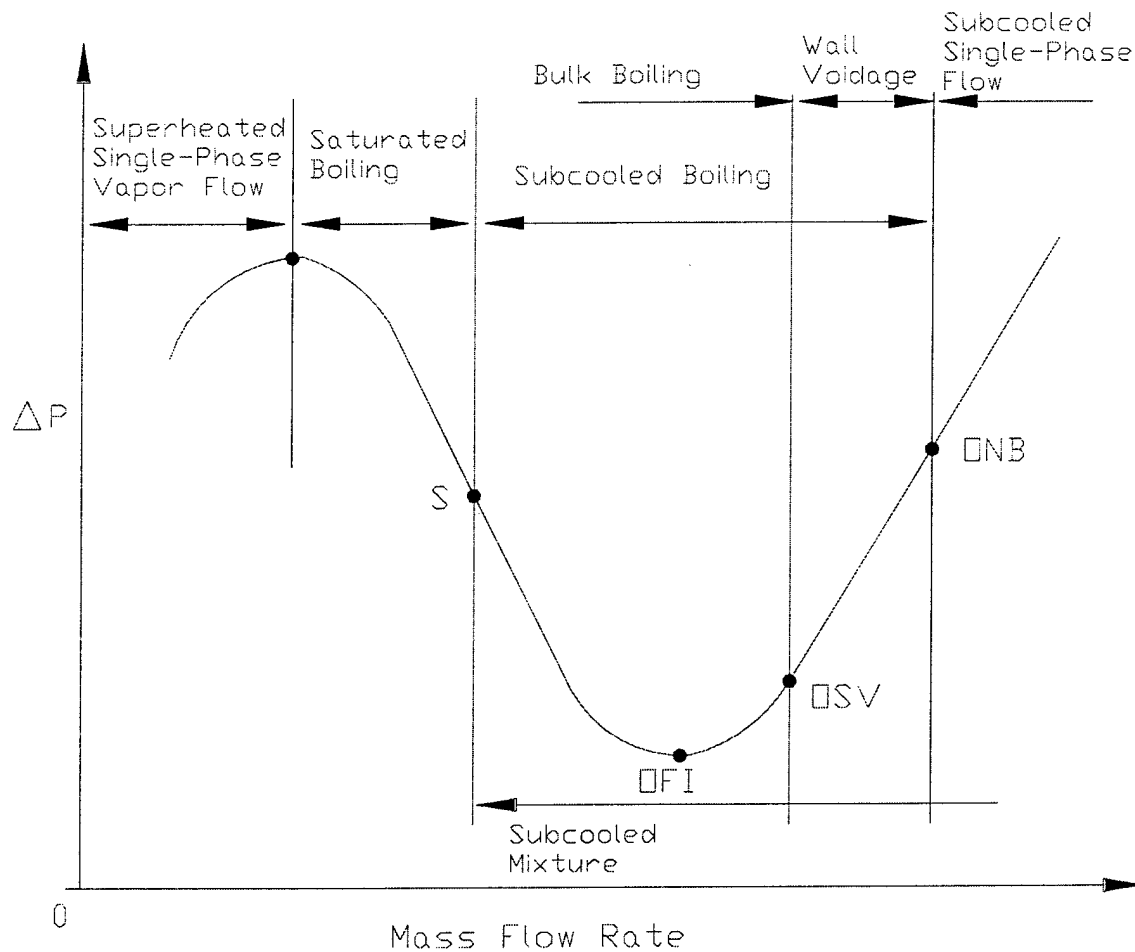


Figure 1.1: Schematic Diagram of the Demand Curve for a Heated Channel

saturated boiling, and finally single-phase convection to superheated vapor takes place (Kennedy, et al., 1997).

In Figure 1.1, the terms ONB, OSV, OFI, and S refer to the onset of nucleate boiling, onset of significant void, onset of flow instability, and saturation conditions, respectively. Prior to the OSV point, the coolant flow is primarily single-phase, subcooled liquid with some bubbles sticking to the walls of the heated channel. These bubbles are unable to withstand condensation and hence collapse when released from the

wall and mix with the bulk fluid flow. At the onset of significant void, the void fraction is approximately five percent and bubbles released from the channel walls survive condensation and become entrained in the bulk fluid flow; the flow becomes two-phase. Flow boiling ensues following the OSV point and a fully developed nucleate boiling regime dominates. For high mass fluxes, the onset of significant void and the initiation of bulk boiling occur at approximately the same point. As the mass flux through the heated channel decreases to the point where pressure drop across the channel is at a minimum on the demand curve (referred to as the onset of flow instability point), a flow excursion can occur resulting in a significant reduction in flow through the channel (Kennedy, et al., 1997).

Referring to the demand curve shown in Figure 1.2, case A represents the situation that would exist if a positive displacement pump were used to circulate coolant through a heated channel (Lahey and Moody, 1979). A positive displacement pump operating at a given speed would force coolant through the boiling channel at a fixed rate regardless of the overall pressure drop. For this reason, the channel could be operated at position 1 by maintaining a constant pump speed. Case B represents the situation where numerous channels operate in parallel with the boiling channel. For this case, operating the system steadily and continuously at position 1 is impossible. A small negative perturbation in the system would immediately shift conditions to position 2 while a small positive perturbation would shift the flow state to position 3. A flow excursion from position 1 to position 2 would result in a significant reduction in flow rate within the heated channel and may lead to dryout or physical burnout of the channel. Case C

represents the situation that would result if a centrifugal pump were used to circulate the coolant through the heated channel. Once again, steady and continuous operation at point 1 is impossible since a small perturbation could result in a flow excursion to either position 2' or position 3'. Finally, case D represents a situation where the circulation pump has a steep characteristic so that position 1 could be maintained and Ledinegg instability would not occur (Kennedy, et al., 1997).

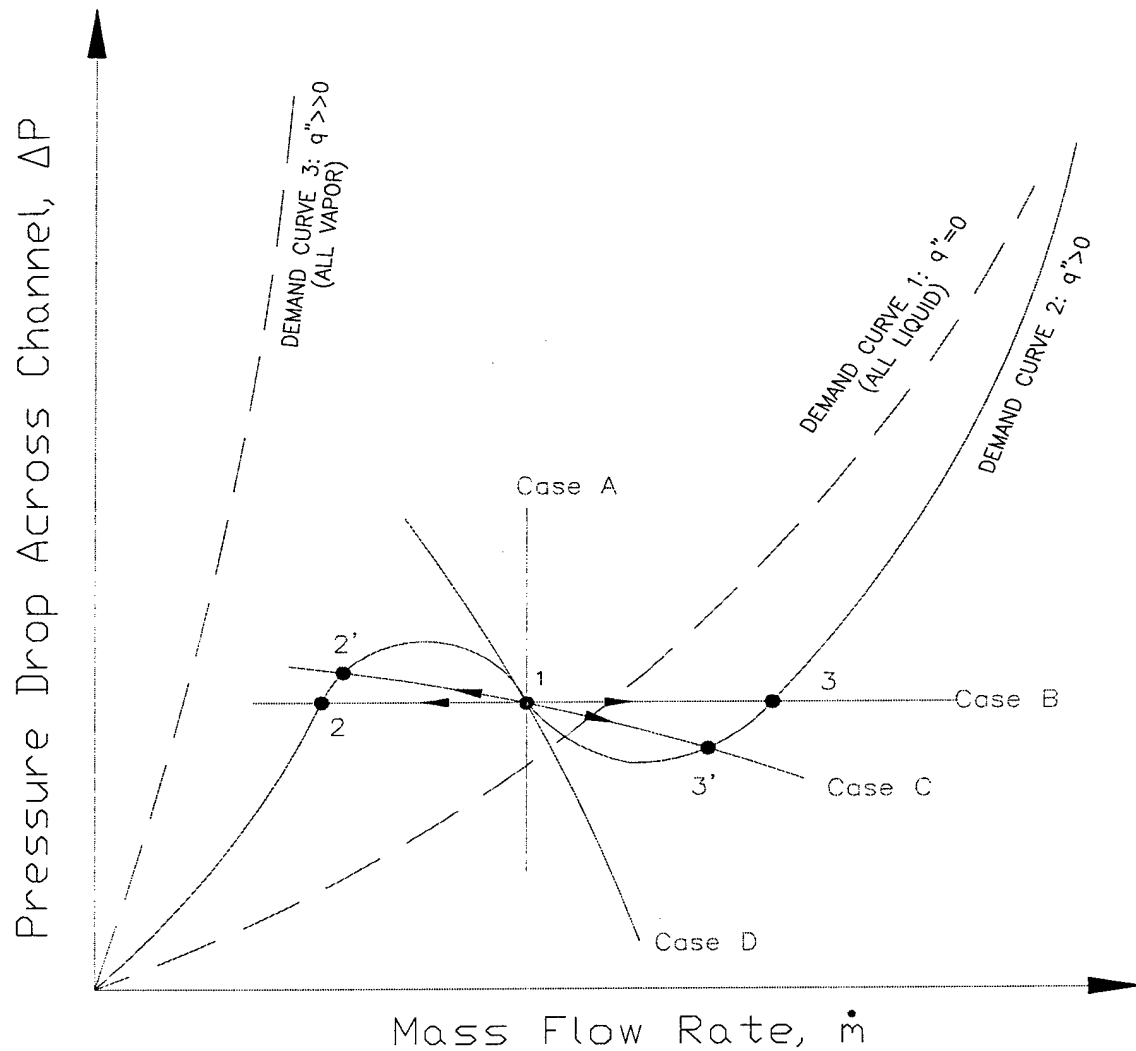


Figure 1.2: Excursive Instability (from Lahey and Moody, 1979)

In order to prevent Ledinegg flow excursions in practical systems, limits are imposed on the channel power input to exclude the possibility of operation within the negatively-sloped segment of the demand curve at all anticipated flow rates. Typically, these power limits are conservatively estimated by using OSV models and/or correlations, where OSV is considered a precursor to the onset of flow instability (OFI) which, in turn, may be viewed as a precursor to the critical heat flux (CHF) (Kennedy, et al., 1997). In this research, the location of the OFI point was compared with commonly used OFI and OSV correlations for large diameter channels. In addition, CHF experiments were performed in order to demonstrate that OFI, rather than CHF, is the limiting phenomenon in microchannel heat transfer.

I.2 Critical Heat Flux

Internal flow critical heat flux (CHF) is one of the most important design limitations in many industrial systems. At CHF, a severe reduction in heat transfer between the heated surface and coolant occurs, frequently referred to as forced convection burnout (Roach, 1998). In situations where the surface heat flux remains constant, CHF is marked by an abrupt increase in the wall temperature of the heated surface. Forced flow CHF is a complicated phenomenon in which thermal and hydrodynamic processes are tightly coupled, but the basic aspects can be outlined as shown in Figure 1.3 (Stoddard, et al., 2000).

Figure 1.3 shows the variation of coolant flow pattern alongside a plot of the typical behavior of the wall and liquid temperatures. In this simplified example, single-phase liquid enters a heated, vertical tube at the bottom and proceeds to boil as it travels through the tube, exiting as superheated vapor. Nucleate boiling begins when the tube wall temperature reaches the saturation temperature of the coolant. As long as liquid

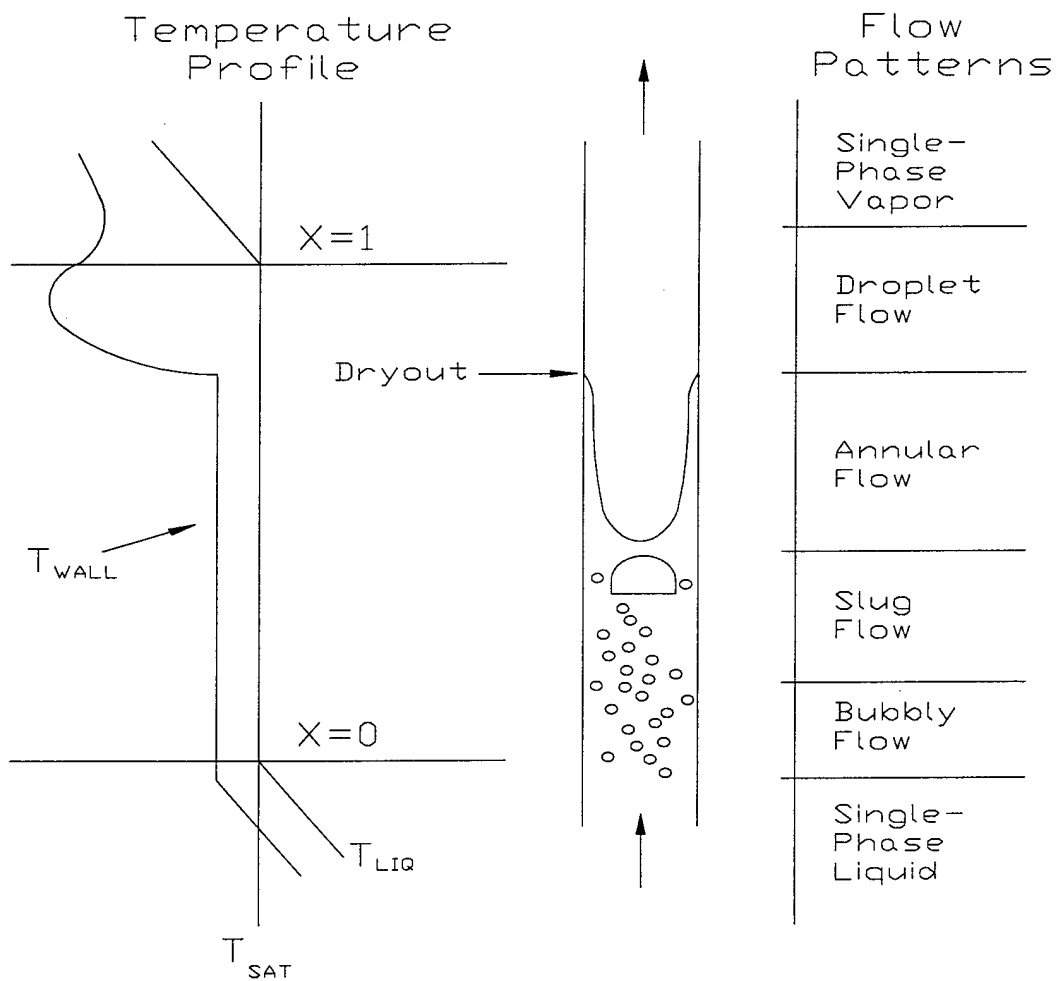


Figure 1.3: Typical Temperature and Flow Regime Variation in a Heated Tube

coolant remains in contact to some degree with the tube wall, the wall temperature remains essentially constant, until the dryout point is reached. Beyond this point, only vapor is in contact with the tube wall, and its temperature increases dramatically (Stoddard, et al., 2000).

As mentioned previously, the complicated coupling of thermal and hydrodynamic effects makes it difficult to generalize or predict the exact progression of the flow pattern as the channel geometry changes. Furthermore, the exact mechanism that leads to CHF can vary depending on the exact nature of the flow, thus not all of the flow regimes shown in Figure 1.3 necessarily occur. For this reason, a large variety of data for different channel geometries and coolant conditions have been generated by past researchers, and several different mechanistic models have been developed for the prediction of CHF, with separate models addressing the various observed mechanisms. The CHF data collected in this investigation will be compared with existing CHF models available in the literature; a new CHF correlation will not be developed. As mentioned previously, the fundamental goal of this research is to demonstrate that OFI, rather than CHF, is the limiting phenomenon in microchannel heat transfer.

I.3 Accelerator Production of Tritium (APT) Project

The Accelerator Production of Tritium (APT) Project is one of the alternatives under consideration by the Department of Energy (DOE) for the production of the tritium necessary to replenish the United States nuclear weapons stockpile. Tritium decays at a

rate of 5.5 percent per year and therefore must be produced regularly. All previous tritium production occurred in several fission reactors located at the DOE Savannah River Site in South Carolina, which have since been shut down (Blasick, 1999).

Tritium would be produced in the APT facility by irradiating a target assembly with a high-energy proton beam to create neutrons; He-3 gas would then be used as the tritium producing feedstock. The proposed APT target design employs D₂O (heavy water) cooled concentric tungsten annuli as the primary neutron source. This tungsten neutron source (TNS) consists of thirteen ladders, each separated by a 0.3 m void region as shown in Figure 1.4. Each ladder has several short rungs consisting of six concentric, Inconel-718 clad tungsten cylinders of varying thickness since the proton beam produces the highest heat fluxes on the front ladders. Hence, the tungsten cylinder wall thickness increases from 2.030 millimeters in the front ladder to 7.703 millimeters in the back. This causes an attendant increase in the rung tube diameter from 43.4 millimeters to 77.7 millimeters. The number of rungs in each ladder assembly ranges from 28 in the front two ladders to 16 in the back ladders, and the rungs are offset from ladder to ladder to eliminate proton streaming. Each rung has a total length of 25 centimeters while the beam spot covers the central 19 centimeters (Pasamehmetoglu, et al., 1998). A cross-section of a rung from ladders one and two, the peak power ladders of the APT target, is shown in Figure 1.5.

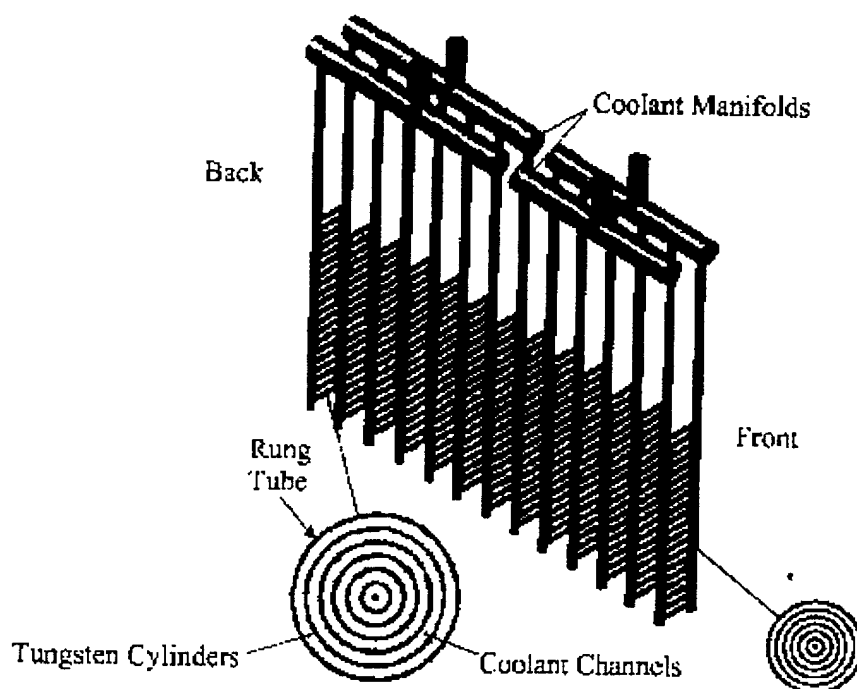


Figure 1.4: Schematic of APT Target Assembly (from Pasamehmetoglu, et al., 1998)

Table 1.1: Summary of Geometric Data for Ladders and Rungs in APT Target

Dimension	Ladders 1 - 2	Ladders 3 - 4	Ladders 5 - 6	Ladders 7 - 8	Ladders 9 - 13
Number of Rungs	28	26	22	19	16
Rung Outer Diameter (cm)	4.343	4.679	5.563	6.477	7.696
Rung Pitch (cm)	7.478	8.052	9.509	11.001	13.052
Tungsten Volume Fraction	58.5%	61.6%	67.9%	72.6%	77.0%
Number of Clad Tungsten Tubes per Rung	6	6	6	6	6
Clad Thickness (cm)	0.0127	0.0127	0.0127	0.0127	0.0127
Center Hole Diameter (cm)	0.2032	0.2032	0.2032	0.2032	0.2032
Tungsten Ring Thickness (cm)	0.2032	0.2311	0.3048	0.3810	0.4826
Total Ring Thickness (cm)	0.2286	0.2565	0.3302	0.4064	0.5080
Flow Gap (cm)	0.1016	0.1016	0.1016	0.1016	0.1016
Rung Tube Thickness (cm)	0.0890	0.0890	0.0890	0.0890	0.0890

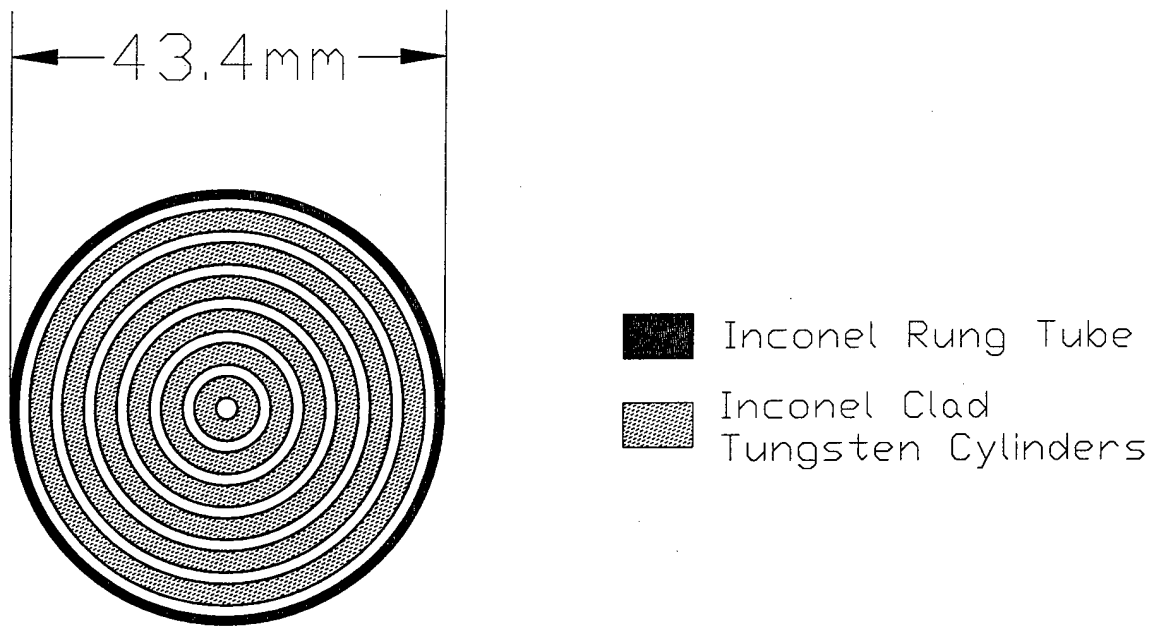


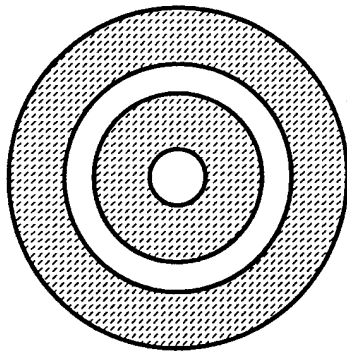


Figure 1.5: Scale Cross-Sectional View of a TNS Rung for Ladder Levels One or Two

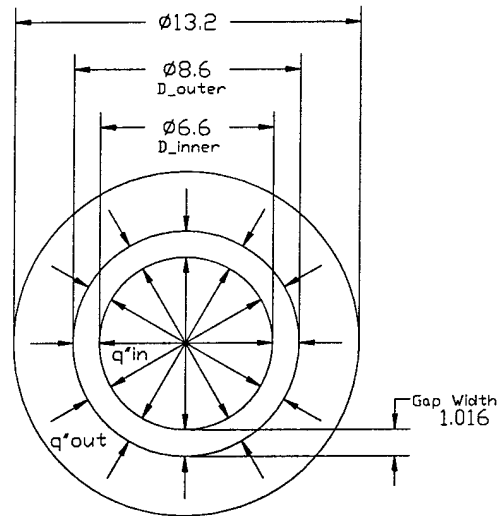
The resultant annular flow regions have a gap width of 1.016 millimeters. The inside and outside diameters are 6.6 and 8.6 millimeters, respectively, for the smallest proposed annular region in the peak power rung. The dimensions of the innermost annular channel are identical in all rungs of each ladder. An illustration of the innermost annular channel, the focus of this investigation, is shown in Figure 1.6. In addition, Table 1.1 provides a summary of the geometric data for all of the ladders and rungs in the APT target as provided by Pasamehmetoglu, et al. (1998).

 Tungsten Tube
 Inconel Cladding



0.5 inch
 1 cm

Cross Sectional View of TNS
 Rung for Ladders
 (Note Scales)



** All dimensions in millimeters.

Simplified View of Innermost
 Coolant Channel.

Figure 1.6: Simplified View of the Innermost Annular Coolant Channel

Coolant water would be provided to the horizontal assemblies through larger diameter vertical inlet and exit plenums as shown in Figure 1.4. For this reason, each rung of each ladder would be connected in parallel with the other rungs of its ladder. In addition, all ladders would be connected in parallel via the inlet and exit coolant manifolds shown in Figure 1.4.

I.4 Motivation and Objectives

As a result of the potentially severe consequences of Ledinegg flow excursion and critical heat flux, several experimental and theoretical studies have been performed by the nuclear industry to quantify the effect of various design and operational parameters on these limits. The existing experimental data and correlations are well established for channels with hydraulic diameters larger than four millimeters. The current APT design has interior coolant channels with a hydraulic diameter of roughly two millimeters. Little data exists in the literature for either OFI or CHF in such small diameter channels. To this end, Blasick (1999), conducted an investigation using light water (H_2O) to determine the effect of various parameters on OFI for a simulated APT innermost annular coolant channel. The work by Blasick (1999) covers the low heat flux range corresponding to operating conditions in off-peak APT ladder assemblies. This investigation will complement the work of Blasick (1999) by determining the effect of various parameters on OFI at high heat flux conditions corresponding to the peak power ladder assemblies in a simulated APT innermost annular coolant channel using light water. Additionally, experiments will be conducted at low mass flux conditions to determine the effect of various parameters on CHF.

The primary purpose of this investigation was to experimentally determine the effect of system parameters on OFI and CHF in heated microchannels. To this end, thirteen different experimental setups were employed to determine the OFI and CHF behavior of annular channels with hydraulic diameters on the order of two millimeters (annular gap of approximately 1.0 mm). The OFI data were then compiled and used to

create two correlations; one comparing OFI heat flux to saturation heat flux and the other comparing OFI mass flux to saturation mass flux. The CHF data acquired in this investigation were compared with several empirical CHF correlations available in the literature and used to demonstrate that OFI, rather than CHF, is the limiting phenomenon in microchannel heat transfer. No new correlations were developed for CHF in microchannels. In conclusion, the data obtained in this investigation were used to quantify the thermal margins for the proposed APT target bundle geometry under both normal operation and accident conditions.

The remainder of this thesis is organized as follows. Chapter II provides a brief overview of the literature available on OFI and CHF in small diameter channels. Chapter III gives a detailed description of the instrumentation and equipment used in all experiments performed during this investigation. Chapter IV outlines the experimental procedures used to setup and perform all OFI and CHF experiments. All OFI and CHF experimental results are reported and compared with available models in Chapter V. Finally, Chapter VI summarizes the conclusions of this investigation and provides recommendations for future microchannel heat transfer research.

CHAPTER II

LITERATURE REVIEW

II.1 Introduction

Two phase flow instability can lead to serious safety problems in the operation of heated channels supporting forced and natural circulatory flows. For this reason, it is important in the design of heated channels to understand and predict the onset of boiling and two phase flow instabilities that can lead to channel dry-out and potential overheating of the system. Reviews of flow instability and critical heat flux have been published by McBeth, et al. (1964), Bowring (1972), Boure, et al. (1973), Ishii (1976), Bergles (1977), Yadigaroglu (1981), Groenenveld, et al. (1986), Bankoff, et al. (1991), and Caira, et al. (1993). The following is a brief overview of previous work on OFI and CHF. In addition, note that the majority of the OFI section of this chapter was derived from the literature review performed by Kennedy, et al. (1997) while the bulk of the CHF section of this chapter was adapted from Roach (1998).

II.2 Onset of Flow Instability

Two phase flow instabilities are generally categorized as either dynamic or static

(Boure, et al., 1973). Dynamic instabilities (e.g., flow regime oscillations) involve transient inertial dynamic and feedback effects and lead to oscillatory flows, which can be analyzed using the transient flow conservation equations. Modeling system behavior during dynamic oscillations, however, requires numerical solution of nonlinear conservation equations when perturbations are imposed on the flow (Gurgenci, et al., 1983). Dynamic instabilities occur over a broad range of conditions and become serious safety problems when their amplitudes become large.

Static instabilities result from pressure drop vs flow rate characteristics of heated channels and can be analyzed using steady state flow conservation equations. The typical demand curve (steady state pressure drop versus flow rate) of a boiling channel has an inverted S-shape (Figure 1.1). The different two phase flow regimes for heated channels are shown in Figure 1.3. As described in Chapter I, when the channel is part of a forced circulation loop, the segment of the demand curve with negative slope can be unstable depending on pump characteristics. If the mass flow rate through the channel drops below the local minimum point on the curve, then a flow excursion can occur resulting in a significant reduction in the flow rate through the channel. Such flow excursions can lead to physical burnout of the heated channel (Roach, 1998).

The onset of flow instability (OFI) is known to occur at a slightly lower flow rate than the flow rate corresponding to the onset of significant void. The onset of significant void (OSV) occurs when a further reduction in flow rate results in a sharp increase in coolant void fraction in the channel. Consequently, the pressure drop due to flow acceleration resulting from increased voidage renders the gradient of the demand curve

negative. OSV can therefore be considered a conservative criterion for avoiding classic Ledinegg flow excursions (Yadigaroglu, 1981). Furthermore, OSV signifies the initiation of bulk boiling in the subcooled flow boiling regime. If significant void fraction develops in a nuclear reactor, then reactor power may be affected (Kennedy, et al., 1997).

In the past, OSV and void fraction have been extensively studied in channels experiencing subcooled boiling (Whittle and Forgan, 1967; Evangelisti and Lupoli, 1969; Chan, 1984; Rogers, et al., 1987; Johnston, 1989; Ahmad, 1970; Dix, 1971; Levy, 1967; Staub, 1968; Unal, 1975). Most of the published studies, however, deal with OSV and OFI in relatively large channels. In this investigation, the onset of flow instability in a horizontal, annular microchannel subject to a uniform and constant wall heat flux is experimentally investigated. The efforts are motivated by the need to assess the thermal limits for the concentric, annular target coolant channels in the proposed Accelerator Production of Tritium (APT) system. The hydraulic diameter of these coolant channels is significantly smaller than the parameter ranges covered by the existing models and data (Kennedy, et al., 1997).

OSV, OFI, and other related phenomena may occur in research reactors where flow channels typically have small hydraulic diameters. However, systematic studies dealing with OSV and OFI in microchannels are scarce. Inasaka, et al. (1989) measured subcooled boiling pressure drop in channels with diameter of 1.0 mm and larger. They noted that the onset of nucleate boiling (ONB) point was well predicted by the correlation of Bergles and Rohsenow (1964), while the correlations of Saha and Zuber (1974) and

Levy (1967) both failed to predict OSV data well in small channels. Their measured two phase friction factor multipliers for capillaries, however, were considerably smaller than the values predicted by the Lockhart and Martinelli (1949) correlation. Inasaka, et al. (1989) attribute the latter discrepancy to the possible overprediction of quality in capillaries by Ahmad's correlation (Ahmad, 1970). Hainoun, et al. (1996) recently reported a two fluid model capable of predicting OFI phenomenon in small channels. Their model applies the aforementioned correlation of Saha and Zuber (1974) for the prediction of OSV.

II.2.1 Flow Instability Initiation

During a hypothetical loss of coolant accident, the coolant flow rate through the heated channels decreases. Under normal operating conditions, the coolant remains subcooled and thus single phase. However, if a substantial drop in flow rate occurs, the onset of nucleate boiling (ONB) may ensue. Bankoff, et al. (1991) presented a comprehensive review of ONB and the mechanics of bubble formation and departure. At the ONB point, bubbles begin to form on the walls of the heated channel. Due to the subcooled status of the bulk coolant, these bubbles either collapse or slide along the channel walls; they do not separate and survive in the bulk flow. The presence of the bubbles on the walls causes the differential pressure across the test section to increase. In turn, the friction factor rises due to the increased differential pressure across the channel. When vapor generation becomes great enough, the bubbles detach from the walls and survive in the subcooled, bulk coolant flow. This is known as the onset of significant

void (OSV). Vapor bubbles in the bulk flow act to lower the average density of the fluid within the channel. The increased apparent friction factor coupled with the increased acceleration term causes the differential pressure across the channel to rise. In parallel channels with an imposed external pressure difference, the flow can easily become unstable and possibly dry out due to a flow excursion (Bankoff, et al., 1991; Lahey and Moody, 1979).

In practice, limits are imposed on channel power input over all anticipated flow rates to avoid operation within the negative sloped region of the demand curve. This measure prevents Ledinegg flow excursions during both normal and accident conditions. At low flow rates, the power limits dictated by the flow excursion are considerably lower than those corresponding to critical heat flux (CHF). Therefore, OFI is the limiting criterion for establishing the maximum power level for safe operation of the system. For high mass flux, however, CHF may become more limiting than OFI. Generally, the design and safety analysis of practical systems require that both criteria be satisfied with an adequate safety margin corresponding to a designer specified confidence level (Kennedy, et al., 1997).

II.2.2 Onset of Significant Void

Many models and correlations exist which predict OSV. Some of these models are based on theoretical arguments while others are based on empirical analysis. In general, two phase flow phenomena are difficult to model theoretically which explains the development and use of empirical correlations. Examples of commonly accepted

formulations include those reported by Bowring (1962), Saha and Zuber (1974), and Unal(1975). Some correlations such as Levy (1967), Staub (1968), and Rogers, et al. (1987) incorporate a theoretical model with empirical adjustments.

II.3 Review of OSV Models

In this section, various theoretical and empirical OSV models published in the literature are reviewed; Bankoff, et al. (1991), reported a comprehensive examination of the subject. The more widely reported correlations and their ranges of applicability are summarized in Tables 2.1 through 2.10, while Tables 2.11 through 2.13 summarize recent OFI correlations produced at Georgia Tech by Kennedy, et al. (1997), Roach (1998), and Blasick (1999) in conjunction with the APT project.

II.3.1 Theoretical OSV Models

Theoretical OSV models are based on vapor bubble mechanics in vertical, upward, subcooled flow. The mechanics involved in analyzing bubble behavior focus on the heat transfer and fluid flow at the bubble-liquid interface. Bubble departure is determined by performing a force balance. Three aspects of the bubble-liquid interface combine to determine when the bubble will depart the channel wall: buoyancy of the bubble within the liquid, shear force exerted on the bubble by the flowing liquid, and the surface tension which holds the bubble to the wall (Kennedy, et al., 1997).

Of the three OSV correlations described by Bankoff, et al. (1991), the one proposed by Levy (1967) is the simplest. Summarized in Table 2.1, the Levy correlation is valid for water under the following conditions: mass flux range of 130 to 1420 kg/m²s, operating pressure between 0.41 and 13.6 MPa, and heat flux from 0.24 to 1.91 MW/m².

The model of Staub (1968) is described in Table 2.2 and is applicable for two channel geometries: circular with hydraulic diameter between 0.006 and 0.20 meter and rectangular with hydraulic diameter between 0.004 and 0.066 meter. The correlation is valid for both water and R-22, but no range is specified for the applicable heat fluxes.

The correlation of Rogers, et al. (1987) is more specific and therefore more restricted than those of Levy and Staub. As tabulated in Table 2.3, this correlation is only valid for annular tube geometry with three specific hydraulic diameters: 0.009, 0.012, and 0.017 meter. Also, this correlation only holds for tube lengths of 0.48 and 0.60 meter. The correlation is valid for water under the following conditions: mass flux range of 70 to 450 kg/m²s, operating pressure between 1.50 and 1.55 MPa, and heat flux from 0.3 to 1.2 MW/m².

Even though the analytical models of OSV are similar, it is interesting to note that different bubble shapes are assumed. Levy assumed a spherical shaped bubble, Staub assumed a hemispherical bubble that took on the contour of the channel, and Rogers, et al. assume that the bubble was a truncated sphere, with a contact angle at the surface equal to the equilibrium contact angle (Bankoff, 1991).

II.3.2 Empirical OSV Models

Often it is easier to use empirical correlations as opposed to theoretical models for OSV prediction due to the complex mechanisms that exist in two phase flow. Several empirical models are summarized in Tables 2.4 through 2.13. Note that for each of these correlations, the liquid subcooling at the OSV point can be expressed as a function of pressure, hydraulic diameter, heated length, heat flux, mass flux, inlet temperature, and fluid properties at designated temperature and pressure. For example, a pressure term is used in the Bowring (1962) correlation while other correlations only consider the effect of pressure on fluid properties. It is also interesting to note that Bowring (1962) and Thom, et al. (1966) are the only dimensional correlations; Saha and Zuber (1974), Unal (1975), Ahmad (1970), and Sekoguchi, et al. (1974) are all dimensionless. In fact, the Saha and Zuber (1974) correlation includes both the Stanton and Nusselt numbers. This signifies that under low mass flux conditions, flow behavior is thermally controlled, while under high mass flux conditions, flow behavior is hydrodynamically controlled. The Unal (1975) correlation suggests a similar split into two different regimes that depend on flow velocity.

The theoretical models described above have been compared with the empirical models. Both the theoretical Levy (1967) correlation and the empirical Bowring (1962) correlation predict that as liquid flow rate through the channel increases, the degree of subcooling at the OSV point decreases. Similarly, the theoretical Staub (1968) correlation was compared with the empirical models of Costa (1967), Griffith, et al. (1968), Christensen (1961), and Kroeger and Zuber (1968). The experimental data as

compared to the predictions of the Staub (1968) correlation were 15% higher for circular channels and 15% lower for rectangular channels.

All models reviewed did not deal with microchannels. The size range was generally limited to channels with hydraulic diameter greater than 4 millimeters. Peng and Wang (1993) have provided evidence indicating significant differences between the characteristics of boiling microchannels and larger channels. The aim of this investigation was to examine the effect of microchannel geometry and operating conditions on OFI. Comparisons were made between experimental OFI data and predictions of the more widely used OSV models.

Table 2.1: Levy's Theoretical OSV Model (1967)

Author:	Levy (1967)
Model Type:	Theoretical, Dimensionless
Tube Shape:	No Restriction
Tube Diameter:	No Restriction
Tube Length:	No Restriction
Tube Orientation:	Vertical
Flow Direction:	Upwards
Medium:	Water
Mass Flux:	130 to 1420 (kg/m ² s)
Pressure:	0.41 to 13.6 (MPa)
Heat Flux:	0.24 to 1.91 (MW/m ²)

Model

Dimensional Distance to Tip of Bubble:

$$Y_B^+ = 0.015 \frac{\sqrt{\sigma D_h \rho_f}}{\mu_f}$$

Heat Transfer Coefficient:

$$h = 0.023 \frac{k_f}{D_h} \text{Re}_f^{0.8} \text{Pr}_f^{0.4}$$

Wall Shear and Friction Factor:

$$\tau_w = \frac{f}{8} \rho_f V_f^2$$

$$f = 0.0055 \left[1 + \left(20,000 \frac{\varepsilon}{D_h} + \frac{10^6}{\text{Re}_f} \right)^{1/3} \right]$$

$$\frac{\varepsilon}{D_h} = 10^{-4}$$

Table 2.1 (continued)

Heat Flux Parameter:

$$Q = \frac{q''}{\rho_f C_{pf} \sqrt{\frac{\tau_w}{\rho_f}}}$$

Conditions for Onset of Bubble Departure:

$0 < Y_B^+ < 5$	$T_s - T_{f,d} = \frac{q''}{h} - Q \text{Pr}_f Y_B^+$
$5 < Y_B^+ < 30$	$T_s - T_{f,d} = \frac{q''}{h} - 5Q \left\{ \text{Pr}_f + \ln \left[1 + \text{Pr}_f \left(\frac{Y_B^+}{5} - 1 \right) \right] \right\}$
$Y_B^+ > 30$	$T_s - T_{f,d} = \frac{q''}{h} - 5Q \left\{ \text{Pr}_f + \ln [1 + \text{Pr}_f] + 0.5 \ln \left[\frac{Y_B^+}{30} \right] \right\}$

Table 2.2: Staub's Theoretical OSV Model (1968)

Author:	Staub (1968)
Model Type:	Theoretical, Dimensionless
Tube Shape:	Circular, Rectangular
Tube Diameter:	0.006 to 0.020 (m), 0.004 to 0.066 (m)
Tube Length:	Unknown
Tube Orientation:	Vertical
Flow Direction:	Upwards
Medium:	Water, R-22
Flow Rate:	0.5 to 8.0 (m/s), 0.1 to 0.9 (m/s)
Pressure:	0.17 to 6.8 (MPa)
Heat Flux:	Unknown

Model

Bubble Diameter:

$$\frac{f\rho_f V_f^2 D_B}{32g\sigma f(\beta)} + \frac{D_B^2(\rho_f - \rho_g)}{12\sigma f(\beta)} = 1.0 \quad \text{British Units}$$

$$f(\beta) = 0.02 \quad \text{for } V_f < 0.45 \text{ (m/s)}$$

$$f(\beta) = 0.03 \quad \text{for } V_f > 0.45 \text{ (m/s)}$$

Dimensionless Distance to Tip of Bubble:

$$Y_B^+ = 0.5D_B \frac{\rho_f V_f \sqrt{\frac{f}{8}}}{\mu_f}$$

Wall Shear and Friction Factor:

$$f = \frac{8\tau_w}{\rho_f V_f^2} = f\left(\text{Re}, \frac{D_B}{2D}\right)$$

Table 2.2 (continued)

Conditions for Initial Point of Net Vapor Generation (IPNVG):

$$0 < Y_B^+ < 5 \quad T_s - T_{f,d} = Q \left\{ \text{Pr}_f (5 - Y_B^+) + 5 \ln(1 + 5 \text{Pr}_f) + 2.5 \left[\frac{\ln Y_C^+ / 30}{1 - 30 / Y_C^+} - 1 \right] \right\}$$

$$5 < Y_B^+ < 30 \quad T_s - T_{f,d} = Q \left\{ 5 \ln \left[\frac{1 + 5 \text{Pr}_f}{1 + \text{Pr}_f (Y_B^+ / 5 - 1)} \right] + 2.5 \left[\frac{\ln Y_C^+ / 30}{1 - 30 / Y_C^+} - 1 \right] \right\}$$

$$Y_B^+ > 30 \quad T_s - T_{f,d} = 2.5 Q \left[\frac{\ln Y_C^+ / Y_B^+}{1 - Y_B^+ / Y_C^+} - 1 \right] \left(1 - Y_B^+ / Y_C^+ \right)$$

Where:

$$Y_C^+ = \frac{D}{2} \frac{\rho_f V_f \sqrt{f}}{\mu_f}$$

$$Q = \frac{q''}{C_{pf} \rho_f V_f \sqrt{f}}$$

Table 2.3: Rogers, et al. Theoretical OSV Model (1987)

Author:	Rogers, et al. (1987)
Model Type:	Theoretical, Dimensionless
Tube Shape:	Annulus
Tube Diameter:	$D_h = 0.009, 0.0012, 0.0017$ (m)
Tube Length:	0.48, 0.60 (m)
Tube Orientation:	Vertical
Flow Direction:	Upwards
Medium:	Water
Mass Flux:	70 to 450 (kg/m ² s)
Pressure:	1.50 to 1.55 (MPa)
Heat Flux:	0.3 to 1.2 (MW/m ²)

Model

Dimensionless Distance to Tip of Bubble:

$$Y_B^+ = \frac{\rho_f}{\mu_f} \sqrt{\frac{\tau_w}{\rho_f}} (1 + \cos \theta_0) \left[\frac{3}{4\pi} \frac{c_2}{c_1} \frac{C_d \mu_f^2}{g} \right] \lambda$$

Where:
$$\lambda = \left[1 + \frac{8\pi^2}{3} \frac{c_1 c_2 c_s g \sigma}{c_2^2 C_d^2 \rho_f \mu_r^4} \right]^{0.5} - 1$$

$$c_1 = 2 + 3 \cos \theta_0 - \cos^3 \theta_0$$

$$c_2 = \pi - \theta_0 + \cos \theta_0 \sin \theta_0$$

$$c_3 = \sin \theta_0 [\cos(\theta_0 - 10) - \cos(\theta_0 + 10)]$$

$$c_s = \frac{58}{\theta_0 + 5} + 0.14$$

$$C_d = 1.22 \quad \text{for } 20 < \text{Re}_B < 40$$

$$C_d = \frac{24}{\text{Re}_B} \quad \text{for } 4 < \text{Re}_B < 20$$

Table 2.3 (continued)

$$\text{Re}_B = \frac{\rho_f u_r (2r_B)}{\mu_f}$$

Calculation of u_r :

$$Y_r^+ = 0.5 Y_B^+ (1 + \cos \theta_0)$$

$$Y_r^+ < 5.0$$

$$u_r^+ = Y_r^+$$

$$5.0 < Y_r^+ < 30$$

$$u_r^+ = 5.0 \ln Y_r^+ - 3.08$$

$$Y_r^+ > 30$$

$$u_r^+ = 2.5 \ln Y_r^+ + 5.5$$

Wall Shear and Friction Factor:

$$f = \frac{8\tau_w}{\rho_f V_f^2} = 0.046 \text{Re}^{-0.20}$$

Calculation of T_B^+ :

$$Y_B^+ < 5.0$$

$$T_B^+ = \text{Pr}_f Y_B^+$$

$$5.0 < Y_B^+ < 30$$

$$T_B^+ = 5 \left[\text{Pr}_f + \ln \left\{ 1 + \text{Pr}_f \left(\frac{Y_B^+}{5} - 1 \right) \right\} \right]$$

$$Y_B^+ > 30$$

$$T_B^+ = 5 \left[\text{Pr}_f + \ln(1 + 5 \text{Pr}_f) + 5.0 \ln \left(\frac{Y_B^+}{30} - 1 \right) \right]$$

Conditions for OSV:

$$T_s - T_{f,d} = q'' \left[\frac{1}{F_R h} - \frac{T_B^+}{C_{pf} \rho_f \sqrt{\frac{\tau_w}{\rho_f}}} \right]$$

Where:

$$\text{Nu} = 0.023 \text{Re}_f^{0.8} \text{Pr}_f^{0.4}$$

$$F_R = 1.11 + -0.036 \quad \text{for } \theta_0 = 30^\circ$$

$$F_R = 1.06 + -0.022 \quad \text{for } \theta_0 = 80^\circ$$

Table 2.4: Bowring's Empirical OSV Correlation (1962)

Author:	Bowring (1962)
Model Type:	Empirical, Dimensional
Tube Shape:	Unknown
Tube Diameter:	Unknown
Tube Length:	Unknown
Tube Orientation:	Unknown
Flow Direction:	Unknown
Medium:	Water
Mass Flux:	Unknown
Pressure:	1.1 to 13.8 (MPa)
Heat Flux:	Unknown

Model

$$T_s - T_{f,d} = \eta \frac{q''}{V_f}$$

Where: $\eta = 10^{-6}(14.0 + P)$

Table 2.5: Thom, et al. Empirical OSV Correlation (1966)

Author:	Thom, et al. (1966)
Model Type:	Empirical, Dimensional
Tube Shape:	Unknown
Tube Diameter:	Unknown
Tube Length:	Unknown
Tube Orientation:	Vertical
Flow Direction:	Upwards
Medium:	Water
Mass Flux:	Unknown
Pressure:	5.14 to 6.80 (MPa)
Heat Flux:	Unknown

Model

$$T_s - T_{f,d} = 0.02 h_{fs} \frac{q''}{G h_{fg}}$$

Table 2.6: Ahmad's Empirical OSV Correlation (1970)

Author:	Ahmad (1970)
Model Type:	Empirical, Dimensionless
Tube Shape:	Circular, Rectangular
Tube Diameter:	0.004 to 0.007 (m)
Tube Length:	Unknown
Tube Orientation:	Vertical
Flow Direction:	Upwards
Medium:	Water
Mass Flux:	Less than 8000 (kg/m ² s)
Pressure:	0.17 to 0.5 (MPa), 8.3 and 11.0 (MPa)
Heat Flux:	Unknown

Model

$$T_s - T_{f,d} = \frac{q''}{h}$$

$$h = 2.44 \frac{k_f}{D_h} \text{Re}_f^{0.5} \text{Pr}_f^{1/3} \left(\frac{h_{fi}}{h_{fs}} \right)^{1/3} \left(\frac{h_{fg}}{h_{fs}} \right)^{1/3}$$

Table 2.7: Dix's Empirical OSV Correlation (1971)

Author:	Dix (1971)
Model Type:	Empirical, Dimensionless
Tube Shape:	Annulus
Tube Diameter:	0.018 (m)
Tube Length:	1.07 (m)
Tube Orientation:	Vertical
Flow Direction:	Upwards
Medium:	R-114
Mass Flux:	100 to 210 (kg/m ² s)
Pressure:	0.32 and 0.85 (MPa)
Heat Flux:	0.004 to 0.03 (MW/m ²)

Model

$$T_s - T_{f,d} = 0.00135 \frac{q''}{h} \text{Re}_f^{1/2}$$

Table 2.8: Saha and Zuber Empirical OSV Correlation (1974)

Author:	Saha and Zuber (1974)
Model Type:	Empirical, Dimensionless
Tube Shape:	Circular, Rectangular, Annulus
Tube Diameter:	0.01 to 0.24 (m), 0.004 to 0.012 (m), 0.012 to 0.026 (m)
Tube Length:	Unknown
Tube Orientation:	No Restriction
Flow Direction:	No Restriction
Medium:	Water, R-22, R-114
Mass Flux:	Unknown
Pressure:	0.1 to 13.8 (MPa), 1.1 to 13.8 (MPa), 0.32, 0.85 (MPa)
Heat Flux:	Unknown

Model

$$Nu = \frac{q'' D_h}{k_f (T_s - T_{f,d})} = 455 \quad \text{for } Pe \leq 70,000$$

$$St = \frac{q''}{GC_{pf} (T_s - T_{f,d})} = 0.0065 \quad \text{for } Pe > 70,000$$

Where:

$$Pe = \frac{Nu}{St} = Re Pr = \frac{GD_h C_{pf}}{k_f}$$

Table 2.9: Sekoguchi, et al. Empirical OSV Correlation (1974)

Author:	Sekoguchi, et al. (1974)
Model Type:	Empirical, Dimensionless
Tube Shape:	Annulus
Tube Diameter:	0.002 to 0.003 (m)
Tube Length:	0.7 to 4.5 (m)
Tube Orientation:	Vertical
Flow Direction:	Upwards
Medium:	Water
Mass Flux:	310 to 2100 (kg/m ² s)
Pressure:	0.14 to 1.6 (MPa)
Heat Flux:	0.05 to 1.75 (MW/m ²)

Model

$$T_s - T_{f,d} = 13.5 \frac{h_{fg}}{C_{pf}} \left(\frac{q''}{h_{fg} G} \right)^{0.65}$$

Table 2.10: Unal's Empirical OSV Correlation (1975)

Author:	Unal (1975)
Model Type:	Empirical, Dimensionless
Tube Shape:	Circular, Rectangular, Annulus
Tube Diameter:	0.004 to 0.020 (m)
Tube Length:	Unknown
Tube Orientation:	No Restriction
Flow Direction:	No Restriction
Medium:	Water, R-22
Mass Flux:	132 to 2818 (kg/m ² s), 180 to 1391 (kg/m ² s)
Pressure:	0.1 to 15.8 (MPa), 1.2 and 3.3 (MPa)
Heat Flux:	0.15 to 1.92 (MW/m ²), 0.02 to 0.06 (MW/m ²)

Model

$$\frac{h(T_s - T_{f,d})}{q''} = a \quad (a = \text{constant})$$

For Water:	a = 0.24	(V _f > 0.45 m/s)
	a = 0.11	(V _f < 0.45 m/s)
For R-22:	a = 0.18	(V _f > 0.45 m/s)
	a = 0.11	(V _f < 0.45 m/s)

Heat Transfer Coefficient:

$$\frac{hD_h}{k_f} = 0.023 \text{Re}_f^{0.8} \text{Pr}_f^{0.4} \quad \text{for circular and rectangular tubes}$$

$$\frac{hD_h}{k_f} = 0.020 \left(\frac{D_o}{D_i} \right)^{0.53} \text{Re}_f^{0.8} \text{Pr}_f^{0.4} \quad \text{for annulus}$$

Table 2.11: Kennedy, et al. Empirical OFI Correlation (1997)

Author:	Kennedy, et al. (1997)
Model Type:	Empirical
Tube Shape:	Circular and Prototypical
Tube Diameter:	1.131 to 1.445 (mm)
Tube Length:	0.16 (m)
Tube Orientation:	Horizontal
Medium:	Water
Mass Flux:	800 to 4500 (kg/m ² s)
Pressure:	0.344 to 1.034 (MPa)
Heat Flux:	1.0 to 4.0 (MW/m ²)

Model

$$(\Delta T_{subcooling})_{OFI} = 10.0 \pm 8.7^{\circ}C$$

$$q''_{OFI} = 0.90 q''_{sat} \pm 6.9\%$$

$$G_{OFI} = 1.11 G_{sat} \pm 6.3\%$$

Table 2.12: Roach Empirical OFI Correlation (1998)

Author:	Roach (1998)
Model Type:	Empirical
Tube Shape:	Prototypical
Tube Diameter:	1.131 to 1.445 (mm)
Tube Length:	0.16 (m)
Tube Orientation:	Horizontal
Medium:	Water
Mass Flux:	125 to 950 (kg/m ² s)
Pressure:	0.344 to 1.034 (MPa)
Heat Flux:	0.1 to 0.5 (MW/m ²)

Model

Fully-Degassed:

$$q''_{OFI} = 1.1q''_{sat} \pm 10\%$$

$$G_{OFI} = 0.89G_{sat} \pm 10\%$$

Air-Saturated:

$$q''_{OFI} = 1.07q''_{sat} \pm 10\%$$

$$G_{OFI} = 0.91G_{sat} \pm 10\%$$

Table 2.13: Blasick, Empirical OFI Correlation (1999)

Author:	Blasick (1999)
Model Type:	Empirical
Tube Shape:	Annulus
Tube Diameter:	1.448 to 2.002 (mm)
Tube Length:	0.19 (m)
Tube Orientation:	Horizontal
Medium:	Water
Mass Flux:	85 to 1428 (kg/m ² s)
Pressure:	0.344 to 1.034 (MPa)
Heat Flux:	0.124 to 1.0 (MW/m ²)

Model

$$q''_{OFI} = 0.900q''_{sat} \pm 11.3\%$$

$$G_{OFI} = 1.086G_{sat} \pm 9.90\%$$

II.4 Critical Heat Flux

Forced flow critical heat flux (CHF) is an important design limitation for industrial systems. Recent experimental studies have provided understanding of the basic phenomenology of various modes of CHF. In vertical, upward flow channels, CHF may occur in three different patterns. These basic patterns are illustrated in Figure 2.1. First, at high void fraction, annular-dispersed flow is common and ultimately results in channel film dryout (Diagrams "C" & "D" of Figure 2.1). Second, when the flow is in the slug or plug regime, the dryout of the liquid film layer between the slug and the wall leads to localized CHF events (Diagram "B" of Figure 2.1). Third, in high mass flux systems, departure from nucleate boiling will occur at low quality. Coalescence of bubbles on the heated surface leads to local critical void fraction which, in turn, leads to the evaporation of the liquid layer between the bubble region and the heated surface (Diagram "A" of Figure 2.1). For high mass flux systems using highly subcooled coolant, CHF is generally attributed to departure from nucleate boiling (DNB) by the mechanism just described. It has been determined that the critical heat flux will actually increase as channel diameter decreases. The formation of bubbles at the channel walls will be hampered in channels with very small diameters (i.e., microchannels), therefore, CHF will occur at higher heat fluxes. In this study, the coolant mass fluxes will be extremely low. It is therefore expected that channel dryout will be the primary cause of CHF. For CHF driven by dryout, the effect of diameter will be inverted (Roach, 1998).

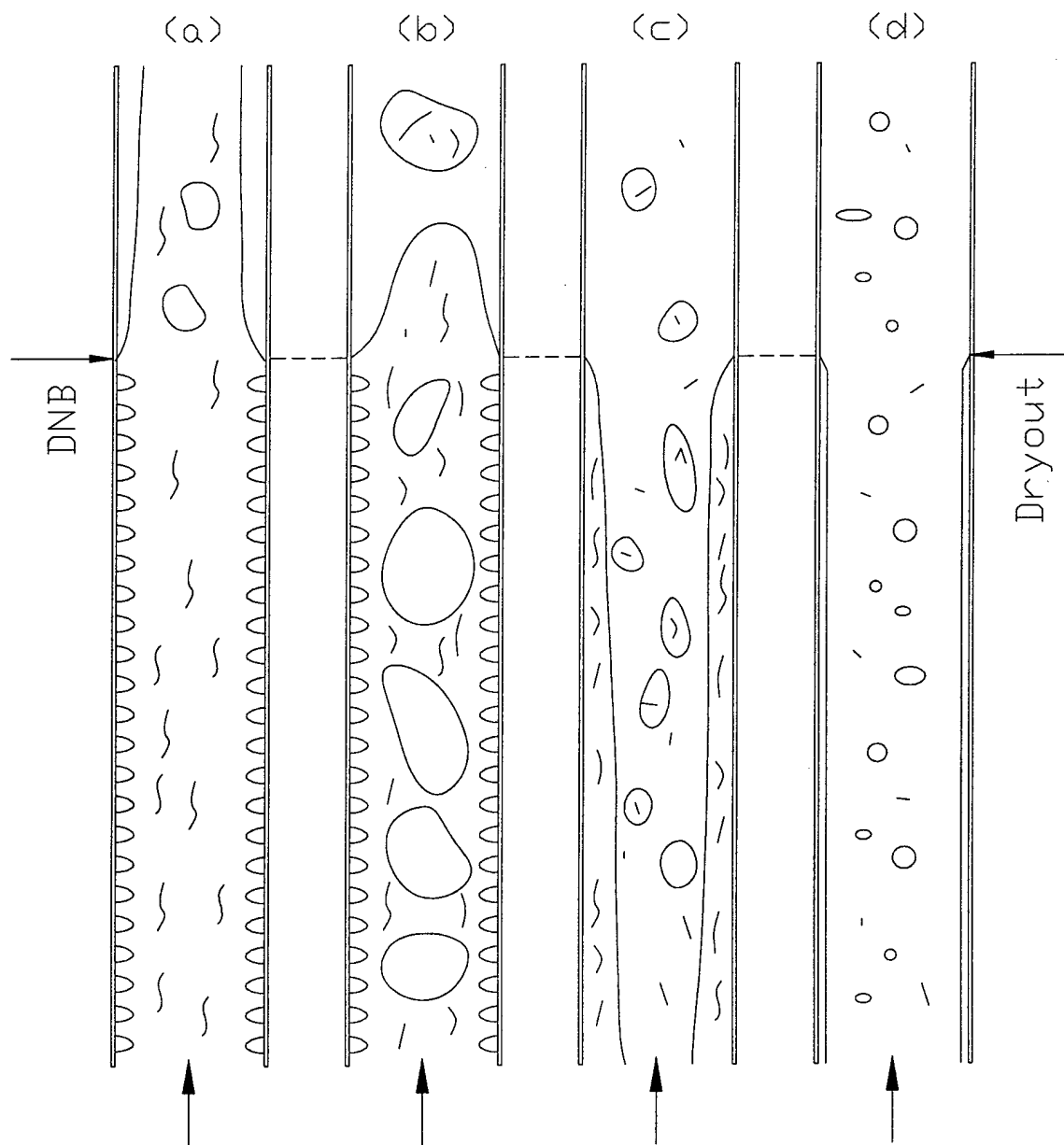


Figure 2.1: CHF Mechanisms for Various Flow Regimes in Upward Flow

II.5 Review of CHF Models

In this section, various empirical and tabular CHF models published in the literature are reviewed. The more widely reported correlations and their ranges of applicability are reported in Tables 2.14 through 2.17.

II.5.1 Empirical CHF Correlations

The thermal-hydraulics group of the APT design team used the Bowring (1972) correlation to predict CHF in the peak power coolant channels. This correlation is ideal for the APT target coolant channels in that its heated length, pressure, and mass flux ranges cover the design parameter ranges under investigation. The extremely broad pressure (0.2 to 19.0 MPa) and mass flux (136 to 18,600 kg/m²s) ranges make this one of the most useful CHF correlations in the literature (Todreas and Kazimi, 1990). The Bowring (1972) correlation along with its ranges of applicability is listed in Table 2.14.

The Caira (1993) correlation was developed with data from uniformly heated circular, rectangular, and annular vertical upflow channels. The correlation is applicable for 0.1 to 8.4 MPa pressure, 2000 to 9000 kg/m²s coolant mass flux, 0.3 to 25.4 mm diameter, and 10 to 61 cm heated length. In predicting CHF, the Caira (1993) correlation incorporates three dimensionless parameters strictly dependent on hydraulic diameter and mass flux. This correlation along with its ranges of applicability is listed in Table 2.15.

The McBeth (1964) correlation was developed from a compilation of burnout data derived from uniformly heated round tubes with vertical upflow. There are two relations

predicting CHF, one for low velocity flow and one for high velocity flow. The minimum value between these two relations is the predicted CHF value. The correlation is valid over a pressure range of 0.1 to 12.1 MPa, a diameter range of 1 to 37.5 mm, and a heated length range of 2.54 to 366 cm (VIPRE – 01 Reference Manual). This correlation along with its ranges of applicability is listed in Table 2.16

The CISE-4 correlation is a modification of CISE-3 in which the critical flow quality (x_c) approaches unity as the mass flux decreases to zero. This correlation is based on the quality-boiling length concept and is typically restricted to boiling water reactor applications. The CISE correlation can be applied to rod bundles by including the ratio of heated to wetted perimeters as shown in Table 2.17 (Todreas and Kazimi, 1990).

II.5.2 Tabular CHF Correlation

The Groeneveld (1986) correlation uses a dimensionless table to predict CHF in uniformly heated 8 mm diameter round channels. This value can then be converted to a CHF value for channels 2 to 16 mm in diameter. The dimensionless tabular value of CHF is determined by entering in the exit quality and two dimensionless quantities that are based on geometry and fluid properties (e.g. density, surface tension, diameter, and mass flux). This correlation involves a tremendous amount of interpolation and extrapolation, and hence is subject to inherent inaccuracies. The dimensionless parameters associated with the Groeneveld (1986) CHF correlation are given in Table 2.18.

Table 2.14: Bowring's Empirical CHF Correlation (1972)

Author:	Bowring (1972)
Model Type:	Empirical
Tube Shape:	Circular
Tube Diameter:	0.002 to 0.045 (m)
Tube Length:	0.15 to 3.7 (m)
Tube Orientation:	Horizontal
Medium:	Water
Mass Flux:	136 to 18,600 (kg/m ² s)
Pressure:	0.2 to 19.0 (MPa)
Heat Flux:	Unknown

Model

$$q''_{CHF} = \frac{A - DGh_{fg}x}{4C}$$

$$A = \frac{2.317 \left(\frac{h_{fg}DG}{4} \right) F_1}{1 + 0.0143 F_2 G \sqrt{D}}$$

$$n = 2.0 - 0.5 P_R$$

$$C = \frac{0.077 F_3 DG}{1 + 0.347 F_4 \left(\frac{G}{1356} \right)^n}$$

$$P_R = 0.145 P$$

$$F_1 = \frac{P_R \exp[20.89(1 - P_R) + 0.917]}{1.917}$$

$$F_3 = \frac{P_R^{17.023} \exp[16.658(1 - P_R) + 0.667]}{1.667}$$

$$F_2 = \frac{1.309 F_1}{P_R^{1.316} \exp[2.444(1 - P_R) + 0.309]}$$

$$F_4 = F_3 P_R^{1.649}$$

Table 2.15: Caira, et al. Empirical CHF Correlation (1993)

Author:	Caira, et al. (1993)
Model Type:	Empirical
Tube Shape:	Circular and Annular
Tube Diameter:	0.03 to 25.4 (mm)
Tube Length:	10 to 61 (cm)
Tube Orientation:	Vertical
Flow Direction:	Upwards
Medium:	Water
Mass Flux:	2000 to 9000 (kg/m ² s)
Pressure:	0.1 to 8.4 (MPa)
Heat Flux:	Unknown

Model

$$q''_{CHF} = \frac{\phi + [0.25(h_f - h)_{inlet}]^{y_3} \theta}{1 + \Omega L^{y_{10}}}$$

$$\phi = y_0 D^{y_1} G^{y_2}$$

$$\theta = y_4 D^{y_5} G^{y_6}$$

$$\Omega = y_7 D^{y_8} G^{y_9}$$

$$y_0 = 10829.55$$

$$y_1 = -0.0547$$

$$y_2 = 0.713$$

$$y_3 = 0.978$$

$$y_4 = 0.188$$

$$y_5 = 0.486$$

$$y_6 = 0.462$$

$$y_7 = 0.188$$

$$y_8 = 1.2$$

$$y_9 = 0.36$$

$$y_{10} = 0.911$$

Table 2.16: McBeth, et al. Empirical CHF Correlation (1964)

Author:	McBeth, et al. (1964)
Model Type:	Empirical
Tube Shape:	Circular
Tube Diameter:	0.04 to 1.475 (in)
Tube Length:	1.0 to 144.0 (in)
Tube Orientation:	Vertical
Flow Direction:	Upwards
Medium:	Water
Mass Flux:	0.0073 to 13.7 (Mlbm/ft ² hr)
Pressure:	15 to 1750 (psia)
Heat Flux:	Unknown

Model

$$q''_{CHF} (low - vel) = 0.00633 h_{fg} D_h^{-0.1} \left(\frac{G}{10^6} \right)^{0.51} (1 - x)$$

$$q''_{CHF} (high - vel) = \frac{A' - 0.25 D_h \left(\frac{G}{10^6} \right) h_{fg} x}{C'}$$

$$q''_{CHF} = \min[q''_{CHF} (low - vel); q'' (high - vel)]$$

$$A' = y_0 D_h^{y_1} G^{y_2}$$

$$C' = y_3 D_h^{y_4} G^{y_5}$$

$$y_0 = 106.5$$

$$y_1 = 0.847$$

$$y_2 = 0.677$$

$$y_3 = 60.3$$

$$y_4 = 1.4$$

$$y_5 = 0.937$$

Table 2.17: CISE-4 CHF Correlation (1975)

Author:	Gaspari, et al. (1975)
Model Type:	Empirical
Tube Shape:	Circular
Tube Diameter:	0.0102 to 0.0198 (m)
Tube Length:	0.76 to 3.66 (m)
Tube Orientation:	Vertical
Flow Direction:	Upwards
Medium:	Water
Mass Flux:	1085 to 4069 (kg/m ² s)
Pressure:	4.96 to 6.89 (MPa)
Heat Flux:	Unknown

Model

$$x_{cr} = \frac{D_h}{D_e} \left(a \frac{L_{cr}}{L_{cr} + b} \right)$$

$$a = \frac{1}{1 + 0.0001481 \left(1 - \frac{P}{P_c} \right)^{-3} G} \quad \text{if } G \leq G^*$$

$$a = \frac{1 - \frac{P}{P_c}}{\left(\frac{G}{1000} \right)^{1/3}} \quad \text{if } G \geq G^*$$

$$G^* = 3375 \left(1 - \frac{P}{P_c} \right)^3$$

$$b = 0.199 \left(\frac{P_c}{P} - 1 \right)^{0.4} GD^{1.4}$$

Table 2.18: Groeneveld, et al. Tabular CHF Correlation (1986)

Author:	Groeneveld, et al. (1986)
Model Type:	Tabular
Tube Shape:	Circular
Tube Diameter:	2.0 to 16.0 (mm)
Tube Length:	Unknown
Tube Orientation:	Vertical
Flow Direction:	Upward
Medium:	Water
Mass Flux:	0 to 7500 (kg/m ² s)
Pressure:	0.10 to 20.0 (MPa)
Heat Flux:	Unknown

Model

Look-up Table to determine CHF for an 8 mm diameter circular tube.

$$\phi_k = \frac{GD^{0.5}}{\sigma^{0.5} \rho_f^{0.5}}$$

$$CHF_D = CHF_{8mm} \left(\frac{8}{D} \right)^{1/3}$$

CHAPTER III

INSTRUMENTATION AND EQUIPMENT

All experiments in this investigation were performed using the Georgia Tech Microchannel Test Facility (GTMTF). The GTMTF is a general purpose test facility designed to examine single and two-phase flow phenomena in microchannels. The facility was previously used by Kennedy, et al. (1997) and Roach (1998) to study OFI and CHF in microchannels with circular cross sections and with cross sections simulating coolant channels in a micro-rod bundle. Blasick (1999) later modified the GTMTF to accommodate test sections with annular flow passages simulating the innermost coolant channels in the APT target. This chapter describes the additional modifications made to the GTMTF as well as the test sections and power supplies used to perform high heat flux OFI and low mass flux CHF experiments for thin, concentric annuli.

III.1 Experimental Test Facility Overview

The GTMTF design criteria, as elucidated by Kennedy, et al. (1997), Roach (1998), and Blasick (1999), were as follows.

- 1) To provide a stable, controllable, and measurable flow of water through the test section over a broad range of mass fluxes.
- 2) To provide for a flexible system configuration and the possibility of running experiments with and without a test section bypass line.
- 3) To allow for control and measurement of the dissolved non-condensable gas content within the system.
- 4) To allow for fine control and measurement of the test section inlet temperature.
- 5) To allow for fine control and measurement of the test section exit pressure.
- 6) To provide stable, controllable, and measurable electrical power for heating of the test section.

The remaining sections of this chapter provide details on the GTMTF hardware, instrumentation, and data recording setups used in this investigation to accomplish these goals. Also, the exact design criteria and assembly specifications are detailed for each test section configuration. A total of thirteen experimental setups were used to perform all of the experiments reported in this investigation: twelve OFI setups and one CHF setup. The experimental setup number was incremented each time the test section or any component of the GTMTF was modified. Consequently, many experimental setups utilize several of the same components. In order to simplify documentation of experimental setups, each component used in an experiment was given a descriptive name and number designation that can be cross-referenced with a figure and matching description as outlined in Section III.2.

III.2 Experimental Setups

Each experiment run in this investigation utilized a uniquely definable experimental setup. As described above, a total of thirteen different experimental setups were employed in this investigation. Each setup was comprised of the following six separate, independently alterable configurations.

- 1) Flow Loop Configuration
- 2) Inner Heater Configuration
- 3) Outer Heater Configuration
- 4) Mounting Configuration
- 5) Insulation Configuration
- 6) Non-Condensable Gas Status

Each time one or more of these system configurations were altered, the setup number was sequentially increased. Table 3.1 outlines the thirteen setups used and their corresponding system configurations.

Table 3.1: Summary of Experimental Setups

Setup	Flow Loop Configuration	Inner Heater Configuration	Outer Heater Configuration	Mounting Configuration	Insulation Configuration	Non-Condensable Gas Status
1	2	1	1	1	None	Air Saturated
2	2	1	2	1	1	Air Saturated
3	2	1	3	1	None	Air Saturated
4	1	2	4	1	None	Air Saturated
5	1	3	4	1	1	Air Saturated
6	3	3	4	1	1	Nitrogen Saturated
7	3	3	4	1	None	Air Saturated (LP)*
8	3	4	5	1	1	Nitrogen Saturated
9	3	5	5	1	1	Nitrogen Saturated
10	3	6	6	2	None	Nitrogen Saturated
11	3	7	7	2	None	Nitrogen Saturated
12	3	8	7	2	None	Nitrogen Saturated
13	4	9	8	2	None	Nitrogen Saturated

* The non-condensable gas status for Setup 7 was saturated with air at atmospheric temperature and pressure. The system was pressurized using a bellows type accumulator, so no new gas was forced into the working fluid during system pressurization.

III.3 Flow Loop Configuration

A total of four flow loop configurations were used during this investigation. The flow loop was modified, depending on the experiment, in order to achieve the necessary flow rate control for a specific set of flow parameters. Before describing the flow paths employed by the different flow loop configurations, the mechanisms used by all four flow loop configurations, regardless of flow path, must be detailed. Figure 3.1 shows a schematic diagram of the GTMTF components and instrumentation used in all four flow loop configurations and Table 3.2 describes the significant hardware components in the system.

III.3.1 System Instrumentation

Table 3.3 provides a list of measuring instruments used in the GTMTF along with their manufacturer, model number, range, and accuracy.

III.3.1.1 Absolute Pressure Transducers

Four Rosemount model 1144A pressure transducers (Components 5 of Figure 3.1) were utilized in the GTMTF to measure test section inlet and exit pressure and pump inlet and exit pressure. All four transducers were mounted below the respective points where the pressure was to be measured in order to avoid potential incorrect readings caused by entrained air bubbles lodged in the transducer.

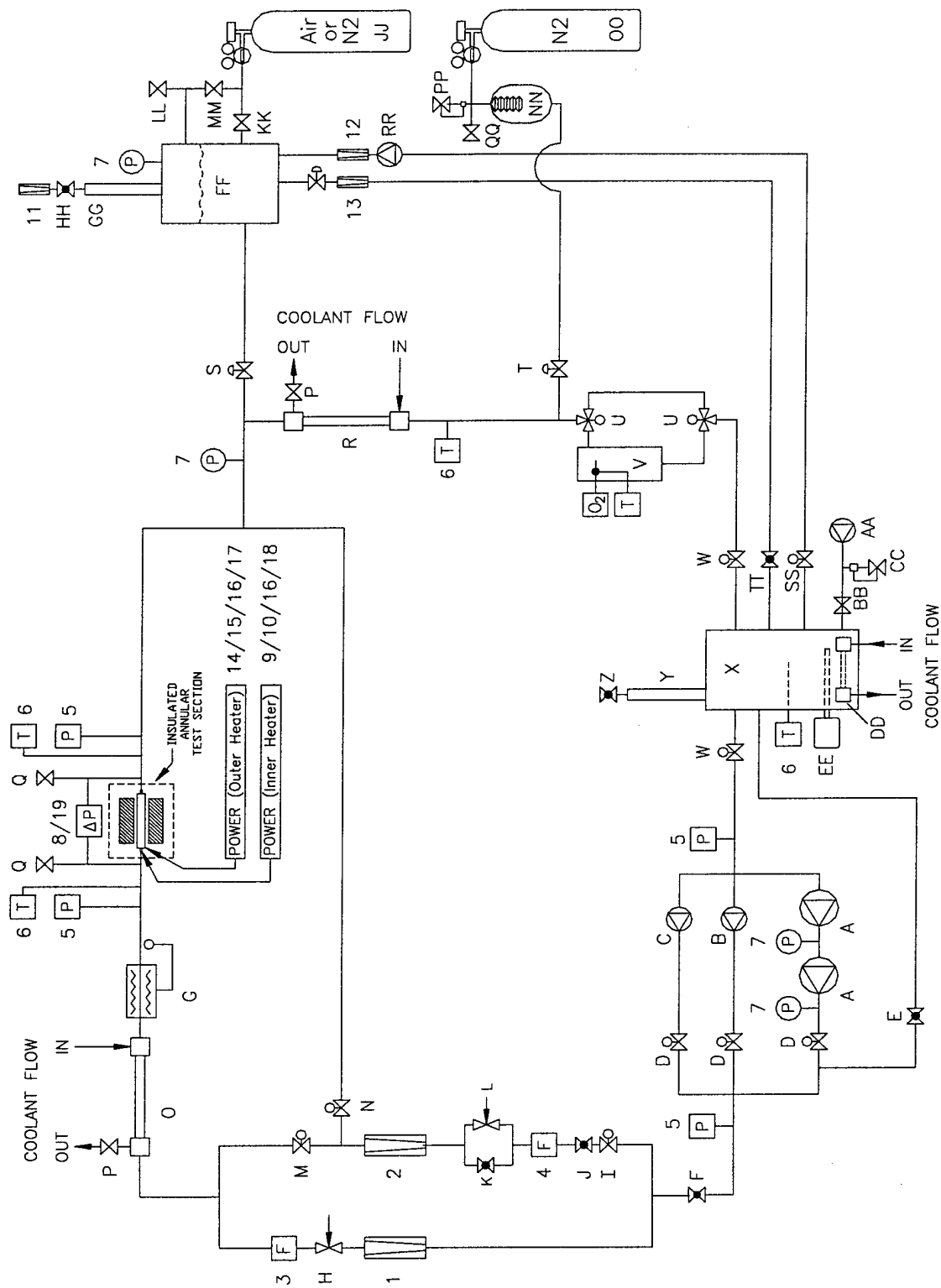


Figure 3.1: Schematic Diagram of the Georgia Tech Microchannel Test Facility

Table 3.2: Listing of GTMTF Hardware Components

Label	Description	Manufacturer	Model
A	Multi-stage centrifugal pump	Teel	2PC45
B	Variable speed positive displacement pump (magnetically-coupled gear)	MicroPump	185
C	Variable speed positive displacement pump (progressing cavity)	Seepex	0015-24MD
D	Pump isolation valves	MCD	-
E	Pump bypass valve	Whitey	SS-12NBS8-SH
F	System throttling valve	Watts	CF8M
G	In-line heater	In house construction	-
H	Low flow measurement line metering valve	Nupro	SS-4LA
I	High flow measurement line isolation valve	Watts	CF8M
J	High flow measurement line throttling valve	Watts	CF8M
K	High flow measurement line metering valve (coarse)	Whitey	SS-3NBF4
L	High flow measurement line metering valve (fine)	Hoke	1315G4B
M	High flow line / Test section line isolation valve	-	-
N	High flow line / Test section bypass line isolation valve	DynaQuip	CF8M
O	Test section heat exchanger (tube-in-tube)	Parker Hannifin	DHTC-SS-8
P	Throttling valve	Teel	A743-CF8M
Q	Bleed valve	Hoke	1513G4S
R	System heat exchanger (tube-in-tube)	Parker Hannifin	DHTC-CU-6
S	Saturation tank pressure regulation line isolation valve	Whitey	SS-3NBF4
T	Accumulator pressure regulation line isolation valve	Teel	A743-CF8M
U	Three-way valve	Whitey	SS-45XS8
V	Oxygen sensor housing	In house construction	-
W	Degassing tank isolation valve	Teel	A743-CF8M
X	Degassing tank	In house construction	-
Y	Degassing tank gas separation column	In house construction	-
Z	Degassing tank gas bleed valve	Whitey	SS-IRS8
AA	Variable-speed positive displacement pump (peristaltic)	Masterflex	7018-20
BB	System water fill valve	Jones Mfg. Co.	150 WSP
CC	System pressure relief valve	Parker	2030 CBBI-1
DD	Degassing tank heat exchanger	In house construction	-
EE	Degassing tank heater (cartridge style)	Watlow	-
FF	Saturation tank	In house construction	-
GG	Saturation tank liquid separation column	In house construction	-
HH	Saturation tank gas bleed valve (integrated with flowmeter)	Omega	5-65 C
JJ	Saturation tank compressed gas supply cylinder	-	-
KK	Saturation tank gas fill valve	Parker	2030 CBBI-1
LL	Saturation tank blow-off valve	Parker	2030 CBBI-1
MM	Saturation tank bubbler select valve	Hoke	1513 G4S
NN	Accumulator (bellows type, Teflon construction)	Sentry	H3020T
OO	Accumulator compressed gas supply cylinder	-	-
PP	Accumulator bleed valve	Teel	A743-CF8M
QQ	Accumulator depressurization valve	Teel	A743-CF8M
RR	Saturation tank recirculation pump (magnetically coupled gear)	MicroPump	000-655
SS	Saturation loop inlet valve	Whitey	SS-3NBF4
TT	Saturation loop exit valve	Whitey	IRS4

Table 3.3: Listing of GTMTF Instrumentation

Label	Description	Manufacturer	Model	Serial Number
1	Rotameter, low range	Fischer & Porter	10A6132N	8712A0041A1
2	Rotameter, high range	Brooks Instruments	1305D08A1A1A	8603HC013
3	Liquid Flow Transducer	EG&G/FTI	FTO-3/RI-51	FO96107517RI5189010
4	Liquid Flow Transducer	EG&G/FTI	FT-8/RI-51	804950RI5189030042
5	Pressure Transducer	Rosemount	1144A-0200A22	Multiple
6	Thermocouple, Type-E	Omega	EMQSS-125G-6	None
7	Pressure Gauge, Bourdon tube type	Various	Multiple	Multiple
8	Differential Pressure Transducer	Rosemount	1151DP4E22B1	11327273
9	Wattmeter, AC	Ohio Semitronics	GW5-020B	49070
10	Wattmeter, DC	Ohio Semitronics	PC8-001-06-X5	8043804
11	Rotameter	Omega	5-65 C	None
12	Rotameter	Fischer & Porter	10A6131M	8911A0675A17
13	Rotameter	Fischer & Porter	10A6131M	8911A0675A17
14	Wattmeter, AC	Ohio Semitronics	GW5-020B	53247
15	Wattmeter, AC with external AC current transducer	Ohio Semitronics / Omega	GW5-020B / CTT-050005	53247 / None
16	Wattmeter, DC	Ohio Semitronics	PC8-001-06-X5	8043804
17	AC/DC Current Shunt	Empro Shunts	C-1500 50	None
18	AC/DC Current Shunt	Empro Shunts	C-1500 50	None
19	Differential Pressure Transducer	Rosemount	1151DP5E22	1072957
20	Data Acquisition / Switch Unit	Hewlett Packard	HP 34970A	GT 0091257

Table 3.3 (continued)

Label	Manufacturer Stated Range	Manufacturer Stated Accuracy	Calibration Source	Calibration Date
1	1.5 – 21 gph, water	0.5 gph	-	-
2	0.2 – 2.5 gpm, water	0.1 gpm	-	-
3	0.02 – 0.4 gpm	0.1% repeatability	Blasick, GT	03/26/98
4	0.2 – 10 gpm	0.1% repeatability	Dowling, GT	10/12/99
5	0 – 1375 kPa	0.25% cal. range	Dowling, GT	09/17/97
6	-200° – 425°C	0.1°C	Dowling, GT	11/04/96
7	0 – 200 psi	2 psi	-	-
8	0 – 100 inch H ₂ O	0.2% calibrated range	Blasick, GT	04/09/98
9	0 – 1 mA, 0 – 4 kW	0.2% reading, 0.04% F.S.	Manufacturer	12/17/96
10	± 5V, 0 – 25 kW	1.0% reading F.S.	Manufacturer	01/21/98
11	0 – 9 gph, water	1 gph	-	-
12	0 – 3.4 scfm, air	0.2 scfm, air	-	-
13	0 – 3.4 scfm, air	0.2 scfm, air	-	-
14	0 – 1 mA, 0 – 4 kW	0.2% reading, 0.04% F.S.	Manufacturer	01/21/98
15	0 – 1 mA, 0 – 4 kW 0 – 50 A	0.2% reading, 0.04% F.S. ± 1.5% at 60 Hz with max burden	Manufacturer	01/21/98
16	± 5V, 0 – 25 kW	1.0% reading F.S.	Manufacturer	01/21/98
17	0 – 1500 A	0.5% reading, with 50 mV drop	Manufacturer	June 1999
18	0 – 1500 A	0.5% reading, with 50 mV drop	Manufacturer	June 1999
19	0 – 750 inch H ₂ O	0.2% calibrated range	Narrow, GT	09/16/97
20	100mV – 300V -150° – 1000°C	0.0040% of reading ± 1.0°C	Manufacturer	-

III.3.1.2 Differential Pressure Transducer

Two differential pressure transducers (Components 8 and 19) were mounted on the GTMTF for the purpose of measuring the differential pressure across the test section. Both transducers were Rosemount style 1151DP transducers; however, Component 8 had a differential pressure range of 0 – 100 inch H₂O while Component 19 had a differential pressure range of 0 – 750 inch H₂O. Due to the high flow rates and associated large pressure drops required by this investigation, only Component 19 was utilized.

The differential pressure transducer was mounted above the test section which caused entrained gas bubbles to become trapped in the transducer. For this reason, two toggle valves (Components Q) were installed and used as bleed valves to rid the differential pressure transducer of any trapped air pockets during the System Filling Procedure described in Section IV.2.

III.3.1.3 Turbine Flowmeters

Two EG&G turbine flowmeters (Components 3 and 4) were used to measure the flowrate through either the test section or the test section bypass line, depending on the flow loop configuration. The flowmeters were installed upstream of the test section in a horizontal orientation to ensure accurate readings.

III.3.1.4 Rotameters

Two rotameters (Components 1 and 2) were mounted in the GTMTF to allow visual verification of flowrate through the primary flow loop. In addition, two identical

low capacity rotameters (Components 12 and 13) were used to monitor and control the flow into and out of the saturation tank during experimentation. The saturation loop rotameters were used to prevent the saturation tank from either overflowing or drying out, while the principal function of the two primary loop rotameters was to provide a means of visually checking the flow for air pockets during the System Filling Procedure described in Section IV.2. Each rotameter was mounted vertically to ensure accurate readings and none of the four rotameters provided information essential to the analysis of experimental data.

III.3.1.5 Thermocouples

All thermocouples (Components 6) used in the GTMTF were Omega type-E with stainless steel sheaths. The thermocouples were mounted in the GTMTF using compression fittings to ensure the tips were positioned near the center of the water stream. During CHF experimentation (Setup 13), three fine gauge, type-E thermocouples (not shown) were mounted radially on the outer heater, 120° apart, one centimeter from the end of the test section heated length. In addition, one stainless steel sheathed, ungrounded, type-T thermocouple was mounted inside the inner heater, one centimeter from the end of the test section heated length. These thermocouples were used to detect CHF; a detailed explanation of their experimental arrangements can be found in Sections III.4 and III.5.

III.3.1.6 Pressure Gauges

Four pressure gauges (Components 7) were used to provide visual verification of pressure levels in the system; these gauges were not used to provide the data necessary for analysis procedures. A pressure gauge manufactured by McDaniel Controls, Inc. and rated for 0 – 200 psig, was used to indicate the test section exit pressure. When filling the system during the System Filling Procedure outlined in Section IV.2, this gauge was monitored to ensure that the system did not pressurize above 20 psig. The peristaltic pump (Component AA) used to fill the system was not rated for high pressure and, thus, forcing the system above 20 psig could have damaged the pump. A second pressure gauge, manufactured by Span Instrumentation and rated for 0 – 300 psig, was used to monitor the pressure in the saturation tank. The reading on this pressure gauge, under normal operating conditions, always exactly matched the reading on the pressure gauge located at the test section exit. This fact allowed the operator to perform a rapid visual check to determine if an error had occurred in the system requiring termination of an experiment.

The final two pressure gauges in the system were placed at the exits of the two centrifugal pumps used in Flow Loop Configuration Three. These pressure gauges, manufactured by U.S. Gauge and rated for 0 – 300 psig, were used to ensure that the centrifugal pumps were not overpowering the flow loop. The pressure gauge located after the second centrifugal pump was fitted with a pressure release valve. If the pressure at the centrifugal pump exit exceeded 300 psig due to an incorrect valving pattern in the system, the pressure release valve would trigger and prevent damage to sensitive

components in the GTMTF.

III.3.1.7 Data Acquisition System (DAS)

Data from all electronic sensors (Components 3 – 6, 8 – 10, and 14 – 19 of Figure 3.1) were recorded using the Keithly MetraByte model DAS-8 data acquisition card with Keithly MetraByte model EXP-16 channel multiplexer/amplification boards. The DAS-8 digitized all analog signals using a 10 kHz system clock and provided for software averaging of the digitized values to remove potential AC noise pick-up. The DAS-8 system was run using an in house Microsoft Visual Basic 3.0 program on a 120-MHz Pentium computer that utilized Microsoft Windows 3.1 as an operating environment. This data acquisition program enabled the operator to control the time interval (1 s, 5 s, 15 s, 1 m, 5 m, or 15 m) at which the data channels were sampled. This investigation only utilized the one and five second sampling time intervals. The DAS recorded all data for a particular experiment to a prescribed text file on the Pentium computer for future analysis.

III.3.1.8: Hewlett Packard Data Acquisition / Switch Unit

The Hewlett Packard Data Acquisition / Switch Unit (not shown in Figure 3.1) was used during CHF experimentation to increment power to the test section and to monitor three type-E thermocouples that were mounted on the outer heater. An input signal was provided to the unit from a Compaq DeskPro 575 personal computer (HP Benchlink Data Logger Software in a Microsoft Windows 95 operating environment) and

the HP unit, in turn, provided a signal to the power supply, which controlled the power input to the test section. The HP unit also monitored the outer heater thermocouples and automatically terminated the experiment by cutting the power supply signal if the outer heater surface temperature exceeded 300°C. The HP unit could sample at rates up to 600 readings per second on a single channel and scan at rates up to 250 channels per second making it ideal for monitoring the outer heater temperature during a CHF experiment. All temperature readings from the outer heater thermocouples were recorded along with a real time stamp by the HP Benchlink software package on the Compaq personal computer for future analysis.

III.3.2 Flow Loop Configuration One

Flow Loop Configuration One was used for high flow / high heat flux OFI experimentation. As shown in Figure 3.2, one multi-stage centrifugal pump was utilized to force water through the high flow measurement line and through the test section. The FT-8 model high capacity flow transducer (Component 4 of Figure 3.2) was used to measure the test section volumetric flowrate which was controlled by the coarse and fine high flow line metering valves (Components K and L). Note that both the test section bypass line and the pump bypass line were closed creating a closed primary flow loop with no branching flow patterns.

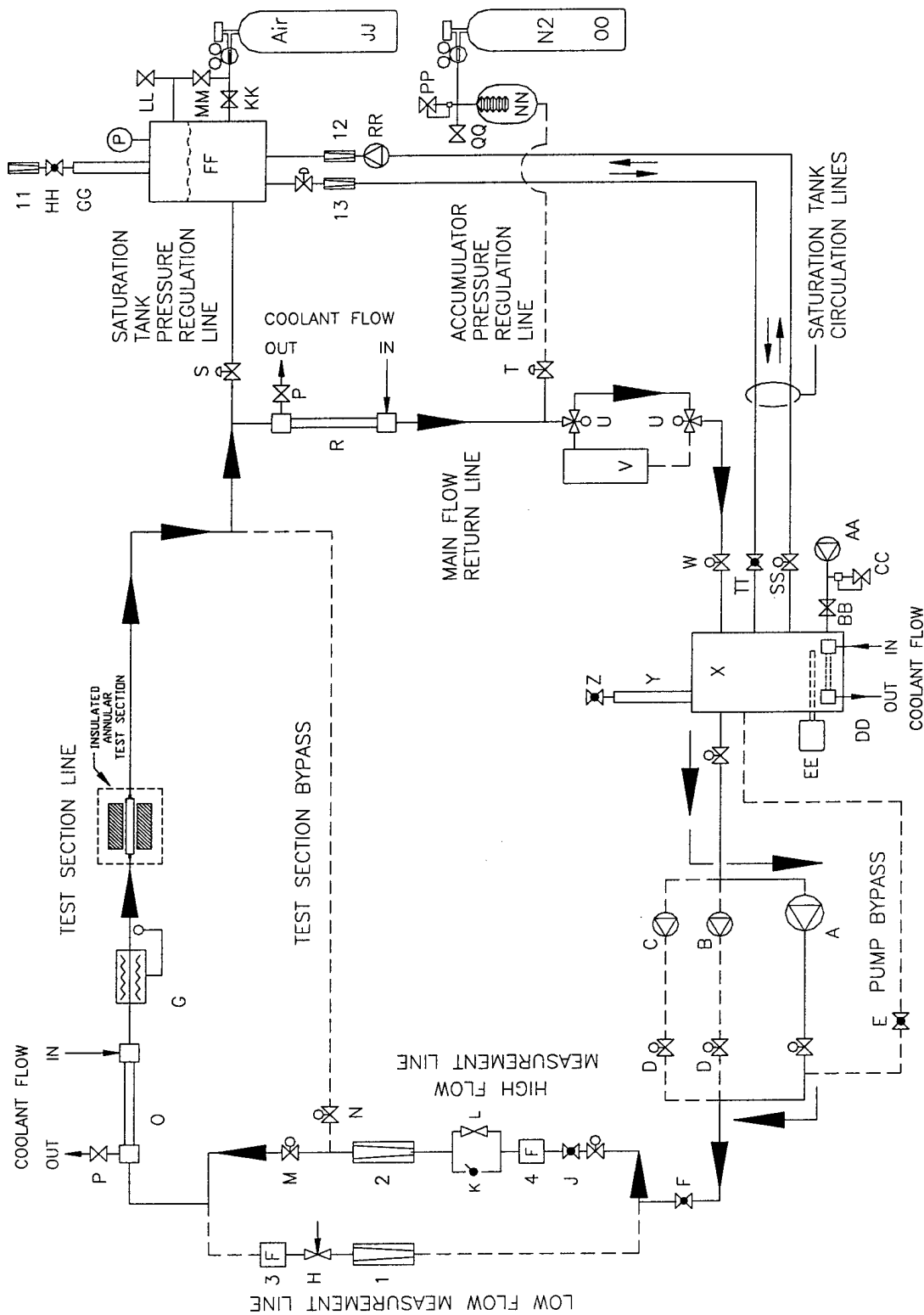


Figure 3.2: Schematic Diagram of Flow Loop Configuration One

III.3.3 Flow Loop Configuration Two

Flow Loop Configuration Two was used for low flow / low heat flux OFI experimentation. While testing new outer heater designs, several experiments (Setups 1 – 3) were run, where only the outer heater was energized; no power was supplied to the inner heater. As a result, the working fluid was heated far less than necessary to make Flow Loop Configuration One effective for OFI experimentation. The FT-8 turbine flowmeter used by Flow Loop Configuration One to measure test section flowrate has a minimum flowrate of 0.2 gpm (45.4 L/hr). This value was far greater than the OFI points experienced in Setups 1 – 3 making alteration of the flow loop configuration necessary.

As shown in Figure 3.3, one multi-stage centrifugal pump was utilized by Flow Loop Configuration Two to force water through both the low flow measurement line and the test section bypass line. This branched flow pattern significantly reduced the flowrate through the test section and allowed a great deal of flow control. The FTO-3 model low capacity flow transducer (Component 3 of Figure 3.3) was used to measure the test section volumetric flowrate, which was controlled by the low flow line metering valve (Component H). Likewise, the FT-8 model high capacity flow transducer was used to measure the test section bypass volumetric flowrate, which could be controlled by the coarse and fine high flow line metering valves (Components K and L). Note that the pump bypass line was closed while the test section bypass line was open, thus creating a closed primary flow loop with a flow pattern that branched immediately before the test section and converged just prior to entering the system heat exchanger (Component R).

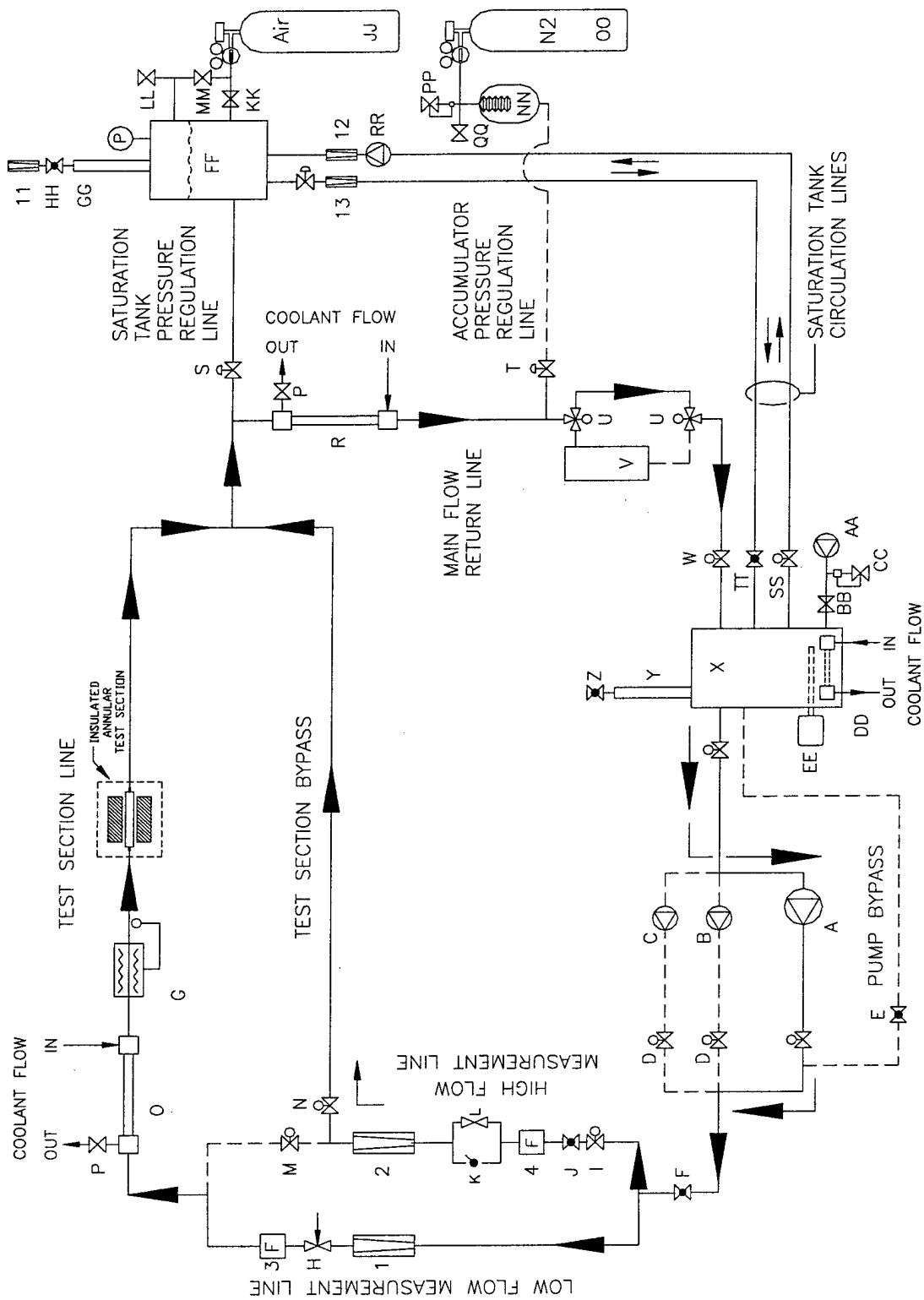


Figure 3.3: Schematic Diagram of Flow Loop Configuration Two

III.3.4 Flow Loop Configuration Three

Flow Loop Configuration Three was used for high flow / high heat flux OFI experimentation and was only a slight modification of Flow Loop Configuration One. As the OFI experimental power levels increased, OFI began to occur at or near the maximum flowrates achievable by Flow Loop Configuration One making modification necessary. A second centrifugal pump was added to the system in series with the original centrifugal pump.

As shown in Figure 3.4, two multi-stage centrifugal pumps were utilized to force water through both the high flow measurement line and the pump bypass line. The FT-8 model high capacity flow transducer (Component 4 of Figure 3.4) was used to measure the test section volumetric flowrate, which was controlled by the coarse and fine high flow line metering valves (Components K and L). Likewise, the flowrate through the pump bypass line was controlled using the pump bypass valve (Component E), but this flowrate was never measured or recorded. The pump bypass valve was only adjusted prior to the initiation of an experiment in order to either increase or decrease the maximum flowrate supplied to the test section. Note that the test section bypass line was closed while the pump bypass line was open, thus creating a closed primary flow loop with a flow pattern that branched immediately after the second centrifugal pump and converged in the degassing tank (Component X).

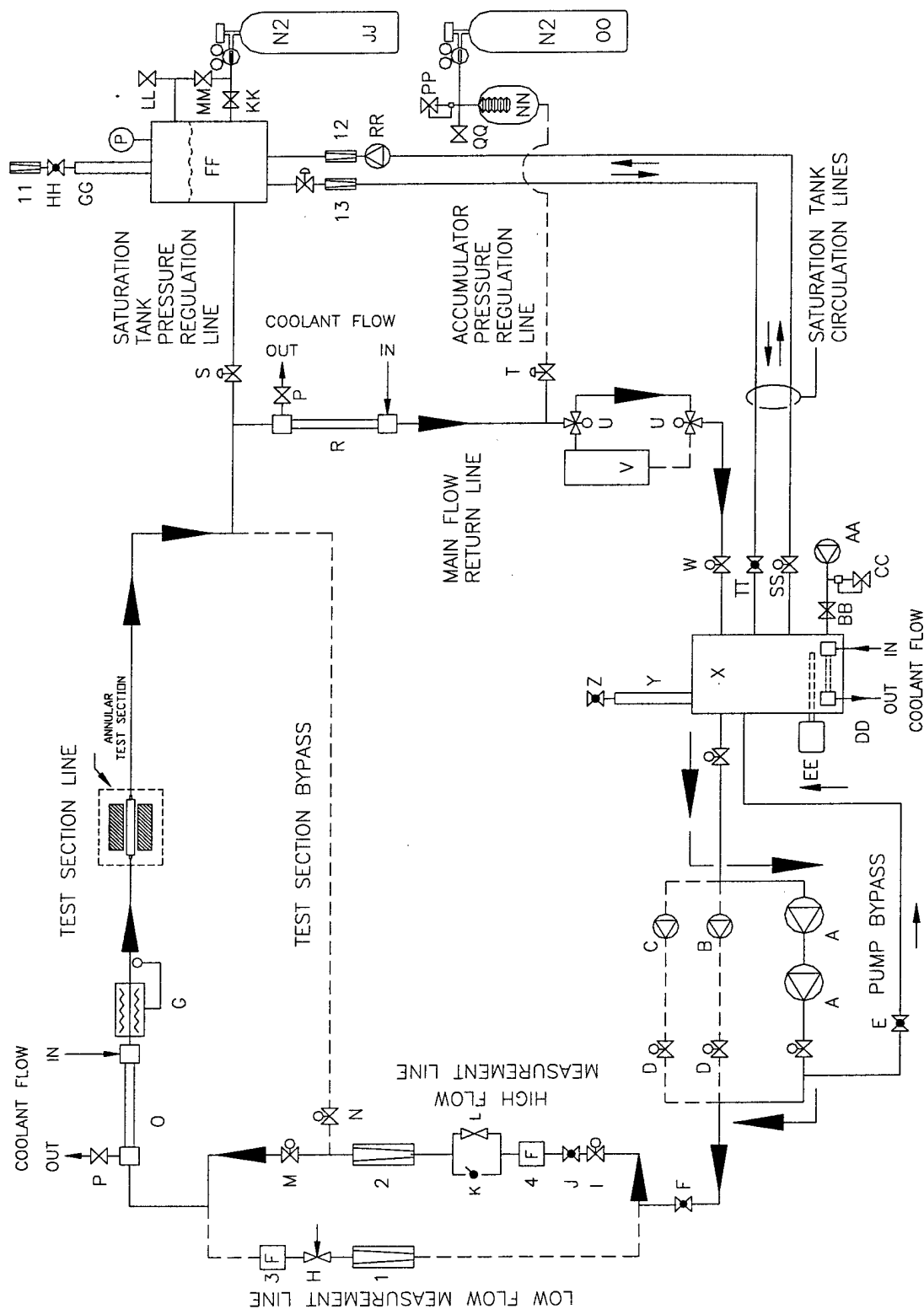


Figure 3.4: Schematic Diagram of Flow Loop Configuration Three

III.3.5 Flow Loop Configuration Four

Flow Loop Configuration Four was used for all CHF experiments. As shown in Figure 3.5, one variable speed positive displacement pump was utilized to force water through the low flow measurement line and through the test section. The FTO-3 model low capacity flow transducer (Component 3 of Figure 3.5) was used to measure the test section volumetric flowrate, which was controlled by the tachometer on the positive displacement pump. The low flow line metering valve (Component H) was partially closed for all CHF experiments to provide the positive displacement pump a small amount of back pressure (100 kPa). This back pressure helped reduce two-phase pressure and flow fluctuations encountered during CHF experimentation. Note that both the test section bypass line and the pump bypass line were closed creating a closed primary flow loop with no branching flow patterns.

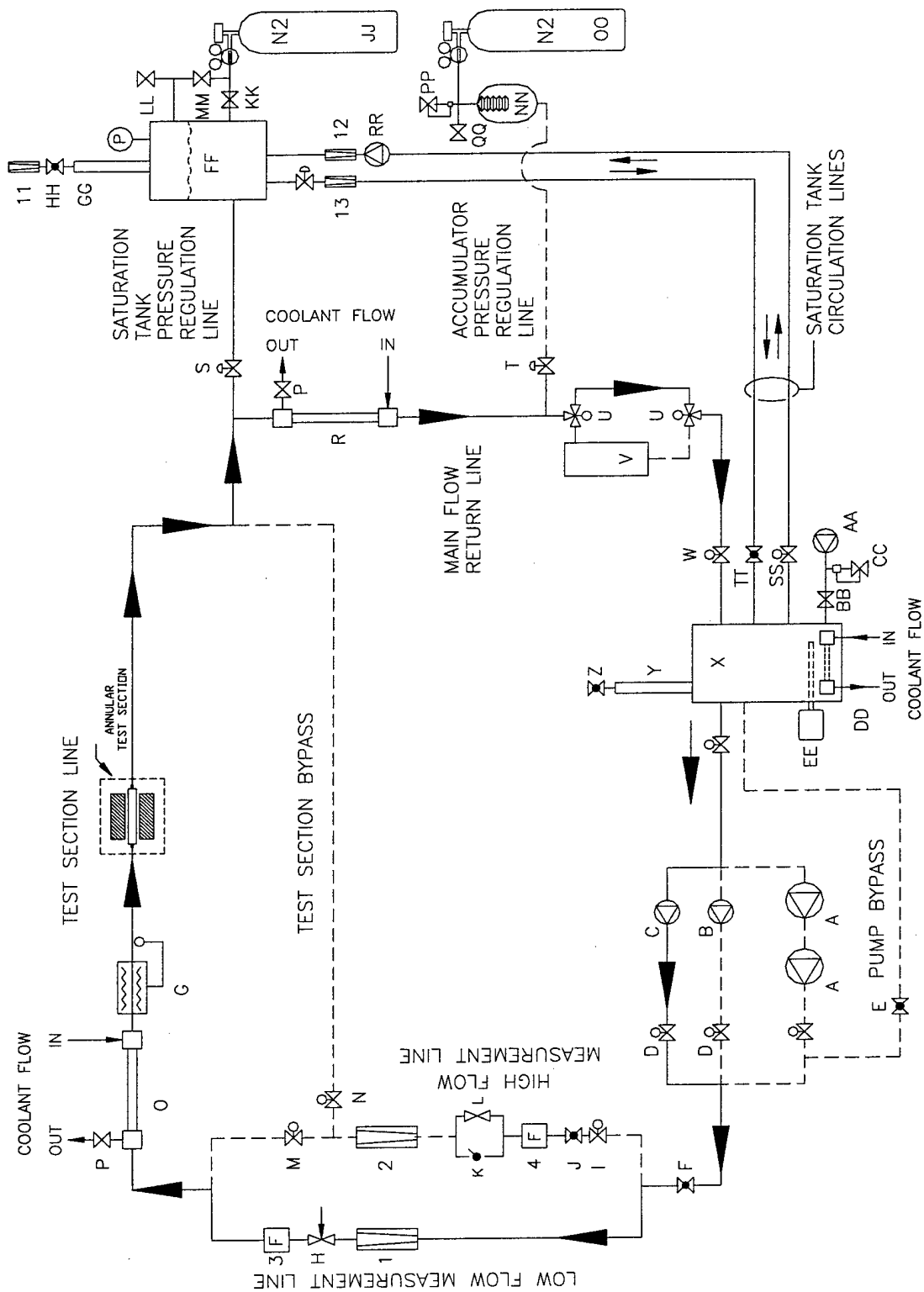


Figure 3.5: Schematic Diagram of Flow Loop Configuration Four

III.3.6 Control of Flow Parameters

Test section inlet temperature and exit pressure were controlled in the same manner for each of the four flow loop configurations described above. As explained earlier, modifications to the flow loop were required in order to achieve the necessary flow rate control for a specific set of flow parameters. This typically involved the addition of a pump to the system or slight modification of the test section flow path or flow rate instrumentation as described in Sections III.3.2 – III.3.5. Regardless of the test section flow path, however, the components used to pressurize the system were identical for all experimental setups except Setup 7, which is described in Section III.3.6.3 below.

III.3.6.1 Test Section Inlet Temperature Preparation

Test section inlet temperature was set and adjusted using three heat exchangers (Components O, R, and DD of Figure 3.1) and/or two degassing tank cartridge style heaters (Components EE). The most significant temperature control system in the GTMTF was the system heat exchanger (Component R). The system heat exchanger was a high capacity, coiled, copper / copper, counter-flow, tube-in-tube heat exchanger that was cooled by the house water line ($17^{\circ} - 20^{\circ}\text{C}$) and located immediately after the test section exit. Due to its location, the system heat exchanger had to remove a large percentage of the heat in the working fluid since two-phase water exited the test section and had to be cooled prior to passing through the pump(s) for recirculation. A throttling valve (Component P) controlled the flow of house water through the secondary side of the system heat exchanger. This flow of house water was typically maximized through

the system heat exchanger to facilitate maximum cooling of the working fluid since manufacturer design specifications dictated that the inlet temperature to the pump(s) could not exceed 70°C.

The test section heat exchanger (Component O) was located immediately before the test section. The test section heat exchanger was a coiled, stainless steel / copper, counter-flow, tube-in-tube heat exchanger, which was connected to a Fisher Scientific Isotemp Refrigerated Circulator (Model 9500) constant temperature bath. The set point of the constant temperature bath was selected manually by the operator and maintained automatically by the unit ($\pm 0.2^{\circ}\text{C}$) during normal operation. The flow provided by the constant temperature bath through the secondary side of the test section heat exchanger was maximized at all times since the constant temperature bath could be set and maintained at a desired level.

A low capacity, copper heat exchanger was located inside the degassing tank. This degassing tank heat exchanger (Component DD) was attached to the house water line and used to remove heat from the working fluid during high heat flux / high mass flux experiments where the system heat exchanger alone was not adequate. The flow through the secondary line of the degassing tank heat exchanger was controlled using a throttling valve (not shown).

For approximately ninety percent of all experiments performed in this investigation, the three heat exchangers working in concert were adequate to maintain the test section inlet temperature. However, during high inlet temperature, low heat flux OFI experiments and high inlet temperature, low mass flux CHF experiments, the system heat

exchanger cooled the working fluid too much. As a result, the test section heat exchanger, which had a much lower capacity, could not maintain the required test section inlet temperature. To counter this effect, two variac controlled (0 – 6 kW), cartridge style degassing tank heaters (Components EE) were used to heat the working fluid prior to its introduction to the pump(s). These two heaters offered much finer control of system temperature than simple throttling of the secondary flow through the system heat exchanger. Note that in order to prevent component damage, care had to be used when operating these heaters. As mentioned earlier, the inlet temperature to the pump(s) could not rise above 70°C and thus, close observation of the degassing tank temperature and control of the degassing tank heaters was required in order to assure operation within such limits.

Finally, a thermostatically controlled in-line heater (Component G) was located just before the test section inlet. This in-line heater was built in house and could deliver 1kW of power to the working fluid; however, due to the control offered by the three heat exchangers and two degassing tank heaters mentioned above, the in-line heater was never used in any of the experiments performed in this investigation.

III.3.6.2 Working Fluid Gas Saturation and System Pressurization

All experiments in which data were acquired in this investigation utilized the same components to pressurize the system and saturate the working fluid with non-condensable gas. A compressed gas cylinder (Component JJ of Figure 3.1) with regulator was used to set the system pressure via the saturation tank (Component FF) by

means of flexible Swagelok tubing (1.70 MPa max) and the saturation tank gas fill valve (Component KK). The regulator (National Gas Cylinder model N1601 for air and The Matheson Company model H63 for nitrogen) was used to set the pressure inside the saturation tank. In turn, the open saturation tank pressure regulation valve (Component S) effectively equalized the test section exit pressure with the saturation tank pressure. During normal operation, there was no flow through this line. Gas saturation of the working fluid was accomplished by allowing the compressed gas to bubble through the saturation tank and escape at a controlled rate through the rotameter (Component 11) located atop the saturation tank liquid separation column (Component GG). The compressed gas bubbled through the saturation tank was either air or nitrogen, depending on the experimental setup. Note, as described in Section III.3.6.3 below, the non-condensable gas supplied to the system was switched from air to nitrogen after Setup 5 to avoid corrosion problems. Circulating the working fluid from the degassing tank, through the saturation tank, and back to the degassing tank ensured saturation of all water in the system. This path was commonly referred to as the saturation loop. The saturation tank recirculation pump (Component RR) circulated water through the saturation loop and the flow into and out of the saturation tank was monitored using two identical rotameters (Components 12 and 13). Equalization of the inlet and exit flow rates ensured that the saturation tank would neither overflow nor dry out; either situation resulting in termination of the experiment being performed. The exact saturation loop startup procedures are detailed in Section IV.3.

III.3.6.3 Minimization of Oxidation / Clarification of Setup 7

Following higher power OFI experiments with Setup 5, a great deal of oxidation was observed on the surface of the inner heater. In an effort to minimize this type of damage, two new setups were tested to reduce the amount of dissolved oxygen present in the working fluid: Setups 6 and 7. For Setup 6, the gas saturation tank used to fix the test section exit pressure was pressurized using nitrogen rather than compressed air. No efforts were made to remove the ambient dissolved oxygen present in the distilled water due to contact with the atmosphere prior to its introduction to the system. In Setup 7, the exit pressure was set using an accumulator rather than the saturation tank. Again, no effort was made to remove the ambient dissolved oxygen present in the distilled water. Use of the accumulator pressurization method, however, was abandoned because maintenance of the test section exit pressure was impossible at high test section flow rates. Instead, all remaining experiments were pressurized using the saturation tank and compressed nitrogen. This pressurization method reduced the dissolved oxygen present in the working fluid while maintaining its non-condensable gas saturation status. Setup 7 was never used to acquire data and, therefore, no further details will be provided about this setup.

III.4 Inner Heater Configuration

The "test section" referred to throughout this thesis was actually comprised of two separate pieces: an inner heater and an outer heater. The inner heater was mounted

concentrically within the outer heater to form an annular channel and the two heaters were typically powered by separate power supplies. This section describes all physical aspects of the inner heater and the power supply used to generate the required surface heat flux. As outlined in Table 3.1, a total of nine different inner heater configurations were used in this investigation. The inner heater configuration used in each experimental setup includes the following information.

- 1) Inner Heater Label
- 2) Power Supply Configuration
- 3) Heated Length

Table 3.4 categorizes the specific components used in these three categories for all nine inner heater configurations. Each time one or more of these three categories was altered, the inner heater configuration number was sequentially incremented.

Table 3.4: Summary of Inner Heater Configurations

Inner Heater Configuration	Inner Heater Label	Power Supply Configuration	Heated Length (mm)
1	D	None (unheated)	N/A
2	E	None (unheated)	N/A
3	E, F, G	2	190
4	H	2	180
5	I, J, L	2	180
6	K	None (unheated)	N/A
7	M	3	180
8	N	3	190
9	O	4	190

Note that the Inner Heater Label category begins with D. Since this investigation was intended to complement the work of Blasick (1999), the integrity of the labeling scheme she adopted was preserved whenever possible and she ended her work with Inner Heater Label C. Also, each individual inner heater used in an experiment was given a label (etched onto the copper electrode at the inlet end). When an effective inner heater

design was found, several duplicates were typically made which explains the multiple Inner Heater Labels shown in Table 3.4 for Inner Heater Configurations 3 and 5.

In order to achieve the high power densities required by this investigation, a robust inner heater was necessary. All of the inner heaters for this research were manufactured in-house from standard, commercially available welded seam tubing and all were heated using direct resistive (Ohmic) heating. The electrodes used for the heaters were made from solid, 1/4" diameter, free-machining copper rods (alloy C14500). Free-machining copper is an electrical-grade alloy notable for its machining properties and an electrical conductivity essentially equal to that of pure copper. The copper rods were cut to length and, using a lathe, the ends were turned down to a diameter equal to the inner diameter of the tubing selected for the heated portion (Inconel-600 or Hastelloy C-276). The copper electrodes were then press-fit into either end of the heater tubing. Next, a small hole was drilled and tapped through the tubing and into, but not through, the electrode. A brass screw (3-48 UNC) was then tightened into this threaded hole and sheared off even with the outer wall of the tubing. These brass stakes ensured that a tight, corrosion free conduction path was always present from the copper electrodes to the heater tubing. In general, this pinning method worked well, so that no oxidation of the copper or of the tubing in the region of contact was ever observed when selected heaters were disassembled after use. This is a remarkable fact given the high electrical currents (≈ 1000 Amps) carried by the inner heater. Thus, it was found that the exact lengths of the electrodes and the precise amount of overlap between the tube wall and electrodes were not critical parameters. Extreme care was taken, however, to manufacture the inner

heaters in a symmetric way, so that measurements made relative to the exposed electrode ends could be used to verify that the heater was mounted with its heated region in the desired location. For all inner heaters, the heated region was considered to begin and end at the tips of the press-fit copper electrodes and the exposed ends of the copper electrodes were used to connect power supply leads to the inner heater.

The following subsections describe the design specifications unique to each of the twelve different inner heaters (D – O) used in this investigation. These subsections will include a discussion on the heated length of each inner heater. The Power Supply Configuration category will be discussed in Section III.6 since three of the four different power supply configurations were used to heat both the inner and outer heaters.

III.4.1 Inner Heater D

Inner Heater D (shown in Figure 3.6) was inherited from Blasick (1999) and used in Setup 1 to test the feasibility of a proposed outer heater design. It was merely used to maintain an annular cross-section flow channel through the test section and, thus, was never heated. The relatively short length of Inner Heater D made construction of a new inner heater imperative before power could be applied to the inner heater. Inner Heater D was too short and thus left an inadequate amount of electrode length protruding from the ends of the outer heater on which to attach power supply leads.

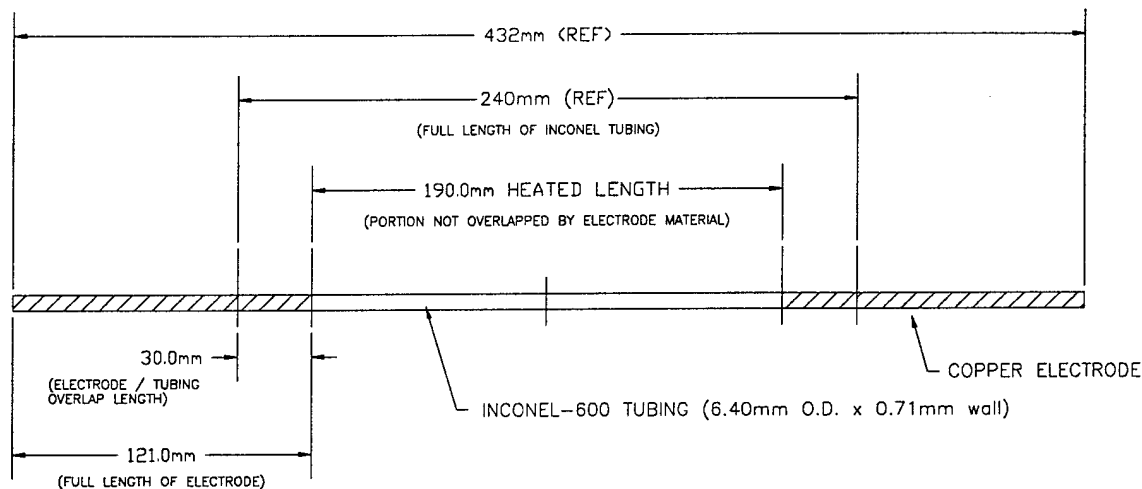


Figure 3.6: Diagram of Inner Heater D

III.4.2 Inner Heaters E, F, and G

Inner Heaters E, F, and G (shown in Figure 3.7) improved upon the design of Inner Heater D, not only by extending the overall length of the heater, but also by adding a rigid alumina rod to the construction. The alumina rod provided stability to the inner heater and prevented it from bowing. Fortunately, such cylindrical rods were readily available in the exact diameter needed to provide a tight fit with the nominal $\frac{1}{4}$ " (6.35 mm) diameter heater tubing with a 0.028" (0.7112 mm) wall thickness. Figure 3.7 shows the design of these heaters with the actual diameter of the Inconel-600 tubing (0.252" / 6.40 mm).

Heat fluxes above 1.5 MW/m^2 tended to cause a significant amount of oxidation at discrete points on the surface of this inner heater design after repeated use. It was unclear whether this damage was caused by electrical arcing (to the grounded inner surface of the AC outer heaters) or by extreme heating caused by highly localized film

boiling. In spite of the visible damage, these heaters remained very straight through all experiments as a result of the alumina rod insert. Typically, failure of this heater design occurred when the localized surface damage was severe enough to damage or break the alumina rod. Catastrophic failure of the heater (i.e., bowing and melting) could then occur.

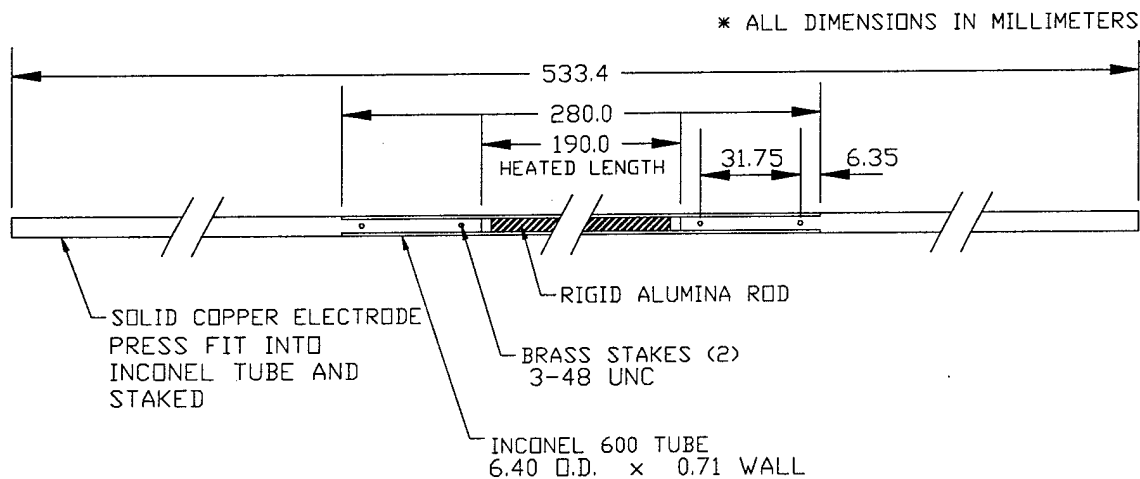


Figure 3.7: Diagram of Inner Heaters E, F, and G

III.4.3 Inner Heater H

Inner Heater H was produced from 1/4" diameter Inconel-600 tubing that had a wall thickness of 0.033" (0.8382 mm). This larger wall thickness made insertion of the alumina support rod impossible, which weakened the structural stability of the heater. In addition, the heated length of Inner Heater H differed from that of Inner Heaters E, F, and G. Due to limitations imposed by the outer heater mounting mechanism, the outer heater heated length was limited to 180 mm at that point in the experimental process. It was

determined that deviation from the nominal heated length of 190 mm was less important than matching the inner and outer heater heated lengths. Inner Heater H bowed and failed rather quickly due to its lack of rigidity and was never duplicated.

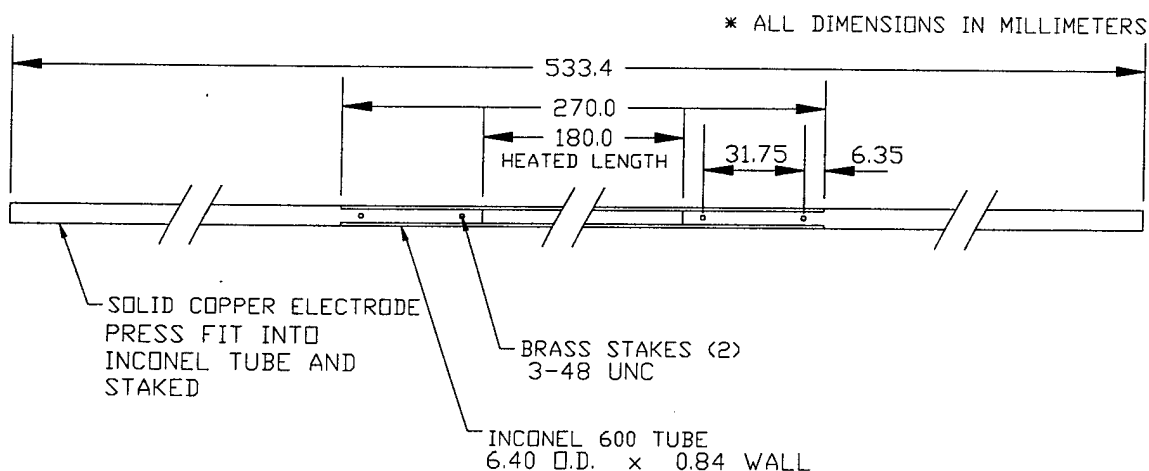


Figure 3.8: Diagram of Inner Heater H

III.4.4 Inner Heaters I, J, K, and L

Inner Heaters I, J, K, and L preserved the 180 mm heated length used in Inner Heater H, but utilized $\frac{1}{4}$ " diameter Inconel-600 tubing with a 0.028" (0.7112 mm) wall thickness. This change in heater tubing allowed the addition of an alumina support rod as outlined in the description of Inner Heaters E, F, and G in Section III.4.2. Shown in Figure 3.9, this inner heater design remained extremely straight in all experiments for which it was used, however, it was plagued by corrosion problems.

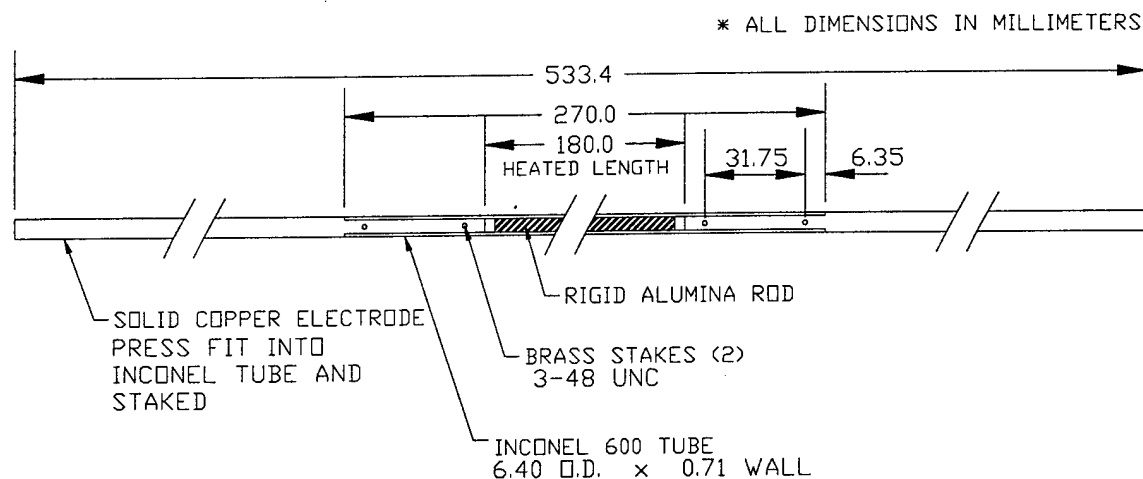


Figure 3.9: Diagram of Inner Heaters I, J, K, and L

III.4.5 Inner Heater M

As shown in Figure 3.10, Inner Heater M matched the design of Inner Heater H exactly, except that Hastelloy C-276 was used for the heated section rather than Inconel-600. This material change was adopted in an attempt to alleviate the localized corrosion encountered with the Inconel-600. Hastelloy C-276 has better corrosion properties than Inconel-600, but only tubing with a wall thickness of 0.033" (0.8382 mm) was available, preventing the use of an alumina support rod. Inner Heater M showed less corrosion than the inner heaters constructed of Inconel-600, but it bowed unacceptably at high heat fluxes thus proving the necessity of the alumina support rod.

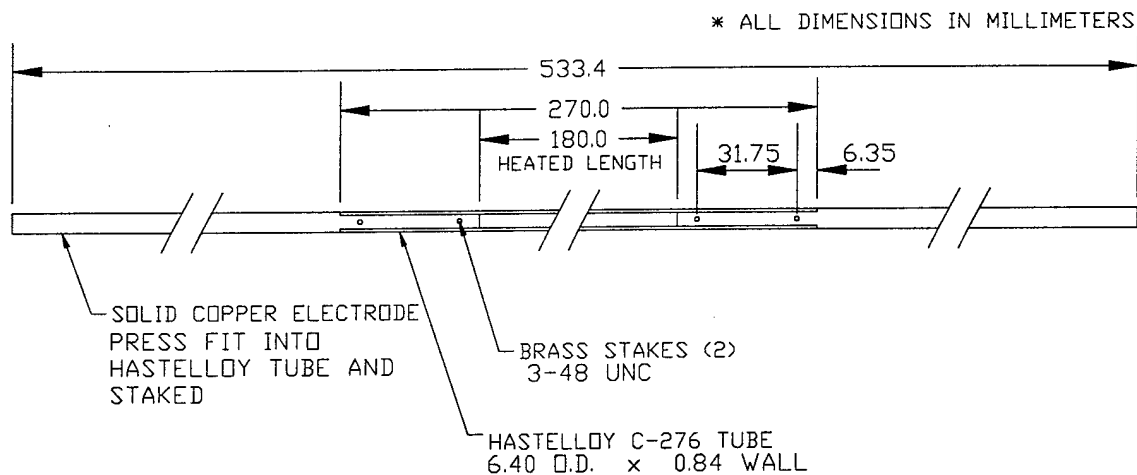


Figure 3.10: Diagram of Inner Heater M

III.4.6 Inner Heaters N and O

Inner Heaters N and O were adapted from the design of Inner Heaters E, F, and G for use primarily in CHF experimentation. As shown in Figure 3.11, Inner Heaters N and O provided the original nominal heated length of 190 mm and they included an alumina support rod. Also, the inlet end electrode was constructed from a 1/4" diameter solid copper rod as with all previously mentioned inner heater designs.

In order to detect the approach of CHF, Inner Heaters N and O were fitted with an internally mounted, type-T, ungrounded thermocouple. A single thermocouple was permanently mounted in a short, 1/4" diameter, nylon sleeve using standard two-part epoxy. The nylon sleeve allowed mounting of the thermocouple to the inner heater while the epoxy provided a permanent, watertight seal around the thermocouple. The heater's exit end electrode was fabricated from a 1/4" diameter, brass tube whose end was turned down and press-fit, but not staked, into the Inconel-600 heater tube. A Swagelok union

fitting was then attached to the end of the brass tube to allow mounting of the thermocouple. Next, the tip of the thermocouple was slightly bent and inserted an appropriate distance into the inner heater. The bend in the tip of the thermocouple ensured contact with the inner heater wall and the thermocouple was inserted such that it would contact the inner heater wall one centimeter before the end of its heated length. Once in position, the thermocouple was secured by tightening the Swagelok union around the nylon sleeve. The presence of the thermocouple in this inner heater design forced the alumina support rod to be shortened by one centimeter during construction. Unlike previous inner heater designs, the alumina support rod was in contact with the inlet end electrode, but not the exit end electrode. This design modification did not significantly weaken the inner heater and no detectable bowing of Inner Heaters N or O was ever observed.

Note that this thermocouple mounting style allowed the same thermocouple to be easily transferred from one inner heater to another, thus eliminating data inconsistency and waste of material. In addition, the brass tube, which acted as the exit end power electrode, allowed insertion of the thermocouple, but it increased the impedance of the electrical connection. The increased resistivity of this electrode and the associated heat produced outside the test section area was countered by active cooling of the power supply connection as detailed in Section III.6. Finally, note that both the nylon sleeve and the epoxy were non-conducting materials, thus ensuring electrical independence between the inner heater and the thermocouple.

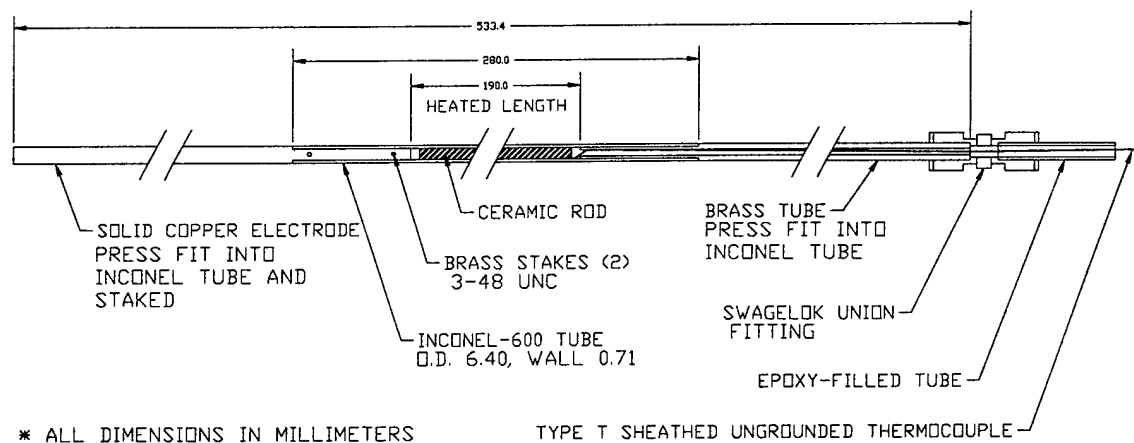


Figure 3.11: Diagram of Inner Heaters N and O

III.5 Outer Heater Configuration

The outer heater configuration describes all physical aspects of the outer heater and the power supply used to generate the required surface heat flux. As outlined in Table 3.1, a total of eight different outer heater configurations were used in this investigation. The outer heater configuration used in each experimental setup includes the following information.

- 1) Outer Heater Label
- 2) Power Supply Configuration
- 3) Heated Length
- 4) Wire Wrapping Style

Table 3.5 categorizes the specific components used in these four categories for all eight outer heater configurations. Each time one or more of these four categories was altered, the outer heater configuration number was sequentially incremented.

Table 3.5: Summary of Outer Heater Configurations

Outer Heater Configuration	Outer Heater Label	Power Supply Configuration	Heated Length (mm)	Wire Wrapping Style
1	H	1	55	1
2	H	1	53	1
3	H	1	123	2
4	H	1	180	3
5	E	1	180	3
6	L	2	185	N/A (tube heater)
7	I, J	3	185	N/A (tube heater)
8	K	4	185	N/A (tube heater)

Note that the Outer Heater Label category begins with E. Since this investigation was intended to complement the work of Blasick (1999), the integrity of the labeling scheme she adopted was preserved whenever possible and she ended her work with Outer Heater Label D. Outer Heaters F and G were fabricated but never used in this investigation, therefore, the specifications of these two outer heaters will not be reported. Also, each individual outer heater used in an experiment was given a label (etched or stamped on the inlet end). In later experiments, when an effective outer heater design was found and tube heaters were expendable, duplicates were typically made which explains the multiple Outer Heater Labels shown in Table 3.5 for Outer Heater Configuration 7.

The following subsections will describe the design specifications of the six different outer heaters (E, H – L) used in this investigation. These subsections will include a discussion on the heated length of each outer heater. In addition, a subsection will be dedicated to the discussion of the various Wire Wrapping Styles utilized on the AC powered outer heaters. The Power Supply Configuration category will be discussed in Section III.6 since three of the four different power supply configurations were used on

both the inner heater and the outer heater.

III.5.1 Outer Heater E

Outer Heater E (shown in Figure 3.12) was constructed entirely of free-machining copper (alloy C14500). First, a piece of 2.5" (63.5 mm) diameter copper bar stock was cut to length (11.5" / 292.1 mm) and sent to Precision Group Inc. / Deep Hole Drilling Division to have a circular channel drilled through it. The circular channel was cut to a tolerance of ± 0.002 " (0.0508 mm) and hone finished to a surface roughness of 0.000032" (0.0008128 mm). This channel served as the outer wall of the annular test section once the inner heater was in place. Next, using the inlet and exit of the circular channel as center, the outer heater was placed in a lathe and the ends were turned down such that they would fit tightly into a 3/4" Swagelok fitting. Also, the 2.5" diameter unfinished outer surface was turned down a few millimeters to ensure that the remaining heater material had a smooth surface finish and was concentrically centered on the drilled circular channel. These actions allowed application of an electrical insulation layer and ensured even heating once the heater wire was wrapped around the outer heater. Next, the inlet and exit ends of the outer heater circular channel were widened in order to ensure that the nominal APT annular channel length of 250 mm was maintained. Note that the Wire Wrapping Style and the placement of the power supply electrodes determined the heated length on Outer Heater E.

After Outer Heater E was constructed it was sent to Cincinnati Thermal Spray who coated the 8.5" (215.9 mm) larger diameter center section of the outer heater with an

electrical insulation layer. The insulating layer consisted of a thin nickel-aluminum bonding layer followed by a 0.007 – 0.010 inch (0.1778 – 0.2540 mm) aluminum oxide layer finished with a thin epoxy scaler. This insulating layer served to electrically isolate the copper structure of Outer Heater E from the heater wire used to heat it. Once the outer heater was constructed and coated, it was wrapped with wire as described in Section III.5.3 and placed in the GTMTF for experimentation.

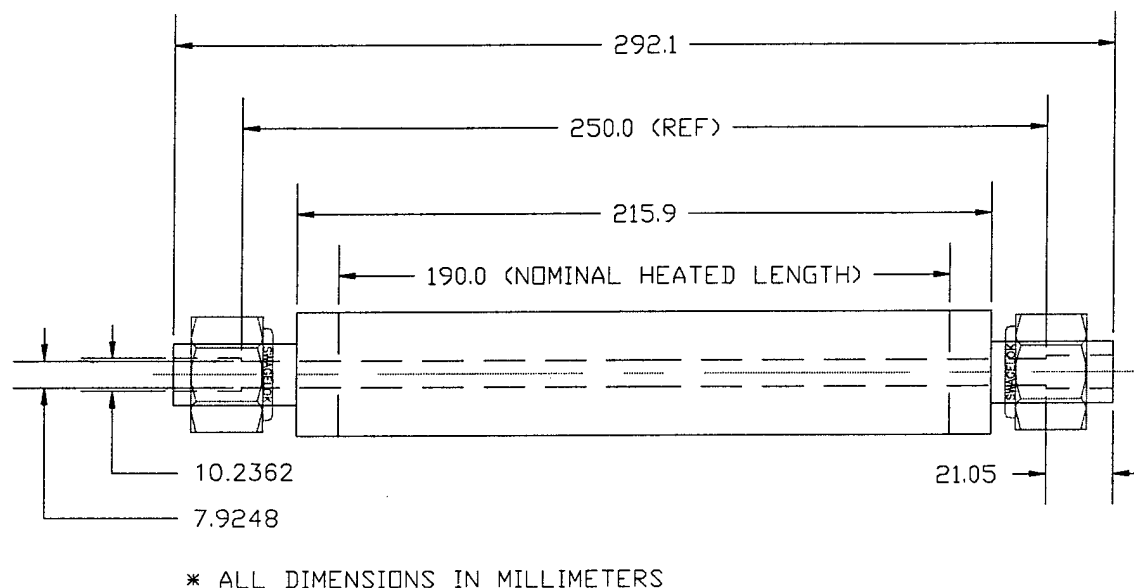
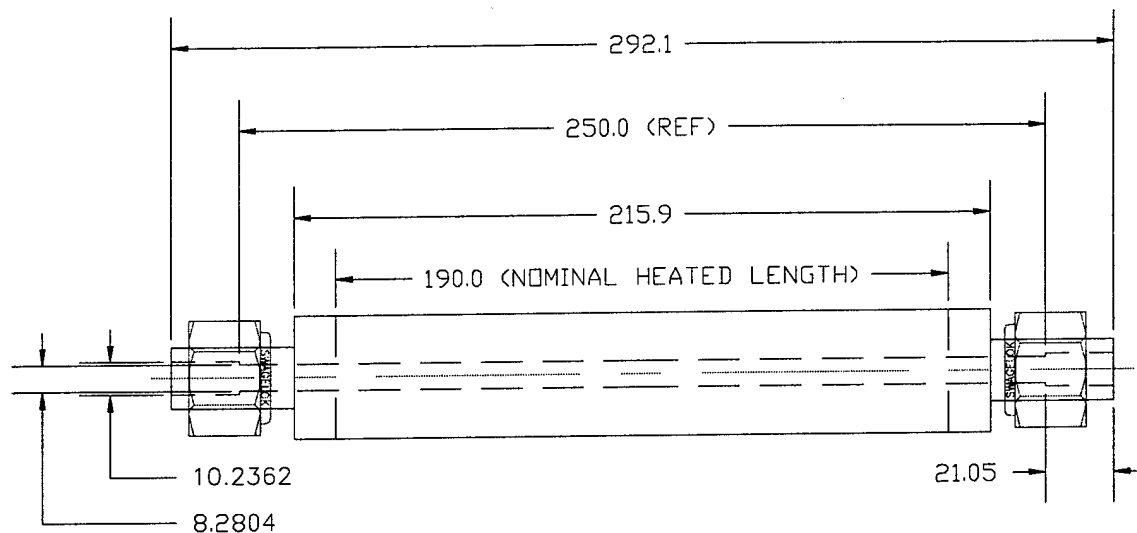


Figure 3.12: Diagram of Outer Heater E

III.5.2 Outer Heater H

Outer Heater H was constructed and heated in an identical manner to Outer Heater E, however, Outer Heater H provided a larger channel diameter which resulted in a larger annular gap width. Figure 3.13 shows a diagram of Outer Heater H.



* ALL DIMENSIONS IN MILLIMETERS

Figure 3.13: Diagram of Outer Heater H

III.5.3 Wire Wrapping Style

Wire Wrapping Style refers to the type of wire and the method of wrapping used for Outer Heaters E and H. Table 3.6 outlines the three different wire wrapping styles used on Outer Heaters E and H.

Table 3.6: Summary of Wire Wrapping Styles

Wire Wrapping Style	Type of Wire	Turns per Inch	Number of Electrodes	Contacts per Electrode
1	NiChrome 80, 26 AWG	22	2	2
2	NiChrome 80, 26 AWG	22	3	3
3	NiChrome 80, 26 AWG	22	4	3

All three wrapping styles utilized the same type of wire and turns per inch on the

outer heater. The bare NiChrome 80, 26 AWG wire had a resistance of 2.647 Ohms per foot (0.00868 Ohms per millimeter) and was wrapped at 22 turns per inch (0.8661 turns per millimeter). A lathe operating at low speed was utilized to wrap the outer heater each time in order to ensure precise duplication of the turns per inch. A small plastic sleeve was slipped over the inlet end of the outer heater, which was in turn mounted in the chuck of the lathe. The lathe's tail stock was then fitted with a live center which, in turn, was tightened into the exit hole of the outer heater. Next, a separate plastic piece was mounted to the lathe's traversing mechanism to act as a guide for the wire. The end of the wire was then fed through the plastic guide and secured to the plastic sleeve. At this point, the appropriate gears were engaged on the lathe to produce the slowest outer heater turning speed and a traversing feed rate of 22 turns per inch. An operator then manually placed tension on the wire by holding the spool as tightly as possible while a second operator energized the lathe. The outer heater was allowed to wrap until the end of the aluminum oxide coated region was reached. At that point, the lathe operator disengaged the lathe while the wire holder maintained constant tension on the wire. The lathe operator then secured the wire to the outer heater using the specially designed steel Heater Wire Clamp shown in Figure 3.14. Once the wire was secured to the outer heater, the wire holder released the tension and the lathe operator cut away the excess wire. A hand-held Fluke 25 Multimeter was then used to check for electrical isolation between the wrapped NiChrome 80 wire and the copper portion of the outer heater. At that point, the outer heater was removed from the lathe and mounted in the GTMTF.

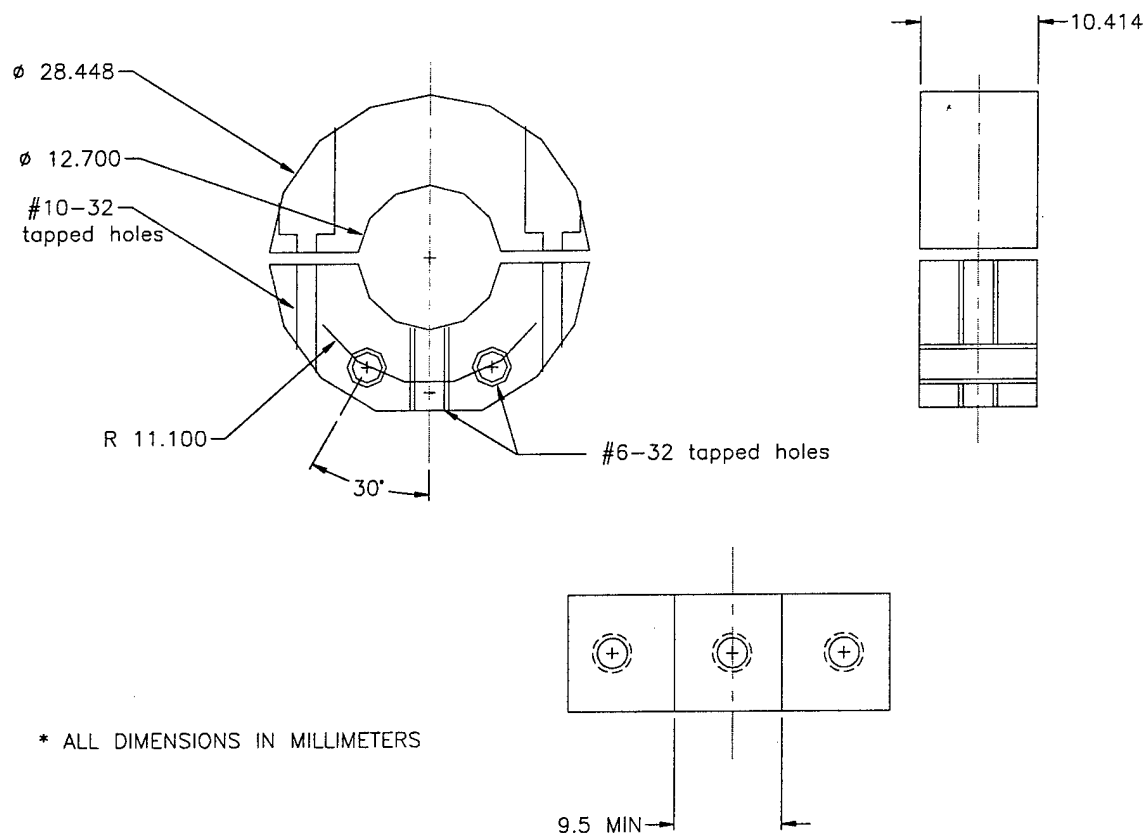
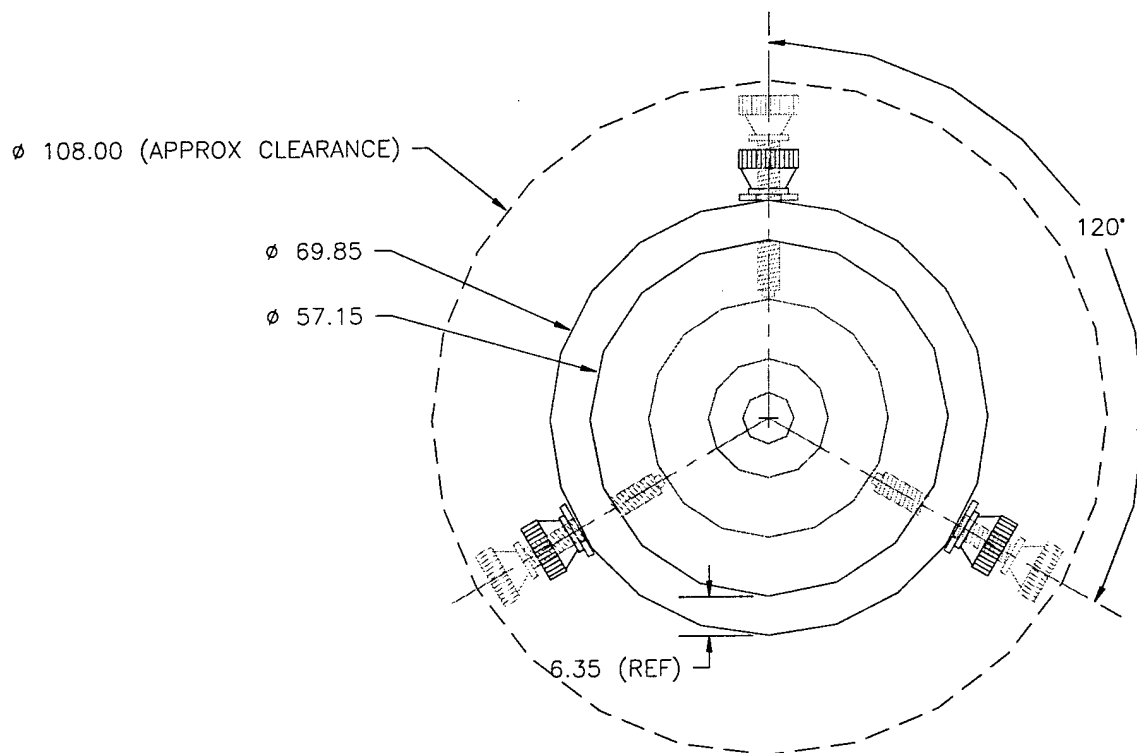


Figure 3.14: Diagram of Heater Wire Clamp

Once mounted, the wire on the outer heater had to be coated with a thin layer of Samereisen Electrical Resistor Cement (No. 78 paste). Normally, unsecured metal wire tends to lengthen as it is heated. When wrapped around the cylindrical outer heater, however, the loops of heated, bare wire became loose and came into contact with their neighboring loops. This contact, in turn, caused a short in the heater wire circuit. The short circuit caused uneven heating over the outer heater and typically lead to melting of the wire and damage to the aluminum oxide coating on the outer heater. The resistor cement was used to hold the wire securely to the outer heater, which ensured good thermal contact with the outer heater and prevented a contact short between two wire

loops. First, the small areas needed for the electrode contacts were masked off using tape. Next, the resistor cement was applied uniformly in an extremely thin layer over the entire outer heater. Care was taken to ensure that the resistor cement penetrated all gaps between the wire loops and that the coating layer did not become too thick. An ideal resistor cement layer just barely covered the heater wire such that, while wet, the heater wire could still be seen through the resistor cement. Trials showed that a thick coating of resistor cement tended to crack and expose highly localized pieces of heater wire to separation from the outer heater and melting. Once the heater wire was completely covered with resistor cement, the masking tape was removed and the cement was allowed to cure for twenty-four hours. After curing, the electrodes were put into place and the outer heater was ready for experimentation.

The Number of Electrodes category outlined in Table 3.6 refers to the number of copper electrodes used to heat the outer heater for a given set of experiments. As many as four, $\frac{1}{4}$ " (6.35 mm) thick, nickel-plated copper electrodes (shown in Figure 3.15) were used to attain the required heated lengths for the OFI experiments that utilized AC powered outer heaters. Current passed into the nickel-plated copper ring and on to the outer heater wire through the nickel-plated brass screws that held the electrode in place. Knurled nuts were used to lock the brass screws in place as shown in Figure 3.15.



* ALL DIMENSIONS IN MILLIMETERS

Figure 3.15: Diagram of Outer Heater Electrode Ring

Due to limitations in Power Supply Configuration One, the heater wire could not be heated as a single, continuous resistor. Instead, multiple electrodes were used to connect different heated zones of equal resistance in parallel on the outer heater. The tests run using Outer Heater Configuration One utilized a single, 55 millimeter heated zone (58.5 Ohms) with two electrodes. Outer Heater Configuration Two also utilized a single heated zone with two electrodes, except the heated length was only 53 millimeters (57.1 Ohms). Outer Heater Configuration Three had two heated zones of 60.0 and 60.2 Ohms that combined electrically in parallel using three electrodes to form a single heated

length of 123 millimeters. Finally, Outer Heater Configuration Four utilized three heated zones of 55.8, 55.1, and 56.5 Ohms that combined electrically in parallel using four electrodes to form a single heated length of 180 millimeters. Electrical resistance readings were taken prior to each set of experiments performed and used to calculate and set the voltage required to generate the necessary heat flux on the outer heater ($V = \sqrt{Power * R_{eq}}$). Note that, due to the parallel nature of the electrical circuit formed, the three heated zones were exposed to the same voltage drop, but different amounts of current flowed through each zone due to the slightly differing resistances. These resistance readings fluctuated from one set of experiments to another since the test section was damaged and re-wrapped multiple times, however, the percent difference between the three resistance readings, i.e. the average heat flux over the different zones, never exceeded five percent.

The Number of Contacts per Electrode simply refers to the number of nickel-plated brass screws that were actually in contact with the heater wire for each electrode. Due to the nature of the power configuration, one brass screw typically carried all or most of the current. For this reason, ideally, only one screw had to contact the heater wire while the other two could rest on the resistor cement used to electrically insulate the heater wire. Experimentation proved, however, that small imperfections in either the tip of the brass screw or the surface of the heater wire lead to rapid failure of a single contact point since there were no alternate paths through which the electricity could pass. Two contact points also proved to be less robust than required, so after Wire Wrapping Style One, all future wrapping styles utilized all three brass screws as electrical contacts.

III.5.4 Outer Heater I and J

After repeated failures of Outer Heaters E and H, a tubular-style outer heater was adopted for use with a DC power supply. Figure 3.16 shows a schematic of Outer Heaters I and J. A single 3/8" (9.525 mm) diameter Hastelloy C-276 welded seam tube was cut in four places using an EDM machine to allow for the inlet and exit of cooling water. In addition, two sets of lines, one marking a 190.0 mm heated length and the other a 180.0 mm heated length, were lightly scribed into the surface of the heater using a lathe. These scribe marks allowed for simple electrode placement and connection at the desired heated length.

Hastelloy C-276 was found to be the ideal material for the outer heaters due to its high strength at elevated temperatures. The single limitation of Outer Heaters I and J was the available inner diameter of the tube. Only an inner diameter of 0.304" (7.7216 mm) was obtainable, which created an annular gap width of only 0.660 mm. In addition, mounting constraints caused by the size of the outer heater electrodes (described in Section III.6) limited the maximum heated length to only 185.0 mm. The inlet end electrode was mounted on the 190.0 mm scribe line while the exit end electrode was mounted on the 180.0 mm scribe line, thus creating a 185.0 mm overall outer heater heated length.

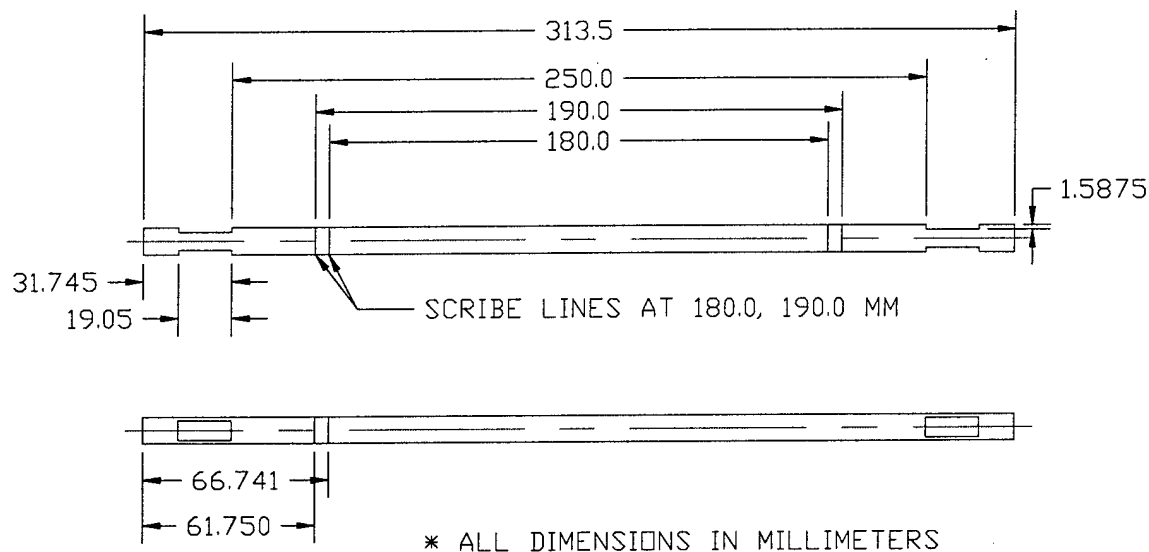
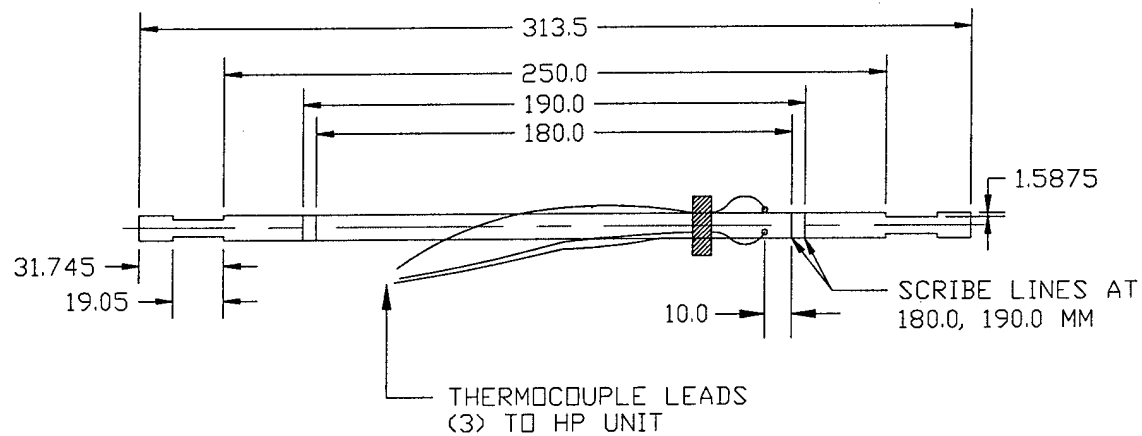


Figure 3.16: Diagram of Outer Heaters I and J

III.5.5 Outer Heater K

Outer Heater K was constructed of Hastelloy C-276 and used to perform all of the CHF experiments conducted in this investigation. As shown in Figure 3.17, the dimensions of Outer Heater K were identical to those of Outer Heaters I and J, however, three type-E thermocouples were mounted one centimeter from the exit end 180.0 mm scribe line and used to detect the heater wall temperature spike associated with CHF. These thermocouples were mounted to Outer Heater K using a ½" diameter clamp with ceramic pieces as 120° spacers. In addition to properly spacing the thermocouples, the ceramic pieces also electrically isolated and thermally protected the thermocouple leads.



* ALL DIMENSIONS IN MILLIMETERS

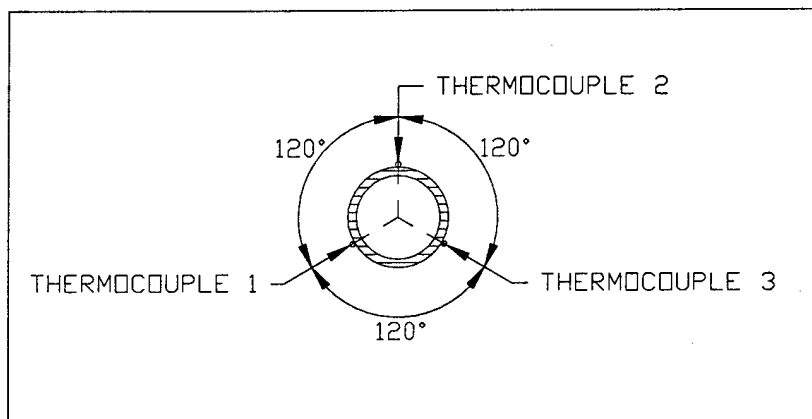
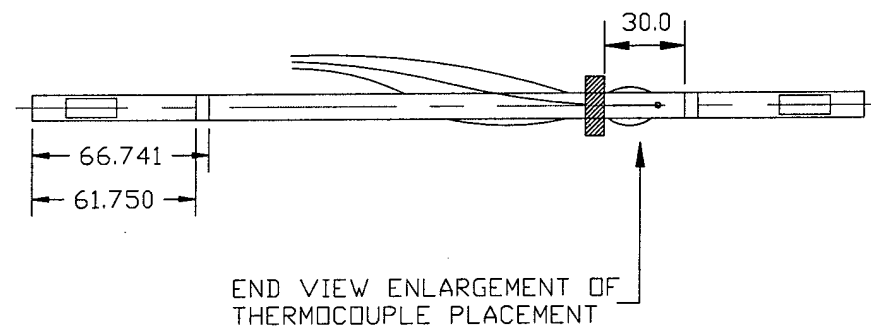


Figure 3.17: Diagram of Outer Heater K

III.5.6 Outer Heater L

Outer Heater L was constructed of Inconel-600 and used to test the feasibility of

Inconel as an outer heater material. As shown in Figure 3.18, Outer Heater L had the same dimensions as Outer Heaters I and J. Only one experiment was attempted using this outer heater design. An OFI experiment with an unheated inner heater and 2.0 MW/m^2 on Outer Heater L caused the outer heater to bend and glow. The experiment was terminated and this outer heater design was never duplicated.

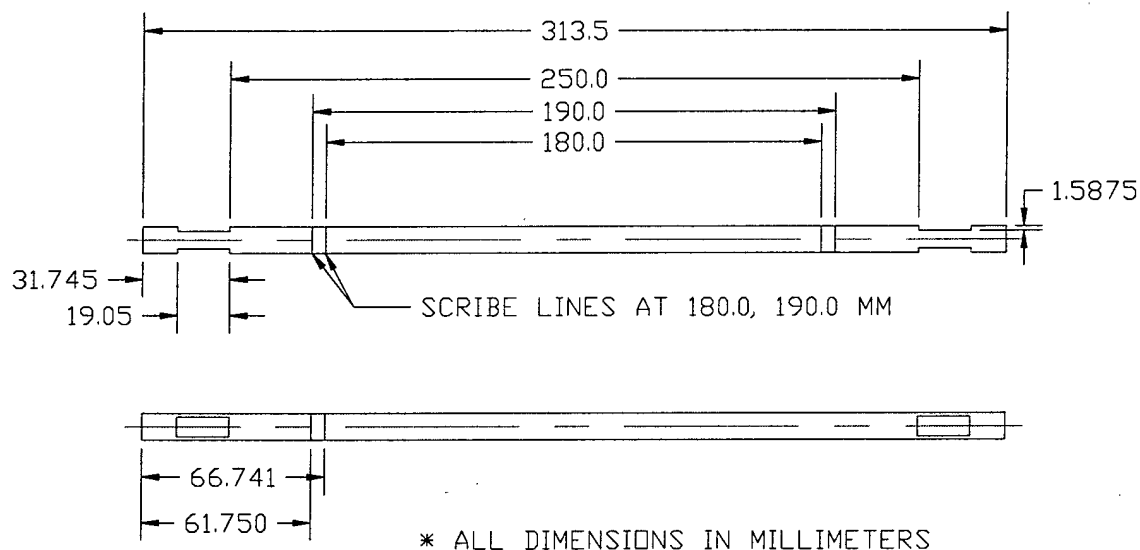


Figure 3.18: Diagram of Outer Heater L

III.6 Power Supply Configuration

As mentioned earlier, all test sections in this investigation were comprised of an inner heater and an outer heater, which together formed a heated annular flow passage. The heat flux for each heater could be set and maintained independently. Tables 3.4 and 3.5 outline the Power Supply Configuration utilized by each heater for all experimental

setups. The following subsections describe the four power supplies used in this investigation and detail the power measurement points. Each circled numerical reference in the following power supply figures indicates a power measurement device detailed in Table 3.3.

III.6.1 Power Supply Configuration One

Power Supply Configuration One was only used to heat Outer Heaters E and H during OFI experimentation. As shown in Figure 3.19, AC power was measured before the transformer and thus was subject to electrical losses of three percent before reaching the outer heater load. Note that experimental measurements taken at the test section using independent voltage and current readings showed that the transformer caused electrical losses of three to five percent. A three percent power loss fraction was used as a conservative estimate for all analysis procedures as described in Section IV.7.

Power Supply Configuration One controlled the in-house 60 Hz, 240 Volt AC electrical power input (in percentage) using two coupled Technipower type W 50 Variacs with 100 % representing a 240 Volt output from the Variacs. The power output from the Variacs was then measured by an Ohio Semitronics AC wattmeter with an external Omega Engineering AC current transducer (Component 15 of Figure 3.1). Next, the voltage was stepped up (2:1) using a General Electric transformer (catalog number 9T21B9109) and supplied to two stationary nodes located near the outer heater using insulated, 6 AWG, stranded copper cables. Power was then supplied directly to the outer heater via two 1/16" (1.5875 mm) diameter, insulated copper wires connected to each of

the Outer Heater Electrode Rings described in Section III.5.3. Note that the copper portion of the outer heater was rigidly connected to the GTMTF via stainless steel Swagelok fittings and hence was electrically grounded. The wound heater wire was electrically isolated from the copper portion of the heater by the aluminum oxide layer described earlier; this was the portion of the outer heater to which power was supplied.

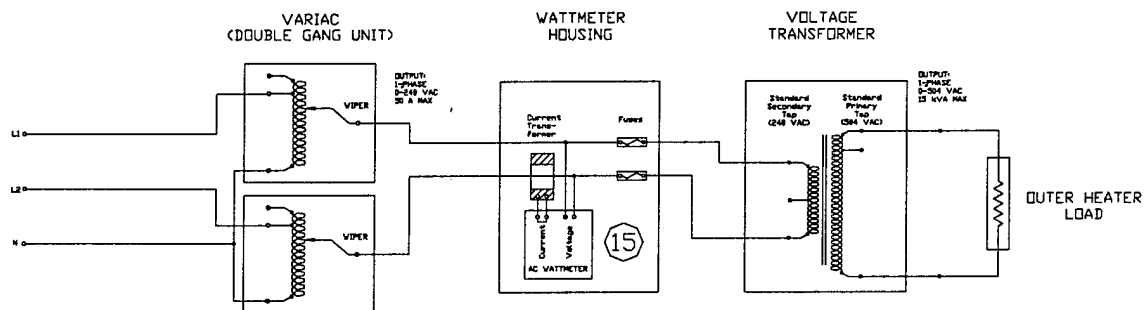


Figure 3.19: Electrical Diagram of Power Supply Configuration One

III.6.2 Power Supply Configuration Two

Power Supply Configuration Two was used independently by both the inner heater and the outer heater for different experimental setups. Referring to Tables 3.1 and 3.4, Inner Heater Configurations 3 – 5 used Power Supply Configuration Two while the outer heater was heated by Power Supply Configuration One. Likewise, referring to Tables 3.1 and 3.5, Outer Heater Configuration 6 used Power Supply Configuration Two to test Outer Heater L while the inner heater was left unheated.

As shown in Figure 3.20, Power Supply Configuration Two used a DC power supply produced by Rapid Power Technologies (serial number 1198224) to supply

electrical power to the connected heater. The power level produced by this DC power supply was controlled using a set of two rheostats. The first rheostat controlled the maximum current produced by the power supply (in percentage) with 100 % representing a potential maximum current of 2500 Amps. The second rheostat controlled the voltage drop produced by the power supply (in percentage) with 100 % representing a maximum electrical potential of 25 Volts. Note that these two rheostats are not shown in Figure 3.20. Power Supply Configuration Two measured the power output using an Ohio Semitronics DC wattmeter (Component 16 of Figure 3.1). When used to power the outer heater, Power Supply Configuration Two supplied power directly to the heater via one fifteen foot long, flexible, 1.25" (31.75 mm) diameter, 1000 MCM, insulated, copper cable connected to each of the two Outer Heater Electrode Plates (shown in Figure 3.21) that were mounted to the heater. When used to power the inner heater, electrical power was sent to a stationary positive node via a 1000 MCM, insulated copper cable. From there, power was applied to the inner heater using two flexible, insulated, AWG 4/O copper welding cables that were attached to the inner heater via a one inch wide copper electrical connection block. After passing through the inner heater, the inner heater power loop was completed by the negative side, which was a mirror image of the positive.

III.6.3 Power Supply Configuration Three

Power Supply Configuration Three was used simultaneously by both the inner heater and the outer heater during the last five OFI experiments performed in this investigation. In order to increase the surface heat flux on the outer heater above 2.0 MW/m^2 , a DC powered tube heater design had to be adopted. This tube heater (Outer Heaters I – L), then had to be connected electrically in parallel with the inner heater to the Rapid Power Technologies (RPT) DC power supply described in Section III.6.2.

Since Power Supply Configuration Three used the RPT DC power supply to supply electrical power to both the inner and the outer heater simultaneously, a method of connecting the heaters electrically in parallel had to be devised such that the inner-to-outer surface heat flux ratio remained unity. Due to the larger heater wall thickness of the outer heater tube, the outer heater leg of the power supply loop had a lower electrical resistance. Note that the outer heater, due to its larger diameter and accompanying larger heated area, required more power to attain the required surface heat flux. However, due to the nature of Power Supply Configuration Three, the outer-to-inner heater resistance ratio produced a much higher outer surface heat flux than that for the inner heater. This problem was corrected by the addition of a series resistor to the outer heater leg of the power supply loop as shown in Figure 3.22. The following paragraphs describe the components of the inner and outer heater legs of the power supply loop independently. In addition, Figure 3.23, though not drawn to scale, provides a general, less detailed overview of the order in which the components of Power Supply Configuration Three

were connected.

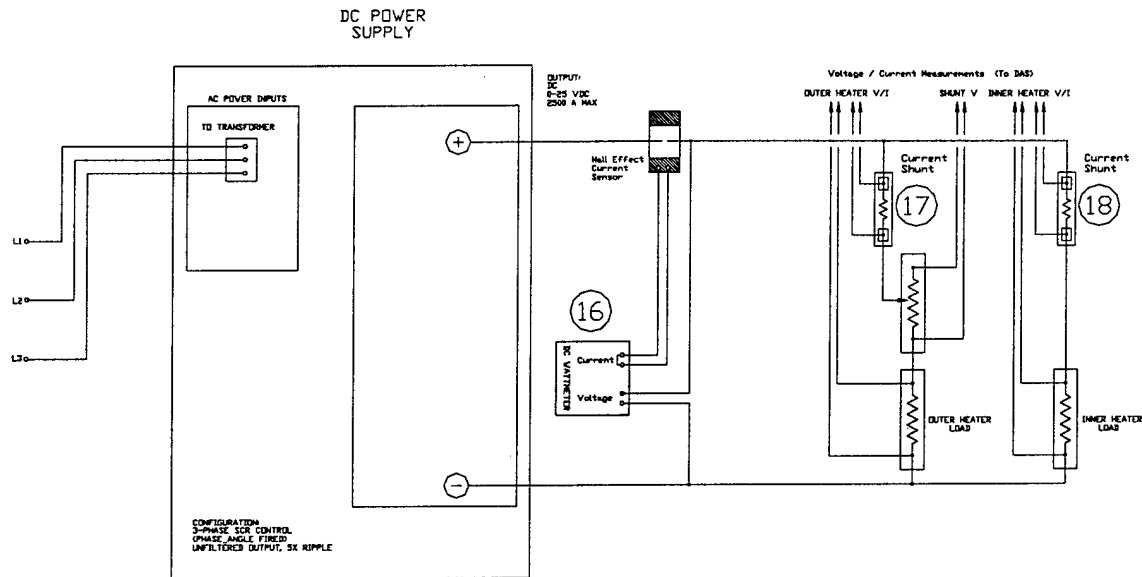


Figure 3.22: Electrical Diagram of Power Supply Configuration Three

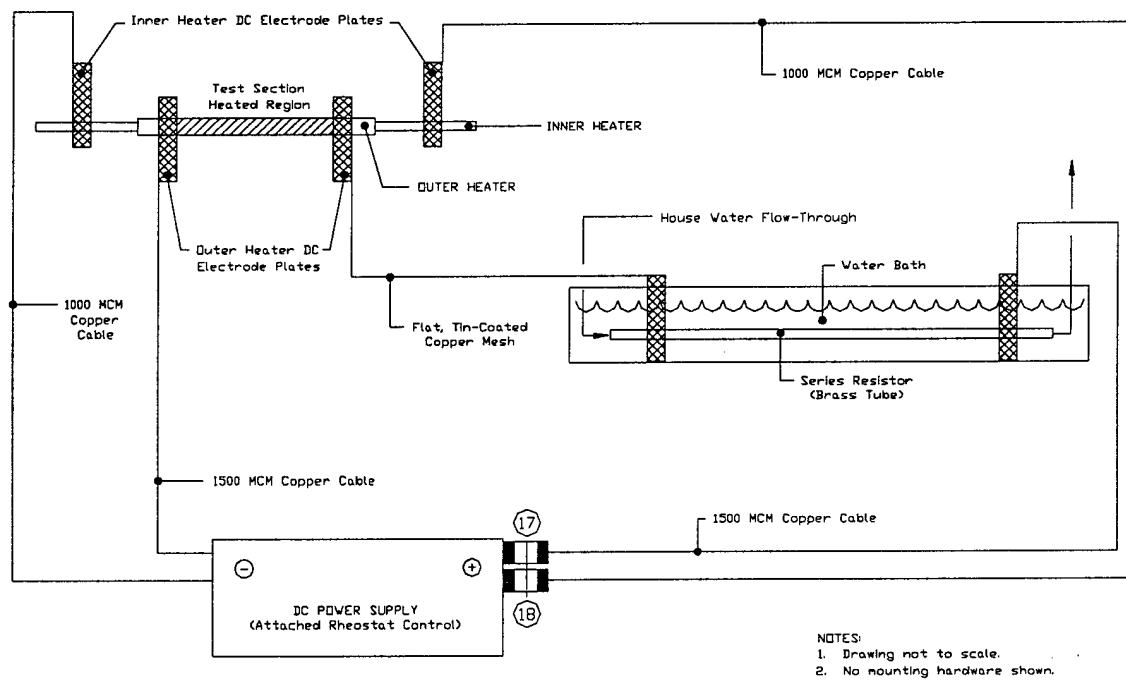


Figure 3.23: Component Diagram of Power Supply Configuration Three

The inner heater leg of Power Supply Configuration Three began at the positive node of the DC power supply and ran through an Empro DC current shunt (Component 18 of Figure 3.1) and on to a flexible, 1000 MCM, copper cable. Next, power was applied directly to the inner heater using an Inner Heater DC Electrode Plate (Figure 3.24). The 1000 MCM copper cable bolted directly to this electrode plate using a single $\frac{1}{2}$ "-13 bolt; the hole for this bolt was drilled and tapped in the center of the plate (hole not shown in Figure 3.24). After passing through the inner heater, the inner heater leg of the power supply loop was completed by a second Inner Heater DC Electrode Plate that was connected to the negative node of the DC power supply via a second 1000 MCM copper cable. Note that the voltage drop across the inner heater was taken using taps that were connected to the electrode plates. The DAS system multiplied this voltage drop by the current reading taken by the Empro DC current shunt to determine the power supplied to the inner heater. In addition, using this power level and an operator defined inner heater heated surface area, the DAS system continuously calculated and displayed the surface heat flux on the inner heater, which allowed proper adjustment of the power level prior to the commencement of an OFI experiment.

The outer heater leg of Power Supply Configuration Three began at the positive node of the DC power supply and ran through an Empro DC current shunt (Component 17 of Figure 3.1) and on to a fifteen foot long, flexible, 1.5" (38.1 mm) diameter, 1500 MCM, insulated, copper cable. Next, a part of the supplied electrical power was dissipated in a variable series resistor. This series resistor was constructed from a $\frac{1}{4}$ " (6.35 mm) diameter brass tube that was cooled by a water bath and a house water flow-

through line. Power from the 1500 MCM copper cable was applied to the brass heater using an Inner Heater DC Electrode Plate (Figure 3.24). Moving the electrical connection point in order to make the resistor length longer or shorter altered the resistance of the series resistor as required. Next, power was applied to the outer heater using a flat, tin coated, copper mesh that was connected to an Outer Heater DC Electrode Plate (Figure 3.21). The copper mesh connected to both the brass tube electrode plate and the outer heater electrode plate using eight 10-32 screws that were fitted with washers, forced through the mesh, and threaded into the holes shown in Figures 3.21 and 3.24. After electricity passed through the outer heater, the outer heater leg of the power supply loop was completed by a second Outer Heater DC Electrode Plate that was connected to the negative node of the DC power supply via a second 1500 MCM copper cable. The 1500 MCM copper cable bolted directly to the electrode plate using a single $\frac{1}{2}$ "-13 bolt; the hole for this bolt was drilled and tapped in the center of the plate (hole not shown in Figure 3.24). Note that the voltage drop across both the outer heater and the series resistor was taken using taps that were connected to the electrode plates. The DAS system multiplied these voltage drops by the current reading taken by the Empro DC current shunt to determine the power supplied to the outer heater and the power dissipated by the series resistor. In addition, using the outer heater power level and an operator defined outer heater heated surface area, the DAS system continuously calculated and displayed the surface heat flux on the outer heater, which allowed proper adjustment of the power level prior to the commencement of an OFI experiment.

Finally, a measurement was made of the total power level supplied by the DC

power supply using an Ohio Semitronics DC wattmeter (Component 16 of Figure 3.1). In both OFI and CHF experimentation this redundant reading became invaluable since the two DC current shunts proved unreliable. Due to an unidentified ground in the DAS system, the readings from both DC current shunts became too erratic for experimental analysis. Therefore, the power applied to the test section was determined using an energy balance and the total power reading from the DC power supply. This procedure is described in Sections IV.7.2 and IV.8.2.

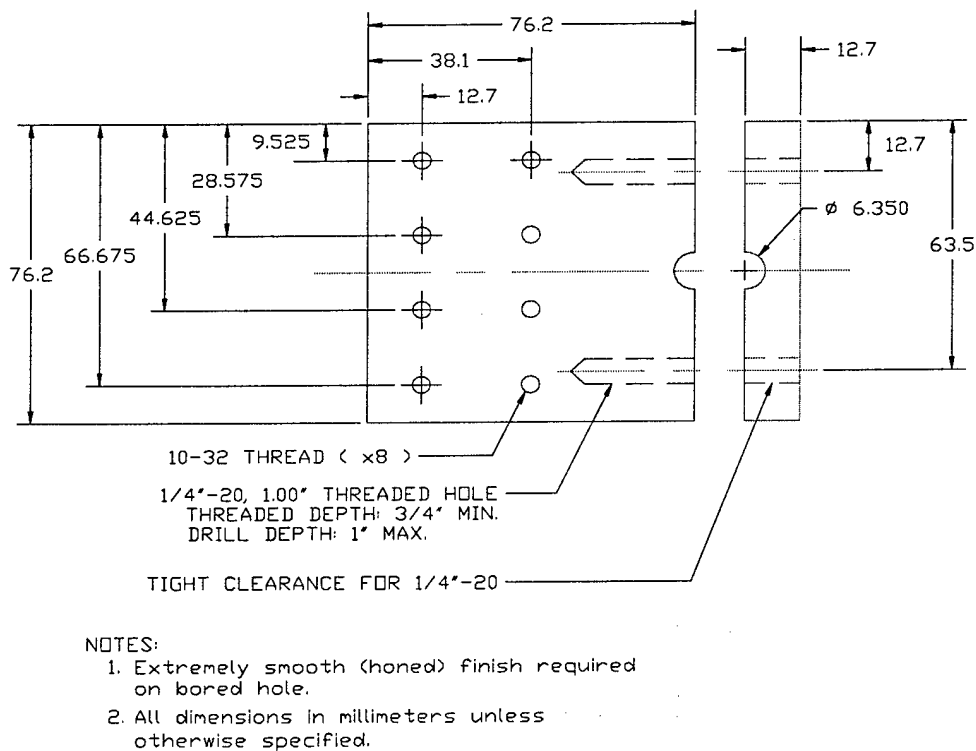


Figure 3.24: Diagram of Inner Heater DC Electrode Plate

III.6.4 Power Supply Configuration Four

Power Supply Configuration Four (shown in Figure 3.25) was used for all CHF experiments performed in this investigation. The power supply loop was identical to that of Power Supply Configuration Three, however, the power supplied by the RPT DC power supply was not controlled using the two rheostats described in Section III.6.2. Instead, power was controlled using a Hewlett Packard Data Acquisition / Switch Unit (Component 20 in Table 3.3) that was connected to a Compaq DeskPro 575 personal computer (HP Benchlink Data Logger Software in a Microsoft Windows 95 operating environment). An input signal was provided to the HP unit from the Compaq personal computer and the HP unit, in turn, provided a signal to the power supply, which controlled the power input to the test section. The HP unit also monitored the outer heater thermocouples mounted on Outer Heater K (Figure 3.17) and automatically terminated the experiment by cutting the power supply signal if the outer heater surface temperature exceeded 300°C. The HP unit could sample at rates up to 600 readings per second on a single channel and scan at rates up to 250 channels per second making it ideal for monitoring the outer heater temperature during a CHF experiment. All temperature readings from the outer heater thermocouples were recorded along with a real time stamp by the HP Benchlink software package on the Compaq personal computer for future analysis. Figure 3.26, though not drawn to scale, provides a general, less detailed overview of the order in which the components of Power Supply Configuration Four were connected.

During the first CHF experiment, all four DC electrode plates became extremely

hot due to contact resistance between the plates and their respective heaters. For this reason, an external, copper $\frac{1}{4}$ " (6.35 mm) diameter coolant tube was silver soldered to each of the four electrode plates attached to the test section. Each coolant tube was 10 inches (254 mm) long and bent into a U-shape such that it would fit around the central row of 10-32 tapped holes with each leg of the U-shape running perpendicular to the $\frac{1}{4}$ "-20 electrode connection holes. The four coolant tubes were then attached in series using flexible, $\frac{1}{4}$ " (6.35 mm) diameter nylon tubing. Next, the house water flow-through line that cooled the adjustable series resistor described in Section III.6.3 was connected to the inlet of the coolant tube series circuit and the exit of the circuit was fed into the house water drain. . Due to the copper construction of the electrode plates, the U-shaped coolant tubes provided adequate cooling and no further problems were encountered. Note that the coolant circuit described in this paragraph is not shown in Figure 3.26 in order to maintain the relative simplicity of the diagram

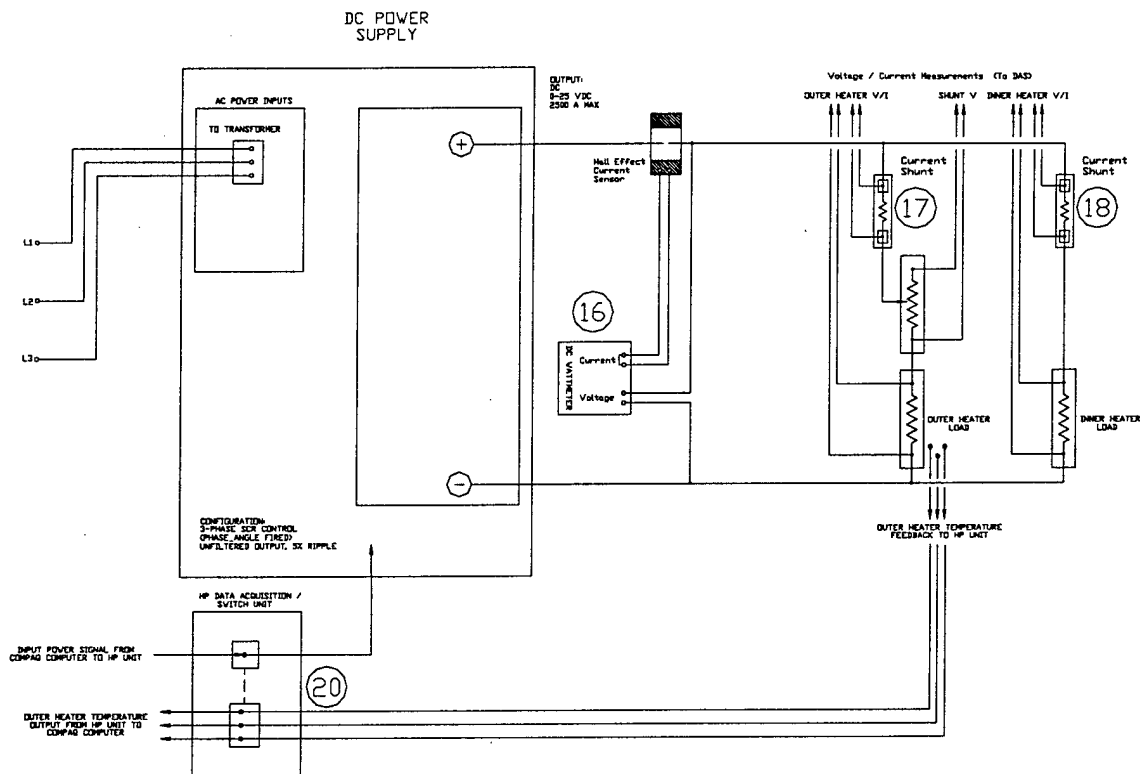


Figure 3.25: Electrical Diagram of Power Supply Configuration Four

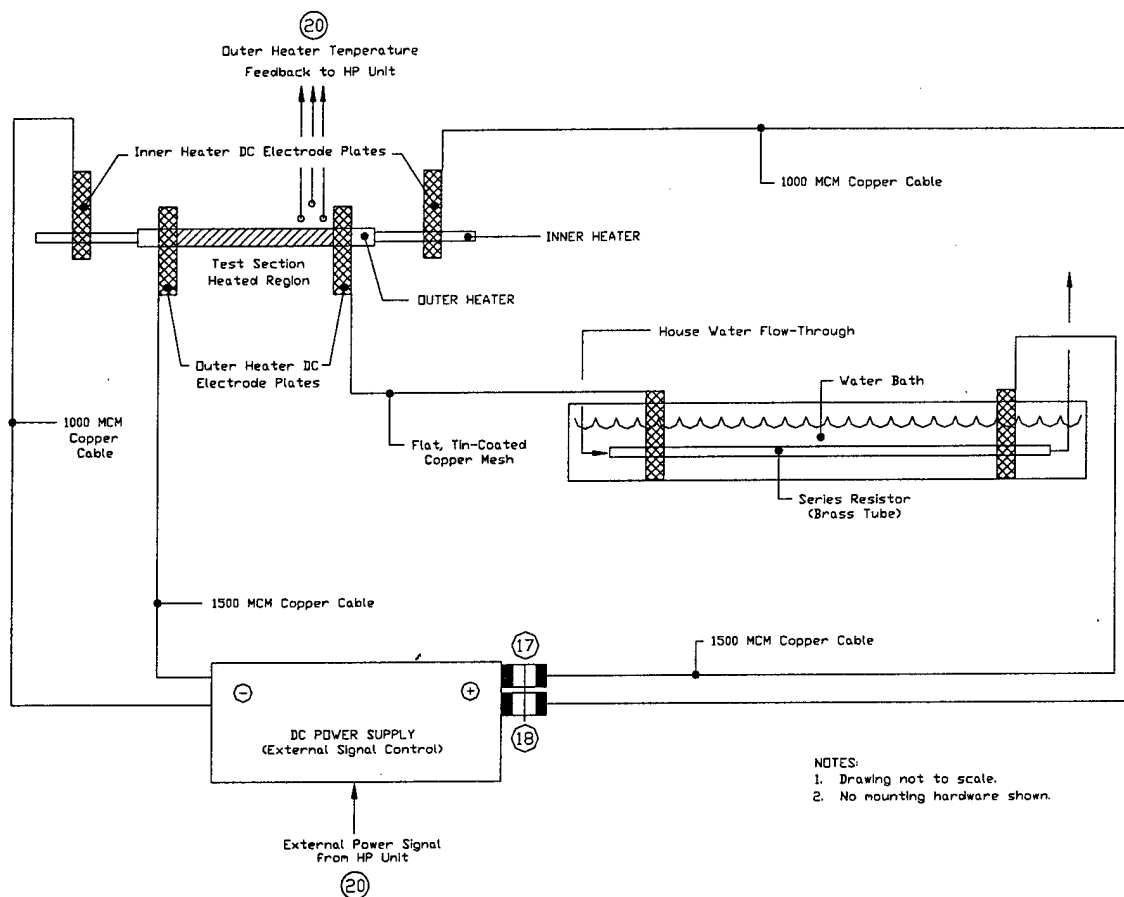


Figure 3.26: Component Diagram of Power Supply Configuration Four

III.7 Mounting Configuration

The annular test sections used in this investigation involved long flow passages with very narrow gaps between the independent cylindrical heaters. This geometry introduced significant difficulty to the design and construction of an effective mounting configuration. Significant effort was expended in the production of two different mounting configurations that would allow precise alignment of the multiple test section

components used in this research. The base for both mounting configurations was a standard triangular optical rail that was bolted to a Unistrut supported particleboard table (Figure 3.27, bolts not shown). The custom-made supports used by both mounting configurations to secure the Swagelok T-fittings that connected the test section to the GTMTF flow loop were attached to the mounting rail using standard, screw-tightened optical rail mounts. The custom made supports (Figure 3.28) were constructed in house out of steel and aluminum components and incorporated an adjustable, telescoping support column. This telescoping support allowed either end of the test section to be precisely adjusted to guarantee a level configuration.

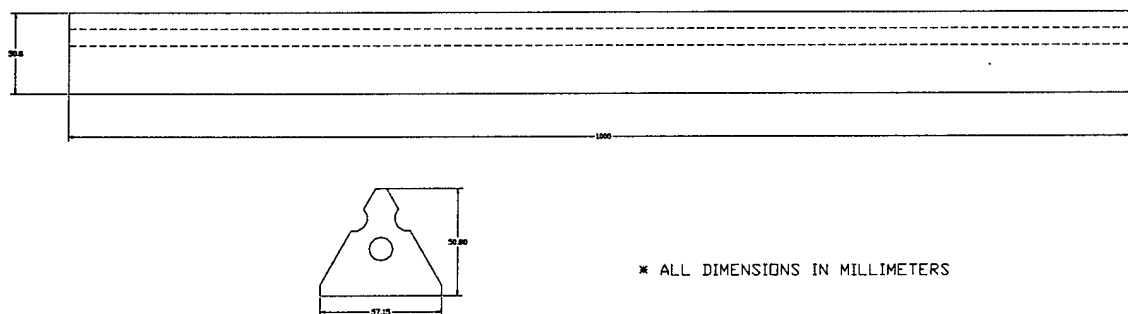


Figure 3.27: Diagram of Triangular Optical Mounting Rail

The Swagelok T-fittings used in both mounting configurations were standard, stainless steel, $\frac{3}{4}$ " compression fittings and served as the inlet and exit plenums for the test section coolant flow. Since these fittings were stainless steel, their connection to the GTMTF flow loop effectively grounded the mounting configuration, thus necessitating the need for non-conducting inserts that would isolate the inner and outer heaters from ground as well as from each other. The inserts used by both mounting configurations

also had to maintain the test section in a level, horizontal configuration. To this end, Mounting Configurations One and Two used both flexible rubber stoppers and precisely machined Teflon inserts to align and isolate the test sections. The following subsections characterize the design details of these components.

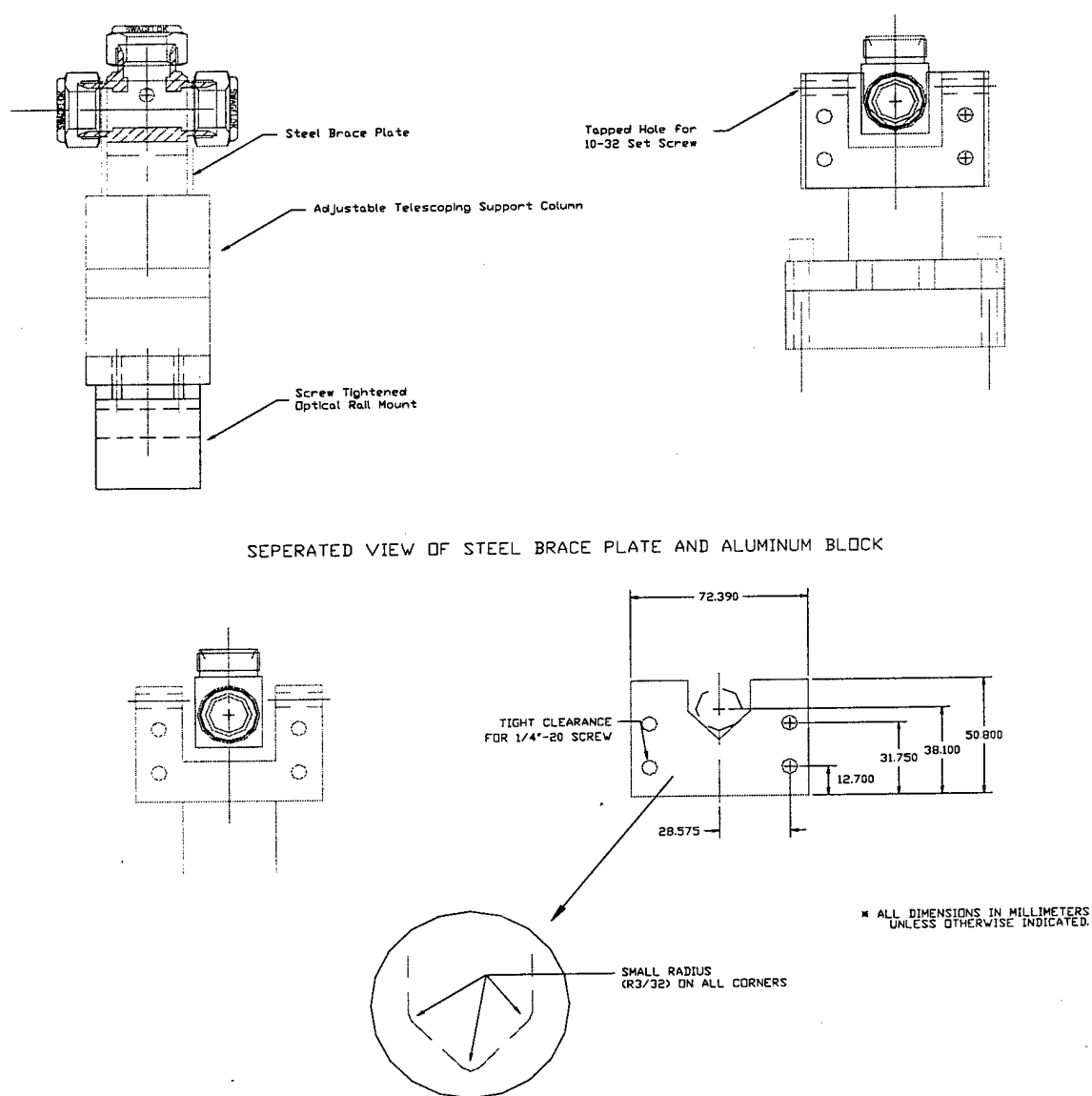


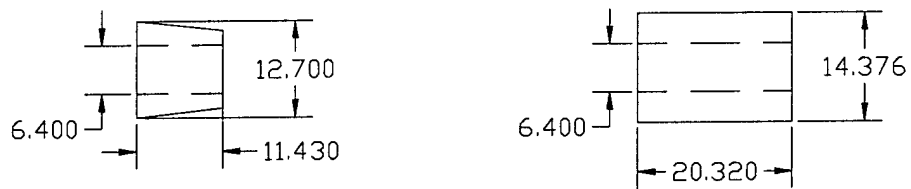
Figure 3.28: Diagram of Custom Made Swagelok T-Fitting Mount

III.7.1 Mounting Configuration One

Mounting Configuration One accommodated the AC powered outer heaters (Outer Heaters E and H) and, therefore, was only utilized during OFI experimentation. The Teflon insert and rubber stopper shown in Figure 3.29 were inserted into the Swagelok T-fittings in order to isolate the inner heater from the outer heater. Note that, as described earlier, the copper structure of the outer heater was grounded to the GTMTF via the Swagelok T-fittings. The NiChrome wire wrapped around the outer heater provided the required outer heater power input. The Teflon sleeve (Figure 3.29, upper right corner) was placed on the outer end (away from the heated region) of the Swagelok T-fitting. This Teflon sleeve was used to align the inner heater concentrically within the Swagelok T-fitting and electrically isolate the inner heater from the outer heater. As shown in Figure 3.29, the Teflon sleeve was attached to the Swagelok T-fitting by a stainless steel extender piece. This extender was 1.70 inches (43.18 mm) long and was sealed by a rubber stopper (Figure 3.29, upper left corner). The primary function of the rubber stopper was to prevent leakage from the system, but it also helped support the inner heater and maintain its alignment.

Figure 3.30 shows the entire diagram of Mounting Configuration One. This figure clearly shows that the large diameter part of the outer heater was completely wrapped with NiChrome heater wire. The steel Heater Wire Clamps held the wire on the outer heater and copper Electrode Rings were used to apply power to the outer heater. Note that the heated length of the outer heater was measured from the center of the first Electrode Ring to the center of the last electrode ring. The brass screws that carried

current to the outer heater and attached the Electrode Rings to the outer heater were located in the center of the Electrode Rings, which corresponded to the beginning of the heated section of the outer heater.



* ALL DIMENSIONS IN MILLIMETERS

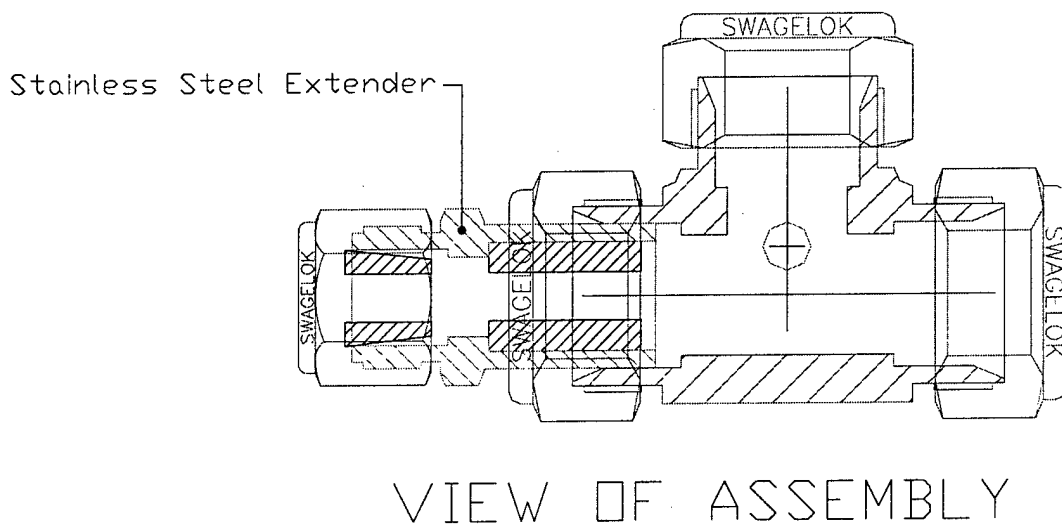


Figure 3.29: Diagram of Teflon and Rubber Inserts for Swagelok T-Fitting

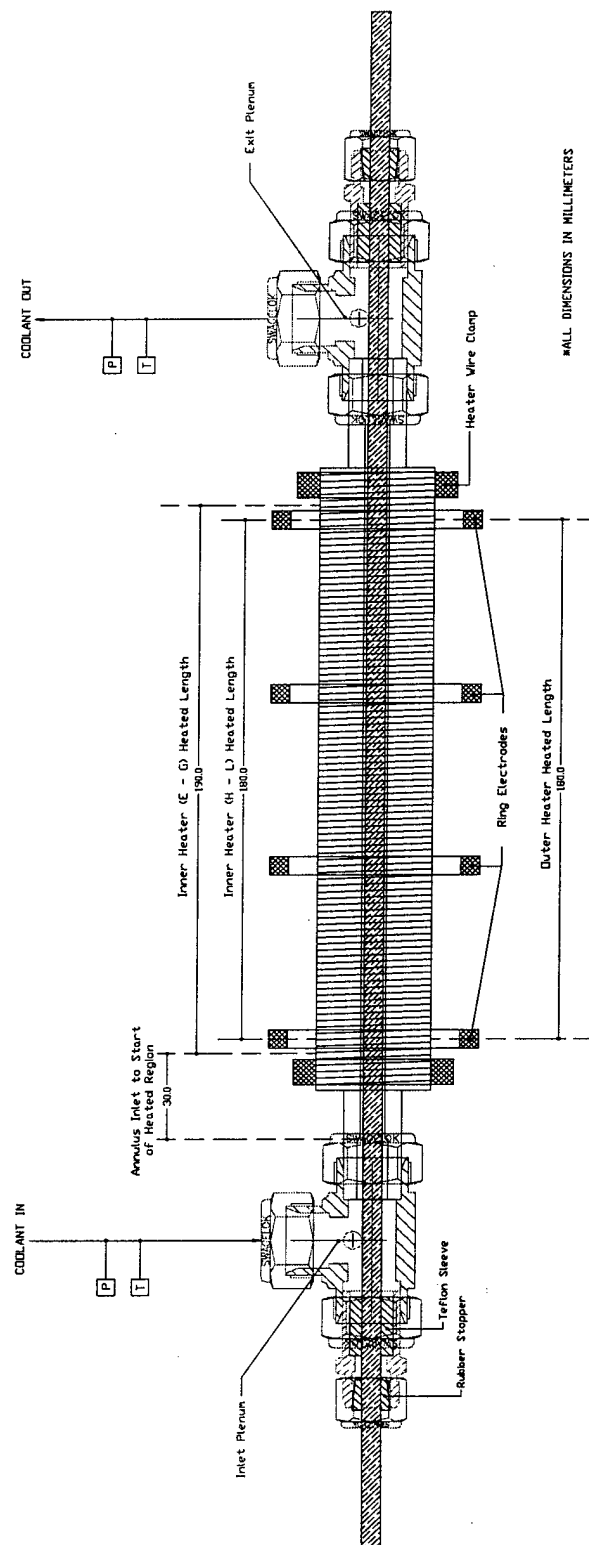
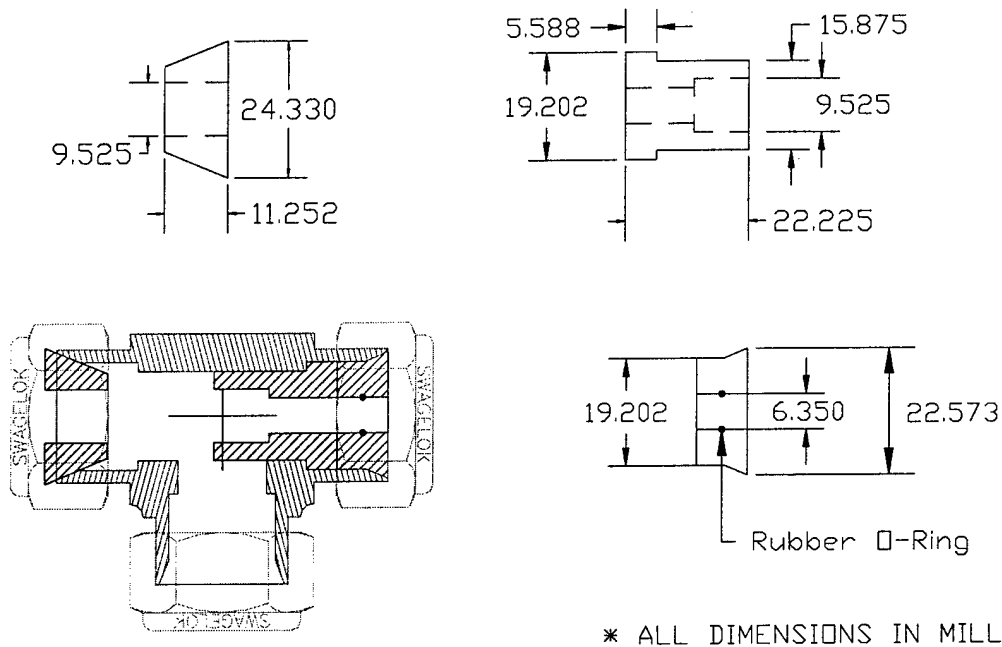


Figure 3.30: Diagram of Mounting Configuration One

III.7.2 Mounting Configuration Two

Mounting Configuration Two accommodated the DC powered, tube style outer heaters (Outer Heaters I – L) used in the highest heat flux OFI experiments and all CHF experiments. The Teflon components and the rubber stopper shown in Figure 3.31 were inserted into the Swagelok T-fittings in order to isolate the inner heater from the outer heater and the outer heater from ground. The angled Teflon piece (Figure 3.31, lower right corner) was placed on the outer end (away from the heated region) of the Swagelok T-fitting. This angled Teflon component was used to seat the innermost insert securely within the Swagelok T-fitting. In addition, the angled Teflon insert incorporated a rubber O-ring that helped prevent leakage from the system. The innermost Teflon insert (Figure 3.31, upper right corner) provided the bulk of the support needed to keep the inner heater straight and isolated from the outer heater. As shown in Figures 3.31 and 3.32, this insert effectively created the annular flow passage required by this investigation by simultaneously supporting the inner heater while providing a concentric seat for the outer heater. The final insert placed in the Swagelok T-fitting was a simple rubber stopper (Figure 3.31, upper left corner) that fit tightly over the outer heater on the heated side of the Swagelok T-fitting. The primary function of this rubber stopper was to maintain the watertight integrity of the configuration, but it also helped support the outer heater.



VIEW OF ASSEMBLY

Figure 3.31: Diagram of Teflon and Rubber Inserts for Swagelok T-Fitting

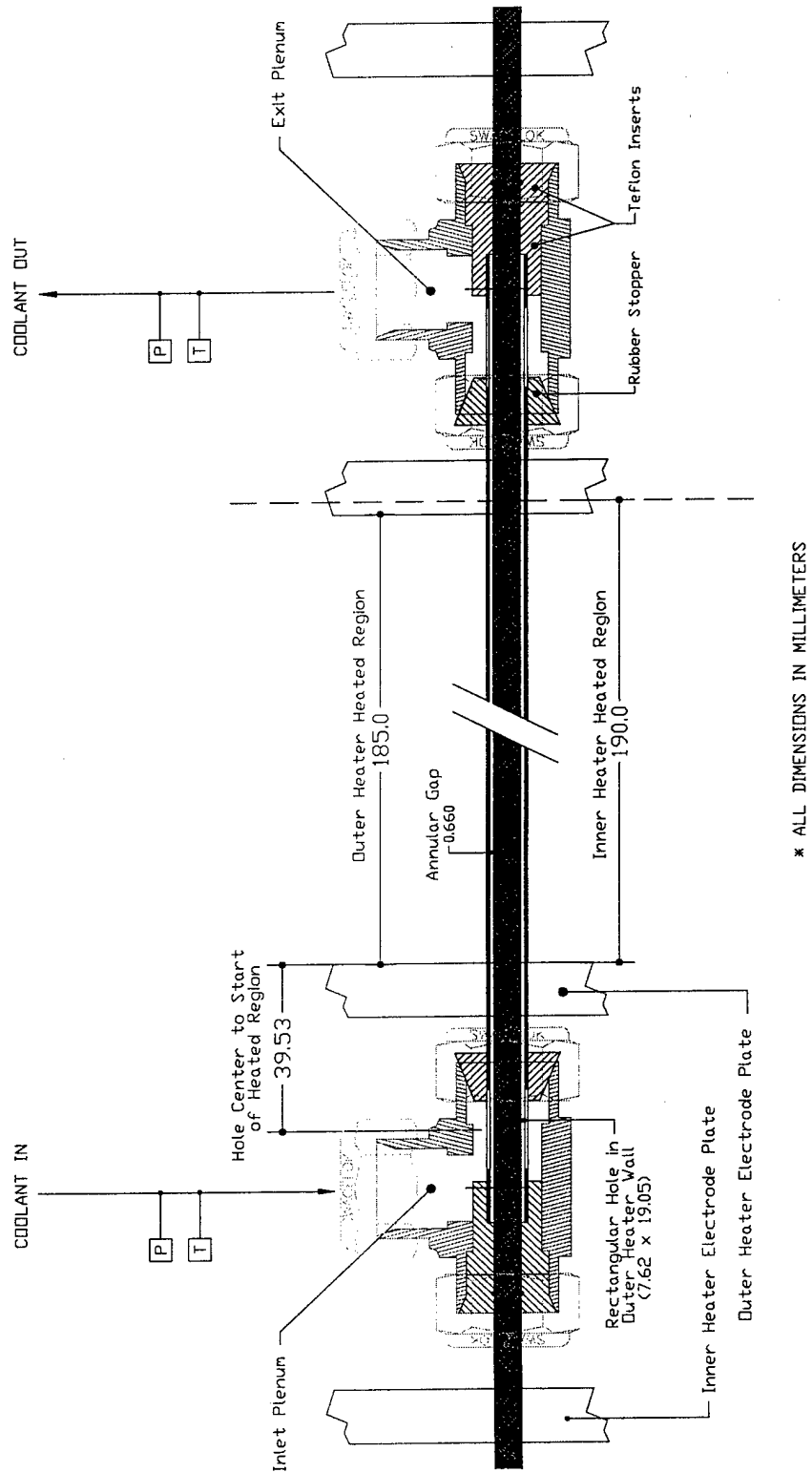


Figure 3.32: Diagram of Mounting Configuration Two

III.8 Insulation Configuration

Due to limitations imposed by Mounting Configuration Two, only experiments that utilized an AC powered outer heater (Outer Heaters E and H) were insulated. As shown in Figure 3.33, Insulation Configuration One consisted of a cylindrical sleeve of calcium silicate (maximum temperature of 2300°F / 1260°C) with calcium silicate end caps. Each end cap had a one inch (25.4 mm) diameter hole cut in its center to allow for connection of the test section to the flow loop and the entire insulation assembly was cut lengthwise to allow placement over the test section. Once in place, the insulation covered the entire heated length of the test section and was of adequate diameter to clear the outer heater electrodes. The insulation was held in place by mounts placed on the optical rail described in Section III.7. These mounts were constructed in house and are not shown in Figure 3.33.

Note that the calcium silicate cylindrical sleeve was formed by the manufacturer (Thermal Ceramics) using a binder that was only rated to 500°F / 260°C. This binder was slowly baked off in a high temperature oven prior to using the insulation in experimentation. Previous experimental experience showed that this binder, if not properly removed, had a tendency to smoke and catch fire while the test section was energized.

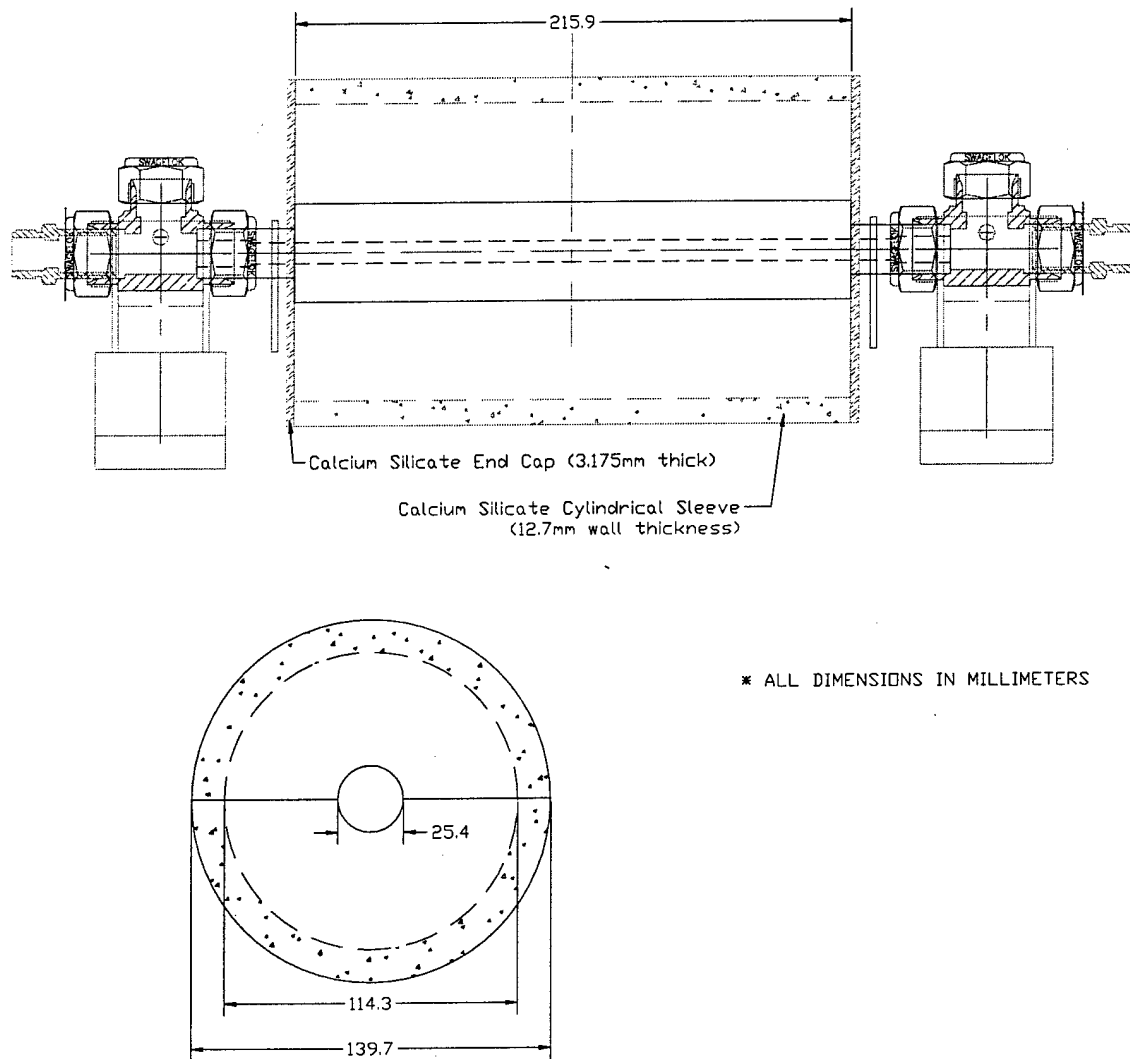


Figure 3.33: Diagram of Insulation Configuration One

III.9 Non-Condensable Gas Status

The amount of non-condensable gas in the coolant was set using the components described in Section III.3.6.2 and the procedures outlined in Section IV.3. Each experimental setup specifically included the Non-Condensable Gas Status so that

comparisons could be made between experiments that utilized degassed water, air-saturated water, or nitrogen-saturated water as a working fluid.

CHAPTER IV

EXPERIMENTAL PROCEDURES

This chapter provides a complete description of system preparation and control procedures. Many of these procedures are similar to those used by Kennedy, et al. (1997), Roach (1998), and Blasick (1999).

IV.1 Initial System Preparation

As described in Chapter III, the test section used in the GTMTF was comprised of two pieces: an inner heater held concentrically within an outer heater. The mounting configurations described in Chapter III required leveling and alignment prior to the filling of the system. Each of the two braces affixed to the optical mounting rail could be swiveled and vertically adjusted independently. In order to ensure that the Swagelok fittings, which supported the two pieces of the test section, were aligned and horizontal, a half inch diameter solid stainless steel rod was placed in the braces. This solid rod forced the four contact points on the two braces to align. Also, a level was placed on the bar in order to even out the heights of the two braces. Once in place, the supports on the braces were tightened so that the braces would remain stationary. At this point, the Swagelok

fittings were placed into the braces and the outer heater was installed. Next, the inner heater was carefully fed through the outer heater and centered horizontally using a ruler. The appropriate teflon seals were then placed over the ends of the inner heater and the Swagelok fittings were tightened into place making the test section leg of the GTMTF water tight. The teflon seals, coupled with the teflon supports located within the Swagelok fittings, effectively centered the inner heater concentrically within the outer heater. Next, electrical isolation between the inner heater, the outer heater, and the metal frame (ground) had to be checked. This was accomplished using a Fluke 25 hand held multi-meter. Once electrical isolation was ensured, the appropriate power cables were attached to the inner and outer heaters.

The GTMTF was frequently modified in order to repair broken components or to change flow conditions. Most modifications required opening the watertight system to the atmosphere. After any such occasion, the integrity of the system had to be visually checked for leaks before resuming experiments.

IV.2 System Filling Procedure

The system filling procedure was nearly identical for all experimental setups. Also, the primary components used while filling the system did not change among the four flow loop configurations used. Any minor differences in the filling procedure associated with a specific flow loop configuration will be clarified as necessary.

First, all internal system valves within the flow loop were opened in preparation for filling the system. Also, the saturation loop was isolated by closing the saturation loop inlet valve (Component SS in Figure 4.1), the saturation loop exit valve (Component TT), and the saturation tank pressure regulation valve (Component S). The saturation loop had to be isolated since the filling procedure required slight pressurization of the system using a peristaltic pump. The saturation tank gas bleed valve (Component HH), located within the saturation loop, was always left open to the atmosphere to allow the water-saturation gas to bubble through the saturation tank (Component FF) during experimentation. This means that any attempt to slightly pressurize the system during filling resulted in system overflow through the saturation tank gas bleed valve (located ten feet above the ground) if the saturation loop was not isolated. After isolating the saturation loop, the system was filled with distilled water using a variable speed peristaltic pump (Component AA) attached to the system fill valve (Component BB). The pump was switched on and the system relief valve (Component CC) was opened to allow air to escape the peristaltic pump line. Once water began flowing out of the system relief valve, it was closed and the system fill valve (Component BB) was opened and water entered the degassing tank (Component X). At this point, the degassing tank gas bleed valve (Component Z) located atop the degassing tank gas separation column (Component Y) was opened to allow any air in the degassing tank to be displaced by the incoming water. The degassing tank gas bleed valve was left open as water entered the system until a steady stream of water could be seen exiting the valve. At this point, the degassing tank bleed valve was closed.

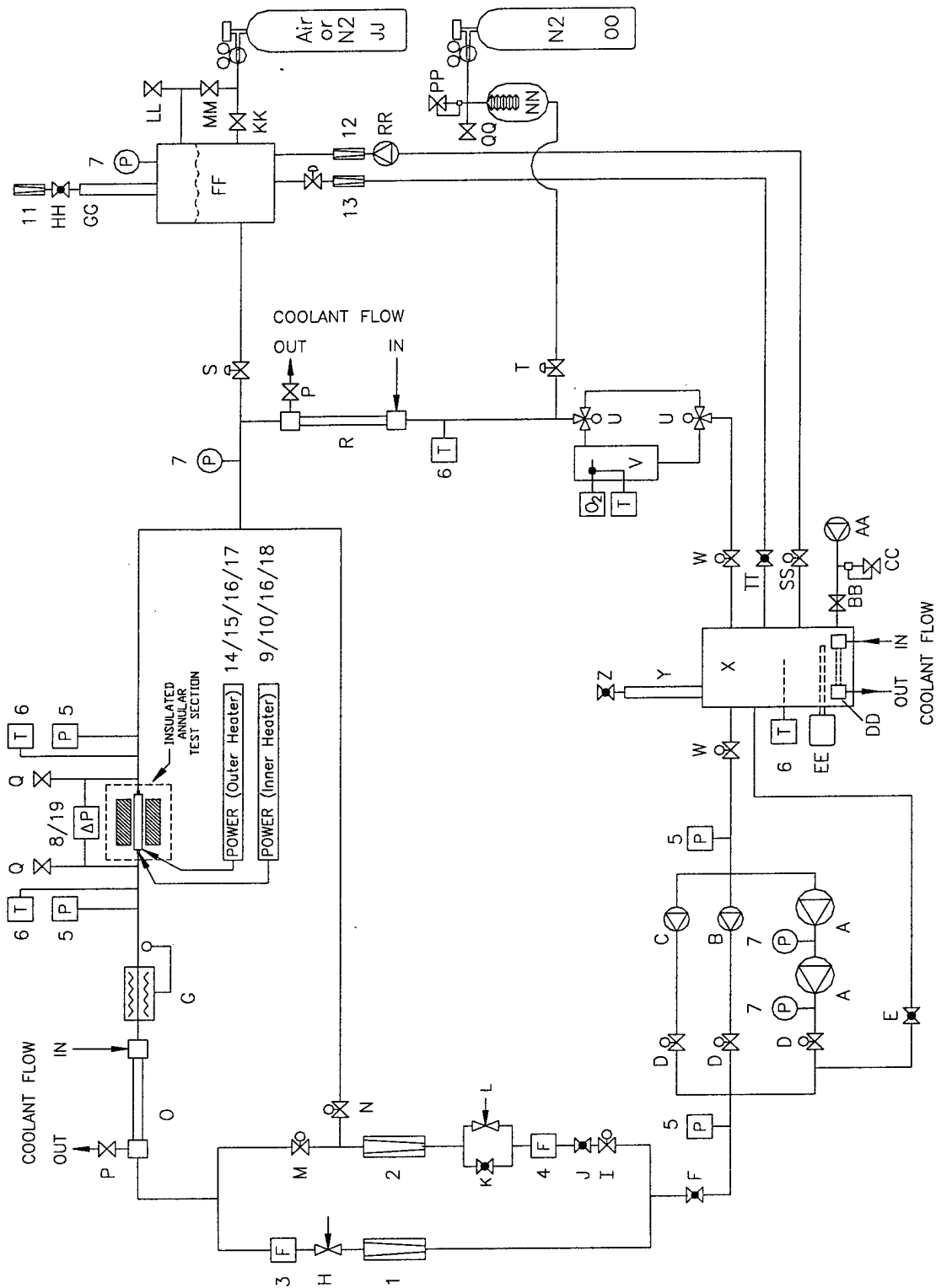


Figure 4.1: Schematic Diagram of the Georgia Tech Microchannel Test Facility

Note that as the system was being filled, all flow loop valves were open and water could flow through the entire flow loop during the filling procedure; the saturation loop was still isolated at this point. As water continued to flow into the system, the toggle valves (Components Q) located on the differential pressure transducer (Component 8) were periodically opened to release air pockets from the system. These toggle valves were always opened simultaneously to prevent possible damage to the differential pressure transducer. In addition, the degassing tank gas bleed valve (Component Z) and accumulator bleed valve (Component PP) were opened periodically to release air pockets from the system. These four valves were intentionally placed at the highest positions in the flow loop in order to capture and bleed off air bubbles. Note that throughout the filling process, care was taken to prevent the system pressure from exceeding 20 psig. The peristaltic pump used to fill the system was not rated for high pressure and thus could have been damaged if forced to operate above 20 psig.

Once the system was filled and cleared of most air pockets, the four valves mentioned above were closed and the system was allowed to pressurize to 20 psig. At this point, the peristaltic pump was turned off and the system fill valve (Component BB) was closed. Next, either the centrifugal pump (Component A) for Flow Loop Configurations 1, 2, or 3, or the positive displacement pump (Component C) for Flow Loop Configuration 4 was used to circulate water through the flow loop and cause any remaining air pockets to move to the high points in the system. Before switching on the pump, the system throttling valve (Component F) was completely closed while the pump bypass valve (Component E) was left open. This was done to prevent a sudden surge of

water from damaging the turbine flowmeters (Components 3 and/or 4). The pump bypass valve was left open to prevent "dead heading" of the pump. Once the pump was switched on, the system throttling valve was slowly opened to allow water to flow through the loop. The saturation loop was still isolated at this point.

The pump was turned off after running for approximately five minutes. The toggle valves (Components Q), the degassing tank gas bleed valve (Component Z), and the accumulator bleed valve (Component PP) were once again opened to allow the release of air pockets. Also, the peristaltic pump was turned back on and the system fill valve (Component BB) was reopened. After clearing the air pockets from the four bleed valves, the system was re-pressurized to 20 psig, the peristaltic pump was turned off, and the system fill valve was closed. Next, the system throttling valve (Component F) was closed and the appropriate pump (Component A or C) was turned on. The system throttling valve was then slowly opened to allow circulation of water through the flow loop. Again, this was done to free any trapped air pockets within the system.

This process of filling the flow loop, running the pump, and bleeding off air pockets was repeated until no bubbles could be seen in the flow through the rotameters (Components 1 and/or 2). Once the flow loop was completely free of air pockets and pressurized once again to 20 psig, the saturation loop was filled. First, the saturation loop inlet valve (Component SS) was opened to allow water to flow from the degassing tank into the saturation loop. Since the flow loop was pressurized to 20 psig and the saturation tank was open to the atmosphere via the saturation tank gas bleed valve (Component HH), water flowed into the saturation loop and no additional air passed into the primary

flow loop. Next, the peristaltic pump was turned on and the system fill valve (Component BB) was opened. Also, the saturation loop exit valve (Component TT) and the saturation tank pressure regulation valve (Component S) were opened. Note that the saturation tank pressure regulation valve was simply used to set the pressure at the test section exit. No water actually flowed through this line during experimental operation, but it still had to be filled and cleared of air pockets to ensure accurate experimental pressure settings. As the saturation loop filled, air was displaced from the saturation tank (Component FF) and released through the saturation tank gas bleed valve. The saturation tank blow-off valve (Component LL) located at the top of the saturation tank was also opened to release air. Once water began to flow out of the saturation tank blow-off valve, the peristaltic pump was turned off and both the system fill valve and the saturation tank blow-off valve were closed. At this point, the filling procedure was complete. Note that the system could not be pressurized above ambient using the peristaltic pump due to the partially opened saturation tank gas bleed valve (Component HH) located atop the saturation tank. Continued filling of the system would have lead to overflow through the saturation tank gas bleed valve.

IV.3 Working Fluid Gas Saturation and System Pressurization

Prior to the start of any set of OFI or CHF experiments, the system was filled / cleared of air pockets using the procedure outlined in Section IV.2 above. After the system was filled it had to be pressurized to a predetermined level (50, 65, 100, or 150

psia exit pressure) and the water had to be saturated with either air or nitrogen. Both of these conditions were satisfied using the saturation tank (Component FF of Figure 4.1) and a compressed gas supply cylinder (Component JJ). Note that OFI experiments were performed using water saturated with either air or nitrogen while CHF experiments utilized only nitrogen-saturated water to minimize corrosion of the test section and other components.

First, the saturation tank recirculation pump (Component RR) was started. This pump drew water from the degassing tank (Component X) into the saturation tank (Component FF). Next, the saturation tank compressed gas supply cylinder (Component JJ) was opened to allow compressed air (Setups 1 – 5) or compressed nitrogen (Setups 6, 8 – 13) to bubble through the saturation tank and saturate the water. Note that the saturation tank gas bleed valve (Component HH) was left partially opened to the atmosphere at all times. This ensured that compressed gas could continuously bubble through the saturation tank and keep the working fluid saturated. After becoming saturated, the water passed back into the primary flow loop via the saturation loop exit valve (Component TT). Two identical rotameters (Components 12 and 13) allowed observation of the flow into and out of the saturation tank. The flow could be adjusted and equalized using the various valves available in order to prevent either dryout or overflow of the saturation tank. The saturation tank pressure regulation valve (Component S) allowed the test section exit pressure to be set via the saturation tank. During operation, this valve was left completely open which effectively equalized the pressure between the saturation tank and the test section exit. The compressed gas

cylinder was fitted with a pressure regulator, which allowed precise pressurization of the system to the desired level. At this point the saturation loop was set and the system was pressurized for operation.

IV.4 OFI Primary Flow Loop Preparation

After saturating the working fluid and pressurizing the system as outlined in Section IV.3, the primary flow loop could be started. In preparation for starting the primary flow loop for OFI experimentation, the system throttling valve (Component F of Figure 4.1) was completely closed and the pump bypass valve (Component E) was completely opened. As stated earlier, these actions were taken in order to prevent a sudden surge of water from damaging the turbine flowmeters (Components 3 and/or 4) as the primary loop circulation pump was started. At this point, the startup procedure varied slightly for each of the three flow loop configurations used for OFI experimentation.

IV.4.1 Flow Loop Configuration One

Flow Loop Configuration One (shown in Figure 4.2) was used for high flow / high heat flux OFI experiments. One multi-stage centrifugal pump (Component A in Figure 4.2) was started and the system throttling valve (Component F) was slowly opened while the pump bypass valve (Component E) was slowly closed.

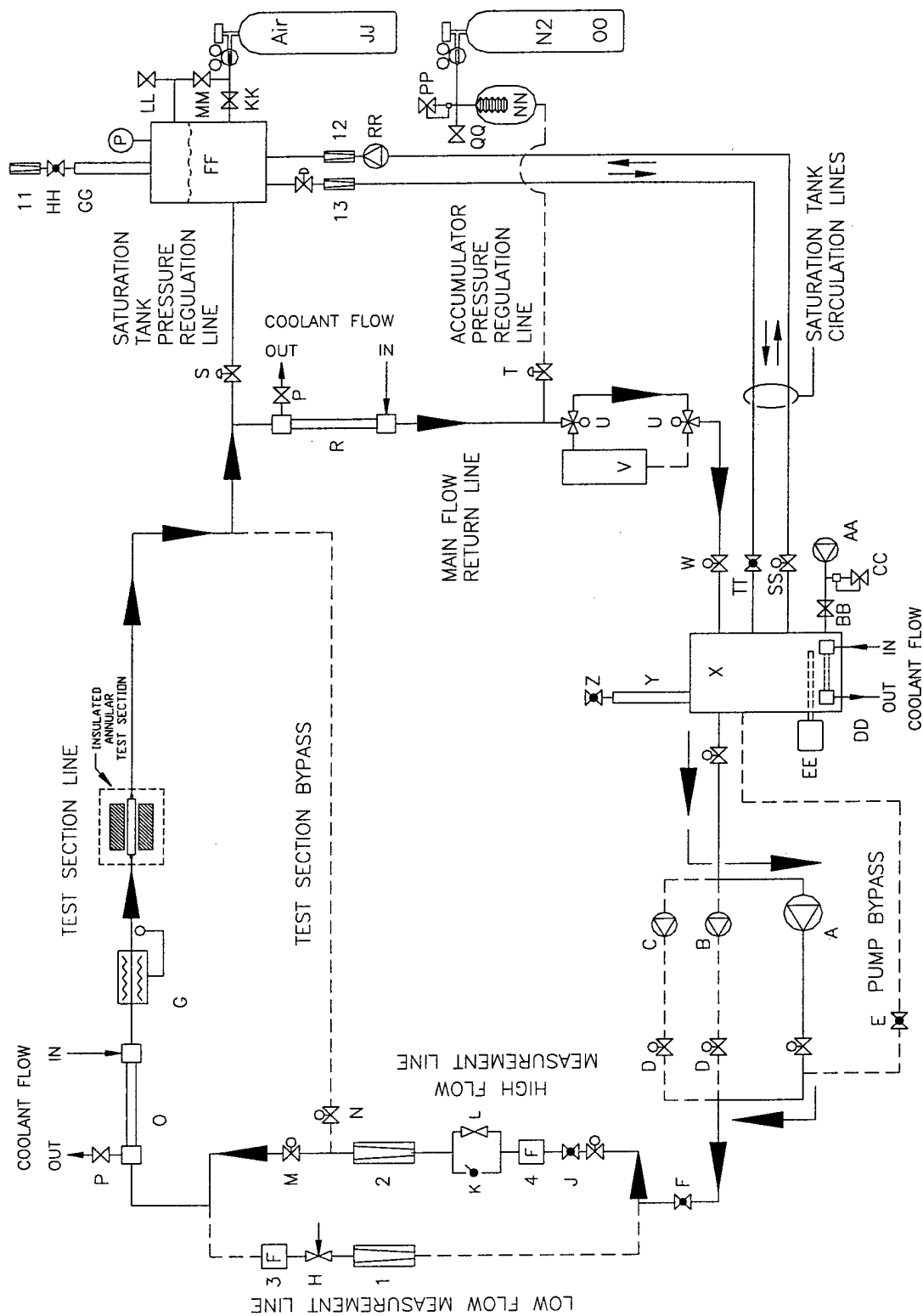


Figure 4.2: Schematic Diagram of Flow Loop Configuration One

At this point, air-saturated water was being pumped from the degassing tank through the centrifugal pump, up through a high capacity turbine flowmeter (Component 4) and a rotameter (Component 2), through the test section heat exchanger (Component O), through the test section, through the system heat exchanger (Component R) and finally back to the degassing tank for re-saturation. The flow rate through the test section was controlled using the coarse high flow line metering valve (Component K) and the fine high flow line metering valve (Component L). Also, the volumetric flow rate through the test section was monitored by the high capacity turbine flowmeter (Component 4). At the beginning of each OFI experiment that utilized Flow Loop Configuration One, both of the coarser and the fine high flow line metering valves were completely open. This means that at this point in the setup procedure, air-saturated water was flowing through the entire system at full capacity and it was pressurized to the appropriate level for experimentation. All system parameters were set for Flow Loop Configuration One except for test section inlet temperature which was simply adjusted using three heat exchangers (Components O, R, and DD) and/or two degassing tank cartridge style heaters (Components EE) as described in Section IV.6.

IV.4.2 Flow Loop Configuration Two

Flow Loop Configuration Two (shown in Figure 4.3) was used for low flow / low heat flux OFI experiments. One multi-stage centrifugal pump (Component A in Figure 4.3) was started and the system throttling valve (Component F) was slowly opened while the pump bypass valve (Component E) was slowly closed.

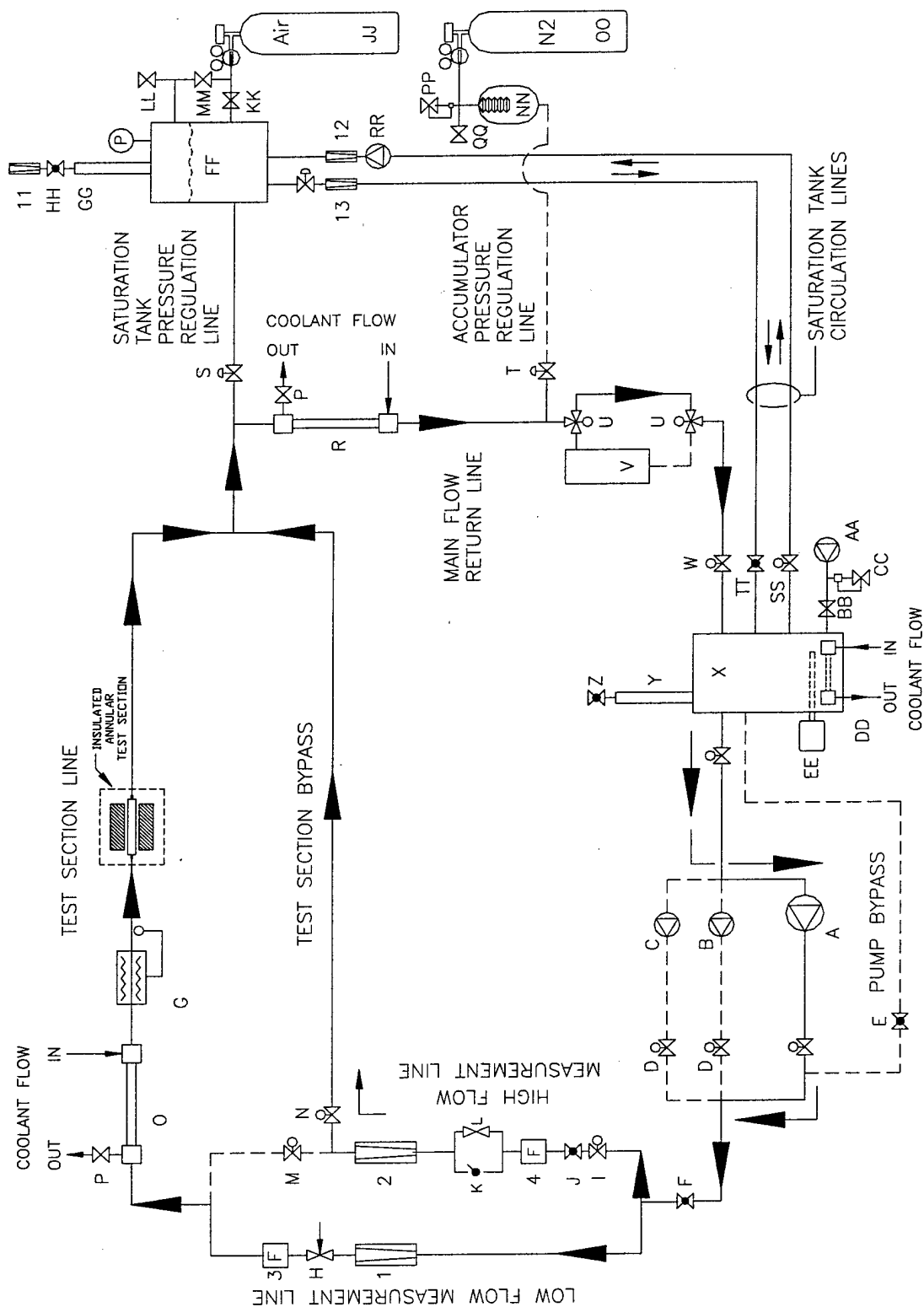


Figure 4.3: Schematic Diagram of Flow Loop Configuration Two

At this point, air-saturated water was being pumped from the degassing tank through the centrifugal pump, after which point the flow branched. The test section line continued up through a rotameter (Component 1) and a low capacity turbine flowmeter (Component 3), through the test section heat exchanger (Component O), through the test section, then converged with the test section bypass line. The test section bypass line left the centrifugal pump, entered a high capacity turbine flowmeter (Component 4), passed through a rotameter (Component 2), and went through the test section bypass line before converging with the test section flow. The combined flow then passed through the system heat exchanger (Component R) and returned to the degassing tank for re-saturation. The flow rate through the test section was controlled using the low flow line metering valve (Component H), while the flow rate through the test section bypass line was controlled using the coarse and the fine high flow line metering valves (Components K and L). Also, the volumetric flow rate through the test section was monitored by the low capacity turbine flowmeter (Component 3) and the volumetric flow rate through the test section bypass line was monitored by the high capacity turbine flowmeter (Component 4). At the beginning of each OFI experiment that utilized Flow Loop Configuration Two, all three flow metering valves (Components H, K, and L) were completely open. This means that at this point in the setup procedure, air-saturated water was flowing through the entire system at full capacity and it was pressurized to the appropriate level for experimentation. If needed, the two test section bypass line metering valves (Components K and L) could be slightly closed in order to increase flow through the test section. Care had to be exercised while adjusting these valves since the

low capacity turbine flow meter could not exceed a volumetric flowrate of 90 L/hr. Now, all system parameters were set for Flow Loop Configuration Two except for test section inlet temperature which was simply adjusted using three heat exchangers (Components O, R, and DD) and/or two degassing tank cartridge style heaters (Components EE) as described in Section IV.6.

IV.4.3 Flow Loop Configuration Three

Flow Loop Configuration Three (shown in Figure 4.4) was used for high flow / high heat flux OFI experiments and was merely a slight modification of Flow Loop Configuration One. Two multi-stage centrifugal pumps (Components A in Figure 4.4) were started and the system throttling valve (Component F) was slowly opened while the pump bypass valve (Component E) was left open. At this point, nitrogen-saturated water was being pumped from the degassing tank through the centrifugal pumps, up through a high capacity turbine flowmeter (Component 4) and a rotameter (Component 2), through the test section heat exchanger (Component O), through the test section, through the system heat exchanger (Component R) and finally back to the degassing tank for re-saturation. Water was also being pumped directly from the degassing tank, through the centrifugal pumps, and back to the degassing tank via the pump bypass line. This was necessary due to the high flow rate created by the two centrifugal pumps in series. The primary flow loop line could not withstand such a high volume of water. The flow rate through the test section was controlled using the coarse and the fine high flow line metering valves (Components K and L).

Also, the volumetric flow rate through the test section was monitored by the high capacity turbine flowmeter (Component 4). At the beginning of each OFI experiment that utilized Flow Loop Configuration Three, both flow metering valves (Components K and L) were completely open. This means that at this point in the setup procedure, nitrogen-saturated water was flowing through the entire system at full capacity and it was pressurized to the appropriate level for experimentation. All system parameters were set for Flow Loop Configuration Three except for test section inlet temperature which was simply adjusted using three heat exchangers (Components O, R, and DD) and/or two degassing tank cartridge style heaters (Components EE) as described in Section IV.6.

IV.5 CHF Primary Flow Loop Preparation

After saturating the working fluid and pressurizing the system as outlined in Section IV.3, the primary flow loop could be started. Flow Loop Configuration Four (shown in Figure 4.5) was used for all CHF experiments. In preparation for starting the primary flow loop for CHF experimentation, the system throttling valve (Component F of Figure 4.5) was completely closed and the pump bypass valve (Component E) was completely opened. As stated earlier, these actions were taken in order to prevent a sudden surge of water from damaging the turbine flowmeter (Component 3) as the primary loop circulation pump was started. At this point, the variable speed positive displacement pump (Component C) was started. The system throttling valve was then slowly opened and the pump bypass valve was slowly closed. Now, nitrogen-saturated

water was being pumped from the degassing tank through the positive displacement pump, up through a rotameter (Component 1) and a low capacity turbine flowmeter (Component 3), through the test section heat exchanger (Component O), through the test section, through the system heat exchanger (Component R) and finally back to the degassing tank for re-saturation. During CHF experiments, precisely setting the positive displacement pump's rotational speed controlled the coolant flowrate which was monitored by the low capacity turbine flowmeter (Component 3). The low flow line metering valve (Component H) was slightly closed to provide the positive displacement pump with a moderate back pressure (100 kPa). This back pressure helped reduce flow oscillations resulting from boiling and two-phase pressure fluctuations encountered during CHF experiments. At this point in the setup procedure, nitrogen-saturated water was flowing through the entire system at a prescribed flowrate and it was pressurized to the appropriate level for experimentation. All system parameters were set for Flow Loop Configuration Four except for test section inlet temperature which was simply adjusted using three heat exchangers (Components O, R, and DD) and/or two degassing tank cartridge style heaters (Components EE) as described in Section IV.6.

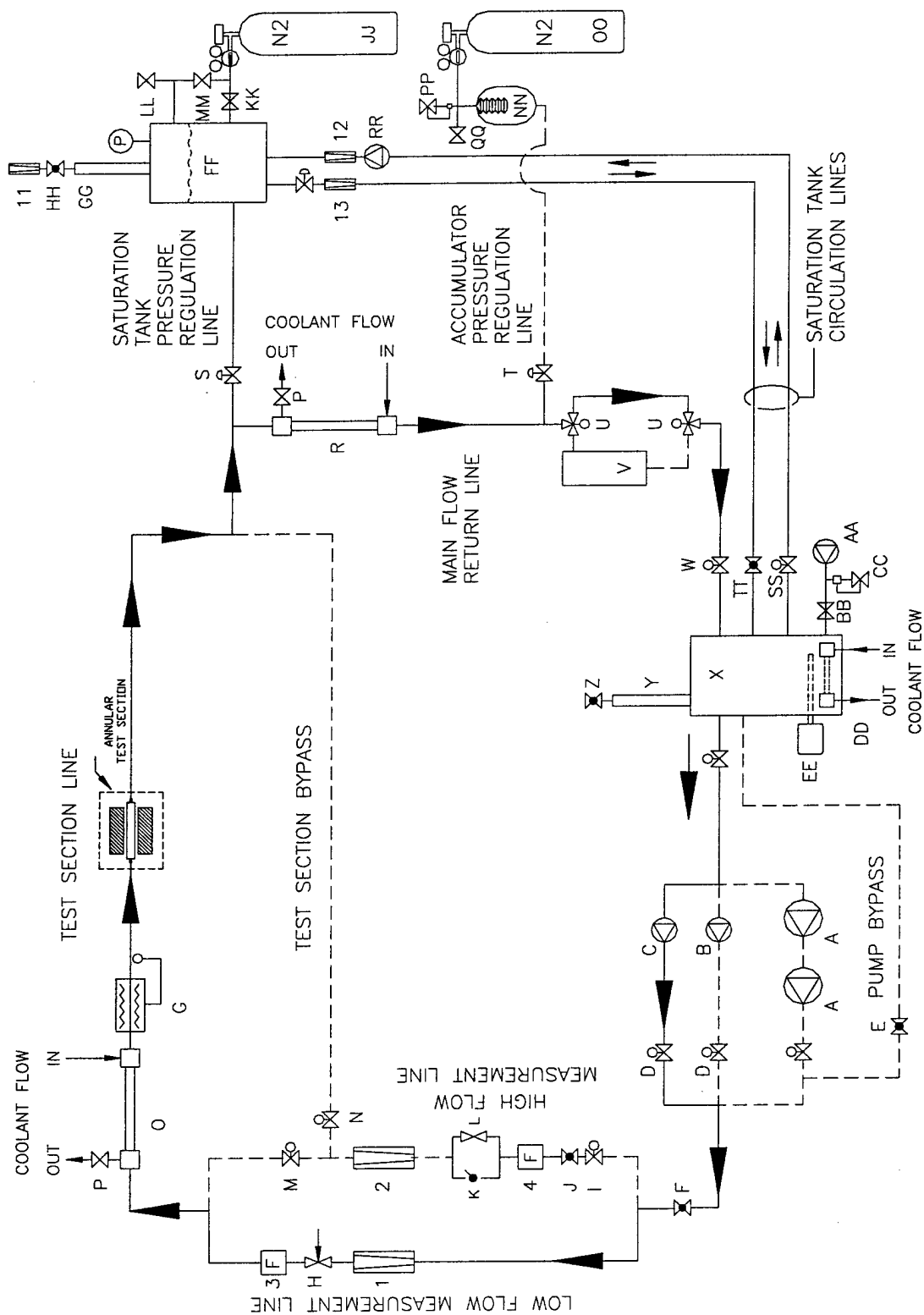


Figure 4.5: Schematic Diagram of Flow Loop Configuration Four

IV.6 Test Section Inlet Temperature Control

The test section heat exchanger (Component O of Figure 4.1) was connected to a constant temperature bath which allowed precise setting of the heat exchanger temperature; however, the flow rate of the cooling water could not be adjusted. On the other hand, both the system heat exchanger (Component R) and the degassing tank heat exchanger (Component DD) were attached to the house water line (17° - 20°C) which allowed no control of heat exchanger temperature, but permitted adjustment of the cooling jacket water flowrate. The system heat exchanger was typically left at its maximum capacity due to the large amount of heat it had to remove from the water immediately after the test section. The degassing tank heat exchanger was, by design, a relatively low capacity heat exchanger even when its cooling jacket water flowrate was maximized and thus was used to fine-tune the water temperature as needed prior to being pumped through the test section heat exchanger. These three heat exchangers, working in concert, were used to control and maintain the test section inlet temperature at the desired value for about ninety percent of all OFI and CHF experiments run without the aid of the two degassing tank cartridge style heaters. However, during low mass flux OFI and CHF experiments, the water was often cooled too much by the system heat exchanger and thus had to be reheated prior to being pumped through the test section heat exchanger. The two degassing tank cartridge style heaters (Components EE) could be adjusted independently in order to accomplish this task. Use of all of these components allowed the test section inlet temperature to be set and maintained at the desired level (30°, 50°, 65°, or 70°C).

IV.7 OFI Experimental Procedure and Analysis Techniques

IV.7.1 OFI Experimental Procedure

Once the system was running and all experimental parameters were set, an OFI experiment could be performed. Each OFI experiment began with the test section flowrate maximized and all test section power supplies energized and set to zero. The inner heater was consistently more reliable than the outer heater during OFI experimentation since it was powered by Power Supply Configuration Two, which utilized a DC power supply. For this reason, the surface heat flux of the AC supplied outer heater (Power Supply Configuration One) was slowly raised to the prescribed level first. Once the outer heater surface heat flux was set, the apparatus was allowed to run for five minutes before continuing the startup procedure. The inner heater surface heat flux was then slowly raised to the prescribed level. Note that outer heater failure within the first five minutes of the OFI experimental startup procedure accounted for most experimental failures. Thus, allowing the system to run for five minutes prior to increasing inner heater power permitted observation of the outer heater performance. Any perceived overheating (which resulted in glowing) of the outer heater triggered immediate manual termination of the experiment by the operator since the glowing indicated that the heater wire had separated from the outer heater and was about to melt. Note that as explained in Chapter III, the power input to the test section during OFI experimentation was supplied by two independent sources (Power Supply Configurations One and Two) for all but the last five OFI experiments. These final five OFI experiments

utilized Power Supply Configuration Three, which used a single DC power supply to provide power to both heaters. Thus, for the last five OFI experiments, the surface heat flux on both heaters was increased simultaneously to the designated power level for each particular OFI experiment with little probability of heater failure. After both heaters were set to the appropriate surface heat flux, the DAS system was activated. As explained in Section III.3.1.7, the DAS system acquired data from the GTMTF once every five seconds and, in turn, recorded the data to a prescribed text file on the Pentium computer for future analysis.

With all systems operating correctly and data being acquired every five seconds by the DAS system, the mass flux through the test section was gradually decreased by increments of approximately 1 – 5 L/hr every five to ten seconds until the test section differential pressure reached a minimum and began increasing again. This increase in differential pressure indicated that the test section had passed through OFI and was now operating in the negatively-sloped region of the demand curve. While running the experiment, the operator could reduce the flowrate by smaller increments as the experiment neared OFI, thus ensuring an accurate reading of the OFI point.

IV.7.2 OFI Experimental Analysis Techniques

Once OFI was surpassed, the experiment was terminated and the demand curve for the experiment was generated. Once generated, the demand curve directly provided the OFI conditions, with OFI defined as the flowrate at which the test section differential pressure reached a minimum. Figure 4.6 shows a typical experimental demand curve

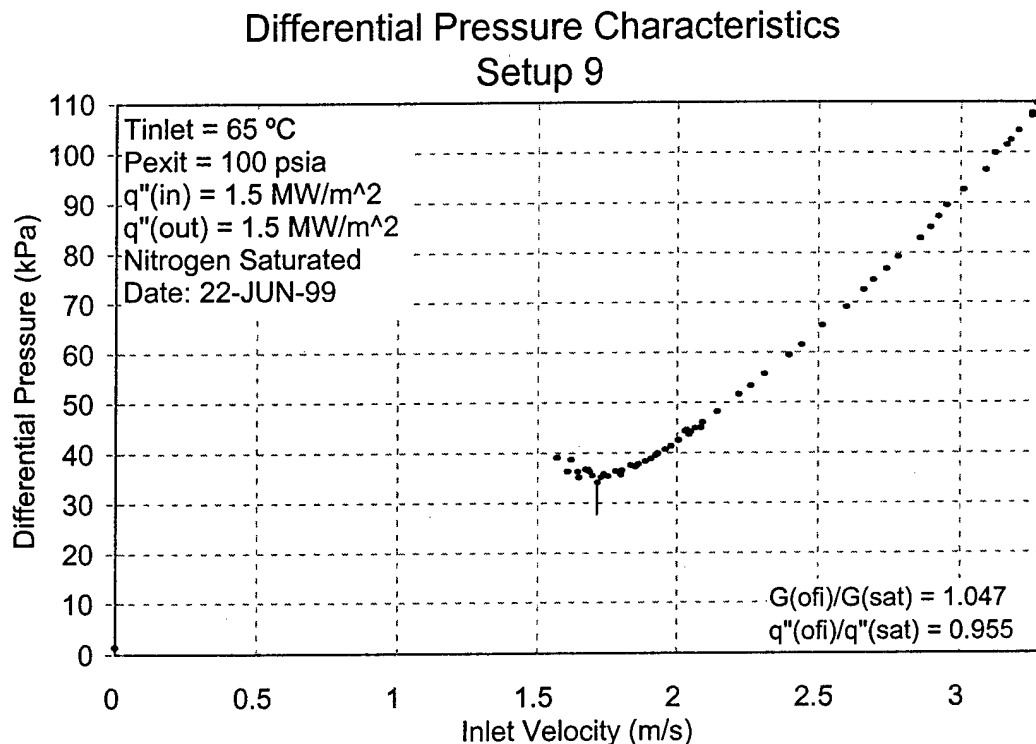


Figure 4.6: Typical Experimental OFI Demand Curve

where the OFI point is marked with a solid vertical line. Note that the nominal conditions for the experiment are indicated in the upper left corner of the graph and the calculated OFI-to-saturation ratios are included in the lower right corner. A plot of this type was generated for every OFI experiment conducted; the OFI conditions for all experiments conducted in this investigation are listed in Appendix B.

For each OFI experiment, several experimental parameters were recorded by the DAS system described in Section III.3.1.7. These parameters included time, volumetric

flow rate through the test section, total power output from each power supply, test section inlet and exit temperatures, and test section inlet and exit pressures. Using these parameters, inlet and exit water conditions could be determined and used to perform an energy balance on the test section. This energy balance served two purposes. First, since the power input to the test section was set and maintained at a prescribed value, the energy balance served to quantify the percentage of heat lost to the environment. Since the OFI point was taken to be a single data point from the experiment instead of an average of several data points, and since the power level fluctuated slightly throughout each OFI experiment, the heat lost to the environment was needed to determine the exact surface heat flux at OFI. Second, the density of the water at the test section inlet was required to determine the exact OFI mass flux. The following paragraphs outline the energy balance procedure used in analyzing all OFI data.

Using the inlet and exit temperatures and pressures, the inlet and exit enthalpy and fluid density were determined using the Engineering Equation Solver (EES) algorithm shown in Appendix A. The nature of OFI experimentation dictated that each experiment begin with single-phase liquid water at the test section inlet and exit and end with single-phase liquid water entering the test section and a two-phase liquid-vapor mixture exiting the test section. As such, the exit enthalpy and density found using EES was only accurate while single-phase liquid water was exiting the test section. Once the water began to boil, the exit temperature and pressure were no longer independent and the exit quality was needed to determine exit enthalpy and density. For this reason, the following techniques were used to determine the exact surface heat flux at OFI.

As stated earlier, the power input to each heater was set and maintained at a prescribed level for each OFI experiment. This power level was recorded every five seconds by the DAS system and corrected during analysis of the OFI experiment in the following manner for the first 61 experiments. First, as stated in Section III.6.1, the wattmeter that measured the power supplied to the outer heater from Power Supply Configuration One was located before the voltage transformer. From early comparisons of the outer heater power level reported by the DAS system and independent measurements of voltage and current after the transformer, the transformer was known to cause electrical losses of roughly three to five percent. A three percent loss was decided upon as a conservative estimate of the power lost through the transformer. This means that the outer heater power reported in the DAS data file was subject to electrical losses of three percent. Thus, in an effort to equalize the inner and outer surface heat fluxes, the outer heater power level was set for each OFI experiment using an independent voltage reading taken after the transformer; however, the power level reported in the DAS data file had to be corrected. Therefore, the first power correction performed in OFI analysis was the subtraction of three percent of the outer heater power level reported in the DAS data file. All other power corrections further manipulated this adjusted outer heater power level. Note that the DC supplied inner heater was not subject to these losses. Second, the test section heat loss to the environment had to be estimated. In order to calculate this loss, an energy balance was performed using recorded flow conditions and compared to the DAS reported value of total electrical power supplied to the test section. As described earlier, the energy balance was only valid while both the test section inlet

and exit flow conditions were single-phase liquid. For this reason, the calculated percent power loss during each of the first ten single-phase data readings were averaged together and applied to the total electrical power reading, i.e., both the inner and outer heater power readings, at the OFI point. This provided the actual power absorbed in the working fluid at OFI. The average surface heat flux was then calculated by simply dividing the total power absorbed in the working fluid by the total heated surface area of the test section. This provided the OFI heat flux for the experiment. Note that the last five OFI experiments, which utilized Power Supply Configuration Three, were not subject to the electrical losses from the transformer as described above.

The energy balance technique just described enumerated the amount of heat lost to the environment from the test section and, thus, had a significant impact on the "exact" calculated OFI heat flux for the experiment. A brief error analysis on the calculated heat loss to the environment, therefore, was necessary. Table 4.1 shows the effect of changing the calculated heat loss by $\pm 50\%$ to three OFI experiments (selected from the first 61 experiments) with different nominal surface heat flux values.

Table 4.1: Effect of Heat Loss Estimation on OFI Calculations

Nominal Heat Flux (MW/m ²)	T _{inlet} (°C)	P _{exit} (kPa)	Calculated Heat Loss (%)	Resulting Q" _{OFI} /Q" _{sat}	- 50 % Heat Loss (%)	Resulting Q" _{OFI} /Q" _{sat}	+ 50 % Heat Loss (%)	Resulting Q" _{OFI} /Q" _{sat}
1.0	65.9	684.5	15.7	0.931	7.85	1.018	23.55	0.845
1.5	50.8	707.4	1.9	0.937	0.95	0.946	2.85	0.928
2.0	26.6	685.9	6.9	0.924	3.45	0.958	10.35	0.889

The OFI correlation developed by this investigation and reported in Section V.1.11 states that the average ratio of OFI heat flux-to-saturation heat flux over all experiments was

0.942 \pm 9.80 %. This range corresponds to a confidence interval of (0.8497, 1.0343), to which all except one of the trial heat loss calculations adhered. This brief error analysis of the calculated test section heat loss to the environment demonstrates that even a radical miscalculation of heat loss (\pm 50 %) results in a relatively minor error in the resulting OFI calculations.

Power Supply Configuration Three was used to heat the test section during the final five OFI experiments and employed a DC wattmeter that measured the total power output of the power supply. Heat was lost in two places by Power Supply Configuration Three and, thus, a different analysis technique was employed to determine the OFI point in these final five experiments. As stated earlier, the DAS system recorded the total power supply output in addition to the water conditions at the inlet and exit of the test section. While the coolant was single-phase, an energy balance performed on the coolant using inlet and exit enthalpy and mass flow rate could be compared to the recorded total power supply output in order to determine the percentage of power lost to the environment. This loss was then averaged over the first ten single-phase data points and applied to the two-phase regime of the experiment. The losses generally accounted for approximately 30 percent of the total power supply output. Power was lost primarily in two places. First, by design, some power was dissipated in the adjustable series shunt resistance used to equalize the inner and outer heater surface heat fluxes. Second, the test section was not insulated and thus some heat was lost to the environment directly from the test section. From calculations performed using separate current readings and voltage taps placed directly on the test section, the percentage of power lost to the environment

accounted for approximately five percent of the total power supply output, while the power lost through the series resistor accounted for roughly 25 percent of the total power supply output. In actuality, however, the exact amount of power lost by each of these two separate sources was not important since the quantity of interest was the power actually absorbed by the working fluid. With the power input to the test section evaluated, the average surface heat flux over the test section was found by simply dividing the total power absorbed in the working fluid by the total test section heated surface area.

The energy balance technique used to analyze the final five OFI experiments enumerated the total amount of heat lost to the environment from both the test section and the adjustable series resistor. This calculation, thus, had a significant impact on the "exact" calculated OFI heat flux for the experiment. A brief error analysis on the calculated heat loss to the environment, therefore, was necessary. Table 4.2 shows the effect of changing the calculated heat loss by $\pm 50\%$ to two OFI experiments (selected from the final five experiments) with different nominal surface heat flux values.

Table 4.2: Effect of Heat Loss Estimation on OFI Calculations

Nominal Heat Flux (MW/m ²)	T _{inlet} (°C)	P _{exit} (kPa)	Calculated Heat Loss (%)	Resulting Q'' _{OFI} /Q'' _{sat}	- 50 % Heat Loss (%)	Resulting Q'' _{OFI} /Q'' _{sat}	+ 50 % Heat Loss (%)	Resulting Q'' _{OFI} /Q'' _{sat}
2.0	34.3	693.5	24.4	0.830	12.2	0.964	36.6	0.696
2.5	47.8	699.3	30.7	0.950	15.4	1.160	46.1	0.739

This table of heat loss calculations does not adhere to the confidence interval of (0.8497, 1.0343) as well as the data in Table 4.1 due to the large percentage of heat loss to the environment inherently associated with Power Supply Configuration Three. However,

this brief error analysis of the calculated test section heat loss to the environment demonstrates the gross miscalculations of heat loss that are necessary to skew the results of the OFI calculations.

The OFI mass flux, average exit pressure, and average inlet temperature for each OFI experiment were found in the following manner. First, the average inlet temperature was simply the mean inlet temperature over the five data points centered on the OFI point. Likewise, the average exit pressure was the mean exit pressure over the five data points centered on OFI. The standard deviation of each of these mean values was also calculated for each experiment and can be found in Appendix B. The OFI mass flux (G_{OFI}) for each OFI experiment was found by first calculating the mass flux at each data reading taken during the OFI experiment and then picking the value that corresponded to the minimum differential pressure over the duration of the experiment. The mass flux at each data reading was found by multiplying the volumetric flow rate through the test section at that instant by the inlet fluid density and then dividing by the flow area of the test section.

The OFI correlations developed in this investigation compare the OFI mass flux to the saturation mass flux and the OFI heat flux to the saturation heat flux. The procedures above outline the methods used in determining OFI mass flux and OFI heat flux. The following procedures summarize the techniques used in determining saturation mass flux and saturation heat flux. They also set forth the methods used in comparing OFI conditions to saturation conditions.

Saturation mass flux simply refers to the coolant mass which corresponds to

saturated liquid at the test section exit for a specified set of flow parameters, i.e., inlet temperature and pressure, exit pressure, flow area, heated area, and average surface heat flux. In order to calculate the saturation mass flux, the inlet enthalpy was found using the average inlet temperature described above and the inlet pressure at the OFI point. Note that the inlet pressure was not averaged since the enthalpy of a subcooled liquid is a much stronger function of temperature than of pressure. Any small pressure fluctuations encountered within fifteen seconds of OFI were not significant to analysis calculations and any large pressure fluctuations would have triggered fatal experimental errors requiring termination of the OFI experiment. Next, the saturation enthalpy of the working fluid (h_f) at the average exit pressure was found. The difference of the two enthalpy values dictated the required change in enthalpy from inlet to exit necessary to saturate the working fluid. Finally, the saturation mass flux was calculated using the following equation.

$$G_{sat} = q''_{OFI} \frac{A_{heated}}{A_{flow} (h_f [P_{exit}] - h [T_{inlet}, P_{inlet}])} \quad (4.1)$$

Note that Equation 4.1 provided the coolant mass flux required to saturate the working fluid at the test section exit given the experimentally fixed value of OFI heat flux. Since the OFI mass flux corresponding to the OFI heat flux used in Equation 4.1 was known, a direct ratio comparison between the OFI mass flux and the calculated saturation mass flux was possible. This provided the means to develop the OFI mass flux correlation

located in Chapter V.

Similarly, saturation heat flux refers to the average surface heat flux required for the working fluid to become saturated liquid at the test section exit for given certain flow parameters, i.e., inlet temperature and pressure, exit pressure, flow area, heated area, and coolant mass flux. Once again, the first step in the saturation heat flux calculation was to determine the inlet enthalpy using the average inlet temperature and the inlet pressure at the OFI point. Next, the saturation enthalpy of the working fluid at the average exit pressure was found. As stated above, the difference of these two enthalpy values dictated the required change in enthalpy from inlet to exit necessary to saturate the working fluid. Finally, the saturation heat flux was calculated using the following equation.

$$q''_{sat} = G_{OFI} \frac{A_{flow}}{A_{heated}} (h_f[P_{exit}] - h[T_{inlet}, P_{inlet}]) \quad (4.2)$$

Equation 4.2 provided the average surface heat flux necessary to saturate the working fluid at the test section exit based on the assumption that the experimentally determined value of OFI mass flux was actually fixed. Once again, since the OFI heat flux corresponding to the OFI mass flux used in Equation 4.2 was known, a direct ratio comparison between the OFI heat flux and the saturation heat flux was possible. This provided the means to develop the OFI heat flux correlation located in Chapter V.

IV.8 CHF Experimental Procedure and Analysis Techniques

IV.8.1 CHF Experimental Procedure

Once the system was running and all experimental parameters were set, a CHF experiment could be performed. After the DAS system was initialized, each CHF experiment began by energizing the power supply and setting its input signal to zero. As explained in Chapter III, the power input to the test section during CHF experiments was controlled using a Hewlett Packard Data Acquisition / Switch Unit. An input signal was provided to the unit from a Compaq DeskPro 575 personal computer (Microsoft Windows 95 operating environment) and the HP unit, in turn, provided a signal to the power supply, which controlled the power input to the test section. The HP unit also monitored the outer heater thermocouples and automatically terminated the experiment by interrupting the power supply signal if the outer heater surface temperature exceeded 300°C. All temperature readings from the outer heater thermocouples were recorded along with a real time stamp by the Compaq personal computer for future analysis.

With the DC power supply energized, the surface heat flux on both the inner and outer heaters was slowly raised from zero by increments of roughly 0.01 MW/m² per minute until CHF was attained. Once a definite pattern for CHF was determined, later experiments incremented power more quickly early in the experiment until the heat flux exceeded a value equal to two times the predicted OFI heat flux. At that point, the power was increased slowly until CHF was attained, after which the power supply was de-

energized, the experiment was terminated, and the data were analyzed. For purposes of this research, CHF was said to have occurred if either the outer heater or the inner heater surface temperature exceeded 300°C.

IV.8.2 CHF Experimental Analysis Techniques

Once CHF was attained, the experiment was terminated and four plots were generated for each experiment: inner heater surface temperature versus time, outer heater surface temperature versus time, average surface heat flux versus time, and coolant mass flux versus time. The two plots of surface temperature were compared with the average surface heat flux in order to show the rapid rise in wall temperature associated with CHF. Note that CHF experiments were performed using a positive displacement pump making the phenomenon of OFI impossible. The predicted OFI value mentioned in Section IV.8.1 above was calculated using the empirically developed OFI correlation reported in Section V.1.11 and the averaged experimentally measured values of inlet temperature, exit pressure, and mass flux. The predicted OFI value was reported on the plots of surface wall temperature versus time in order to compare the predicted OFI heat flux corresponding to the inlet test parameters with the actual CHF point and to emphasize the fact that CHF for a specific set of test parameters occurred at a much higher surface heat flux than the predicted OFI heat flux for the same set of parameters.

For each CHF experiment, several experimental parameters were recorded by the DAS system described in III.3.1.7. These parameters included time, volumetric flow rate, inner heater wall temperature, total power output from the power supply, test section

coolant inlet and exit temperatures, and test section inlet and exit pressures. Using these parameters, inlet and exit water conditions could be determined and used to perform an energy balance on the test section. Note that the exact CHF heat flux for each experiment was not known until this analysis was performed. First, using the inlet and exit temperatures and pressures, the inlet and exit enthalpy and fluid density were found using the Engineering Equation Solver (EES) algorithm shown in Appendix A. The nature of CHF experimentation dictated that each experiment begin with single-phase liquid water at the test section inlet and exit and end with single-phase liquid water entering the test section and a two-phase liquid-gas mixture exiting the test section. As such, the exit enthalpy and density found using EES was only accurate while single-phase liquid water was exiting the test section. Once the water began to boil, the exit temperature and pressure were no longer independent and the exit quality was needed to determine exit enthalpy and density. For this reason, the following modified energy balance technique was used to determine the surface heat flux in the two-phase regime.

As stated earlier, the DAS system recorded the total power supply output in addition to the water conditions at the inlet and exit of the test section. While the coolant was single-phase, an energy balance performed on the coolant using inlet and exit enthalpy and mass flow rate could be compared to the recorded total power supply output in order to determine the percentage of power lost to the environment. This loss was then averaged over the last ten single-phase data points and applied to the two-phase regime of the experiment. The losses generally accounted for approximately 30 percent of the total power supply output. Power was primarily lost in two places. First, by design, some

power was dissipated in the adjustable series shunt resistance used to equalize the inner and outer heater surface heat fluxes. Second, the test section was not insulated and thus some heat was lost to the environment directly from the test section. From calculations performed on the OFI experiments that utilized Setup 12, the percentage of power lost to the environment accounted for approximately five percent of the total power supply output, while the power lost through the series resistor accounted for roughly 25 percent of the total power supply output. In actuality, however, the exact amount of power lost by each of these two separate sources was not important since the quantity of interest was the power actually absorbed by the working fluid.

The energy balance technique used to analyze all 35 CHF experiments enumerated the total amount of heat lost to the environment from both the test section and the adjustable series resistor. This calculation, thus, had a potentially significant impact on the "exact" calculated CHF heat flux for the experiment. An error analysis investigating the effect of altering the heat loss values was not performed, however, since this CHF investigation was performed only for comparison with OFI and no new CHF correlation was developed. Nevertheless, from the heat loss error analysis performed on the last five OFI experiments, the estimation of heat loss to the environment allows considerable room for error without significant alteration of the overall analysis results.

With the total power input to the test section evaluated as described above, the average surface heat flux over the test section was found by simply dividing the total power absorbed in the working fluid by the total heated surface area. This average surface heat flux was then plotted against time and compared with the inner and outer

heater wall temperatures in order to show the wall temperature spike associated with CHF. Figure 4.7 shows a typical plot of heater wall temperature versus time compared with average surface heat flux. As stated in Section III.5.5, the outer heater wall temperature was measured one centimeter from the end of the test section heated length by three separate thermocouples placed 120° apart around the test section. The readings from these thermocouples were recorded on a Compaq personal computer via the Hewlett Packard Data Acquisition / Switch Unit, not on the DAS system. Since CHF was most likely to occur on the outer heater, the HP unit was set to read each thermocouple three times per second (the fastest available setting). This sampling rate was much faster than that of the DAS system. For analysis purposes, the outer heater wall temperature data had to be imported into the Quattro Pro analysis spreadsheet and matched with the DAS system real time data column. Once this was done, the data could be easily plotted and compared with the average surface heat flux data for the experiment. Note that a temperature spike on the upper most thermocouple on the outer heater terminated every CHF experiment, so typically this was the only thermocouple data plotted for an experiment.

Figure 4.7 shows that the inner heater wall temperature remained above the saturation temperature (164.4°C at 100 psia) of the coolant water for the twenty minutes preceding CHF; however, the outer heater wall temperature did not. This fact can be directly attributed to the placement of the outer heater thermocouples. The outer heater produced heat volumetrically and lost heat to the environment since insulation was not used during CHF experiments. These two facts combined to make the outer surface of

the outer heater (the surface on which the temperature was measured) the coolest surface on the test section. Even though the inner surface temperature of the outer heater was inevitably well above the saturation temperature of the coolant water, the outer surface of the outer heater registered a temperature that was roughly 20°C less than the saturation temperature of the coolant water. Due to the nature of this investigation, precise knowledge of the inner and outer heater temperatures was unnecessary. Instead, the factor of interest in this investigation was the abrupt spike in the surface temperature of either heater associated with CHF; detection of this temperature spike was the sole purpose of the four thermocouples employed.

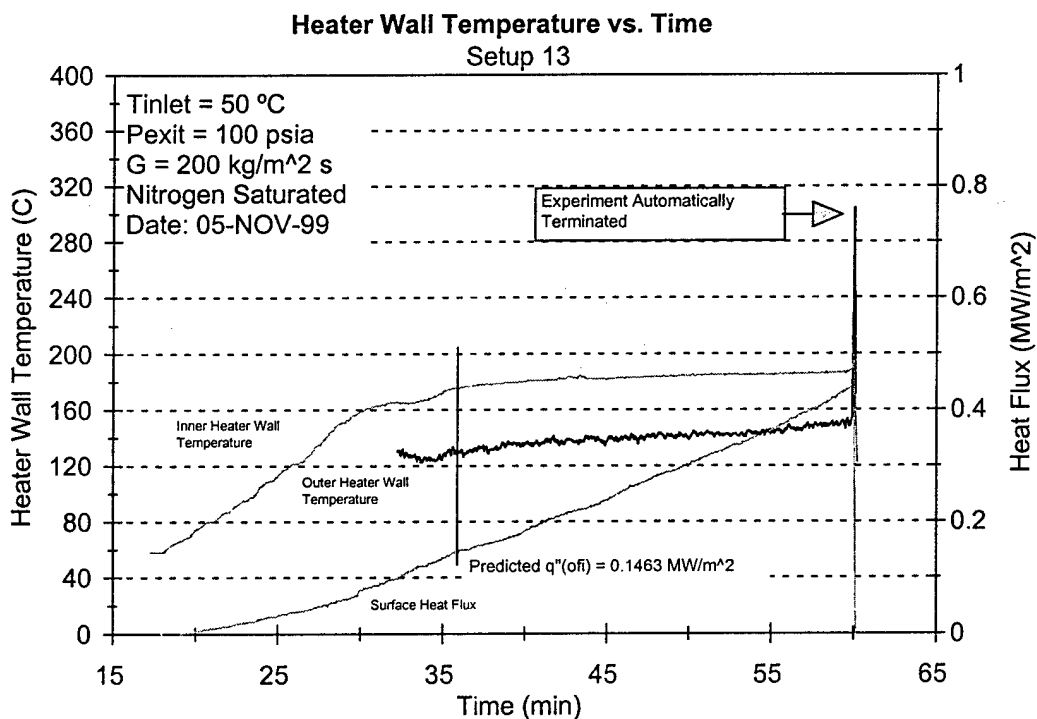


Figure 4.7: Typical Experimental Plot of Heater Wall Temperature Versus Time

The average mass flux, inlet temperature, and exit pressure used in the predicted OFI calculation outlined above were found in the following manner for each CHF experiment. First, the average inlet temperature was simply the mean inlet temperature over the duration of the experiment. Likewise, the average exit pressure was the mean exit pressure over the duration of the experiment. The standard deviation of each of these mean values was also calculated for each experiment and can be found in Appendix C. Both the inlet temperature and exit pressure were measured at least once every five seconds by the DAS system for each experiment. Averaging these values over the entire experiment provided adequate accuracy due to the consistency of the inlet temperature and exit pressure maintenance systems. The average mass flux (G) for each CHF experiment was found by first calculating the mass flux at each data reading taken during the CHF experiment and then averaging these values over the last five minutes of the experiment. The mass flux at each data reading was found by multiplying the volumetric flow rate through the test section at that instant by the inlet fluid density and then dividing by the flow area of the test section. Figure 4.8 shows a typical plot of mass flux versus time. This plot reports the nominal conditions of the experiment as well as the average and standard deviation of the mass flux. Note that mass flux was not averaged over the entire duration of the experiment since it did not remain as steady as inlet temperature and exit pressure. Figures 4.9 and 4.10 show typical plots of inlet temperature and exit pressure versus time, respectively. These two plots were not generated for every CHF experiment performed. They are merely included in this

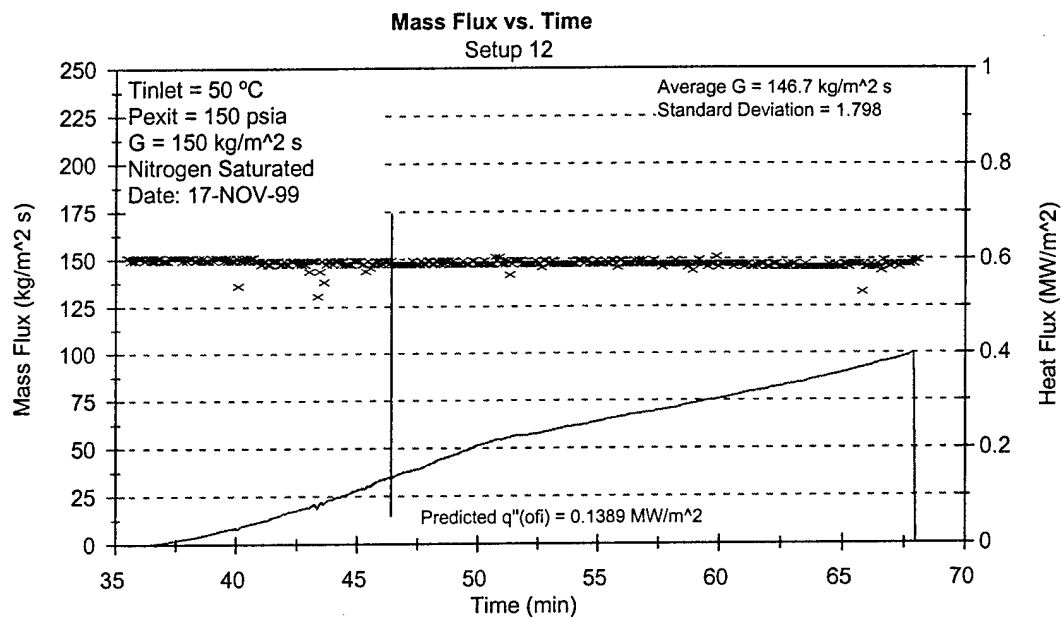


Figure 4.8: Typical Experimental Plot of Coolant Mass Flux Versus Time

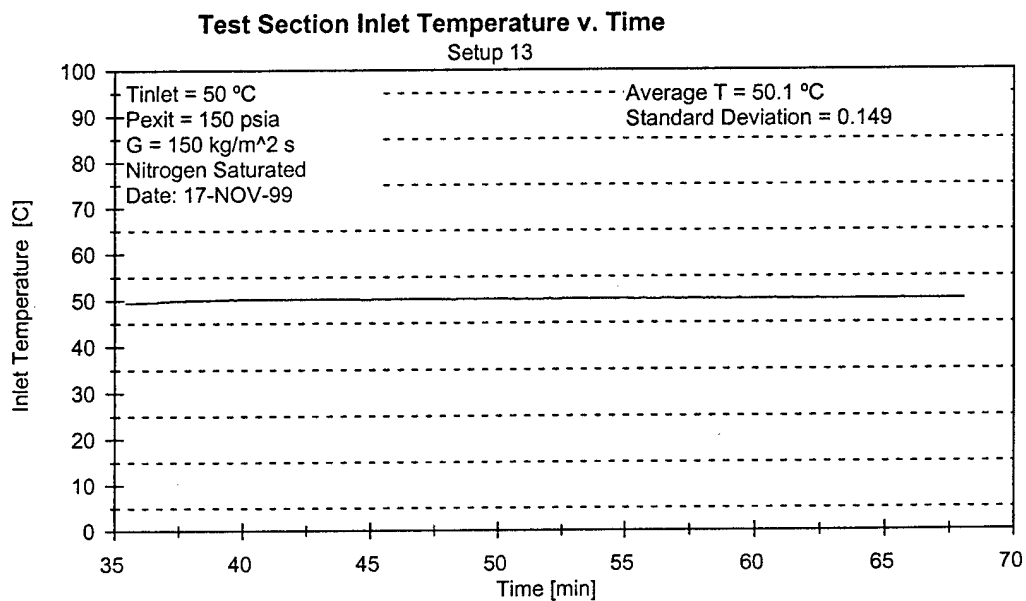


Figure 4.9: Typical Experimental Plot of Test Section Inlet Temperature Versus Time

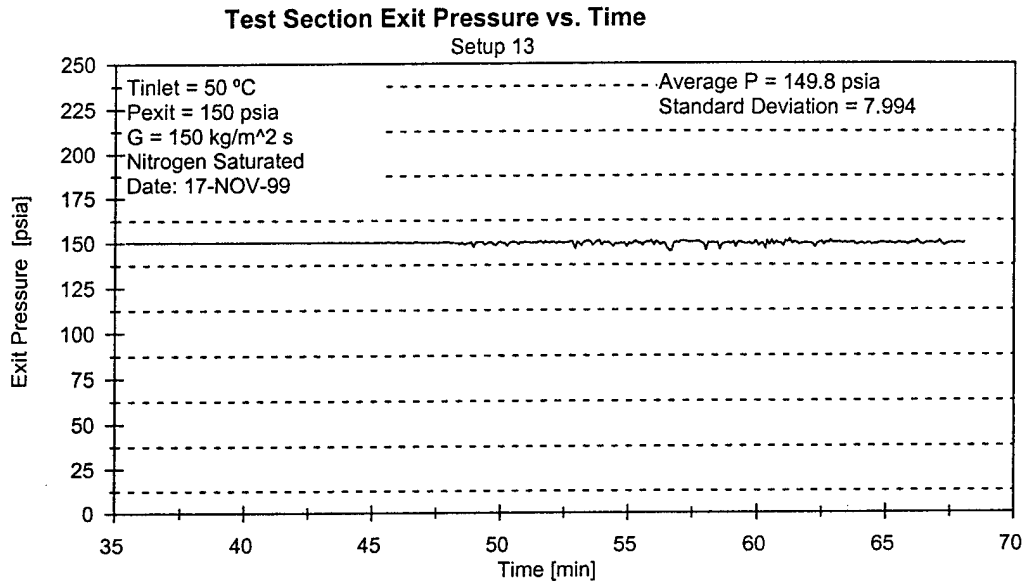


Figure 4.10: Typical Experimental Plot of Test Section Exit Pressure Versus Time

discussion to justify the averaging technique used for test section inlet temperature and exit pressure.

The value considered to be the CHF point for each experiment was actually an average of the last five calculated surface heat flux values up to and including the heat flux matching the wall temperature spike that terminated the experiment. A standard deviation associated with this mean value was also calculated and reported with the data in Appendix C. Due to the gradual rate of power increase used during CHF experimentation and the relatively fast sampling rate of the DAS system, the standard deviations were very low for every CHF value generated ($\leq 1.43\%$). These CHF values were compared with several CHF correlations in the literature and used to show that OFI, rather than CHF, is the limiting phenomenon in microchannel heat transfer.

CHAPTER V

RESULTS AND DISCUSSION

In this chapter, the experimental results obtained in this investigation are presented. Section V.1 provides the results for the OFI experiments, while Section V.2 contains the results of the CHF experiments.

V.1 Onset of Flow Instability

This investigation, combined with the study performed by Blasick (1999), produced a total of 195 OFI experiments. Appendix B lists the OFI conditions for all experiments conducted; the data include the non-condensable gas content, the annular gap width, the inlet temperature, the exit pressure, the coolant mass flux, the average surface heat flux, and the inner-to-outer heat flux ratio. Among the 195 OFI experiments listed in Appendix B, 129 experiments were conducted by Blasick, while 66 were performed in this investigation. All 195 OFI data points were used to develop an OFI correlation that covers a heat flux range of $0.125 - 2.4 \text{ MW/m}^2$. A brief summary of Blasick's findings will first be discussed, followed by the results obtained here and the empirical correlations developed.

V.1.1 Brief Discussion of the Findings of Blasick (1999)

Blasick (1999) investigated the effect of non-condensables on OFI by conducting experiments with either a fully-degassed working fluid (zero non-condensable gas content) or a working fluid saturated with air at the test section inlet temperature and exit pressure. Figure 5.1 shows the effect of non-condensables on OFI for two different heat fluxes and three different exit pressures. For each pressure, it can be seen that OFI occurred slightly earlier (that is, at a slightly higher mass flux value for a given applied heat flux) when the working fluid was air-saturated rather than fully-degassed. However, this effect became less pronounced with increased exit pressure because the air in the saturated working fluid came out of solution more readily at lower pressures, thus increasing the void fraction and leading to premature OFI. Roach (1998) also observed this effect while investigating OFI in micro-rod bundle coolant channels. It was concluded that the use of air-saturated working fluid provided a more conservative estimate of OFI than a degassed working fluid, and would, therefore, be appropriate for use in developing design correlations since the amount of non-condensables present in practical systems during accident conditions may not be accurately known. Using this logic, the majority of experiments in both this investigation and the investigation of Blasick (1999) were run using air-saturated water. Figure 5.1 also shows the effect of test section exit pressure on OFI. For the same inlet temperature, a reduction in pressure resulted in decreased subcooling which caused OFI to occur earlier since OFI is related to bulk exit saturation.

Unlike the work of Blasick (1999), this investigation did not specifically examine the effect of non-condensables on OFI; however, two different gases were used to saturate the working fluid (air and nitrogen). As described in Section III.3.6.3, while running air-saturated experiments at higher heat fluxes, the inner heaters became pitted and showed signs of severe corrosion. In an effort to minimize destruction of the inner heaters, the saturation gas was changed from air to nitrogen. With the decrease in dissolved oxygen content, the damage to the inner heaters was significantly reduced. From Blasick's results, air saturation was known to produce conservative OFI results as compared to fully-degassed conditions; nitrogen saturation was assumed to produce the same effect, because of its comparable solubility.

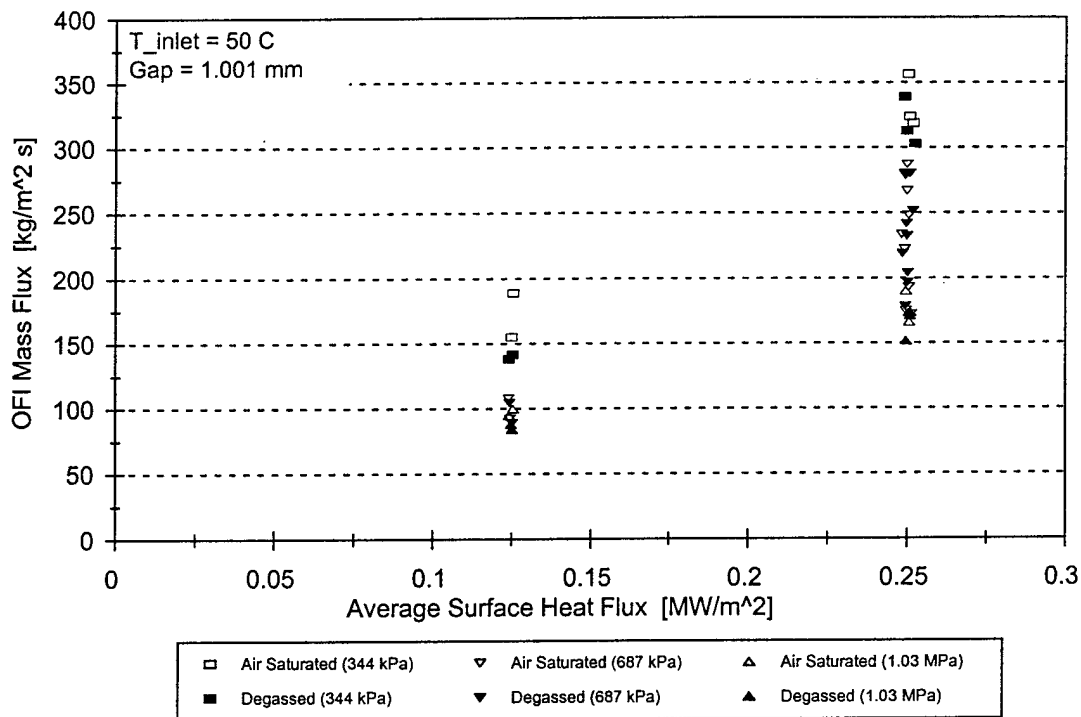


Figure 5.1: Effect of Non-Condensable Gas Content on OFI (from Blasick, 1999)

Blasick (1999) also investigated the effect of inner-to-outer power distribution on OFI by conducting experiments with inner-to-outer surface heat flux ratios ranging from 0 to infinity. Figure 5.2 shows the effect of power distribution on OFI mass flux at two different values of average surface heat flux. Note that the average surface heat flux used in Figure 5.2 was not the simple numerical average of the separate heat fluxes applied to the inner and outer surfaces. Since the surfaces had different areas, the average heat flux was calculated by dividing the total power input by the total heated surface area. The resulting value represents the heat flux one would obtain had the same total power input been applied to the test section to produce identical heat fluxes on the inner and outer

surfaces. From the plot in Figure 5.2, it can be seen that decreasing exit pressure results in earlier occurrence of OFI, as previously noted. Furthermore, the power distribution between the inner and outer surfaces of the annulus evidently had an insignificant effect on OFI as long as the total power input was held constant. As a result of this finding, the majority of the OFI experiments in this investigation, as well as the experiments performed by Blasick (1999), were run with a heat flux ratio of unity (equal heat flux on the inner and outer surfaces of the annulus), which is the expected nominal condition for the APT target.

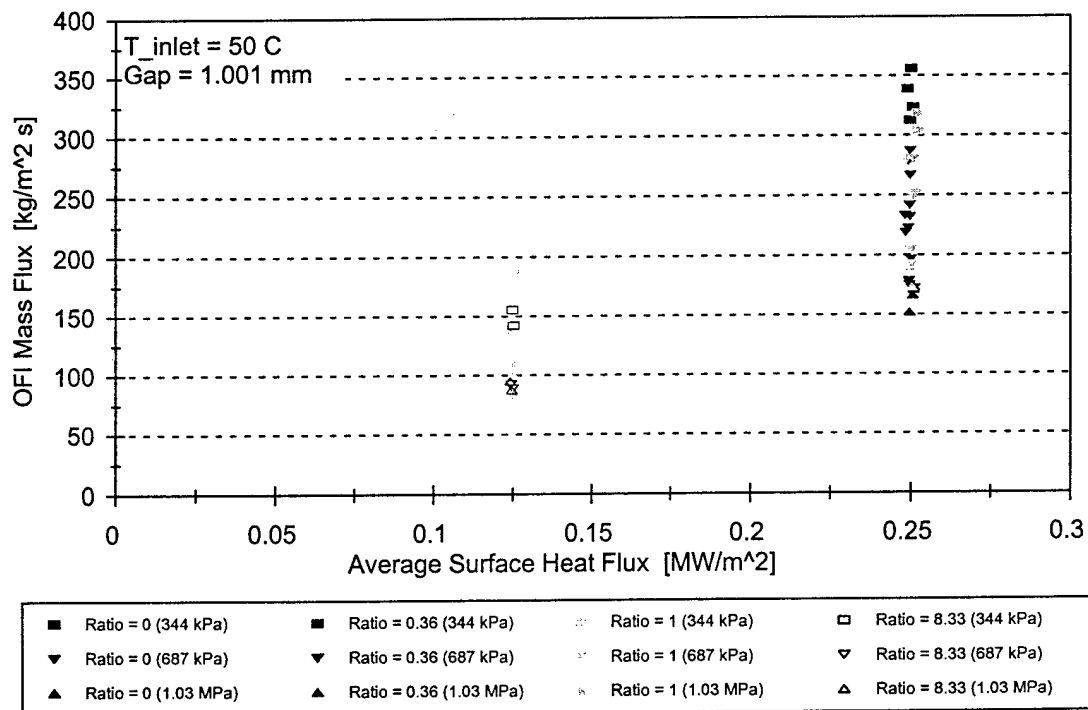


Figure 5.2: Effect of Inner-to-Outer Surface Heat Flux Ratio on OFI

It should be noted that because of test section design constraints, the data of Blasick (1999) were limited to moderate heat flux levels up to 1.0 MW/m^2 . The remaining OFI subsections of this chapter present the results obtained in this investigation, which extended the heat flux range of the Blasick (1999) data to 2.4 MW/m^2 .

V.1.2 Effect of Annular Gap Width on OFI

The effect of annular gap width on OFI was investigated by running experiments with annular gap widths ranging from 0.660 mm to 1.001 mm. These experiments provided the means to assess the possible effect of manufacturing tolerances on OFI. Figure 5.3 shows the effect of annular gap width on the OFI mass flux. It was found that, at equivalent heat fluxes, OFI occurred at a slightly lower mass flux in channels with larger gap widths (1.001, 0.914, and 0.940 mm).

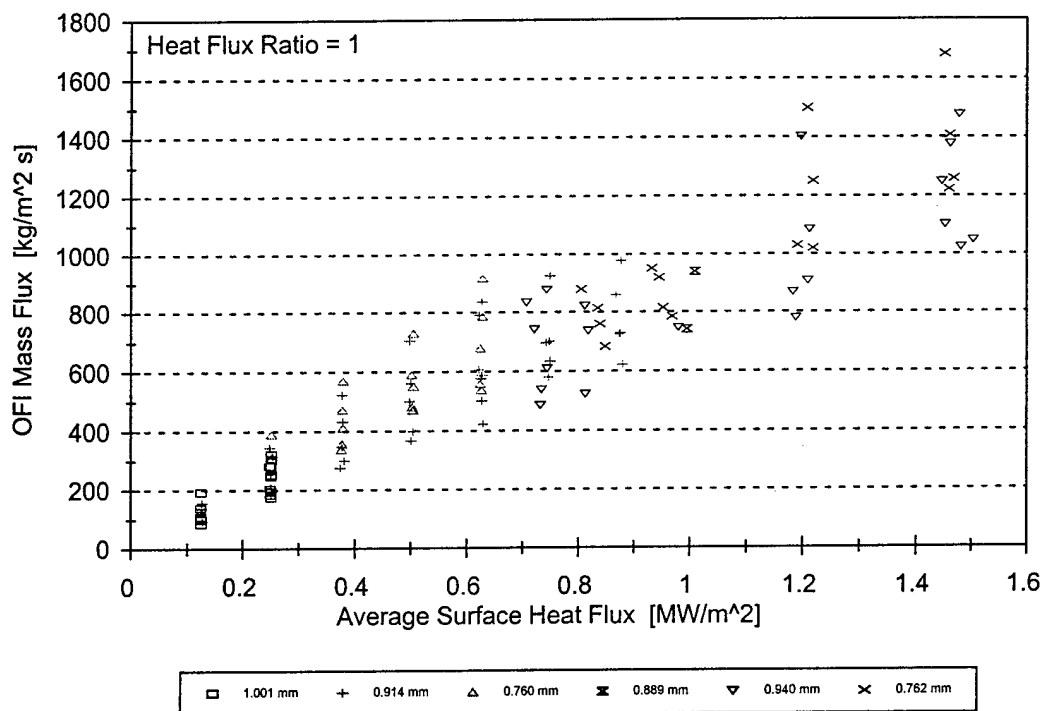


Figure 5.3: Effect of Annular Gap Width on OFI

V.1.3 Effect of Inner-to-Outer Heat Flux Ratio and Heated Length on OFI

Unlike the work of Blasick (1999), this investigation did not specifically examine the effect of inner-to-outer surface heat flux ratio on OFI, however, two different surface heat flux ratios (zero and unity) were utilized to collect the OFI data located in Table B.2. From Blasick's results, inner-to-outer surface heat flux ratio was known to have an insignificant effect on OFI as long as the total power input to the working fluid remained the same. For this reason, the bulk of OFI experiments were performed with a heat flux ratio of unity, however, while testing the AC powered outer heaters, several experiments were run that utilized an unheated inner heater. The experimental values of OFI collected

during these experiments were compared with the results reported by Blasick (1999). Figures 5.4 and 5.5 show the OFI experimental data collected at a heat flux ratio of zero (shown in Table B.2) compared with the OFI heat flux and OFI mass flux correlations developed for a heat flux ratio of unity. These two correlations are reported below in Section V.1.11; the zero heat flux ratio data appear to match the correlation's predictions, which supports the conclusion of Blasick (1999).

Figures 5.4 and 5.5 also demonstrate a more significant and previously unobserved effect. All data points included in the two figures were generated using a heat flux ratio of zero; however, four different heated lengths were used on the outer heater (53, 55, 123, and 180 mm). All data obtained in this investigation for these different heated lengths fell along the line generated from correlating the data with a heat flux ratio of unity. In other words, both the heat flux ratio and the test section heated length had an insignificant effect on OFI, only the total power input to the test section was important.

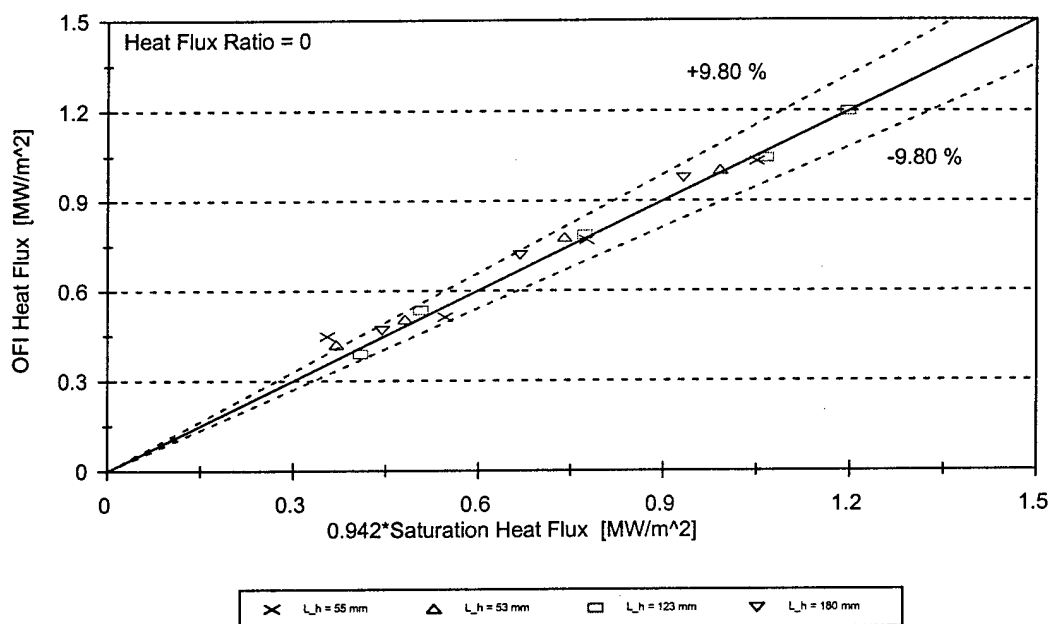


Figure 5.4: Comparison of Zero Heat Flux Ratio Data to OFI Heat Flux Correlation

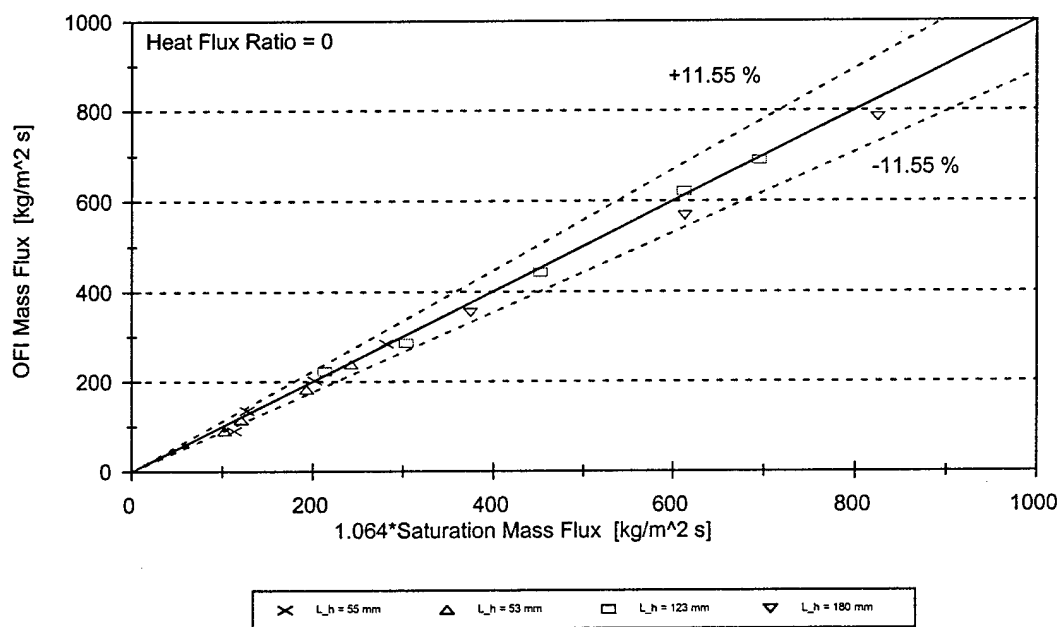


Figure 5.5: Comparison of Zero Heat Flux Ratio Data to OFI Mass Flux Correlation

V.1.4 Effect of Surface Heat Flux on OFI

Figure 5.6 illustrates the effect of increasing surface heat flux on OFI. The test section inlet temperature and exit pressure were held nominally constant at 30 °C and 100 psia, respectively, for these three experiments. As expected, the data showed that as the surface heat flux was increased, the mass flux at which OFI occurred increased.

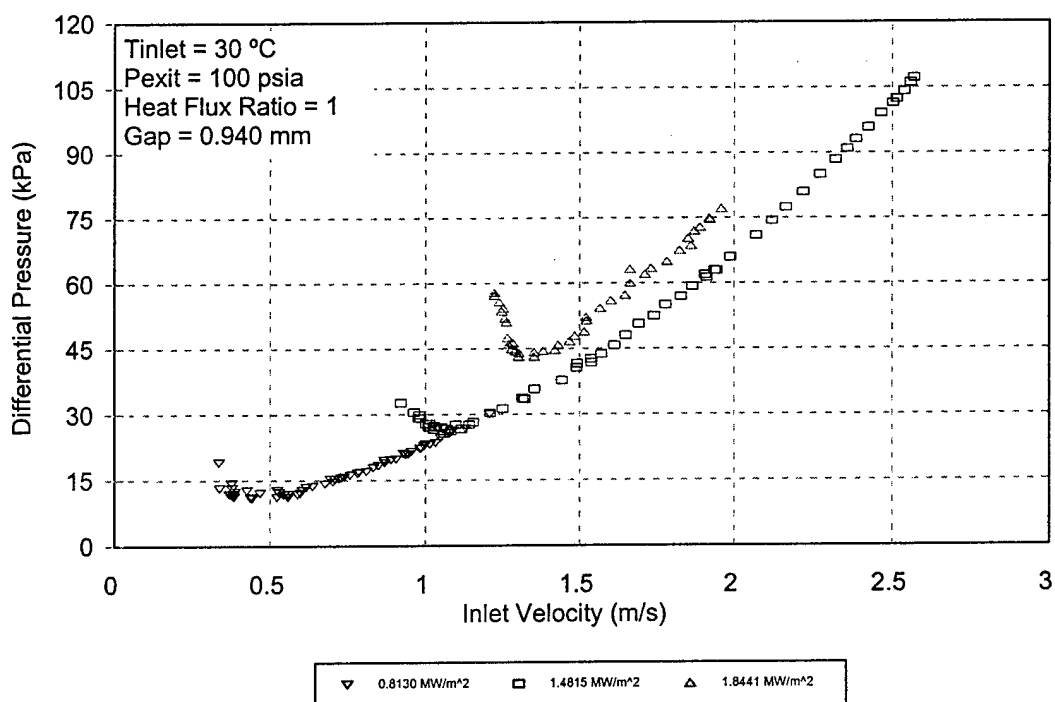


Figure 5.6: Effect of Surface Heat Flux on OFI

V.1.5 Effect of Test Section Inlet Temperature on OFI

Figure 5.7 illustrates the effect of test section inlet temperature on OFI. For a given set of parameters, demand curve data were obtained at nominal inlet temperatures of 30, 50, and 65 °C. As observed in the figure, increasing the coolant inlet temperature resulted in decreased subcooling of the working fluid which caused OFI to occur at a higher mass flux.

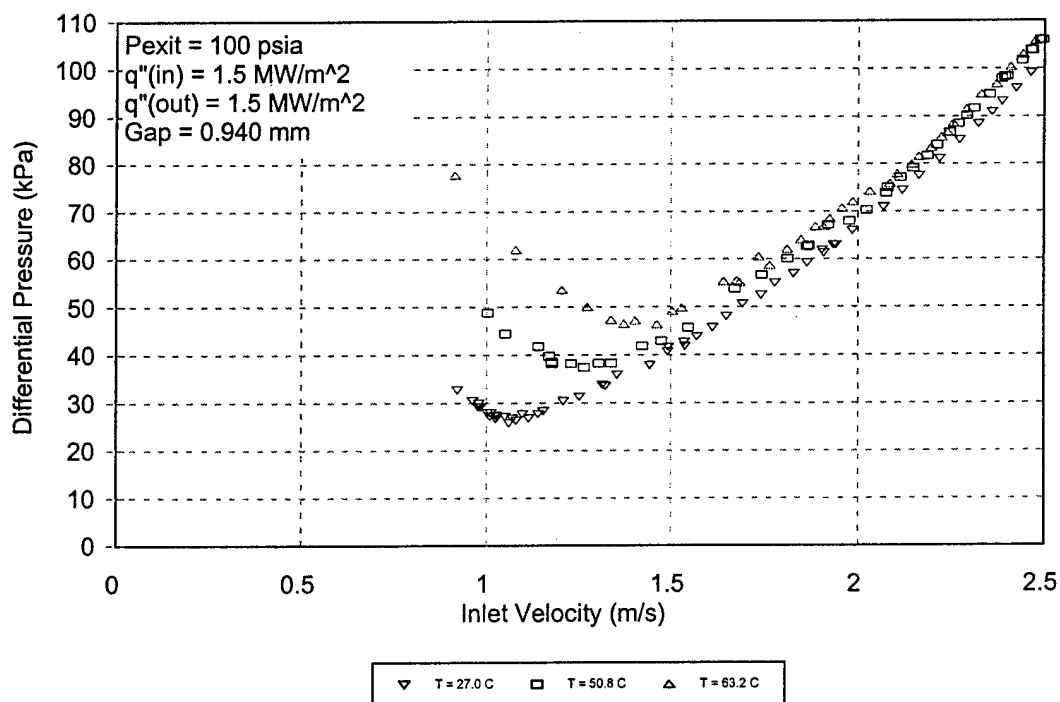


Figure 5.7: Effect of Test Section Inlet Temperature on OFI

V.1.6 Effect of Test Section Exit Pressure on OFI

Figure 5.8 illustrates the effect of test section exit pressure on OFI. For a given

set of parameters, demand curve data were obtained at nominal exit pressures of 50, 100, and 150 psia. For the same inlet temperature and surface heat flux values, OFI mass flux decreased as the test section exit pressure increased. This result is consistent with the findings of Blasick and others. The effect of pressure was quite significant; typically, the OFI mass flux for the 150 psia experiments differed from the 50 psia experiments by a factor of two, regardless of gap width.

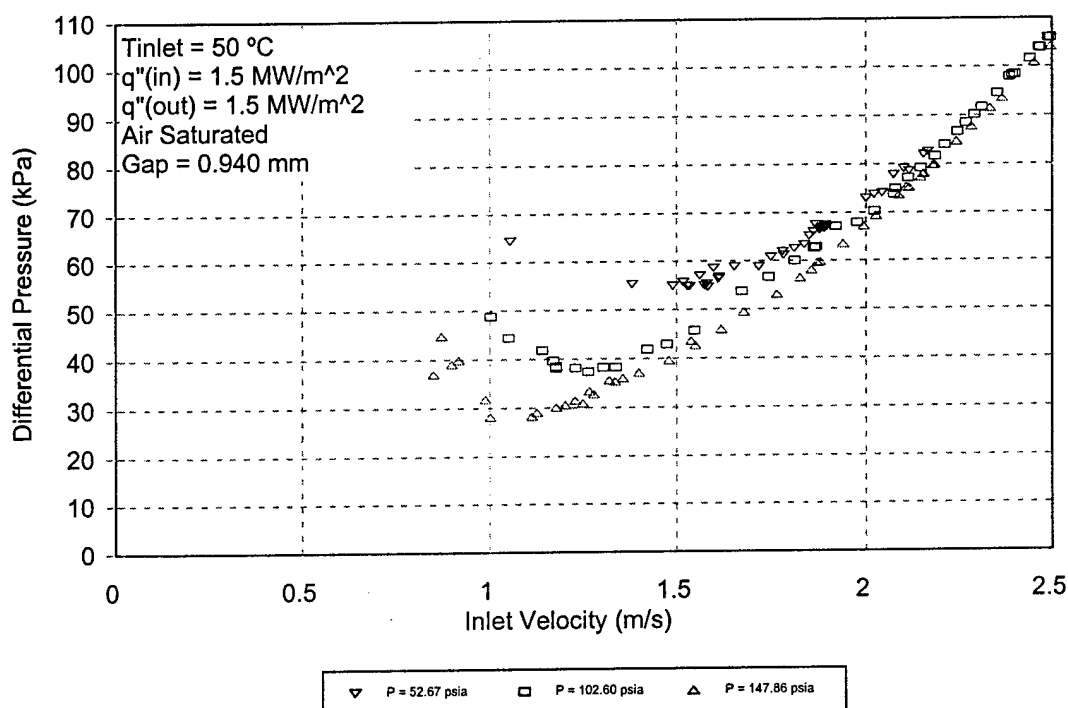


Figure 5.8: Effect of Test Section Exit Pressure on OFI

V.1.7 Comparison with Kennedy's OFI Model

Kennedy, et al. (1997) conducted OFI experiments using four test sections with

either circular or microbundle interior subchannel cross-sections. Based on the results of those experiments, the empirical OFI correlations listed in Table 2.11 were developed. Kennedy, et al. (1997) determined that the heat flux necessary to cause OFI was approximately 90% of the heat flux required for the working fluid to reach bulk exit saturation. Likewise, Kennedy, et al. (1997) found that, for a given heat flux, the mass flux at OFI was approximately 1.11 times the mass flux required for the working fluid to reach bulk exit saturation. Figures 5.9 and 5.10 compare the OFI data obtained by Blasick (1999) and the OFI data from this investigation with the correlations of Kennedy, et al. (1997). These figures show that the Kennedy correlations provide an acceptable, though slightly conservative, fit to the data.

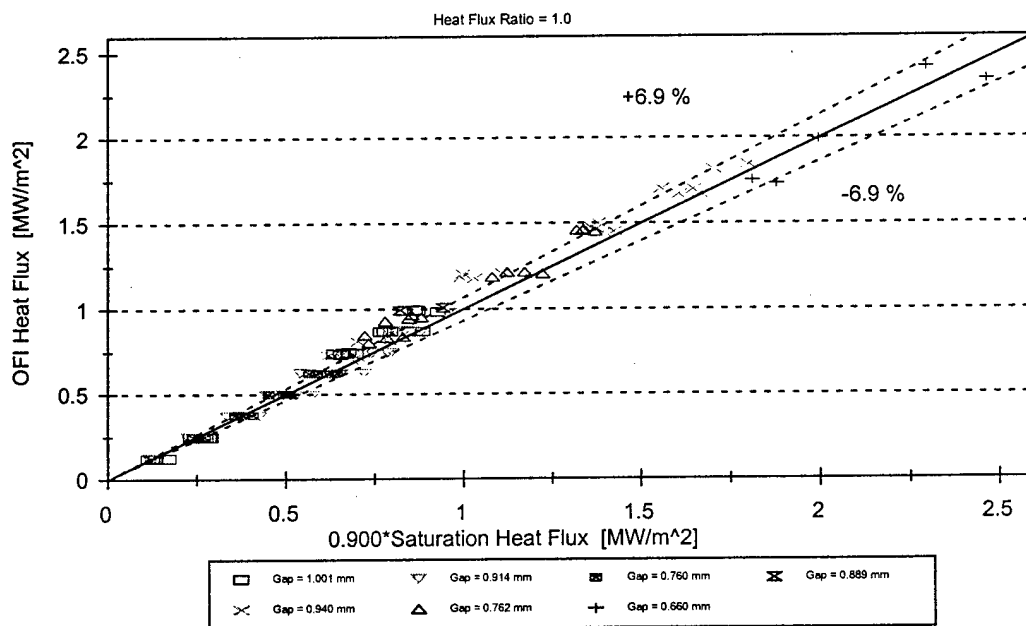


Figure 5.9: Comparison of OFI Heat Flux Data with Kennedy, et al. (1997) OFI Model

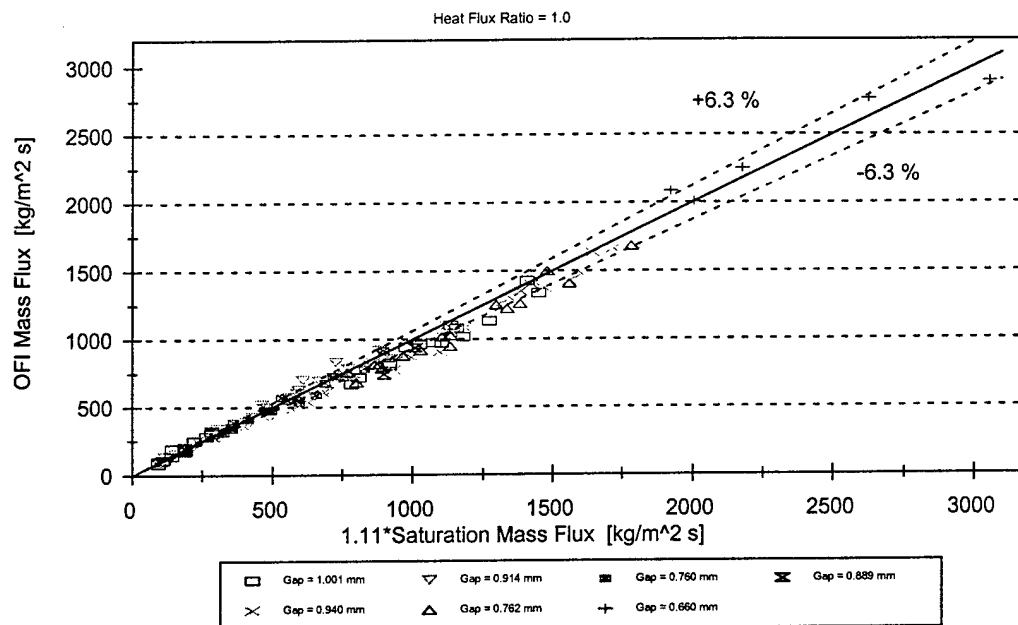


Figure 5.10: Comparison of OFI Mass Flux Data with Kennedy, et al. (1997) OFI Model

V.1.8 Comparison with Roach (1998) OFI Model

Roach (1998) conducted experiments using the same four test sections as Kennedy, et al. (1997) in order to develop the empirical OFI correlations listed in Table 2.12. Roach (1998) worked primarily with lower mass flux conditions and ultimately separated their correlations into subsets of fully-degassed and air-saturated. According to Roach (1998), the heat flux necessary to cause OFI under fully-degassed conditions was approximately 110% of the heat flux required for the working fluid to reach bulk exit saturation; 107% under conditions where the working fluid was air-saturated. Likewise, Roach (1998) found that, for a given heat flux, the mass flux at OFI was approximately

0.89 times the mass flux required for the working fluid to reach bulk exit saturation under fully-degassed conditions; 0.91 times under air-saturated conditions. Figures 5.9 and 5.10 compare the OFI data obtained by Blasick (1999) and the OFI data from this investigation with the air-saturated correlations of Roach (1998). These figures show that, for the thin, annular channels studied by Blasick (1999) and this investigation, the Roach (1998) low-flow OFI correlations do not provide a good fit to the data; the correlations were generally non-conservative.

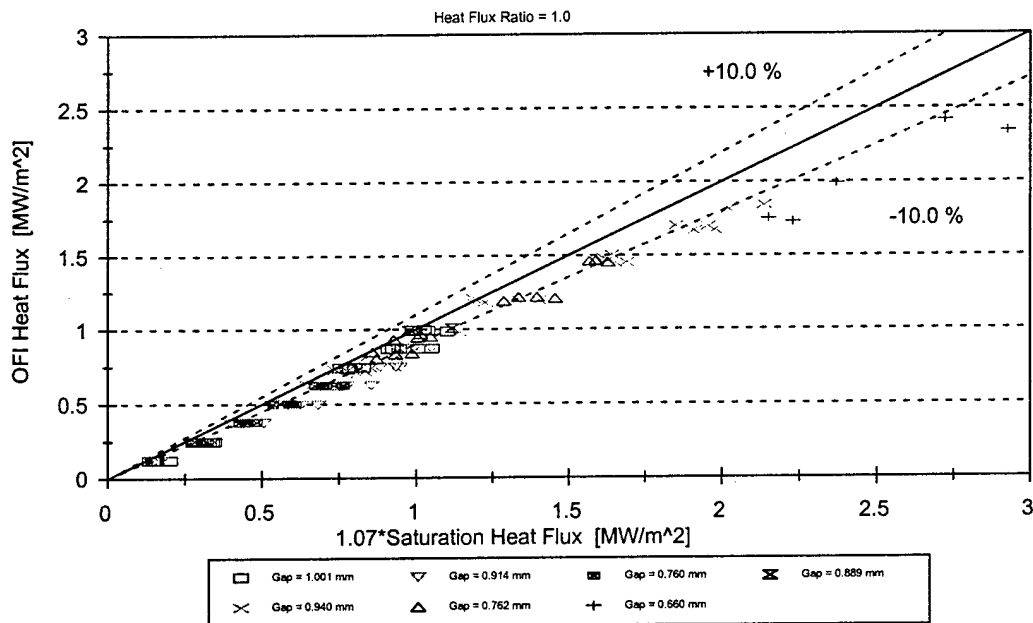


Figure 5.11: Comparison of OFI Heat Flux Data with Roach (1998) Low-Flow, Air-Saturated OFI Model

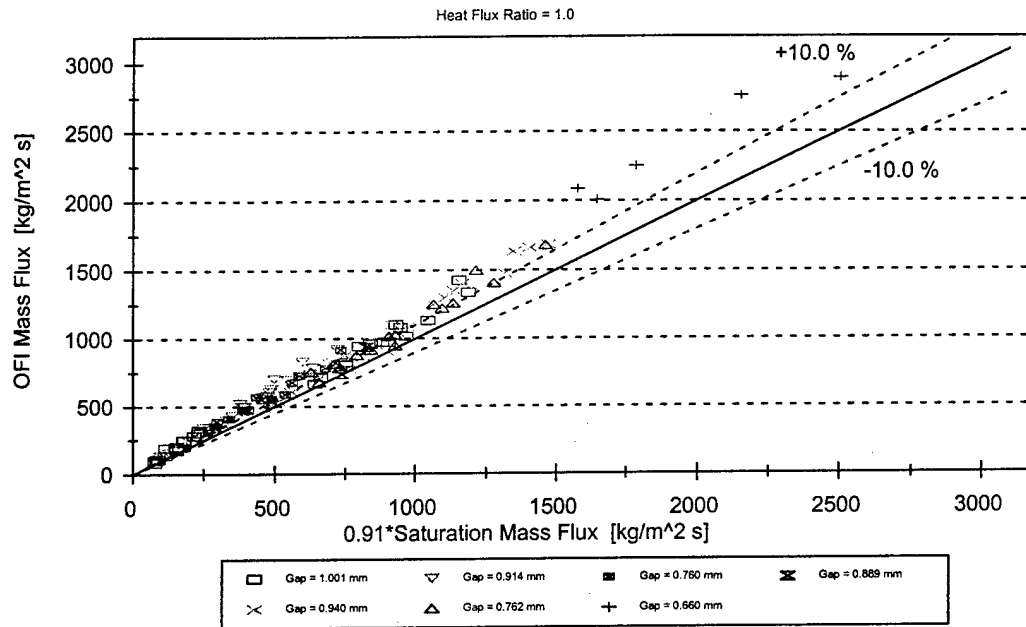


Figure 5.12: Comparison of OFI Mass Flux Data with Roach (1998) Low-Flow, Air-Saturated OFI Model

V.1.9 Comparison with the Saha and Zuber (1974) OSV Model

Next, the OFI data were compared with predictions of the Saha-Zuber OSV model. Correlation against the Saha-Zuber OSV model gave the following results.

$$q''_{OFI} = 1.000 * q''_{S-Z} \pm 11.93\% \quad (5.1)$$

$$G_{OFI} = 0.998 * G_{S-Z} \pm 15.65\% \quad (5.2)$$

This suggests that the Saha-Zuber OSV model can be accurately used to predict OFI for

the thin, annular channels used in this investigation over the experimental range of parameters, with appropriate safety factors given the uncertainty of the correlations. Figures 5.13 and 5.14 show graphic representations of the OFI data against OSV predictions by the Saha-Zuber correlations.

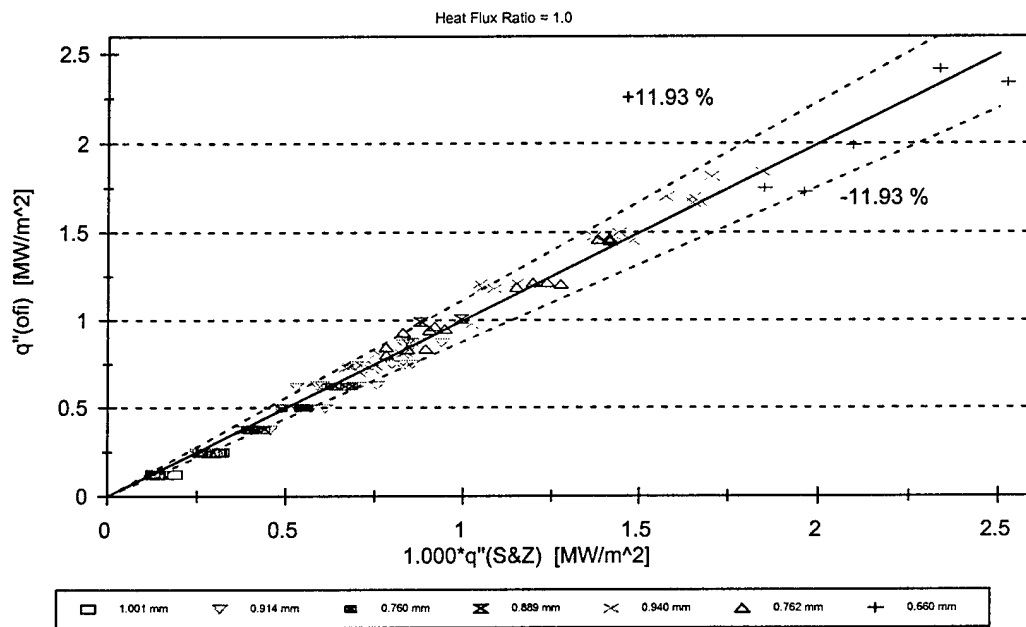


Figure 5.13: Correlation of OFI Heat Flux Data Against Saha & Zuber OSV Model

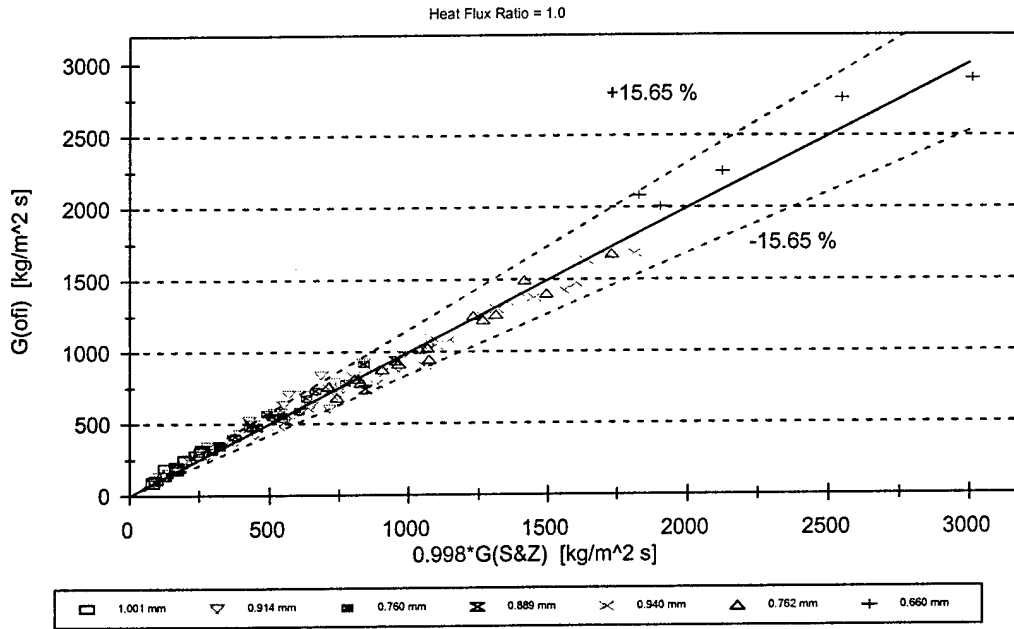


Figure 5.14: Correlation of OFI Mass Flux Against Saha & Zuber OSV Model

V.1.10 Comparison with the Unal (1975) IPNVG Model

Using a similar approach, correlation against the Unal (1975) IPNVG model yielded the following.

$$q''_{OFI} = 1.082 * q''_{Unal} \pm 13.15\% \quad (5.3)$$

$$G_{OFI} = 0.922 * G_{Unal} \pm 17.50\% \quad (5.4)$$

This relationship indicates that the Unal (1975) IPNVG model provides a conservative estimate of OFI. Again, graphic representations of the OFI data against these correlations

are shown in Figures 5.15 and 5.16. As with the Saha-Zuber correlations above, the uncertainty range (\pm) listed in the correlation equals twice the standard deviation of the percent error between the prediction and the raw OFI data.

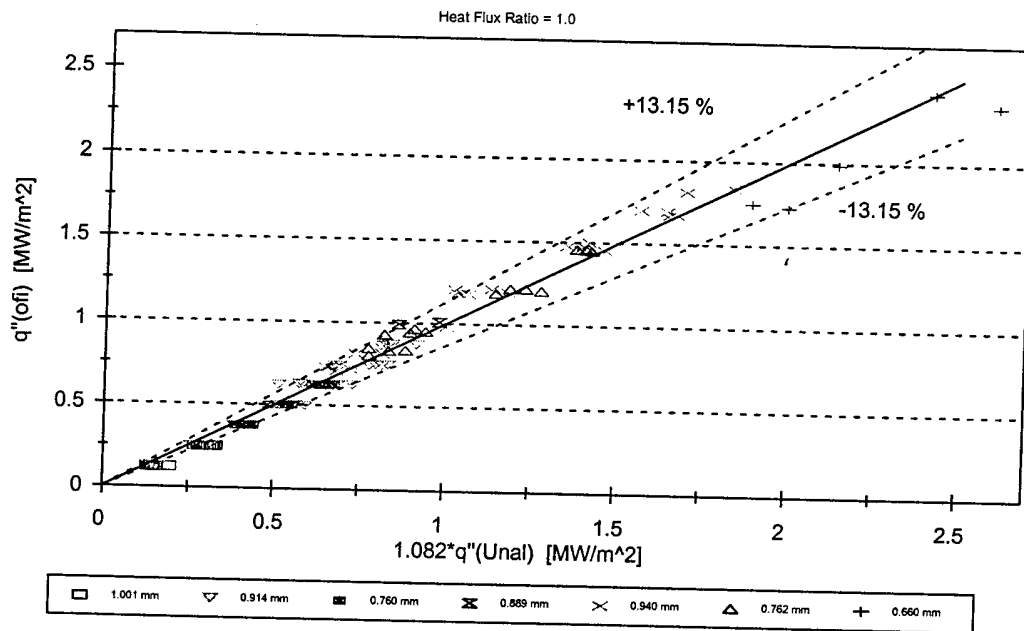


Figure 5.15: Correlation of OFI Heat Flux Data Against Unal (1975) IPNVG Model

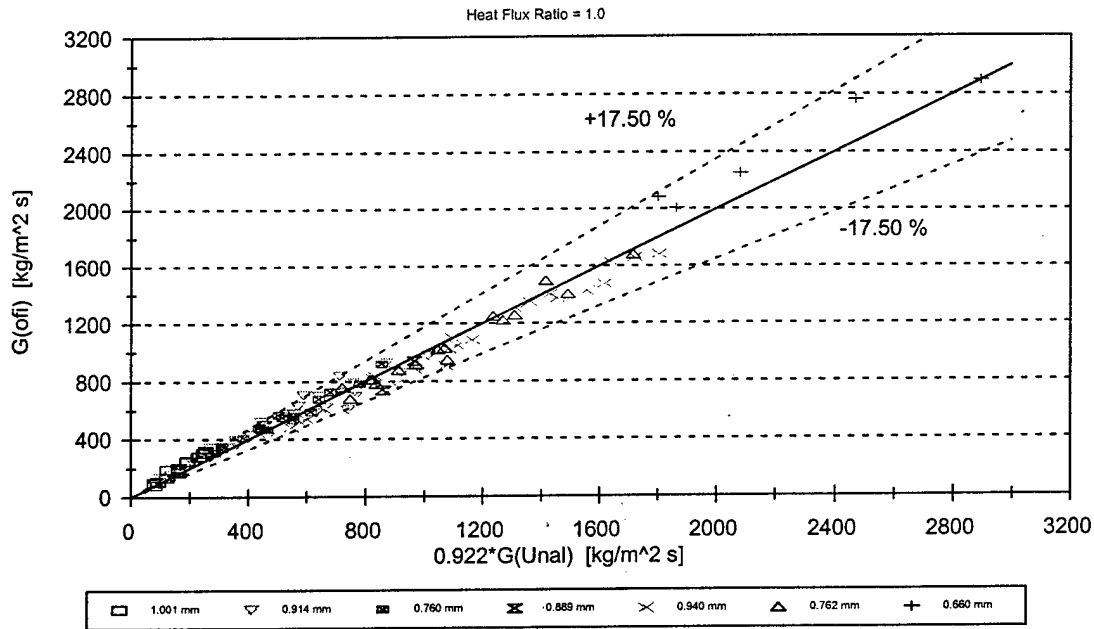


Figure 5.16: Correlation of OFI Mass Flux Data Against Unal (1975) IPNVG Model

V.1.11 Development of OFI Correlation

As described in Section IV.7.2, with OFI mass flux, OFI heat flux, inlet enthalpy, and exit pressure known for each experiment, an energy balance was used to calculate the corresponding heat flux and mass flux that would lead to saturation at the test section exit:

$$G_{sat} = q''_{OFI} \frac{A_{heated}}{A_{flow} (h_f[P_{exit}] - h[T_{inlet}, P_{inlet}])} \quad (5.5)$$

$$q''_{sat} = G_{OFI} \frac{A_{flow}}{A_{heated}} (h_f[P_{exit}] - h[T_{inlet}, P_{inlet}]) \quad (5.6)$$

Based on these energy balances, simple correlations were developed for the OFI heat flux (or mass flux) as functions of the corresponding saturation heat flux (or mass flux). Using this approach, Kennedy, et al. (1997) and Roach (1998) developed correlations for OFI representing high and low mass fluxes through circular microchannels and micro-rod bundle coolant subchannels, respectively. The data obtained in this investigation were augmented by the data produced by Blasick (1999) and used to develop the following correlations. Note that only the experimental data with an inner-to-outer heat flux ratio of unity were used, since this was the nominal condition of the APT target. For a given mass flux or heat flux, the following correlations were developed to predict the corresponding heat flux or mass flux at OFI:

$$q''_{OFI} = 0.942 * q''_{sat} \pm 9.80\% \quad (5.7)$$

$$G_{OFI} = 1.064 * G_{sat} \pm 11.55\% \quad (5.8)$$

These correlations were obtained by minimizing the sum of the squares of the absolute error (i.e., the difference between the experimental and predicted values of q''_{OFI} and G_{OFI}). These correlations predict the data within $\pm 9.80\%$ for OFI heat flux given a known mass flux and $\pm 11.55\%$ for OFI mass flux given a known heat flux, with a 95% confidence level. The uncertainty ranges equal twice the standard deviation of the percent error between the prediction and the raw OFI data. Figures 5.17 and 5.18

compare predictions of the above correlations with the data. The correlations are valid for the following parameter ranges:

Heat Flux:	$0.125 \rightarrow 2.4 \text{ MW/m}^2$
Mass Flux:	$85 \rightarrow 2900 \text{ kg/m}^2 \text{ sec}$
Inlet Temperature:	$30 \rightarrow 70^\circ\text{C}$
Exit Pressure:	$50 \rightarrow 150 \text{ psia}$
Non-Condensable Gas Content:	Saturated at T_{inlet} and P_{exit}
Inner-to-Outer Heat Flux Ratio:	1.0
Coolant Channel Geometry:	Annulus
Coolant Channel Gap Thickness:	$0.660 \rightarrow 1.001 \text{ mm}$

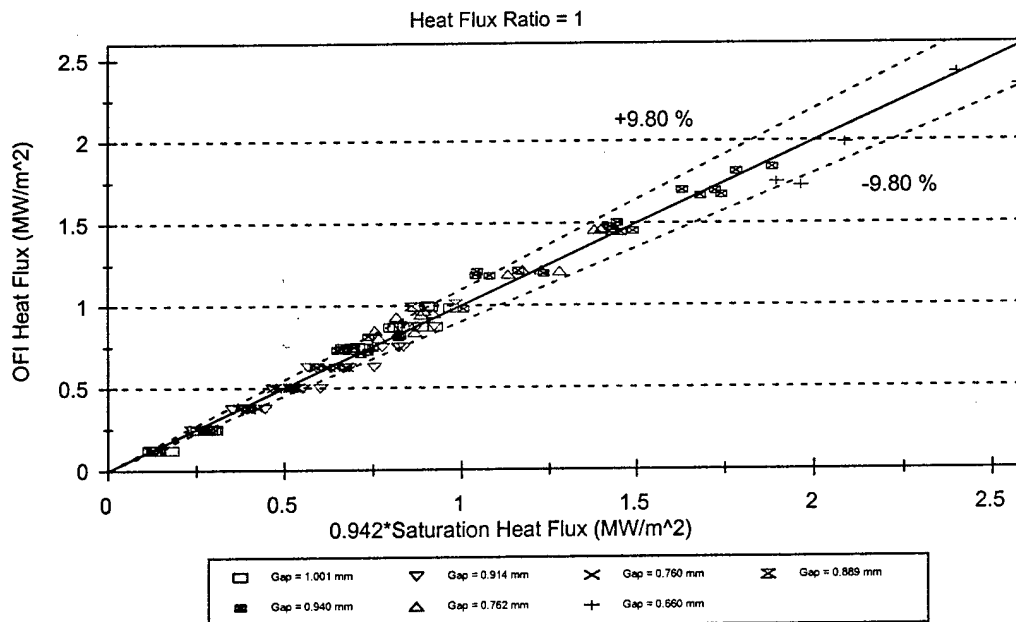


Figure 5.17: OFI Heat Flux Correlation

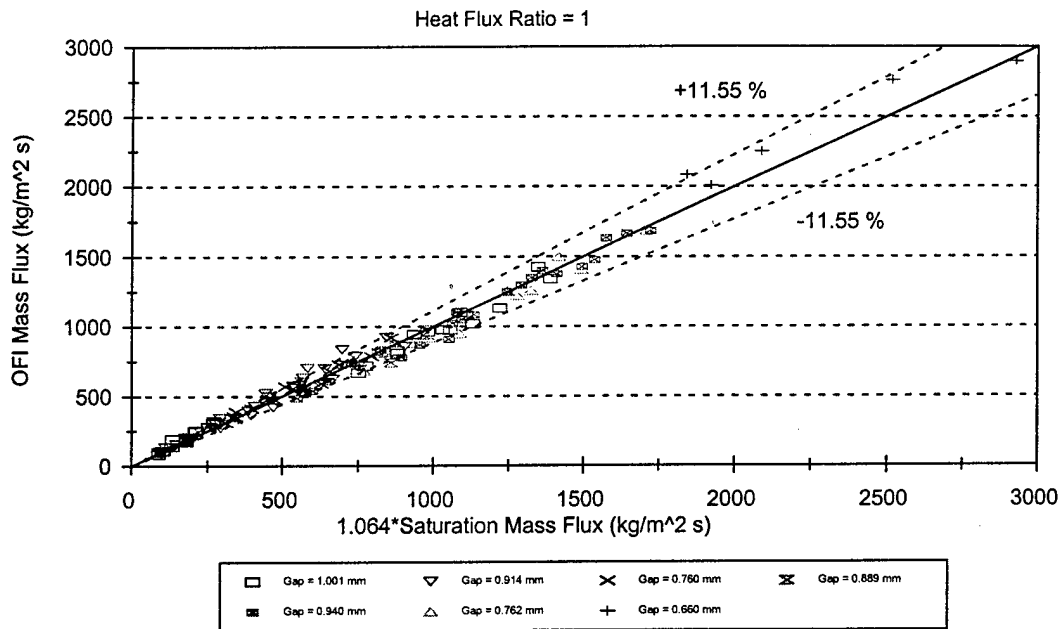


Figure 5.18: OFI Mass Flux Correlation

V.2 Critical Heat Flux (CHF)

In this section, the results of the CHF experiments conducted in this investigation are presented. A total of 35 low mass flux CHF experiments were conducted. The primary goal of these experiments was to show that OFI, rather than CHF, is the limiting phenomenon in microchannel heat transfer. Appendix C lists the CHF conditions for all experiments conducted; the data include the non-condensable gas content, the annular gap width, the inlet temperature, the exit pressure, the coolant mass flux, the average surface heat flux, and the calculated exit quality.

V.2.1 Effect of Coolant Mass Flux on CHF

Figure 5.19 illustrates the effect of increased coolant mass flux on CHF. In this figure, the test section inlet temperature and exit pressure were nominally maintained at 30°C and 100 psia, respectively, while the coolant mass flux was varied. The data showed that, as coolant mass flux was increased, the surface heat flux at which CHF occurred increased. Roach (1998) also observed this intuitive result after performing a similar investigation of CHF in circular microchannels and in a micro-rod bundle subchannel.

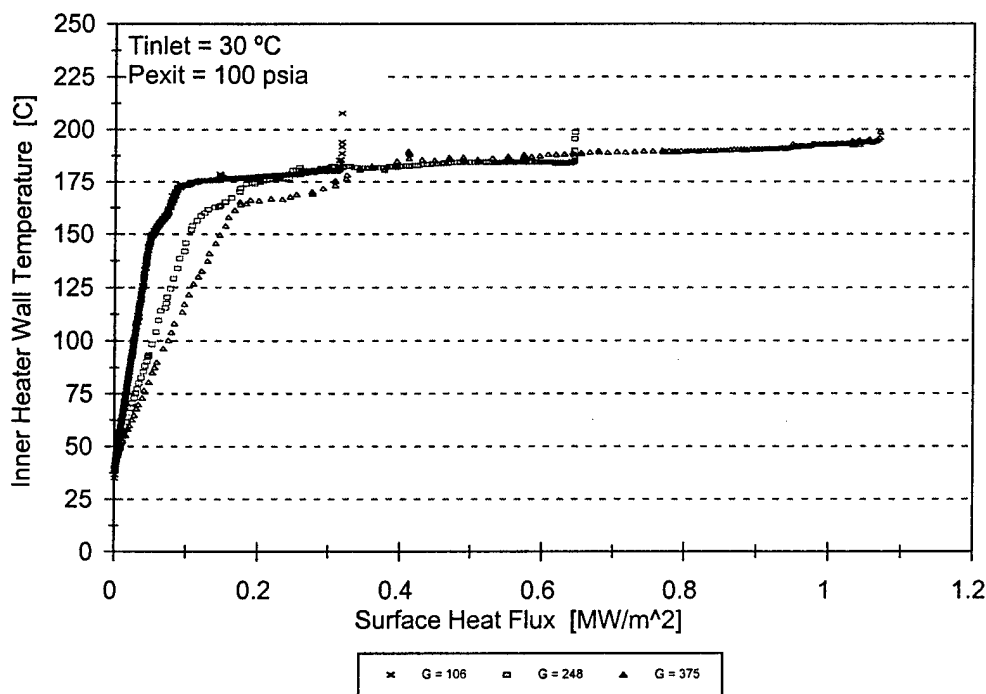


Figure 5.19: Effect of Coolant Mass Flux on CHF

V.2.2 Effect of Test Section Inlet Temperature on CHF

Figure 5.20 illustrates the effect of test section inlet temperature on CHF. For a given set of parameters, CHF experiments were conducted at nominal inlet temperatures of 30, 50, and 65 °C. As observed in the figure, increased inlet temperature resulted in decreased subcooling of the working fluid which caused CHF to occur at a lower heat flux. The effect appears to become more significant at higher mass flux values.

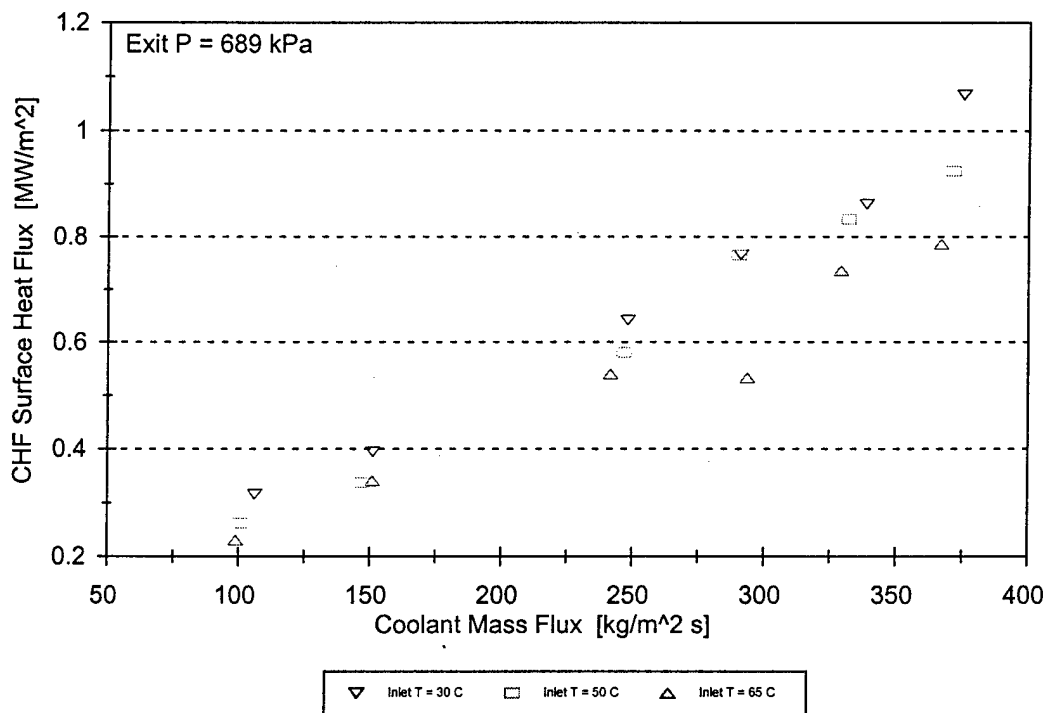


Figure 5.20: Effect of Test Section Inlet Temperature on CHF

V.2.3 Effect of Test Section Exit Pressure on CHF

Figure 5.21 illustrates the effect of test section exit pressure on CHF. For a given

set of parameters, CHF experiments were conducted at nominal exit pressures of 50, 100, and 150 psia. With inlet temperature and coolant mass flux set, the CHF heat flux increased as the test section exit pressure increased. This result was consistent with the findings of Roach (1998) and can be directly attributed to the higher saturation temperatures associated with higher system pressures. The effect appears to be more significant at elevated mass flux values.

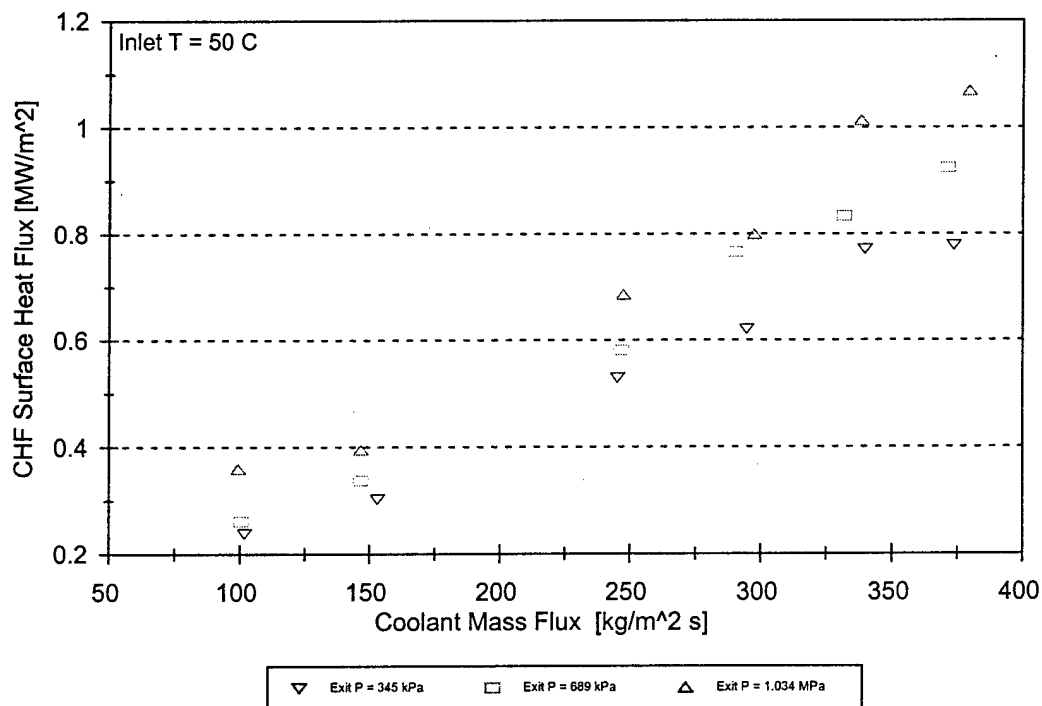


Figure 5.21: Effect of Test Section Exit Pressure on CHF

V.2.4 Comparison with the Caira, et al. (1993) Empirical CHF Correlation

Next, the CHF data were compared with predictions of the Caira, et al. (1993)

empirical CHF model (Table 2.15). Correlation against the Caira CHF model gave the following results.

$$q''_{CHF} = 0.785 * q''_{Caira} \pm 24.03\% \quad (5.9)$$

This suggests that the Caira CHF model is not a conservative predictor of low mass flux CHF in horizontal, thin annuli. The large uncertainty value associated with the comparison ($\pm 24.03\%$) detracts from the possible use of Equation 5.9 for CHF predictions (Figure 5.22).

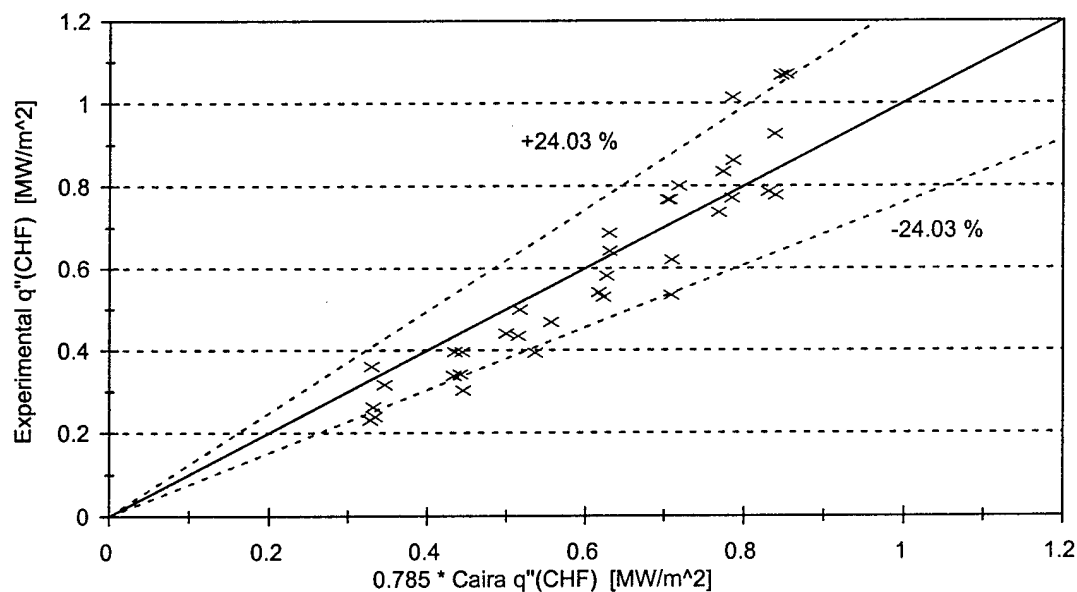


Figure 5.22: Correlation of Experimental CHF Data Against Caira, et al. (1993) CHF Model

V.2.5 Comparison with the Bowring (1972) Empirical CHF Correlation

Next, the CHF data were compared with predictions of the Bowring (1972) empirical CHF model (Table 2.14). Correlation against the Bowring (1972) CHF model yielded the following results.

$$q''_{CHF} = 0.586 * q''_{Bowring} \pm 16.28\% \quad (5.10)$$

As with the Caira, et al. (1993) comparison, Equation 5.10 suggests that the Bowring (1972) CHF model is not a conservative predictor of low mass flux CHF in horizontal, thin annuli. The lower uncertainty values associated with the comparison ($\pm 16.28\%$) suggest that the model represented by Equation 5.10 may be used for design purposes (Figure 5.23).

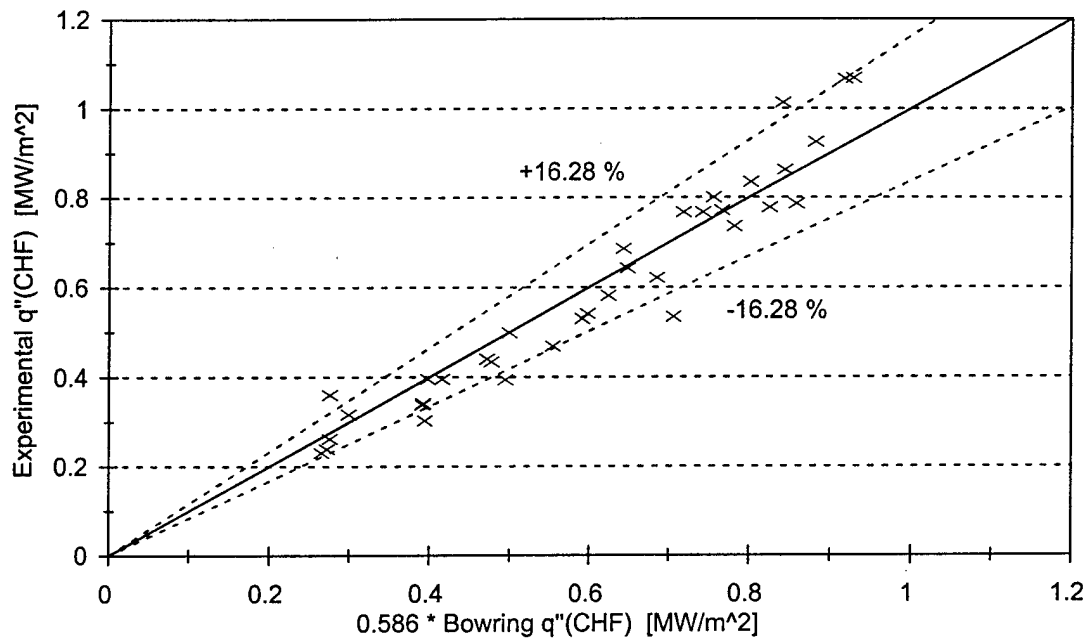


Figure 5.23: Correlation of Experimental CHF Data Against Bowring (1972) CHF Model

V.2.6 Comparison with Predicted OFI Correlation

As stated earlier, the primary goal of this CHF study was to show that OFI, rather than CHF, was the limiting heat transfer phenomenon in microchannel heat transfer. Figure 5.24 shows a plot of experimentally determined CHF surface heat fluxes versus the corresponding OFI values predicted using Equation 5.7. The experimental conditions for the CHF experiments listed in Appendix B. A least square fit of the CHF data and the corresponding predicted OFI values produced the following correlation.

$$q''_{CHF} = 3.047 * q''_{OFI} \pm 12.63\% \quad (5.11)$$

Figure 5.25 shows a plot of the experimental CHF data against this correlation. Equation 5.11 and Figure 5.24 clearly show that for a given set of conditions, CHF occurs at a surface heat flux of more than three times the predicted OFI heat flux, thus proving that OFI, not CHF, is the limiting heat transfer phenomenon in microchannel heat transfer.

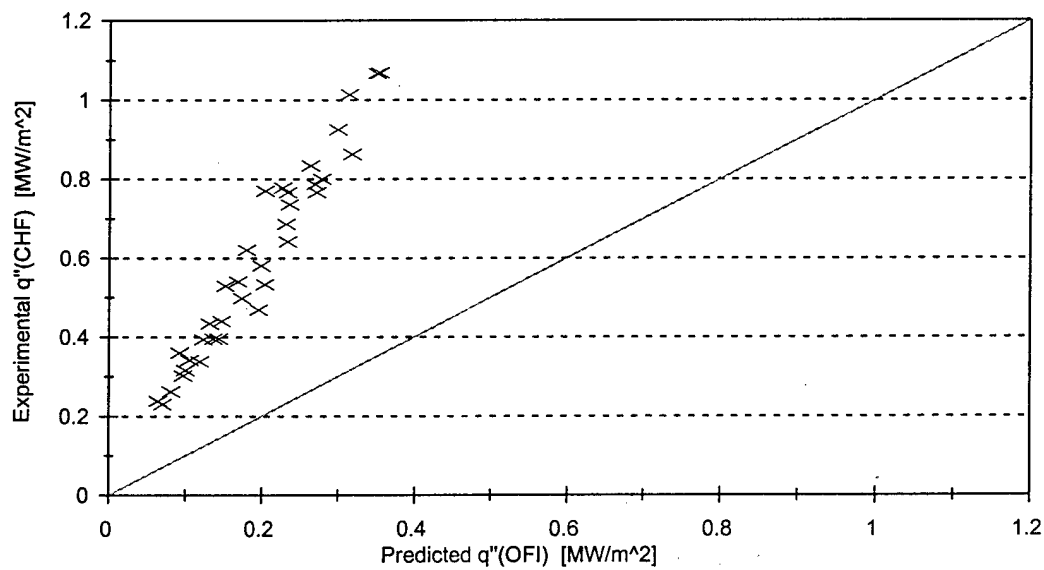


Figure 5.24: Experimental CHF Data Versus Predicted OFI Heat Flux

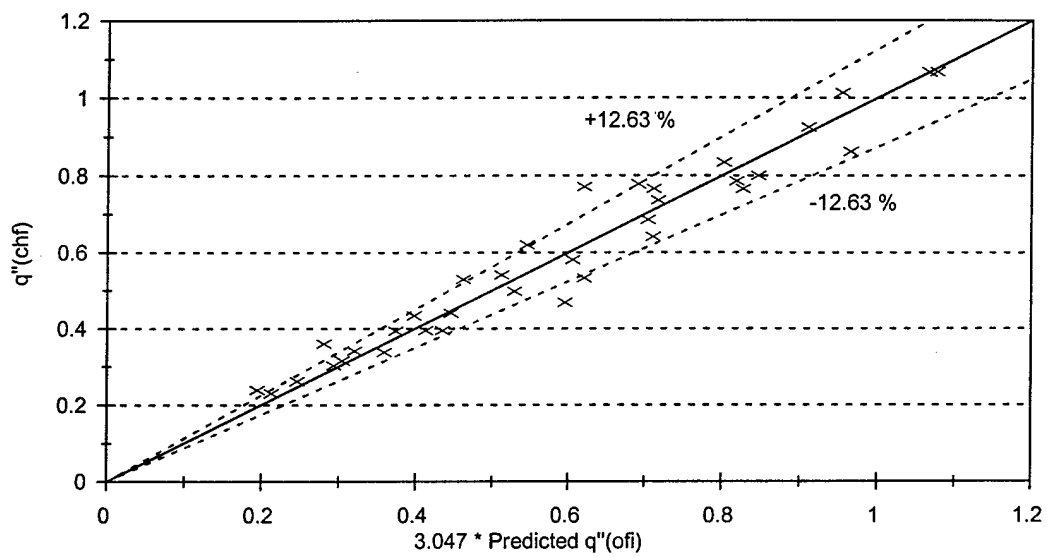


Figure 5.25: Experimental CHF Data Versus 3.047 Times Predicted OFI Heat Flux

CHAPTER VI

CONCLUSIONS

Ledinegg flow instability and critical heat flux experiments were conducted with water flowing through thin, concentric annuli in thirteen different experimental setups using the Georgia Tech Microchannel Test Facility. Subcooled water at a controlled flow rate, pressure, temperature, and dissolved non-condensable gas concentration was delivered to the annular test section. The inner and outer surfaces of the annulus were heated electrically up to 2.5 MW/m^2 using four different variable power supply configurations. A total of 66 OFI and 35 CHF experiments were conducted in this investigation and combined with the 129 OFI experiments conducted in the investigation of Blasick (1999) for analysis and comparison with known two-phase models. The tables located in Appendices B and C provide all of the OFI and CHF data collected and used during this study.

VI.1 OFI Conclusions

1. Inner-to-outer surface heat flux ratio was found to have an insignificant effect on OFI, only the total power input to the test section was important. This finding is

consistent with the conclusions of Blasick (1999).

2. The test section heated length was found to have an insignificant effect on OFI. Once again, only the total power input to the test section was important, not the method of application.
3. With all other operating parameters constant, OFI occurred at higher mass fluxes as the surface heat flux applied to the test section was increased.
4. With all other operating parameters constant, OFI occurred at higher mass fluxes as the test section inlet temperature was increased.
5. With all other operating parameters constant, OFI occurred at higher mass fluxes as the test section exit pressure was decreased.
6. With all other operating parameters constant, OFI occurred at higher mass fluxes as the test section annular gap width was decreased.
7. An integral OFI correlation was developed relating the heat flux required to cause bulk exit saturation of the working fluid with the heat flux required to initiate OFI. A second integral OFI correlation was developed for the coolant mass flux data.

$$q''_{OFI} = 0.942 * q''_{sat} \pm 9.80\% \quad (6.1)$$

$$G_{OFI} = 1.064 * G_{sat} \pm 11.55\% \quad (6.2)$$

The data fit each of these correlations within a 95% (2σ) confidence level. The

parameter ranges used to develop these correlations were:

Heat Flux:	0.125 \rightarrow 2.4 MW/m ²
Mass Flux:	85 \rightarrow 2900 kg/m ² sec
Inlet Temperature:	30 \rightarrow 70°C
Exit Pressure:	50 \rightarrow 150 psia
Non-Condensable Gas Content:	Saturated at T _{inlet} and P _{exit}
Inner-to-Outer Heat Flux Ratio:	1.0
Coolant Channel Geometry:	Annulus
Coolant Channel Gap Thickness:	0.660 \rightarrow 1.001 mm

8. The Saha and Zuber (1974) OSV model gives an accurate fit to the data while the Unal (1975) IPNVG model provides a slightly conservative estimate of OFI.

VI.2 CHF Conclusions

1. With all other operating parameters constant, CHF occurred at lower heat fluxes as the coolant mass flux supplied to the test section was decreased.
2. With all other operating parameters constant, CHF occurred at lower heat fluxes as the test section inlet temperature was increased.
3. With all other operating parameters constant, CHF occurred at lower heat fluxes as the test section exit pressure was decreased.
4. Neither the Caira, et al. (1993) CHF model nor the Bowring (1972) CHF model provides an accurate fit to the experimental CHF data. In addition, correlation of the experimental data against both models produces a relatively large amount of

error (24.03% and 16.28%). Of the two, however, the Bowring (1972) correlation produced the least amount of error, which lends to the conviction with which the Bowring (1972) correlation, with a multiplier of 0.586, can be used to predict CHF in thin, annular channels over the parameter range used in this investigation.

5. Finally, OFI, rather than CHF, is the limiting heat transfer phenomenon in microchannel heat transfer. Comparison of the CHF experimental data to the OFI correlation shown in Equation 6.1 showed that, for a given set of operating conditions, CHF occurs at a surface heat flux of more than three times the predicted OFI heat flux.

$$q''_{CHF} = 3.047 * q''_{OFI} \pm 12.63\% \quad (6.3)$$

APPENDIX A

EES PROPERTIES ALGORITHM

This appendix lists the algorithm used in Engineering Equation Solver (EES) to determine the coolant properties at the test section inlet and exit. These properties were the viscosity, density, enthalpy, thermal conductivity, specific heat, and saturation temperature of the working fluid. For a particular set of OFI data, analysis began by copying each combination of inlet temperature and inlet pressure from the Quattro Pro analysis spreadsheet into an EES parametric table. The EES algorithm below was then run and the six fluid properties mentioned earlier were generated for each combination of temperature and pressure. These values were then copied from EES into the Quattro Pro analysis spreadsheet. An identical procedure was followed in order to determine the coolant properties at the test section exit.

Two important facts about the algorithm must be noted. First, the pressure read by the DAS system and reported in the Quattro Pro analysis spreadsheet was gauge pressure. The EES algorithm below converted this gauge pressure into absolute pressure by adding 101.325 kPa to the value copied from the Quattro Pro analysis spreadsheet. Second, EES required input values of pressure and temperature for the properties calculated. Since both OFI and CHF experimentation required operation in a two-phase

flow regime, temperature and pressure were not independent during a portion of each experiment and, therefore, temperature had to be altered in order to determine the coolant properties. To this end, 0.5°C was subtracted from each data point during analysis.

EES Algorithm

```
viscosity=viscosity(WATER,T=T_corrected, P=P+101.325)
rho=density(WATER,T=T_corrected, P=P+101.325)
h=enthalpy(WATER,T=T_corrected, P=P+101.325)
k=conductivity(WATER,T=T_corrected, P=P+101.325)
cp=1000*specheat(WATER,T=T_corrected, P=P+101.325)
temp_sat=temperature(WATER,P=P+101.325, x=1)
T_corrected=temp-0.5
```

APPENDIX B

SUMMARY OF OFI EXPERIMENTAL DATA

The conditions corresponding to OFI for all experiments conducted by Blasick (1999) and in this investigation are tabulated in Tables B.1 and B.2, respectively. The non-condensable gas content, annular gap width, inlet temperature, sample standard deviation of the inlet temperature, exit pressure, OFI mass flux, average surface heat flux, and inner-to-outer surface heat flux ratio are given in Table B.1. Table B.2 includes this same information along with the sample standard deviation of the exit pressure.

Table B.1: OFI Experimental Data from Blasick (1999)

Non-Condensable Gas Content	Gap Width	T_{inlet}	$\sigma(T_{inlet})$	P_{exit} (absolute)	OFI Mass Flux	OFI Heat Flux	Inner-to-Outer Heat Flux Ratio
	(mm)	(°C)	(°C)	(kPa)	(kg/m ² s)	(MW/m ²)	
Air Saturated	1.001	50.0	0.063	345	356.54	0.2501	0
Air Saturated	1.001	50.2	0.040	348	323.98	0.2506	0.36
Air Saturated	1.001	50.5	0.065	346	319.11	0.2517	1
Air Saturated	1.001	50.0	0.051	346	189.11	0.1254	1
Air Saturated	1.001	49.5	0.060	346	155.41	0.1250	8.33
Air Saturated	1.001	49.6	0.110	694	233.73	0.2484	0
Air Saturated	1.001	51.1	0.101	686	222.72	0.2493	0.36
Air Saturated	1.001	50.3	0.143	690	248.12	0.2505	1
Air Saturated	1.001	49.6	0.094	689	108.42	0.1240	1
Air Saturated	1.001	49.1	0.118	693	92.80	0.1245	8.33
Air Saturated	1.001	50.2	0.232	1041	173.49	0.2510	0
Air Saturated	1.001	50.1	0.277	1035	166.25	0.2506	0.36
Air Saturated	1.001	49.6	0.031	1026	190.34	0.2495	1
Air Saturated	1.001	50.5	0.246	1031	219.16	0.3062	0
Air Saturated	1.001	49.8	0.065	1035	245.75	0.3083	0.28
Air Saturated	1.001	49.7	0.098	1037	227.68	0.3076	0.71
Air Saturated	1.001	49.1	0.052	1034	100.04	0.1254	1

Table B.1 (continued)

Non-Condensable Gas Content	Gap Width	T _{inlet}	σ(T _{inlet})	P _{exit} (absolute)	OFI Mass Flux	OFI Heat Flux	Inner-to-Outer Heat Flux Ratio
	(mm)	(°C)	(°C)	(kPa)	(kg/m ² s)	(MW/m ²)	
Air Saturated	1.001	49.3	0.040	1036	95.17	0.1242	8.33
Air Saturated	1.001	30.0	0.047	685	172.43	0.2512	0
Air Saturated	1.001	29.9	0.050	689	174.89	0.2496	0.36
Air Saturated	1.001	29.7	0.093	687	193.10	0.2505	1
Air Saturated	1.001	71.0	0.081	695	266.90	0.2500	0
Air Saturated	1.001	69.6	0.092	695	287.39	0.2499	0.36
Air Saturated	1.001	70.2	0.104	690	280.15	0.2490	1
Fully Degassed	1.001	51.9	0.122	342	339.39	0.2491	0
Fully Degassed	1.001	50.2	0.040	341	313.15	0.2498	0.36
Fully Degassed	1.001	49.8	0.077	357	303.58	0.2523	1
Fully Degassed	1.001	49.1	0.321	343	138.56	0.1241	1
Fully Degassed	1.001	49.1	0.093	356	142.20	0.1253	8.33
Fully Degassed	1.001	49.8	0.104	696	219.25	0.2485	0
Fully Degassed	1.001	49.9	0.245	730	232.50	0.2499	0.36
Fully Degassed	1.001	49.8	0.050	680	251.76	0.2518	1
Fully Degassed	1.001	49.2	0.054	728	104.82	0.1244	1
Fully Degassed	1.001	50.4	0.101	704	89.11	0.1251	8.33
Fully Degassed	1.001	49.0	0.053	1050	151.86	0.2495	0
Fully Degassed	1.001	49.8	0.052	1033	171.07	0.2509	0.36
Fully Degassed	1.001	49.7	0.082	1045	173.49	0.2505	1
Fully Degassed	1.001	49.2	0.075	1037	84.33	0.1251	1
Fully Degassed	1.001	48.9	0.121	1042	87.97	0.1247	8.33
Fully Degassed	1.001	30.9	0.104	701	178.45	0.2494	0
Fully Degassed	1.001	30.4	0.063	693	196.70	0.2502	0.36
Fully Degassed	1.001	30.0	0.045	677	204.03	0.2502	1
Fully Degassed	1.001	70.4	0.040	697	241.98	0.2498	0
Fully Degassed	1.001	70.9	0.306	697	278.84	0.2494	0.36
Fully Degassed	1.001	69.8	0.245	677	280.20	0.2508	1
Air Saturated	0.914	49.7	0.113	343	145.04	0.1309	Infinity
Air Saturated	0.914	49.0	0.065	344	269.25	0.2233	Infinity
Air Saturated	0.914	50.8	0.032	347	330.40	0.2717	Infinity
Air Saturated	0.914	50.1	0.047	344	467.68	0.3800	Infinity
Air Saturated	0.914	50.3	0.054	344	505.52	0.4300	Infinity
Air Saturated	0.914	49.5	0.000	344	158.13	0.1272	1
Air Saturated	0.914	49.2	0.040	685	137.24	0.1260	1
Air Saturated	0.914	49.5	0.214	1030	95.41	0.1286	1
Air Saturated	0.914	30.4	0.047	688	94.79	0.1258	1
Air Saturated	0.914	68.4	0.135	685	141.05	0.1261	1
Air Saturated	0.914	49.4	0.127	343	346.29	0.2492	1
Air Saturated	0.914	49.7	0.157	689	257.40	0.2508	1
Air Saturated	0.914	51.1	0.224	1028	186.73	0.2505	1
Air Saturated	0.914	29.9	0.047	688	209.43	0.2512	1
Air Saturated	0.914	67.9	0.101	680	315.88	0.2537	1
Air Saturated	0.914	50.1	0.054	349	523.84	0.3775	1
Air Saturated	0.914	49.7	0.052	684	204.81	0.3776	1
Air Saturated	0.914	50.2	0.070	1031	276.96	0.3748	1
Air Saturated	0.914	30.0	0.081	685	301.61	0.3812	1
Air Saturated	0.914	68.8	0.089	688	433.47	0.3780	1
Air Saturated	0.914	49.9	0.100	348	705.48	0.4980	1
Air Saturated	0.914	50.1	0.118	692	500.33	0.4980	1
Air Saturated	0.914	50.2	0.104	1037	368.37	0.5015	1
Air Saturated	0.914	29.9	0.079	699	399.06	0.5040	1
Air Saturated	0.914	69.3	0.168	691	561.53	0.5005	1
Air Saturated	0.914	50.5	0.052	341	791.51	0.6222	1
Air Saturated	0.914	49.8	0.060	349	607.54	0.6220	1
Air Saturated	0.914	49.3	0.098	346	837.67	0.6275	1

Table B.1 (continued)

Non-Condensable Gas Content	Gap Width	T _{inlet}	$\sigma(T_{inlet})$	P _{exit} (absolute)	OFI Mass Flux	OFI Heat Flux	Inner-to-Outer Heat Flux Ratio
	(mm)	(°C)	(°C)	(kPa)	(kg/m ² s)	(MW/m ²)	
Air Saturated	0.914	49.5	0.172	702	577.56	0.6259	1
Air Saturated	0.914	49.6	0.069	1036	423.33	0.6296	1
Air Saturated	0.914	29.2	0.067	687	501.95	0.6267	1
Air Saturated	0.914	65.6	0.113	690	587.22	0.6275	1
Air Saturated	0.914	49.8	0.082	342	926.33	0.7508	1
Air Saturated	0.914	49.3	0.081	701	701.76	0.7490	1
Air Saturated	0.914	49.8	0.138	1033	581.42	0.7472	1
Air Saturated	0.914	33.0	0.077	678	634.14	0.7506	1
Air Saturated	0.914	67.3	0.192	688	696.72	0.7428	1
Air Saturated	0.914	49.7	0.052	345	978.62	0.8768	1
Air Saturated	0.914	49.9	0.054	688	730.32	0.8756	1
Air Saturated	0.914	50.5	0.067	1020	623.01	0.8802	1
Air Saturated	0.914	38.0	0.089	682	726.13	0.8743	1
Air Saturated	0.914	69.9	0.172	692	859.89	0.8676	1
Air Saturated	0.760	48.3	0.215	343	145.27	0.1246	1
Air Saturated	0.760	47.1	0.681	691	83.30	0.1216	1
Air Saturated	0.760	46.5	0.385	1036	70.23	0.1225	1
Air Saturated	0.760	29.3	0.175	691	75.63	0.1192	1
Air Saturated	0.760	63.8	0.717	691	113.42	0.1260	1
Air Saturated	0.760	50.4	0.173	342	396.29	0.2518	1
Air Saturated	0.760	49.6	0.323	690	221.85	0.2526	1
Air Saturated	0.760	48.3	0.356	1035	169.74	0.2504	1
Air Saturated	0.760	29.4	0.069	689	189.11	0.2517	1
Air Saturated	0.760	67.7	0.269	689	315.19	0.2521	1
Air Saturated	0.760	48.2	0.246	341	579.52	0.3797	1
Air Saturated	0.760	49.8	0.077	693	419.22	0.3792	1
Air Saturated	0.760	49.5	0.077	1034	344.24	0.3767	1
Air Saturated	0.760	29.9	0.070	686	363.43	0.3778	1
Air Saturated	0.760	69.2	0.082	687	479.70	0.3782	1
Air Saturated	0.760	49.7	0.050	344	740.58	0.5049	1
Air Saturated	0.760	49.7	0.065	684	559.55	0.5053	1
Air Saturated	0.760	50.0	0.141	1033	477.92	0.5040	1
Air Saturated	0.760	30.1	0.060	689	488.38	0.5034	1
Air Saturated	0.760	68.7	0.163	689	599.36	0.5020	1
Air Saturated	0.760	50.2	0.050	346	932.90	0.6285	1
Air Saturated	0.760	49.8	0.079	684	690.02	0.6250	1
Air Saturated	0.760	49.9	0.054	1035	546.42	0.6267	1
Air Saturated	0.760	32.4	0.081	691	566.80	0.6251	1
Air Saturated	0.760	69.6	0.143	690	797.68	0.6289	1
Air Saturated	0.889	50.3	0.157	690	939.89	1.0102	1
Air Saturated	0.889	37.8	0.052	687	741.66	0.9957	1
Air Saturated	0.724	48.4	0.163	349	1082.51	0.7452	1
Air Saturated	0.724	50.4	0.090	692	827.53	0.7494	1
Air Saturated	0.724	49.1	0.138	1027	669.85	0.7431	1
Air Saturated	0.724	36.8	0.047	688	719.00	0.7369	1
Air Saturated	0.724	70.0	0.351	688	975.70	0.7473	1
Air Saturated	0.724	52.6	0.887	356	1428.26	0.8719	1
Air Saturated	0.724	51.1	0.047	693	978.64	0.8729	1
Air Saturated	0.724	49.5	0.110	1032	809.39	0.8692	1
Air Saturated	0.724	39.1	0.196	687	946.53	0.8725	1
Air Saturated	0.724	69.4	0.104	697	1134.30	0.8733	1
Air Saturated	0.724	-	-	-	-	-	1
Air Saturated	0.724	50.9	0.121	689	1024.11	0.9936	1
Air Saturated	0.724	51.0	0.141	1032	923.19	0.9995	1
Air Saturated	0.724	42.0	0.070	684	1063.58	0.9878	1
Air Saturated	0.724	71.5	0.223	692	1305.94	0.9941	1

Table B.2: OFI Experimental Data (Stoddard)

Non-Condensable Gas Content	Gap Width	T _{inlet}	σ(T _{inlet})	P _{exit} (absolute)	σ(P _{exit})	OFI Mass Flux	OFI Heat Flux	Inner-to-Outer Heat Flux Ratio
	(mm)	(°C)	(°C)	(kPa)	(kPa)	(kg/m ² s)	(MW/m ²)	
Air Saturated	0.940	49.3	0.054	696	1.700	89.92	0.4482	0
Air Saturated	0.940	52.4	0.045	788	1.214	135.33	0.5124	0
Air Saturated	0.940	53.2	0.172	690	2.378	203.55	0.7691	0
Air Saturated	0.940	56.5	0.270	683	3.448	285.25	1.0333	0
Air Saturated	0.940	48.9	0.145	690	0.982	89.95	0.4220	0
Air Saturated	0.940	47.8	0.100	700	2.676	115.33	0.5051	0
Air Saturated	0.940	52.0	0.129	710	3.885	183.40	0.7786	0
Air Saturated	0.940	50.9	0.258	707	5.108	239.21	1.0046	0
Air Saturated	0.940	49.7	0.140	716	2.857	222.88	0.3907	0
Air Saturated	0.940	49.8	0.067	705	8.438	286.18	0.5357	0
Air Saturated	0.940	51.0	0.615	697	3.012	442.95	0.7869	0
Air Saturated	0.940	52.2	0.205	676	2.386	622.31	1.0461	0
Air Saturated	0.940	51.1	0.276	693	7.846	690.84	1.2005	0
Air Saturated	0.940	43.3	0.067	687	2.844	354.31	0.4689	0
Air Saturated	0.940	50.8	0.054	688	1.849	568.29	0.7190	0
Air Saturated	0.940	49.2	0.135	685	1.640	785.26	0.9781	0
Air Saturated	0.940	43.6	0.298	691	3.075	539.66	0.7356	1
Air Saturated	0.940	53.2	0.573	339	1.059	874.78	0.7445	1
Air Saturated	0.940	50.8	0.294	1037	1.506	486.07	0.7328	1
Air Saturated	0.940	52.0	0.143	690	1.804	609.72	0.7452	1
Air Saturated	0.940	67.5	0.270	690	1.044	741.84	0.7220	1
Air Saturated	0.940	25.2	0.121	690	3.446	522.93	0.8130	1
Air Saturated	0.940	52.0	1.094	344	1.618	801.03	0.7074	1
Air Saturated	0.940	51.7	0.476	1034	1.027	-	-	1
Air Saturated	0.940	53.8	0.149	684	2.183	736.89	0.8182	1
Air Saturated	0.940	65.9	0.318	685	3.898	821.50	0.8121	1
Air Saturated	0.940	26.6	0.052	686	0.809	1350.83	1.8441	1
Air Saturated	0.940	45.2	0.490	745	3.722	869.17	1.1980	1
Air Saturated	0.940	53.2	0.241	361	3.833	1402.13	1.1974	1
Air Saturated	0.940	50.7	0.110	1035	2.730	779.70	1.1879	1
Air Saturated	0.940	51.0	0.162	689	6.008	907.41	1.2089	1
Air Saturated	0.940	65.9	0.140	695	2.296	-	-	1
Air Saturated	0.940	27.0	0.070	694	2.420	1.4815	1022.25	1
Air Saturated	0.940	45.3	0.490	363	3.430	1.4793	1475.87	1
Air Saturated	0.940	48.3	0.386	1019	4.989	1.4536	1101.23	1
Air Saturated	0.940	50.8	0.340	707	2.663	1.4478	1249.29	1
Air Saturated	0.940	63.2	0.217	708	5.143	1.4630	1377.32	1
Nitrogen Saturated	0.940	29.1	0.000	700	1.700	1.5039	1048.31	1
Nitrogen Saturated	0.940	59.4	0.121	692	2.490	1.2128	1085.26	1
Nitrogen Saturated	0.940	52.8	0.751	690	2.366	1.7037	1426.83	1
Nitrogen Saturated	0.940	59.7	0.370	688	3.027	1.6746	1633.30	1
Nitrogen Saturated	0.940	52.6	0.668	990	2.252	1.6689	1298.76	1
Nitrogen Saturated	0.940	47.2	0.070	991	4.143	0.9803	746.70	1
Nitrogen Saturated	0.940	45.6	0.291	449	2.697	1.6987	1663.18	1
Nitrogen Saturated	0.940	43.8	0.200	452	1.695	1.8165	1683.66	1
Nitrogen Saturated	0.940	30.0	0.122	699	6.113	0.8400	759.85	1
Nitrogen Saturated	0.762	46.1	0.114	701	7.346	0.8352	814.31	1
Nitrogen Saturated	0.762	62.3	0.104	698	3.197	0.8057	879.55	1
Nitrogen Saturated	0.762	64.0	0.291	698	2.867	0.9324	950.36	1
Nitrogen Saturated	0.762	51.3	0.518	697	3.270	0.9462	919.51	1
Nitrogen Saturated	0.762	30.5	0.163	699	2.014	0.9692	785.50	1
Nitrogen Saturated	0.762	47.2	0.140	1001	2.828	0.9533	815.52	1

Table B.2 (continued)

Non-Condensable Gas Content	Gap Width	T _{inlet}	σ(T _{inlet})	P _{exit} (absolute)	σ(P _{exit})	OFI Mass Flux	OFI Heat Flux	Inner-to-Outer Heat Flux Ratio
	(mm)	(°C)	(°C)	(kPa)	(kPa)	(kg/m ² s)	(MW/m ²)	
Nitrogen Saturated	0.762	49.8	0.050	997	2.892	0.8491	683.34	1
Nitrogen Saturated	0.762	28.9	0.083	698	4.309	1.2181	1019.99	1
Nitrogen Saturated	0.762	49.1	0.212	696	6.440	1.2185	1251.79	1
Nitrogen Saturated	0.762	64.2	0.189	696	6.857	1.2088	1499.75	1
Nitrogen Saturated	0.762	51.2	0.534	1002	7.846	1.1909	1030.09	1
Nitrogen Saturated	0.762	29.7	0.045	697	3.663	1.4607	1222.95	1
Nitrogen Saturated	0.762	49.3	0.205	698	0.701	1.4620	1407.01	1
Nitrogen Saturated	0.762	64.7	0.079	697	2.300	1.4527	1682.18	1
Nitrogen Saturated	0.762	48.9	0.344	990	3.503	1.4691	1259.97	1
Nitrogen Saturated	0.660	34.3	0.052	694	0.751	1.7302	2086.20	1
Nitrogen Saturated	0.660	50.0	0.070	691	0.809	1.7519	2251.86	1
Nitrogen Saturated	0.660	32.6	0.052	699	1.921	2.3419	2762.58	1
Nitrogen Saturated	0.660	47.8	0.070	699	0.632	2.4177	2897.07	1
Nitrogen Saturated	0.660	32.4	0.000	986	0.786	1.9925	2008.69	1

APPENDIX C

SUMMARY OF CHF EXPERIMENTAL DATA

The conditions corresponding to CHF for all experiments conducted in this investigation are tabulated in Table C.1. The non-condensable gas content, annular gap width, inlet temperature, sample standard deviation of the inlet temperature, exit pressure, sample standard deviation of the exit pressure, coolant mass flux, sample standard deviation of the coolant mass flux, observed critical heat flux, sample standard deviation of the critical heat flux, and the calculated exit quality are given in Table C.1.

Table C.1: CHF Experimental Data (Stoddard)

Non-Condensable Gas Content	Gap Width	T _{inlet}	$\sigma(T_{inlet})$	P _{exit} (absolute)	$\sigma(P_{exit})$	Mass Flux	$\sigma(G_{CHF})$	Heat Flux	$\sigma(q''_{CHF})$	x _{exit}
	(mm)	(°C)	(°C)	(kPa)	(kPa)	(kg/m ² s)	(kg/m ² s)	(MW/m ²)	(MW/m ²)	(%)
Nitrogen Saturated	0.660	30.1	0.231	690	7.055	207.74	15.66	0.4689	0.0067	34.5
Nitrogen Saturated	0.660	48.4	0.206	694	4.028	179.38	2.44	0.4409	0.0031	43.7
Nitrogen Saturated	0.660	65.1	0.797	688	2.801	187.34	1.39	0.4343	0.0002	43.2
Nitrogen Saturated	0.660	50.0	0.293	344	6.298	198.86	3.25	0.3940	0.0004	35.0
Nitrogen Saturated	0.660	50.2	0.360	1033	2.841	187.63	2.68	0.4986	0.0023	47.3
Nitrogen Saturated	0.660	30.0	0.055	689	2.749	106.28	2.91	0.3167	0.0004	54.3
Nitrogen Saturated	0.660	50.0	0.112	690	3.329	100.68	0.86	0.2625	0.0003	48.1
Nitrogen Saturated	0.660	64.5	0.125	692	5.188	99.19	1.31	0.2309	0.0010	43.4
Nitrogen Saturated	0.660	49.6	0.175	354	2.735	102.01	2.60	0.2392	0.0002	44.4
Nitrogen Saturated	0.660	50.1	0.071	1037	5.209	99.42	1.31	0.3606	0.0014	74.6
Nitrogen Saturated	0.660	31.8	1.882	695	5.856	291.15	12.81	0.7671	0.0024	45.1
Nitrogen Saturated	0.660	49.7	1.053	687	3.976	290.25	9.16	0.7668	0.0053	49.0
Nitrogen Saturated	0.660	65.8	1.476	690	2.728	293.57	4.95	0.5340	0.0021	29.7
Nitrogen Saturated	0.660	51.4	1.842	345	5.231	294.68	7.18	0.6209	0.0038	38.6
Nitrogen Saturated	0.660	49.2	1.171	1039	2.863	297.63	10.88	0.8004	0.0032	47.9
Nitrogen Saturated	0.660	29.8	0.042	692	2.838	151.16	3.34	0.3958	0.0012	44.3
Nitrogen Saturated	0.660	49.8	0.512	689	5.627	146.59	2.39	0.3383	0.0018	39.9
Nitrogen Saturated	0.660	65.3	0.467	691	3.405	150.97	5.09	0.3419	0.0018	41.8

Table C.1 (continued)

Non-Condensable Gas Content	Gap Width	T _{inlet}	σ(T _{inlet})	P _{exit} (absolute)	σ(P _{exit})	Mass Flux	σ(G _{CHF})	Heat Flux	σ(q'' _{CHF})	x _{exit}
	(mm)	(°C)	(°C)	(kPa)	(kPa)	(kg/m ² s)	(kg/m ² s)	(MW/m ²)	(MW/m ²)	(%)
Nitrogen Saturated	0.660	48.9	0.639	351	1.963	153.14	2.67	0.3031	0.0008	34.6
Nitrogen Saturated	0.660	50.1	0.149	1033	5.512	146.74	1.80	0.3961	0.0025	48.4
Nitrogen Saturated	0.660	30.6	1.213	694	2.611	248.22	9.33	0.6422	0.0016	43.6
Nitrogen Saturated	0.660	49.5	0.983	688	3.550	246.55	10.64	0.5818	0.0032	41.2
Nitrogen Saturated	0.660	65.6	1.356	689	3.001	241.67	3.78	0.5412	0.0030	41.2
Nitrogen Saturated	0.660	50.3	1.128	349	3.982	245.44	7.21	0.5302	0.0022	39.7
Nitrogen Saturated	0.660	49.4	0.341	1040	2.114	247.55	8.32	0.6867	0.0026	50.4
Nitrogen Saturated	0.660	31.4	2.441	700	4.769	338.46	11.92	0.8629	0.0036	42.7
Nitrogen Saturated	0.660	51.0	2.760	684	16.217	331.58	12.25	0.8348	0.0044	45.9
Nitrogen Saturated	0.660	63.9	1.732	710	8.564	328.99	11.36	0.7366	0.0046	40.6
Nitrogen Saturated	0.660	52.5	2.048	343	13.967	339.69	10.96	0.7716	0.0041	43.1
Nitrogen Saturated	0.660	49.8	1.866	1029	8.420	338.09	12.24	1.0142	0.0020	56.9
Nitrogen Saturated	0.660	32.2	2.988	705	7.200	375.14	11.95	1.0674	0.0022	50.9
Nitrogen Saturated	0.660	49.5	2.037	686	4.663	371.22	12.89	0.9253	0.0044	44.9
Nitrogen Saturated	0.660	61.9	3.070	717	12.812	366.80	13.73	0.7869	0.0016	37.6
Nitrogen Saturated	0.660	51.3	2.501	343	9.894	373.54	13.15	0.7786	0.0018	38.0
Nitrogen Saturated	0.660	49.2	1.537	1031	3.737	379.39	13.12	1.0686	0.0034	51.6

APPENDIX D

OFI ERROR ANALYSIS

This appendix presents an error analysis of the experimentally obtained OFI mass flux and OFI heat flux values for all experiments performed in this investigation. Blasick (1999) performed a similar analysis after which this examination is modeled.

D.1 Mass Flux Error Analysis

Mass flux can be calculated as a function of the coolant mass flowrate and the test section cross-sectional area.

$$G = \frac{\dot{m}}{A_{cs}} \quad (D.1)$$

Likewise, the variance of the coolant mass flux can be expressed by the following error propagation formula.

$$\sigma_G^2 = \left(\frac{\partial G}{\partial \dot{m}} \right)^2 \sigma_{\dot{m}}^2 + \left(\frac{\partial G}{\partial A_{cs}} \right)^2 \sigma_{A_{cs}}^2 \quad (D.2)$$

where

$$\frac{\partial G}{\partial \dot{m}} = \frac{1}{A_{cs}} \quad \text{and} \quad \frac{\partial G}{\partial A_{cs}} = -\frac{\dot{m}}{A_{cs}^2} \quad (\text{D.3})$$

Since the variance of the coolant mass flowrate and the test section cross-sectional area were not directly known, these quantities were expanded into known components until all variances were in terms of experimentally measured variables (i.e., volumetric flowrate, power, test section diameter, and test section length). In this analysis, the calculated variance (σ^2) and standard deviation (σ) values were considered with units, while the uncertainty values (u) were considered in percentage terms.

Mass flowrate (\dot{m}) was a function of the experimentally measured and controlled volumetric flowrate (\dot{V}) and the coolant density (ρ).

$$\dot{m} = \dot{V}\rho \quad (\text{D.4})$$

The variance of the mass flowrate can be expressed in the following manner.

$$\sigma_{\dot{m}}^2 = \left(\frac{\partial \dot{m}}{\partial \dot{V}} \right)^2 \sigma_{\dot{V}}^2 + \left(\frac{\partial \dot{m}}{\partial \rho} \right)^2 \sigma_{\rho}^2 \quad (\text{D.5})$$

The two partial derivatives in Equation D.5 have the following simplified form.

$$\frac{\partial \dot{m}}{\partial \dot{V}} = \rho \quad \text{and} \quad \frac{\partial \dot{m}}{\partial \rho} = \dot{V} \quad (\text{D.6})$$

The first partial derivative in Equations D.6 had to be multiplied by the variance of the volumetric flowrate. The variance of the single experimental volumetric flowrate at OFI, measured using an FT-8 liquid flow transducer manufactured by EG&G/FTI, was calculated as the sum of the squares of the individual bias errors and precision errors associated with the measurement. The four individual bias errors were:

1. The DAS voltage conversion error was calculated by determining the bit range over which the flow transducer was used. The calibration curve for the FT-8 flow transducer was:

$$gph = 4.224 \text{ gph} + 0.088135(mV_{EXP16}) \frac{\text{gph}}{\text{mV}_{EXP16}} \quad (\text{D.7})$$

- with EXP16 gain of unity. Since the gain was unity, the millivolt reading on the DAS-8 board was equivalent to the millivolt reading on the EXP16. The conversion from millivolts to bits was 2047 bits = 5000 millivolts, accurate to ± 1 bit. The operational flowrate range associated with this investigation was 10.1 \rightarrow 40.9 gph, which corresponded to a bit range of 28 \rightarrow 171 bits. Therefore, for the minimum flowrate of 10.1 gph, $u_{1-\text{Low}} = 1/28 = 0.0357 = 3.57\%$, and for the maximum flowrate of 40.9 gph, $u_{1-\text{High}} = 1/171 = 0.00585 = 0.585\%$.
2. The 20.2 liter jar used to calibrate the FT-8 flowmeter was accurate to 10 mL and, therefore, $u_2 = 0.010/20.2 = 0.000495 = 0.0495\%$.
 3. The stopwatch used during the FT-8 flowmeter calibration procedure was accurate to 0.001 seconds and the minimum time interval during calibration was 150.753 (2 minutes, 30.753 seconds) and, therefore, $u_3 = 0.001/150.753 = 0.00000663 = 0.000663\%$.
 4. The standard error associated with the linear regression calibration curve fit was 0.300158 gph. For the flowrate range mentioned above (10.1 \rightarrow 40.9 gph), $u_{4-\text{Low}} = 0.0297 = 2.97\%$ for the lowest flowrate and $u_{4-\text{High}} = 0.00734 = 0.734\%$ for the highest flowrate.

The only precision error encountered in this investigation with respect to the volumetric flowrate came directly from the method of choosing the OFI point visually from the plot of ΔP versus flowrate. As described in Section IV.7.2, the OFI point was chosen to be the flowrate (L/hr) associated with the smallest pressure drop (kPa) through the test section. Since this value was chosen visually by the operator, some precision error was unavoidable. In an attempt to quantify this precision error, a representative set of OFI data was fit with two separate quadratic formulas: a fourth order fit (Equation D.8) and a fifth order fit (Equation D.9).

$$\Delta P = 255.5 - 7.304\dot{V} + 8.071 \times 10^{-2} \dot{V}^2 - 3.646 \times 10^{-4} \dot{V}^3 + 6.248 \times 10^{-7} \dot{V}^4 \quad (\text{D.8})$$

$$\Delta P = 766.2 - 28.36\dot{V} + 0.4176\dot{V}^2 - 2.979 \times 10^{-3} \dot{V}^3 + 1.049 \times 10^{-5} \dot{V}^4 - 1.449 \times 10^{-8} \dot{V}^5 \quad (\text{D.9})$$

A plot of the representative data set (Setup 5 with nominal conditions 1.5 MW/m² heat flux, 30°C inlet temperature, 689 kPa exit pressure) is located in Figure D.1 along with the two quadratic curve fits.

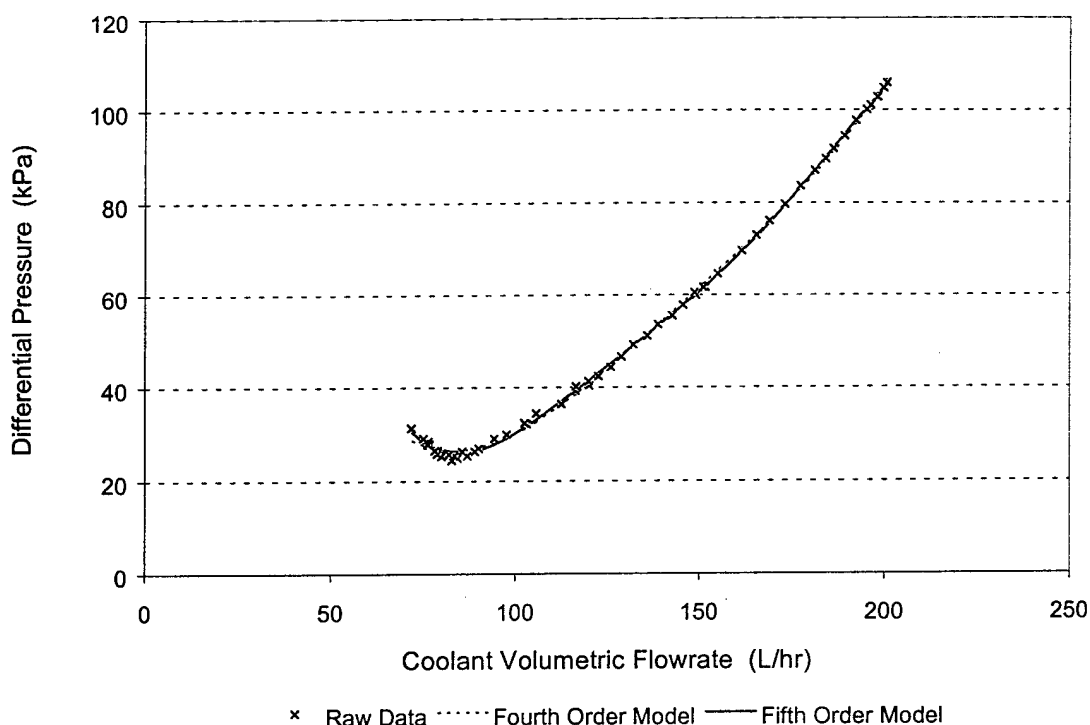


Figure D.1: OFI Plot with Fourth and Fifth Order Quadratic Fits

Obviously, both quadratic equations fit the data well. By taking the first derivative of each quadratic equation with respect to the volumetric flowrate and setting it equal to zero, the flowrate value associated with the minimum ΔP was easily calculated. For the fourth and fifth order fits, the respective coolant volumetric flowrates were 83.4 and 84.4 L/hr for the minimum differential pressures. These values compare favorably to the visually chosen OFI volumetric flowrate of 80.0 L/hr, which corresponds to a G_{OFI} value of 1022.2 kg/m²s (Table B.2). Since the fifth order fit shows the most discrepancy from the reported value, its value of coolant volumetric flowrate was used to calculate the precision error associated with determining the volumetric flowrate at OFI, therefore,

$$u_5 = \frac{84.4 - 80.0}{80.0} = 0.055 = 5.50\%.$$

By summing the squares of the four bias errors and the single precision error associated with the volumetric flowrate measurement at OFI, the error estimate for the volumetric flowrate at OFI was found.

Table D.1: Summary of Volumetric Flowrate Uncertainties at OFI

	Error Type	Uncertainty (@ 10.1 gph)	Uncertainty ² (@ 10.1 gph)	Uncertainty (@ 40.9 gph)	Uncertainty ² (@ 40.9 gph)
u ₁	Bias	3.57 %	1.274 E -3	0.585 %	3.422 E -5
u ₂	Bias	0.0495 %	2.450 E -7	0.0495 %	2.450 E -7
u ₃	Bias	0.000663 %	4.396 E -11	0.000663 %	4.396 E -11
u ₄	Bias	2.97 %	8.821 E -4	0.734 %	5.388 E -5
u ₅	Precision	5.50 %	3.025 E -3	5.50 %	3.025 E -3
Sum	--	--	5.181 E -3	--	3.113 E -3

Using this analysis procedure, the error was 7.20 % or 0.727 gph at the lower end of the operational flowrate range and 5.58 % or 2.28 gph at the higher end of the operational flowrate range. For analysis purposes, the volumetric flowrate error estimate was 7.20 % or 2.28 gph, whichever was smaller for the volumetric flowrate value in question. Basically, this means that the 7.20 % error value was applied to the lower end of the operational flowrate range, while the 2.28 gph error value was applied to the higher end of the operational flowrate range.

The second partial derivative in Equations D.6 had to be multiplied by the variance of the coolant density. The precision error associated with the coolant density came from the standard deviation of the inlet temperature to the test section during an

OFI experiment. The maximum inlet temperature standard deviation encountered over all OFI experiments was 1.094°C (from Table B.2), which occurred on an experiment that had an average inlet temperature of 52.0°C and an average absolute inlet pressure of 386.8 kPa. This inlet temperature standard deviation thus created a range of possible inlet densities: 986.6 → 987.7 kg/m³. The density value obtained when the average values of temperature and pressure were used was 987.2 kg/m³. Thus, the representative deviation in density from the reported value for all OFI experiments was 0.6 kg/m³, which corresponded to a $u_{\rho-1}$ of 0.000608 or 0.0608 %. This value came from the standard deviation of the inlet temperature, which depended on the bias error of the inlet thermocouple ($\pm 0.1^\circ\text{C}$). The lowest inlet temperature encountered during all OFI experiments was 25.2°C, which produced a $u_{\rho-2}$ of 0.00397 or 0.397 %. By combining these two terms as shown in Equation D.10, the final value of u_ρ was 0.00402 or 0.402 %, which means that the standard deviation of the inlet temperature contributes very little to the error associated with the coolant density at the test section inlet.

$$u_\rho = \sqrt{u_{\rho-1}^2 + u_{\rho-2}^2} = 0.00402 \quad (\text{D.10})$$

Referring to Equation D.5, all values were known at this point such that the variance of the coolant mass flowrate could be determined. Since the value of importance to this investigation was coolant mass flux, the variance of the test section cross sectional area had to be determined for the error analysis to be complete, as shown in Equation D.2. The cross sectional area or flow area of the test section is a function of the inner diameter of the outer heater (outer wall of the annulus) and the outer diameter of

the inner heater (inner wall of the annulus).

$$A_{cs} = \frac{\pi}{4} (D_{out}^2 - D_{in}^2) \quad (D.11)$$

The variance of the test section cross sectional area can be expressed in the following manner.

$$\sigma_{A_{cs}}^2 = \left(\frac{\partial A_{cs}}{\partial D_{out}} \right)^2 \sigma_{D_{out}}^2 + \left(\frac{\partial A_{cs}}{\partial D_{in}} \right)^2 \sigma_{D_{in}}^2 \quad (D.12)$$

where:

$$\frac{\partial A_{cs}}{\partial D_{out}} = \frac{\pi}{2} D_{out} \quad \text{and} \quad \frac{\partial A_{cs}}{\partial D_{in}} = -\frac{\pi}{2} D_{in} \quad (D.13)$$

The outer diameter (inner diameter of the outer heater) was measured using both precision ground pins and a Starrett dial caliper. The tolerance of the caliper was known to be $\sigma_{D_{out}} = 0.001 \text{ inch} = 0.0254 \text{ mm}$, which created a maximum bias uncertainty estimate of $u_{D_{out}} = 0.001/0.304 = 0.00329 = 0.329 \%$ for the smallest diameter outer heater used (Outer Heaters I, J, and K). This tolerance was used instead of the tolerance of the pins to provide a more conservative estimate of the error associated with the cross sectional area of the test section. The inner diameter (outer diameter of the inner heater) was also measured using a Starrett dial caliper ($\sigma_{D_{in}} = 0.001 \text{ inch} = 0.0254 \text{ mm}$). All inner heaters were constructed of tubing that had been manufactured with a nominal outer diameter of 0.250 inch; thus, all inner heaters had roughly the same diameter. During construction, all inner heaters were found to have diameters slightly larger than 0.250 inch, but 0.250 inch was utilized in this error analysis to maintain a conservative

estimate. The bias uncertainty estimate of the inner diameter was found to be $u_{D_{in}} = 0.001/0.250 = 0.00400 = 0.400 \%$.

Finally, combining Equations D.2 through D.13 yielded the following estimate of the coolant mass flux variance.

$$\sigma_G^2 = \left(\frac{1}{A_{cs}} \right)^2 [\rho^2 \sigma_{\dot{V}}^2 + \dot{V}^2 \sigma_{\rho}^2] + \left(\frac{-\dot{m}}{A_{cs}^2} \right)^2 \left[\left(\frac{\pi}{2} D_{out} \right)^2 \sigma_{D_{out}}^2 + \left(-\frac{\pi}{2} D_{in} \right)^2 \sigma_{D_{in}}^2 \right] \quad (D.14)$$

By applying this formula along with the appropriate error estimates from Table D.2 to the set of experiments performed in this investigation, the average uncertainty in mass flux was calculated to be 7.46 %. Note that the σ values for coolant volumetric flowrate in Table D.2 are given in terms of both gph and percentage since the error estimate of the flowrate in question depends on the magnitude of the flowrate. The mass flux error analysis results for the data with heat flux ratio of unity are listed in Table D.3

Table D.2: Summary of Coolant Mass Flux Error Sources at OFI

$\sigma_{\dot{V}}$	u_{ρ}	$\sigma_{D_{out}}$	$\sigma_{D_{in}}$
7.20 % or 2.28 gph	0.402 %	0.0254 mm	0.0254 mm

Table D.3: OFI Coolant Mass Flux Error Analysis Results

Sigma(Vol. Flow):		2.40E-06		(m^3/sec)	
or		7.20		(%)	
Sigma(Density):		0.402		(%)	
Sigma(D_out):		2.54E-05		(m)	
Sigma(D_in):		2.54E-05		(m)	

Setup	Run	Inlet Density @OFI (kg/m^3)	Inlet Density sigma (kg/m^3)	Vol Flowrate @OFI (m^3/sec)	Vol Flowrate sigma (m^3/sec)	Mass Flowrate (kg/s)	Inner Diameter (mm)	Outer Diameter (mm)	A_cs (m^2)	G(ofi) (kg/m^2 s)	Sigma_G (kg/m^2 s)	Uncertainty_G (%)
5	6	991	3.98	1.18E-05	8.50E-07	0.0117	6.401	8.280	2.167E-05	539.66	40.30	7.47
5	7	987	3.97	1.92E-05	1.38E-06	0.0190	6.401	8.280	2.167E-05	874.78	65.32	7.47
5	8	988	3.97	1.07E-05	7.68E-07	0.0105	6.401	8.280	2.167E-05	486.07	36.30	7.47
5	9	987	3.97	1.34E-05	9.64E-07	0.0132	6.401	8.280	2.167E-05	609.72	45.53	7.47
5	10	980	3.94	1.64E-05	1.18E-06	0.0161	6.401	8.280	2.167E-05	741.84	55.40	7.47
5	11	998	4.01	1.14E-05	8.18E-07	0.0113	6.401	8.280	2.167E-05	522.93	39.05	7.47
5	12	988	3.97	1.76E-05	1.27E-06	0.0174	6.401	8.280	2.167E-05	801.03	59.82	7.47
5	13	989	3.97	--	--	--	6.401	8.280	2.167E-05	--	--	--
5	14	987	3.97	1.62E-05	1.17E-06	0.0160	6.401	8.280	2.167E-05	736.89	55.03	7.47
5	15	980	3.94	1.82E-05	1.31E-06	0.0178	6.401	8.280	2.167E-05	821.50	61.34	7.47
5	16	998	4.01	2.94E-05	2.11E-06	0.0293	6.401	8.280	2.167E-05	1350.83	100.87	7.47
5	20	990	3.98	1.90E-05	1.37E-06	0.0188	6.401	8.280	2.167E-05	869.17	64.90	7.47
5	21	987	3.97	3.08E-05	2.22E-06	0.0304	6.401	8.280	2.167E-05	1402.13	104.70	7.47
5	22	988	3.97	1.71E-05	1.23E-06	0.0169	6.401	8.280	2.167E-05	779.70	58.22	7.47
5	23	988	3.97	1.99E-05	1.43E-06	0.0197	6.401	8.280	2.167E-05	907.41	67.76	7.47
5	24	980	3.97	--	--	--	6.401	8.280	2.167E-05	--	--	--
5	25	997	4.01	2.22E-05	1.60E-06	0.0222	6.401	8.280	2.167E-05	1022.25	76.34	7.47
5	26	991	3.98	3.23E-05	2.33E-06	0.0320	6.401	8.280	2.167E-05	1475.87	110.21	7.47
5	27	989	3.98	2.41E-05	1.74E-06	0.0239	6.401	8.280	2.167E-05	1101.23	82.23	7.47
5	28	988	3.97	2.74E-05	1.97E-06	0.0271	6.401	8.280	2.167E-05	1249.29	93.29	7.47
5	29	982	3.95	3.04E-05	2.19E-06	0.0299	6.401	8.280	2.167E-05	1377.32	102.85	7.47
5	30	997	4.01	2.28E-05	1.64E-06	0.0227	6.401	8.280	2.167E-05	1048.31	78.28	7.47
6	32	984	3.96	2.39E-05	1.72E-06	0.0235	6.401	8.280	2.167E-05	1085.26	81.04	7.47
6	33	987	3.97	3.13E-05	2.26E-06	0.0309	6.401	8.280	2.167E-05	1426.83	106.55	7.47

Table D.3 (continued)

Setup	Run	Inlet Density @OFI (kg/m ³)	Inlet Density sigma (kg/m ³)	Vol Flowrate @OFI (m ³ /sec)	Vol Flowrate sigma (m ³ /sec)	Mass Flowrate (kg/s)	Inner Diameter (mm)	Outer Diameter (mm)	A_cs (m ²)	G(ofi) (kg/m ² s)	Sigma_G (kg/m ² s)	Uncertainty_G (%)
6	34	984	3.95	3.60E-05	2.40E-06	0.0354	6.401	8.280	2.167E-05	1633.30	113.47	6.95
6	35	987	3.97	3.13E-05	2.26E-06	0.0309	6.401	8.280	2.167E-05	1298.76	106.55	8.20
6	36	990	3.98	1.64E-05	1.18E-06	0.0162	6.401	8.280	2.167E-05	746.70	55.76	7.47
6	37	990	3.98	3.64E-05	2.40E-06	0.0361	6.401	8.280	2.167E-05	1663.18	114.33	6.87
6	39	991	3.98	3.68E-05	2.40E-06	0.0365	6.401	8.280	2.167E-05	1683.66	114.54	6.80
8	1	996	4.01	1.31E-05	9.42E-07	0.0130	6.401	7.925	1.715E-05	759.85	57.71	7.59
8	2	990	3.98	1.41E-05	1.02E-06	0.0140	6.401	7.925	1.715E-05	814.31	61.85	7.59
9	3	982	3.95	1.54E-05	1.11E-06	0.0151	6.401	7.925	1.715E-05	879.55	66.80	7.59
9	4	982	3.95	1.66E-05	1.20E-06	0.0163	6.401	7.925	1.715E-05	950.36	72.18	7.59
9	5	988	3.97	1.60E-05	1.15E-06	0.0158	6.401	7.925	1.715E-05	919.51	69.84	7.59
9	6	996	4.00	1.35E-05	9.74E-07	0.0135	6.401	7.925	1.715E-05	785.50	59.66	7.59
9	7	990	3.98	1.41E-05	1.02E-06	0.0140	6.401	7.925	1.715E-05	815.52	61.94	7.59
9	8	988	3.97	1.19E-05	8.54E-07	0.0117	6.401	7.925	1.715E-05	683.34	51.90	7.59
9	9	997	4.01	1.76E-05	1.26E-06	0.0175	6.401	7.925	1.715E-05	1019.99	77.47	7.59
9	10	989	3.97	2.17E-05	1.56E-06	0.0215	6.401	7.925	1.715E-05	1251.79	95.07	7.59
9	11	981	3.94	2.62E-05	1.89E-06	0.0257	6.401	7.925	1.715E-05	1499.75	113.90	7.59
9	12	988	3.97	1.79E-05	1.29E-06	0.0177	6.401	7.925	1.715E-05	1030.09	78.23	7.59
9	13	996	4.01	2.11E-05	1.52E-06	0.0210	6.401	7.925	1.715E-05	1222.95	92.88	7.59
9	14	989	3.97	2.44E-05	1.76E-06	0.0241	6.401	7.925	1.715E-05	1407.01	106.86	7.59
9	15	981	3.94	2.94E-05	2.12E-06	0.0289	6.401	7.925	1.715E-05	1682.18	127.76	7.59
9	16	989	3.97	2.19E-05	1.57E-06	0.0216	6.401	7.925	1.715E-05	1259.97	95.69	7.59
11	1	995	4.00	3.08E-05	2.22E-06	0.0307	6.401	7.722	1.465E-05	2086.20	161.45	7.74
11	2	988	3.97	3.35E-05	2.40E-06	0.0331	6.401	7.722	1.465E-05	2251.86	173.35	7.70
12	4	995	4.00	4.08E-05	2.40E-06	0.0406	6.401	7.722	1.465E-05	2762.58	179.98	6.51
12	5	989	3.98	4.31E-05	2.40E-06	0.0426	6.401	7.722	1.465E-05	2897.07	180.70	6.24
12	6	995	4.00	2.97E-05	2.14E-06	0.0295	6.401	7.722	1.465E-05	2008.69	155.45	7.74

D.2 Heat Flux Error Analysis

Heat flux can be calculated as a function of the power applied to the test section and the test section heated area.

$$Q'' = \frac{Q_{total}}{A_s} = \frac{Q_{in} + Q_{out}}{A_s} \quad (D.15)$$

The variance of the surface heat flux can be expressed by the following error propagation formula.

$$\sigma_{Q''}^2 = \left(\frac{\partial Q''}{\partial Q_{in}} \right)^2 \sigma_{Q_{in}}^2 + \left(\frac{\partial Q''}{\partial Q_{out}} \right)^2 \sigma_{Q_{out}}^2 + \left(\frac{\partial Q''}{\partial A_s} \right)^2 \sigma_{A_s}^2 \quad (D.16)$$

where

$$\frac{\partial Q''}{\partial Q_{in}} = \frac{\partial Q''}{\partial Q_{out}} = \frac{1}{A_s} \quad \text{and} \quad \frac{\partial Q''}{\partial A_s} = -\frac{(Q_{in} + Q_{out})}{A_s^2} = -\frac{Q_{total}}{A_s^2} \quad (D.17)$$

The variance of the inner and outer heater power levels at OFI was calculated as the sum of the squares of the individual bias errors and precision errors associated with the measurement. The first 61 OFI experiments utilized an AC wattmeter manufactured by Ohio Semitronics with an external Omega AC current transducer (Components 15 of Table 3.3) to measure the power supplied to the outer heater, while the inner heater power was measured using an Ohio Semitronics DC wattmeter (Component 16 of Table 3.3). The final five OFI experiments measured the inner and outer heater power levels using redundant sensors. Since only the total power level reading supplied by the Ohio Semitronics DC wattmeter (Component 16 of Table 3.3) was used for analysis of these

last five OFI experiments, only the tolerances of this wattmeter were considered in this error analysis.

During the first 61 OFI experiments, there were three individual bias errors and no precision errors that contributed to the variance of the outer heater power:

1. The manufacturer stated accuracy of the Ohio Semitronics AC wattmeter was $\pm 0.2\%$ of the power reading, thus $u_1 = 0.002 = 0.2\%$.
2. The manufacturer stated accuracy of the external Omega AC current transducer was $\pm 1.5\%$, thus $u_2 = 0.015 = 1.5\%$.
3. The DAS voltage conversion error was calculated by determining the bit range over which the wattmeter was used. The calibration curve for the wattmeter was:

$$Power (W) = -2.31 W + 6.4097(mV_{EXP16}) \frac{W}{mV_{EXP16}} \quad (D.18)$$

with EXP16 gain of unity. Since the gain was unity, the millivolt reading on the DAS-8 board was the same as on the EXP16 board. The conversion from millivolts to bits was $2047 \text{ bits} = 5000 \text{ mV}$, accurate to ± 1 bit. The outer heater power over the first 61 OFI experiments ranged from a minimum of 1230 W to a maximum of 9311 W , which converted to a range of $80 \rightarrow 596$ bits. Therefore, for the 1230 W power level, $u_{3-Low} = 1/80 = 0.0125 = 1.25\%$ and for the 9311 W power level, $u_{3-High} = 1/596 = 0.00168 = 0.168\%$.

By summing the squares of the three individual bias errors associated with the outer heater power measurement at OFI, the error estimate for the outer heater power for

the first 61 OFI experiments was found.

Table D.4: Summary of Outer Heater Power Uncertainties at OFI (first 61 experiments)

	Error Type	Uncertainty (@ 1230 W)	Uncertainty ² (@ 1230 W)	Uncertainty (@ 9311 W)	Uncertainty ² (@ 9311 W)
u_1	Bias	0.2 %	4.00 E -6	0.2 %	4.00 E -6
u_2	Bias	1.5 %	2.25 E -4	1.5 %	2.25 E -4
u_3	Bias	1.25 %	1.56 E -4	0.168 %	2.82 E -6
Sum	--	--	3.85 E -4	--	2.32 E -4

Using this analysis procedure, the error was 1.96 % or 24.1 W at the lower end of the operational power range and 1.52 % or 141.5 W at the higher end of the operational power range. For analysis purposes, the outer heater power error estimate was 1.96 % or 141.5 W, whichever was smaller for the outer heater power value in question. Basically, this means that the 1.96 % error value was applied to the lower end of the operational power range, while the 141.5 W error value was applied to the higher end of the operational power range.

During the first 61 OFI experiments, there were two individual bias errors that contributed to the variance of the inner heater power measurement:

1. The manufacturer stated accuracy of the Ohio Semitronics DC wattmeter was ± 1.0 % of the power reading, thus $u_1 = 0.01 = 1.0$ %.
2. The DAS voltage conversion error was calculated by determining the bit range over which the wattmeter was used. The calibration curve for this DC wattmeter was the same as that of the AC wattmeter used on the outer heater:

$$Power (W) = -2.31 W + 6.4097(mV_{EXP16}) \frac{W}{mV_{EXP16}} \quad (D.19)$$

with EXP16 gain of unity. Since the gain was unity, the millivolt reading on the DAS-8 board was the same as on the EXP16 board. The conversion from millivolts to bits was 2047 bits = 5000 mV, accurate to ± 1 bit. The inner heater power over the first 61 OFI experiments ranged from a minimum of 3134 W to a maximum of 7637 W, which converted to a range of 201 \rightarrow 489 bits. Therefore, for the 3134 W power level, $u_{2-Low} = 1/201 = 0.00498 = 0.498 \%$ and for the 7637 W power level, $u_{2-High} = 1/489 = 0.00204 = 0.204 \%$.

By summing the squares of the two individual bias errors associated with the inner heater power measurement at OFI, the error estimate for the inner heater power for the first 61 OFI experiments was found.

Table D.5: Summary of Inner Heater Power Uncertainties at OFI (first 61 experiments)

	Error Type	Uncertainty (@ 3134 W)	Uncertainty ² (@ 3134 W)	Uncertainty (@ 7637 W)	Uncertainty ² (@ 7637 W)
u_1	Bias	1.0 %	1.000 E -4	1.0 %	1.000 E -4
u_2	Bias	0.498 %	2.480 E -5	0.204 %	4.162 E -6
Sum	--	--	1.248 E -4	--	1.041 E -4

Using this analysis procedure, the error was 1.12 % or 35.1 W at the lower end of the operational power range and 1.02 % or 77.9 W at the higher end of the operational power range. For analysis purposes, the outer heater power error estimate was 1.12 % or 77.9 W, whichever was smaller for the inner heater power value in question. Basically,

this means that the 1.12 % error value was applied to the lower end of the operational power range, while the 77.9 W error value was applied to the higher end of the operational power range.

For the final five OFI experiments, the power supplied to the test section was determined using an energy balance and the total amount of power supplied by the DC power supply as described in Section IV.7.2. Errors in the energy balance heat loss estimation were discussed independently in Section IV.7.2, however, the error associated with the measurement of the total power output from the power supply had to be quantified. This power level was measured using the Ohio Semitronics DC wattmeter (Component 16 of Table 3.3) mentioned earlier. During the final five OFI experiments, there were two individual bias errors that contributed to the uncertainty of the total power reading:

1. The manufacturer stated accuracy of the Ohio Semitronics DC wattmeter was ± 1.0 % of the power reading, thus $u_1 = 0.01 = 1.0$ %.
2. The DAS voltage conversion error was calculated by determining the bit range over which the wattmeter was used. The calibration curve for this DC wattmeter was the same as stated above:

$$Power (W) = -2.31 W + 6.4097(mV_{EXP16}) \frac{W}{mV_{EXP16}} \quad (D.20)$$

with EXP16 gain of unity. Since the gain was unity, the millivolt reading on the DAS-8 board was the same as on the EXP16 board. The conversion from millivolts to bits was 2047 bits = 5000 mV, accurate to ± 1 bit. The total power

level over the final five OFI experiments ranged from a minimum of 14041 W to a maximum of 20160 W, which converted to a range of 897 → 1288 bits. Therefore, for the 14041 W power level, $u_{2-Low} = 1/897 = 0.00111 = 0.111 \%$ and for the 20160 W power level, $u_{2-High} = 1/1288 = 0.000776 = 0.0776 \%$.

By summing the squares of the two individual bias errors associated with the total power measurement at OFI, the error estimate for the inner heater power for the last five OFI experiments was found.

Table D.6: Summary of Total Power Level Uncertainties at OFI (last five experiments)

	Error Type	Uncertainty (@ 14041 W)	Uncertainty ² (@ 14041 W)	Uncertainty (@ 20160 W)	Uncertainty ² (@ 20160 W)
u_1	Bias	1.0 %	1.000 E -4	1.0 %	1.000 E -4
u_2	Bias	0.111 %	1.232 E -6	0.0776 %	6.022 E -7
Sum	--	--	1.012 E -4	--	1.006 E -4

Using this analysis procedure, the error was 1.01 % or 141.8 W at the lower end of the operational power range and 1.00 % or 201.6 W at the higher end of the operational power range. For analysis purposes, the total power error estimate was 1.01 % or 201.6 W, whichever was smaller for the total power value in question. Basically, this means that the 1.01 % error value was applied to the lower end of the operational power range, while the 201.6 W error value was applied to the higher end of the operational power range.

The test section heated surface area was a function of the inner diameter of the

annulus, outer diameter of the annulus, inner heater heated length, and outer heater heated length.

$$A_s = \pi(L_{heated,out}D_{out} + L_{heated,in}D_{in}) \quad (D.21)$$

The variance of the test section heated surface area can be expressed in the following manner.

$$\sigma_{A_s}^2 = \left(\frac{\partial A_s}{\partial D_{out}}\right)^2 \sigma_{D_{out}}^2 + \left(\frac{\partial A_s}{\partial D_{in}}\right)^2 \sigma_{D_{in}}^2 + \left(\frac{\partial A_s}{\partial L_{h,out}}\right)^2 \sigma_{L_{h,out}}^2 + \left(\frac{\partial A_s}{\partial L_{h,in}}\right)^2 \sigma_{L_{h,in}}^2 \quad (D.22)$$

where

$$\frac{\partial A_s}{\partial D_{out}} = \pi L_{h,out} \quad \text{and} \quad \frac{\partial A_s}{\partial D_{in}} = \pi L_{h,in} \quad (D.23)$$

$$\frac{\partial A_s}{\partial L_{h,out}} = \pi D_{out} \quad \text{and} \quad \frac{\partial A_s}{\partial L_{h,in}} = \pi D_{in}$$

As stated earlier, the relevant annulus diameters were measured using a Starrett dial caliper, which had a known tolerance of $\sigma = 0.001$ inch. The heated lengths of all test sections were measured using Fowler vernier calipers, also with a known tolerance of $\sigma = 0.001$ inch.

Finally, combining Equations D.16 through D.23 yielded the following estimate of the surface heat flux variance:

$$\sigma_{Q''}^2 = \left(\frac{1}{A_s}\right)^2 [\sigma_{Q_{in}}^2 + \sigma_{Q_{out}}^2] + \left(\frac{-Q_{total}}{A_s^2}\right)^2 [(\pi L_{h,out})^2 \sigma_{D_{out}}^2 + (\pi L_{h,in})^2 \sigma_{D_{in}}^2 + (\pi D_{out})^2 \sigma_{L_{h,out}}^2 + (\pi D_{in})^2 \sigma_{L_{h,in}}^2] \quad (D.24)$$

By applying this formula along with the appropriate error estimates from Table D.7 to the set of experiments performed in this investigation, the average uncertainty in heat flux was calculated to be 1.25 %. Note that the σ values for all power error estimates in Table D.7 are given in terms of both Watts and percentage since the error estimate of the power level in question depends on the magnitude of the power measurement.

Table D.7: Summary of Heat Flux Uncertainties at OFI

$\sigma_{Q_{in}}$ (first 61)	$\sigma_{Q_{out}}$ (first 61)	$\sigma_{Q_{total}}$ (last 5)	$\sigma_{D_{out}}$	$\sigma_{D_{in}}$	$\sigma_{L_{h,out}}$	$\sigma_{L_{h,in}}$
1.96 % or 141.5 W	1.12 % or 77.9 W	1.01 % or 201.6 W	0.0254 mm	0.0254 mm	0.0254 mm	0.0254 mm

The outline below shows a sample error estimate for an OFI experiment that had the following experimentally measured parameters: $D_{out} = 7.925$ mm, $D_{in} = 6.401$ mm, $L_{h, out} = 180$ mm, $L_{h, in} = 180$ mm, $Q_{in} = 5424$ W, and $Q_{out} = 6651$ W, with an environmental power loss of 1.4 %. The heat flux error analysis results for the data with heat flux ratio of unity are listed in Table D.8

Measurement	Uncertainty	Influence Coefficient, $\left(\frac{\partial q''}{\partial x_i}\right)$	(Uncertainty) ²	Basis
Inner Heater Power	1.96 % = 106.3 W	$\frac{1}{\pi (D_{out} L_{h,out} + D_{in} L_{in})}$ = 123.4 (1/m ²)	1.72 E -4 (MW/m ²) ²	Resolution
Outer Heater Power	1.12 % = 74.5 W	$\frac{1}{\pi (D_{out} L_{h,out} + D_{in} L_{in})}$ = 123.4 (1/m ²)	8.45 E -5 (MW/m ²) ²	Resolution
Outer Diameter	0.0254 mm	$\frac{-\dot{Q}_{total} L_{out}}{\pi (D_{out} L_{out} + D_{in} L_{in})^2}$ = -102.6 (MW/m ³)	6.79 E -6 (MW/m ²) ²	Measurement
Inner Diameter	0.0254 mm	$\frac{-\dot{Q}_{total} L_{in}}{\pi (D_{out} L_{out} + D_{in} L_{in})^2}$ = -102.6 (MW/m ³)	6.79 E -6 (MW/m ²) ²	Measurement
Outer L _h	0.0254 mm	$\frac{-\dot{Q}_{total} D_{out}}{\pi (D_{out} L_{out} + D_{in} L_{in})^2}$ = -4.52 (MW/m ³)	1.32 E -8 (MW/m ²) ²	Measurement
Inner L _h	0.0254 mm	$\frac{-\dot{Q}_{total} D_{in}}{\pi (D_{out} L_{out} + D_{in} L_{in})^2}$ = -3.65 (MW/m ³)	8.60 E -9 (MW/m ²) ²	Measurement
		Sum of Variances =	2.70 E -4 (MW/m ²) ²	
		Uncertainty =	0.0164 MW/m ² = 1.12 %	

Table D.8: OFI Surface Heat Flux Error Analysis Results

		Sigma(L_h, out): 2.54E-05 (m)																			
		Sigma(L_h, in): 2.54E-05 (m)																			
		Sigma(D_out): 2.54E-05 (m)																			
		Sigma(D_in): 2.54E-05 (m)																			
Setup	Run	Inner Power (W)	Q_inner sigma (W)	Outer Power (W)	Q_outer sigma (W)	Power Loss Environment (%)	Total Power (W)	Q_total sigma (W)	Inner Diameter (mm)	Inner L_heated (mm)	Outer Diameter (mm)	Outer L_heated (mm)	A_s (m^2)	Q''(ofi) (MW/m^2)	Sigma_Q'' (MW/m^2)	Uncertainty_Q'' (%)					
5	6	3338	65	4010	45	14.4	6290	--	6.401	190	8.280	180	8.503E-03	0.7356	9.51E-03	1.29					
5	7	3345	66	3995	45	13.2	6371	--	6.401	190	8.280	180	8.503E-03	0.7445	9.51E-03	1.28					
5	8	3331	65	3961	44	14.0	6271	--	6.401	190	8.280	180	8.503E-03	0.7328	9.46E-03	1.29					
5	9	3333	65	3980	45	12.8	6377	--	6.401	190	8.280	180	8.503E-03	0.7452	9.48E-03	1.27					
5	10	3335	65	4015	45	16.0	6174	--	6.401	190	8.280	180	8.503E-03	0.7220	9.50E-03	1.32					
5	11	3787	74	4507	50	16.1	6958	--	6.401	190	8.280	180	8.503E-03	0.8130	1.07E-02	1.32					
5	12	3801	74	4518	51	27.3	6048	--	6.401	190	8.280	180	8.503E-03	0.7074	1.07E-02	1.52					
5	13	--	--	--	--	--	--	--	6.401	190	8.280	180	8.503E-03	--	--	--					
5	14	3781	74	4513	51	15.6	7000	--	6.401	190	8.280	180	8.503E-03	0.8182	1.07E-02	1.31					
5	15	3775	74	4471	50	15.7	6951	--	6.401	190	8.280	180	8.503E-03	0.8121	1.07E-02	1.32					
5	16	7637	142	9311	78	6.9	15778	--	6.401	190	8.280	180	8.503E-03	1.8441	1.95E-02	1.06					
5	20	4752	93	5850	66	3.3	10252	--	6.401	190	8.280	180	8.503E-03	1.1980	1.37E-02	1.14					
5	21	4778	94	5821	65	3.4	10239	--	6.401	190	8.280	180	8.503E-03	1.1974	1.37E-02	1.15					
5	22	4775	94	5923	66	5.0	10163	--	6.401	190	8.280	180	8.503E-03	1.1879	1.38E-02	1.16					
5	23	4763	93	5838	65	2.4	10346	--	6.401	190	8.280	180	8.503E-03	1.2089	1.37E-02	1.14					
5	24	--	--	--	--	--	--	--	6.401	190	8.280	180	8.503E-03	--	--	--					
5	25	5886	115	7070	78	0.6	12878	--	6.401	190	8.280	180	8.503E-03	1.4815	1.68E-02	1.13					
5	26	5697	112	7051	78	0.7	12659	--	6.401	190	8.280	180	8.503E-03	1.4793	1.64E-02	1.11					
5	27	5674	111	6977	78	1.7	12436	--	6.401	190	8.280	180	8.503E-03	1.4536	1.64E-02	1.13					
5	28	5687	111	6934	78	1.9	12381	--	6.401	190	8.280	180	8.503E-03	1.4478	1.64E-02	1.13					
5	29	5716	112	6971	78	1.4	12509	--	6.401	190	8.280	180	8.503E-03	1.4630	1.65E-02	1.13					
5	30	6677	131	8092	78	12.9	12864	--	6.401	190	8.280	180	8.503E-03	1.5039	1.83E-02	1.22					
6	32	4676	92	5943	67	2.3	10375	--	6.401	190	8.280	180	8.503E-03	1.2128	1.37E-02	1.13					
6	33	6635	130	8203	78	1.8	14571	--	6.401	190	8.280	180	8.503E-03	1.7037	1.83E-02	1.08					

Table D.8 (continued)

Outer Power (W)	Q _{outer} sigma (W)	Power Loss Environment (%)	Total Power (W)	Q _{total} sigma (W)	Inner Diameter (mm)	Inner L _{heated} (mm)	Outer Diameter (mm)	Outer L _{heated} (mm)	A _s (m ²)	Q ^(of) (MW/m ²)	Sigma_Q ^(of) (MW/m ²)	Uncertainty_Q ^(of) (%)
8131	78	3.1	14320	--	6.401	190	8.280	180	8.503E-03	1.6746	1.83E-02	1.09
8175	78	3.5	14284	--	6.401	190	8.280	180	8.503E-03	1.6689	1.83E-02	1.10
4805	54	3.0	8387	--	6.401	190	8.280	180	8.503E-03	0.9803	1.12E-02	1.14
8180	78	1.9	14535	--	6.401	190	8.280	180	8.503E-03	1.6987	1.83E-02	1.08
8554	78	1.0	15534	--	6.401	190	8.280	180	8.503E-03	1.8165	1.94E-02	1.07
3803	43	2.9	6808	--	6.401	180	7.925	180	8.101E-03	0.8400	9.61E-03	1.14
3770	42	2.9	6767	--	6.401	180	7.925	180	8.101E-03	0.8352	9.56E-03	1.15
3936	44	7.7	6525	--	6.401	180	7.925	180	8.101E-03	0.8057	9.55E-03	1.19
4437	50	6.0	7552	--	6.401	180	7.925	180	8.101E-03	0.9324	1.09E-02	1.17
4448	50	4.7	7662	--	6.401	180	7.925	180	8.101E-03	0.9462	1.09E-02	1.15
4421	50	2.9	7854	--	6.401	180	7.925	180	8.101E-03	0.9692	1.10E-02	1.14
4440	50	4.0	7721	--	6.401	180	7.925	180	8.101E-03	0.9533	1.09E-02	1.15
3918	44	2.9	6878	--	6.401	180	7.925	180	8.101E-03	0.8491	9.62E-03	1.13
5617	63	2.6	9865	--	6.401	180	7.925	180	8.101E-03	1.2181	1.37E-02	1.13
5653	63	2.7	9874	--	6.401	180	7.925	180	8.101E-03	1.2185	1.37E-02	1.13
5604	63	3.5	9788	--	6.401	180	7.925	180	8.101E-03	1.2088	1.38E-02	1.14
5542	62	3.6	9652	--	6.401	180	7.925	180	8.101E-03	1.1909	1.36E-02	1.14
6658	75	2.1	11832	--	6.401	180	7.925	180	8.101E-03	1.4607	1.65E-02	1.13
6612	74	1.5	11849	--	6.401	180	7.925	180	8.101E-03	1.4620	1.64E-02	1.12
6582	74	1.8	11768	--	6.401	180	7.925	180	8.101E-03	1.4527	1.63E-02	1.12
6651	74	1.4	11906	--	6.401	180	7.925	180	8.101E-03	1.4691	1.64E-02	1.12
--	--	--	14078	141	6.401	180	7.722	185	8.107E-03	1.7302	1.79E-02	1.04
--	--	--	14041	140	6.401	180	7.722	185	8.107E-03	1.7519	1.79E-02	1.02
--	--	--	19528	195	6.401	190	7.722	185	8.308E-03	2.3419	2.43E-02	1.04
--	--	--	20160	202	6.401	190	7.722	185	8.308E-03	2.4177	2.50E-02	1.04
--	--	--	16614	166	6.401	190	7.722	185	8.308E-03	1.9925	2.06E-02	1.04

APPENDIX E

CHF ERROR ANALYSIS

This appendix presents an error analysis of the experimentally obtained CHF heat flux and CHF mass flux values for all experiments performed in this investigation.

E.1 Mass Flux Error Analysis

Mass flux can be calculated as a function of the coolant mass flowrate and the test section cross-sectional area.

$$G = \frac{\dot{m}}{A_{cs}} \quad (\text{E.1})$$

Likewise, the variance of the coolant mass flux can be expressed by the following error propagation formula.

$$\sigma_G^2 = \left(\frac{\partial G}{\partial \dot{m}} \right)^2 \sigma_{\dot{m}}^2 + \left(\frac{\partial G}{\partial A_{cs}} \right)^2 \sigma_{A_{cs}}^2 \quad (\text{E.2})$$

where

$$\frac{\partial G}{\partial \dot{m}} = \frac{1}{A_{cs}} \quad \text{and} \quad \frac{\partial G}{\partial A_{cs}} = -\frac{\dot{m}}{A_{cs}^2} \quad (\text{E.3})$$

Since the variance of the coolant mass flowrate and the test section cross-sectional area were not directly known, these quantities had to be expanded into known components until all variances were in terms of experimentally measured variables (i.e., volumetric flowrate, power, test section diameter, and test section length). In this analysis, the calculated variance (σ^2) and standard deviation (σ) values were considered with units, while uncertainty values (u) were considered in percentage terms.

Mass flowrate (\dot{m}) was a function of the experimentally measured and controlled volumetric flowrate (\dot{V}) and the coolant density (ρ).

$$\dot{m} = \dot{V}\rho \quad (E.4)$$

The variance of the mass flowrate can be expressed in the following manner.

$$\sigma_{\dot{m}}^2 = \left(\frac{\partial \dot{m}}{\partial \dot{V}} \right)^2 \sigma_{\dot{V}}^2 + \left(\frac{\partial \dot{m}}{\partial \rho} \right)^2 \sigma_{\rho}^2 \quad (E.5)$$

The two partial derivatives in Equation E.5 have the following form.

$$\frac{\partial \dot{m}}{\partial \dot{V}} = \rho \quad \text{and} \quad \frac{\partial \dot{m}}{\partial \rho} = \dot{V} \quad (E.6)$$

The first partial derivative in Equations E.6 had to be multiplied by the variance of the volumetric flowrate. The variance of the volumetric flowrate at CHF, measured using an FTO-3 liquid flow transducer manufactured by EG&G/FTI, was calculated as the sum of the squares of the individual bias errors and precision errors associated with the measurement. The four individual bias errors were:

1. The DAS voltage conversion error was calculated by determining the bit range over which the flow transducer was used. The calibration curve for the FTO-3

flow transducer was:

$$gph = 0.432929 \text{ gph} + 0.00495(mV_{EXP16}) \frac{\text{gph}}{mV_{EXP16}}$$

with EXP16 gain of unity. Since the gain was unity, the millivolt reading on the DAS-8 board was equivalent to the millivolt reading on the EXP16. The conversion from millivolts to bits was 2047 bits = 5000 millivolts, accurate to ± 1 bit. The operational flowrate range associated with this investigation was 1.3 \rightarrow 5.5 gph, which corresponded to a bit range of 72 \rightarrow 420 bits. Therefore, for the minimum flowrate of 1.3 gph, $u_{1-Low} = 1/72 = 0.0139 = 1.39\%$, and for the maximum flowrate of 5.5 gph, $u_{1-High} = 1/420 = 0.00238 = 0.238\%$.

2. The 1000 mL graduated cylinder used to calibrate the FTO-3 flowmeter was accurate to 5 mL and, therefore, $u_2 = 5/1000 = 0.005 = 0.5\%$.
3. The stopwatch used during the FTO-3 flowmeter calibration procedure was accurate to 0.001 seconds and the minimum time interval during calibration was 35 seconds and, therefore, $u_3 = 0.001/35 = 0.0000286 = 0.00286\%$.
4. The standard error associated with the linear regression calibration curve fit was 0.116035 gph. For the flowrate range mentioned above (1.3 \rightarrow 5.5 gph), $u_{4-Low} = 0.0893 = 8.93\%$ for the lowest flowrate and $u_{4-High} = 0.0211 = 2.11\%$ for the highest flowrate.

The only precision error encountered in this investigation with respect to the volumetric flowrate came directly from the standard deviation of the flowrate during a

CHF experiment. The maximum standard deviation of the volumetric flowrate was 0.83 L/hr (15.66 kg/m²s), which occurred during an experiment that maintained the flowrate constant at 11.04 L/hr (207.74 kg/m²s), therefore, $u_5 = 0.83/11.04 = 0.0752 = 7.52 \%$.

By summing the squares of the four bias errors and the single precision error associated with the volumetric flowrate measurement at CHF, the error estimate for the volumetric flowrate at CHF was found.

Table E.1: Summary of Volumetric Flowrate Uncertainties at CHF

	Error Type	Uncertainty (@1.3 gph)	Uncertainty ² (@1.3 gph)	Uncertainty (@5.5 gph)	Uncertainty ² (@5.5 gph)
u_1	Bias	1.39 %	1.932 E -4	0.238 %	5.664 E -6
u_2	Bias	0.5 %	2.500 E -5	0.5 %	2.500 E -5
u_3	Bias	0.00286 %	8.180 E -10	0.00286 %	8.180 E -10
u_4	Bias	8.93 %	7.974 E -3	2.11 %	4.452 E -4
u_5	Precision	7.52 %	5.655 E -3	7.52 %	5.655 E -3
Sum	--	--	1.385 E -2	--	6.130 E -3

Using this analysis procedure, the error was 11.8 % or 0.153 gph at the lower end of the operational flowrate range and 7.83 % or 0.431 gph at the higher end of the operational flowrate range. For analysis purposes, the volumetric flowrate error estimate was 11.8 % or 0.431 gph, whichever was smaller for the volumetric flowrate value in question. Basically, this means that the 11.8 % error value was applied to the lower end of the operational flowrate range, while the 0.431 gph error value was applied to the higher end of the operational flowrate range.

The second partial derivative in Equations E.6 had to be multiplied by the variance of the coolant density. The precision error associated with the coolant density

came from the standard deviation of the inlet temperature to the test section during a CHF experiment. The maximum inlet temperature standard deviation encountered over all CHF experiments was 3.070°C (From Table C.1), which occurred on an experiment that had an average inlet temperature of 61.9°C and an average absolute inlet pressure of 793.9 kPa. This inlet temperature standard deviation thus created a range of possible inlet densities: 980.7 → 983.9 kg/m³. The density value obtained when the average values of temperature and pressure were used was 982.3 kg/m³. Thus, the representative deviation in density from the reported value for all CHF experiments was 1.6 kg/m³, which corresponds to a u_{p-1} of 0.00163 or 0.163 %. This value came from the standard deviation of the inlet temperature, which depended on the bias error of the inlet thermocouple ($\pm 0.1^\circ\text{C}$). The lowest inlet temperature encountered during all CHF experiments was 29.8°C, which produced a u_{p-2} of 0.00336 or 0.336 %. By combining these two terms as shown in Equation E.7, the final value of u_p was 0.00373 or 0.373 %, which means that the standard deviation of the inlet temperature contributes very little to the error associated with the coolant density at the test section inlet.

$$u_p = \sqrt{u_{p-1}^2 + u_{p-2}^2} = 0.00373 = 0.373\% \quad (\text{E.7})$$

Referring to Equation E.5, all values were known at this point such that the variance of the coolant mass flowrate could be determined. Since the value of importance to this investigation was coolant mass flux, the variance of the test section cross sectional area had to be determined for the error analysis to be complete, as shown in Equation E.2. The cross sectional area or flow area of the test section was a function

of the inner diameter of the outer heater (outer wall of the annulus) and the outer diameter of the inner heater (inner wall of the annulus).

$$A_{cs} = \frac{\pi}{4} (D_{out}^2 - D_{in}^2) \quad (E.8)$$

The variance of the test section cross sectional area can be expressed in the following manner.

$$\sigma_{A_{cs}}^2 = \left(\frac{\partial A_{cs}}{\partial D_{out}} \right)^2 \sigma_{D_{out}}^2 + \left(\frac{\partial A_{cs}}{\partial D_{in}} \right)^2 \sigma_{D_{in}}^2 \quad (E.9)$$

where:

$$\frac{\partial A_{cs}}{\partial D_{out}} = \frac{\pi}{2} D_{out} \quad \text{and} \quad \frac{\partial A_{cs}}{\partial D_{in}} = -\frac{\pi}{2} D_{in} \quad (E.10)$$

The outer diameter (inner diameter of the outer heater) was measured using both precision ground pins and a Starrett dial caliper. The tolerance of the caliper was known to be $\sigma_{D_{out}} = 0.001 \text{ inch} = 0.0254 \text{ mm}$, which created a maximum bias uncertainty of $u_{D_{out}} = 0.001/0.304 = 0.00329 = 0.329 \%$ for the outer heater used (Outer Heater K). This tolerance was used instead of the tolerance of the pins to provide a more conservative estimate of the error associated with the cross sectional area of the test section. The inner diameter (outer diameter of the inner heater) was also measured using a Starrett dial caliper ($\sigma_{D_{in}} = 0.001 \text{ inch} = 0.0254 \text{ mm}$). The inner heater was constructed of tubing that had been manufactured with a nominal outer diameter of 0.250 inch. During construction, the inner heater was found to have a diameter slightly larger than 0.250 inch, but 0.250 inch was utilized in this error analysis to maintain a conservative

estimate. The bias uncertainty estimate of the inner diameter was found to be $u_{D_{in}} = 0.001/0.250 = 0.00400$ 0.400 %.

Finally, combining Equations E.2 through E.10 yielded the following estimate of the coolant mass flux variance.

$$\sigma_G^2 = \left(\frac{1}{A_{cs}} \right)^2 \left[\rho^2 \sigma_{\dot{V}}^2 + \dot{V}^2 \sigma_{\rho}^2 \right] + \left(\frac{-\dot{m}}{A_{cs}^2} \right)^2 \left[\left(\frac{\pi}{2} D_{out} \right)^2 \sigma_{D_{out}}^2 + \left(-\frac{\pi}{2} D_{in} \right)^2 \sigma_{D_{in}}^2 \right] \quad (E.11)$$

By applying this formula along with the appropriate error estimates from Table E.2 to the set of experiments performed in this investigation, the average uncertainty in mass flux was calculated to be 11.08 %. Note that the σ values for coolant volumetric flowrate in Table E.2 are given in terms of both gph and percentage since the error estimate of the flowrate in question depends in part on the magnitude of the flowrate. The mass flux error analysis results for the data with heat flux ratio of unity are listed in Table E.3.

Table E.2: Summary of Coolant Mass Flux Error Sources at CHF

$\sigma_{\dot{V}}$	u_{ρ}	$\sigma_{D_{out}}$	$\sigma_{D_{in}}$
11.8 % or 0.431 gph	0.373 %	0.0254 mm	0.0254 mm

Table E.3: CHF Coolant Mass Flux Error Analysis Results

Sigma(Vol. Flow):		4.53E-07		(m ³ /sec)	
or		11.8		(%)	
Sigma(Density):		0.373		(%)	
Sigma(D_out):		2.54E-05		(m)	
Sigma(D_in):		2.54E-05		(m)	

D_out =		7.722		(m)	
D_in =		6.401		(m)	
A_cs =		1.465E-05		(m ²)	

Setup	Run	Inlet Density @CHF (kg/m ³)	Inlet Density sigma (kg/m ³)	Vol Flowrate @CHF (m ³ /sec)	Vol Flowrate sigma (m ³ /sec)	Mass Flowrate (kg/s)	G(chf) (kg/m ² s)	Sigma_G (kg/m ² s)	Uncertainty_G (%)
13	1	996	3.72	3.07E-06	3.62E-07	3.06E-03	207.74	25.27	12.16
13	2	989	3.69	2.67E-06	3.15E-07	2.64E-03	179.38	21.81	12.16
13	3	981	3.66	2.81E-06	3.31E-07	2.75E-03	187.34	22.78	12.16
13	4	988	3.69	2.96E-06	3.49E-07	2.92E-03	198.86	24.19	12.16
13	5	988	3.68	2.79E-06	3.29E-07	2.76E-03	187.63	22.81	12.16
13	6	996	3.72	1.57E-06	1.85E-07	1.56E-03	106.28	12.93	12.17
13	7	988	3.69	1.50E-06	1.77E-07	1.48E-03	100.68	12.24	12.16
13	8	981	3.66	1.49E-06	1.75E-07	1.46E-03	99.19	12.06	12.16
13	9	988	3.69	1.52E-06	1.79E-07	1.50E-03	102.01	12.40	12.16
13	10	988	3.69	1.48E-06	1.74E-07	1.46E-03	99.42	12.08	12.15
13	11	996	3.71	4.30E-06	4.53E-07	4.28E-03	291.15	31.83	10.93
13	12	988	3.68	4.32E-06	4.53E-07	4.27E-03	290.25	31.60	10.89
13	13	980	3.66	4.40E-06	4.53E-07	4.31E-03	293.57	31.39	10.69
13	14	987	3.68	4.39E-06	4.53E-07	4.33E-03	294.68	31.59	10.72
13	15	988	3.69	4.43E-06	4.53E-07	4.38E-03	297.63	31.66	10.64
13	16	996	3.72	2.23E-06	2.63E-07	2.22E-03	151.16	18.38	12.16
13	17	989	3.69	2.18E-06	2.57E-07	2.16E-03	146.59	17.83	12.16
13	18	981	3.66	2.26E-06	2.67E-07	2.22E-03	150.97	18.36	12.16
13	19	989	3.69	2.28E-06	2.69E-07	2.25E-03	153.14	18.62	12.16
13	20	988	3.69	2.18E-06	2.58E-07	2.16E-03	146.74	17.85	12.16
13	21	997	3.72	3.66E-06	4.32E-07	3.65E-03	248.22	30.18	12.16
13	22	989	3.69	3.67E-06	4.33E-07	3.63E-03	246.55	29.99	12.16
13	23	980	3.65	3.63E-06	4.28E-07	3.55E-03	241.67	29.40	12.17
13	24	988	3.69	3.65E-06	4.31E-07	3.61E-03	245.44	29.84	12.16

Table E.3 (continued)

Setup	Run	Inlet Density @OFI (kg/m ³)	Inlet Density sigma (kg/m ³)	Vol Flowrate @OFI (m ³ /sec)	Vol Flowrate sigma (m ³ /sec)	Mass Flowrate (kg/s)	G(ofi) (kg/m ² s)	Sigma_G (kg/m ² s)	Uncertainty_G (%)
13	25	989	3.69	3.68E-06	4.34E-07	3.64E-03	247.55	30.09	12.16
13	26	994	3.71	5.00E-06	4.53E-07	4.98E-03	338.46	32.16	9.50
13	27	986	3.68	4.94E-06	4.53E-07	4.88E-03	331.58	31.85	9.61
13	28	981	3.66	4.93E-06	4.53E-07	4.84E-03	328.99	31.70	9.63
13	29	986	3.68	5.06E-06	4.53E-07	4.99E-03	339.69	31.93	9.40
13	30	987	3.68	5.03E-06	4.53E-07	4.97E-03	338.09	31.94	9.45
13	31	994	3.71	5.55E-06	4.53E-07	5.52E-03	375.14	32.45	8.65
13	32	987	3.68	5.53E-06	4.53E-07	5.46E-03	371.22	32.22	8.68
13	33	981	3.66	5.50E-06	4.53E-07	5.39E-03	366.80	31.99	8.72
13	34	987	3.68	5.57E-06	4.53E-07	5.49E-03	373.54	32.23	8.63
13	35	988	3.68	5.65E-06	4.53E-07	5.58E-03	379.39	32.31	8.52

E.2 Heat Flux Error Analysis

The heat flux can be calculated as a function of the power applied to the test section and the test section heated area.

$$Q'' = \frac{Q_{total}}{A_s} \quad (E.12)$$

The variance of the surface heat flux can be expressed by the following error propagation formula.

$$\sigma_{Q''}^2 = \left(\frac{\partial Q''}{\partial Q_{total}} \right)^2 \sigma_{Q_{total}}^2 + \left(\frac{\partial Q''}{\partial A_s} \right)^2 \sigma_{A_s}^2 \quad (E.13)$$

where

$$\frac{\partial Q''}{\partial Q_{total}} = \frac{1}{A_s} \quad \text{and} \quad \frac{\partial Q''}{\partial A_s} = -\frac{Q_{total}}{A_s^2} \quad (E.14)$$

For all 35 CHF experiments, the power supplied to the test section was determined using an energy balance and the total amount of power supplied by the DC power supply as described in Section IV.8.2. Errors in the energy balance heat loss estimation were also discussed independently in Section IV.8.2, however, the error associated with the measurement of the total power output from the power supply had to be quantified. This power level was measured using the Ohio Semitronics DC wattmeter (Component 16 of Table 3.3) mentioned earlier. During CHF experimentation, there were two individual bias errors that contributed to the uncertainty of the total power reading:

1. The manufacturer stated accuracy of the Ohio Semitronics DC wattmeter was

$\pm 1.0\%$ of the power reading, thus $u_1 = 0.01 = 1.0\%$.

2. The DAS voltage conversion error was calculated by determining the bit range over which the wattmeter was used. The calibration curve for this DC wattmeter was the same as stated in Appendix D:

$$Power (W) = -2.31 W + 6.4097(mV_{EXP16}) \frac{W}{mV_{EXP16}} \quad (E.15)$$

with EXP16 gain of unity. Since the gain was unity, the mV reading on the DAS-8 board was the same as on the EXP16 board. The conversion from millivolts to bits was 2047 bits = 5000 mV, accurate to ± 1 bit. The total power level over all 35 CHF experiments ranged from a minimum of 1918 W to a maximum of 8879 W, which converted to a range of 123 \rightarrow 568 bits. Therefore, for the 1918 W power level, $u_{2-Low} = 1/123 = 0.00813 = 0.813\%$ and for the 8879 W power level, $u_{2-High} = 1/568 = 0.00176 = 0.176\%$.

The only precision error encountered in this investigation with respect to the total applied power level came directly from the standard deviation of the power level around CHF. The maximum standard deviation of the total applied power was 55.7 W (0.0067 MW/m²), which occurred during an experiment where CHF occurred at a power level of 3895.6 W (0.4689 MW/m²), therefore, $u_5 = 55.7/3895.6 = 0.0143 = 1.43\%$.

By summing the squares of the two bias errors and the single precision error associated with the total power level at CHF, the error estimate for the total power level at CHF was found.

Table E.4: Summary of Total Power Level Uncertainties at CHF

	Error Type	Uncertainty (@ 1918 W)	Uncertainty ² (@ 1918 W)	Uncertainty (@ 8879 W)	Uncertainty ² (@ 8879 W)
u ₁	Bias	1.0 %	1.000 E -4	1.0 %	1.000 E -4
u ₂	Bias	0.813 %	6.610 E -5	0.176 %	3.098 E -6
u ₃	Precision	1.43 %	2.045 E -4	1.43 %	2.045 E -4
Sum	--	--	3.706 E -4	--	3.076 E -4

Using this analysis procedure, the error was 1.93 % or 37.0 W at the lower end of the operational power range and 1.75 % or 155.4 W at the higher end of the operational power range. For analysis purposes, the total power error estimate was 1.93 % or 155.4 W, whichever was smaller for the total power value in question. Basically, this means that the 1.93 % error value was applied to the lower end of the operational power range, while the 155.4 W error value was applied to the higher end of the operational power range.

The test section heated surface area was a function of the inner diameter of the annulus, outer diameter of the annulus, inner heater heated length, and outer heater heated length.

$$A_s = \pi(L_{heated, out}D_{out} + L_{heated, in}D_{in}) \quad (E.16)$$

The variance of the test section heated surface area can be expressed in the following manner.

$$\sigma_{A_s}^2 = \left(\frac{\partial A_s}{\partial D_{out}}\right)^2 \sigma_{D_{out}}^2 + \left(\frac{\partial A_s}{\partial D_{in}}\right)^2 \sigma_{D_{in}}^2 + \left(\frac{\partial A_s}{\partial L_{h, out}}\right)^2 \sigma_{L_{h, out}}^2 + \left(\frac{\partial A_s}{\partial L_{h, in}}\right)^2 \sigma_{L_{h, in}}^2 \quad (E.17)$$

where

$$\frac{\partial A_s}{\partial D_{out}} = \pi L_{h,out} \quad \text{and} \quad \frac{\partial A_s}{\partial D_{in}} = \pi L_{h,in} \quad (\text{E.18})$$

$$\frac{\partial A_s}{\partial L_{h,out}} = \pi D_{out} \quad \text{and} \quad \frac{\partial A_s}{\partial L_{h,in}} = \pi D_{in}$$

As stated earlier, the relevant annulus diameters were measured using a Starrett dial caliper, which had a known tolerance of $\sigma = 0.001$ inch. The heated lengths of all test sections were measured using Fowler vernier calipers, also with a known tolerance of $\sigma = 0.001$ inch.

Finally, combining Equations E.13 through E.18 yielded the following estimate of the surface heat flux variance at CHF.

$$\sigma_{Q''}^2 = \left(\frac{1}{A_s} \right)^2 \left[\sigma_{Q_{in}}^2 + \sigma_{Q_{out}}^2 \right] + \left(\frac{-Q_{total}}{A_s^2} \right)^2 \left[(\pi L_{h,out})^2 \sigma_{D_{out}}^2 + (\pi L_{h,in})^2 \sigma_{D_{in}}^2 + (\pi D_{out})^2 \sigma_{L_{h,out}}^2 + (\pi D_{in})^2 \sigma_{L_{h,in}}^2 \right] \quad (\text{E.19})$$

By applying this formula along with the appropriate error estimates from Table E.5 to the set of experiments performed in this investigation, the average uncertainty in heat flux was calculated to be 1.92 %. Note that the σ values for all power error estimates in Table E.5 are given in terms of both Watts and percentage since the error estimate of the power level in question depends on the magnitude of the power measurement.

Table E.5: Summary of Heat Flux Uncertainties at CHF

$\sigma_{Q_{total}}$	$\sigma_{D_{out}}$	$\sigma_{D_{in}}$	$\sigma_{L_{h,out}}$	$\sigma_{L_{h,in}}$
1.93 % or 155.4 W	0.0254 mm	0.0254 mm	0.0254 mm	0.0254 mm

The outline below shows a sample error estimate for a CHF experiment that had the following experimentally measured parameters: $D_{out} = 7.722$ mm, $D_{in} = 6.401$ mm, $L_{h, out} = 185$ mm, $L_{h, in} = 190$ mm, and $Q_{total} = 8878$ W. The heat flux error analysis results for the data are listed in Table E.6

Measurement	Uncertainty	Influence Coefficient, $\left(\frac{\partial q''}{\partial x_i}\right)$	(Uncertainty) ²	Basis
Total Power	155.4 W	$\frac{1}{\pi(D_{out} L_{h,out} + D_{in} L_{in})}$ $= 120.4 (1/m^2)$	$3.50 \text{ E } -4 (\text{MW}/m^2)^2$	Resolution
Outer Diameter	0.0254 mm	$\frac{-\dot{Q}_{total} L_{out}}{\pi(D_{out} L_{out} + D_{in} L_{in})^2}$ $= -74.7 (\text{MW}/m^3)$	$3.60 \text{ E } -6 (\text{MW}/m^2)^2$	Measurement
Inner Diameter	0.0254 mm	$\frac{-\dot{Q}_{total} L_{in}}{\pi(D_{out} L_{out} + D_{in} L_{in})^2}$ $= -76.7 (\text{MW}/m^3)$	$3.80 \text{ E } -6 (\text{MW}/m^2)^2$	Measurement
Outer L_h	0.0254 mm	$\frac{-\dot{Q}_{total} D_{out}}{\pi(D_{out} L_{out} + D_{in} L_{in})^2}$ $= -3.12 (\text{MW}/m^3)$	$6.28 \text{ E } -9 (\text{MW}/m^2)^2$	Measurement
Inner L_h	0.0254 mm	$\frac{-\dot{Q}_{total} D_{in}}{\pi(D_{out} L_{out} + D_{in} L_{in})^2}$ $= -2.59 (\text{MW}/m^3)$	$4.33 \text{ E } -9 (\text{MW}/m^2)^2$	Measurement
		Sum of Variances =	$3.50 \text{ E } -4 (\text{MW}/m^2)^2$	
		Uncertainty =	$0.0187 \text{ MW}/m^2 = 1.75 \%$	

Table E.6: CHF Surface Heat Flux Error Analysis Results

Sigma(Power): or		155.4	(W)	D_out =		7.722	(mm)
Sigma(L_h, out):		1.93	(%)	L_h, out =		185	(mm)
Sigma(L_h, in):		2.54E-05	(m)	D_in =		6.401	(mm)
Sigma(D_out):		2.54E-05	(m)	L_h, in =		190	(mm)
Sigma(D_in):		2.54E-05	(m)	A_s =		8.308E-03	(m^2)

Setup	Run	Total Power (W)	Q_total sigma (W)	Q"(CHF) (MW/m^2)	Sigma_Q" (MW/m^2)	Sigma_Q" (%)
13	1	3896	75	0.4689	9.05E-03	1.93
13	2	3663	71	0.4409	8.51E-03	1.93
13	3	3608	70	0.4343	8.38E-03	1.93
13	4	3274	63	0.3940	7.60E-03	1.93
13	5	4143	80	0.4986	9.62E-03	1.93
13	6	2631	51	0.3167	6.11E-03	1.93
13	7	2181	42	0.2625	5.07E-03	1.93
13	8	1918	37	0.2309	4.46E-03	1.93
13	9	1987	38	0.2392	4.62E-03	1.93
13	10	2996	58	0.3606	6.96E-03	1.93
13	11	6373	123	0.7671	1.48E-02	1.93
13	12	6371	123	0.7668	1.48E-02	1.93
13	13	4437	86	0.5340	1.03E-02	1.93
13	14	5159	100	0.6209	1.20E-02	1.93
13	15	6650	128	0.8004	1.54E-02	1.93
13	16	3288	63	0.3958	7.64E-03	1.93
13	17	2811	54	0.3383	6.53E-03	1.93
13	18	2841	55	0.3419	6.60E-03	1.93
13	19	2518	49	0.3031	5.85E-03	1.93
13	20	3291	64	0.3961	7.64E-03	1.93
13	21	5336	103	0.6422	1.24E-02	1.93
13	22	4834	93	0.5818	1.12E-02	1.93
13	23	4497	87	0.5412	1.04E-02	1.93
13	24	4405	85	0.5302	1.02E-02	1.93

Table E.6 (continued)

Setup	Run	Total Power (W)	Q _{total} sigma (W)	Q"(chf) (MW/m ²)	Sigma_Q" (MW/m ²)	Sigma_Q" (%)
13	25	5705	110	0.6867	1.33E-02	1.93
13	26	7169	138	0.8629	1.67E-02	1.93
13	27	6936	134	0.8348	1.61E-02	1.93
13	28	6120	118	0.7366	1.42E-02	1.93
13	29	6411	124	0.7716	1.49E-02	1.93
13	30	8426	155	1.0142	1.87E-02	1.84
13	31	8868	155	1.0674	1.87E-02	1.75
13	32	7688	148	0.9253	1.79E-02	1.93
13	33	6538	126	0.7869	1.52E-02	1.93
13	34	6469	125	0.7786	1.50E-02	1.93
13	35	8878	155	1.0686	1.87E-02	1.75

BIBLIOGRAPHY

Ahmad, S.Y., 1970, "Axial Distribution of Bulk Temperature and Void Fraction in a Heated Channel With Inlet Subcooling," J. Heat Transfer, Vol. 92, pp. 595-609.

Bankoff, S.G., Lee, S.C., and Knaani, A., 1991, "Literature Review on Forced-Convection Subcooled Nucleate Boiling," Westinghouse Savannah River Company Report WSRC-TR-91-98, Evanston, IL.

Bergles, A.E., 1977, "Review of Instabilities in Two-Phase Systems," in Two-Phase Flow and Heat Transfer, S. Kakac and F. Mayinger, Vol. 2, pp. 383-422, Hemisphere, Washington, D.C.

Bergles, A.E. and Rohsenow, W.M., 1964, "The Determination of Forced Convective Surface Boiling Heat Transfer," J. Heat Transfer, Vol. 86, pp. 365-372.

Blasick, A.M., 1999, "Onset of Flow Instability in Heated, Horizontal Annuli," Georgia Institute of Technology Masters Thesis.

Boure, J.A., Bergles, A.E., and Tong, L.S., 1973, "Review of Two-Phase Flow Instability," Nucl. Eng. Des., Vol. 25, pp. 165-192.

Bowring, R.W., 1962, "Physical Model Based on Bubble Detachment and Calculation of Steam Voidage in the Subcooled Region of a Heated Channel," HBR-10, Instituted for Atomenergi, Halden, Norway.

Bowring, R.W., 1972, "A Simple but Accurate Round Tube, Uniform Heat Flux, Dryout Correlation Over the Pressure Range 0.7 – 17 MW/m² (100 – 2500 psia)," AEEW-R789, UKAEA.

Caira, M., Caruso, G., and Naviglio, A., 1993, "Requirements of High Heat Flux for Fusion Reactor Components: Revised Models and Correlations Predict Critical Heat Flux in Subcooled Flow Boiling," Proc. 1993 National Heat Transfer Conf., Atlanta, GA, p. 383, American Nuclear Society.

Chan, A.M.C., 1984, "Point of Net Vapor Generation and its Movement in Transient Horizontal Flow Boiling," ASME HTD-Vol. 34, pp. 145-152.

Christensen, H., 1961, "Power-To-Void Transfer Functions," ANL-6385.

Costa, J., 1967, "Measurement of the Acceleration Pressure Drops; Study of the Appearance of Vapor and Void Fraction in Subcooled Boiling at Low Pressure," European Two-Phase Group Meeting, Winfrith, U.K.

Dix, G.E., 1971, "Vapor Void Fraction for Forced Convection with Subcooled Boiling at Low Flow Rates," Ph.D. Thesis, University of California, Berkeley, CA.

Evangelisti, R. and Lupoli, P., 1969, "The Void Fraction in an Annular Channel at Atmospheric Pressure," Int. J. Heat Transfer, Vol. 12, pp. 699-711.

Griffith, P., Clark, J.A., and Rohsenow, W.M., 1968, "Void Volume in Subcooled Boiling," ASME Paper 58-HT-19.

Groeneveld, D.C. and Snoek, C.W., 1986, "A Comprehensive Examination of Heat Transfer Correlations Suitable for Reactor Safety Analysis," Multiphase Science and Technology, Hewitt, G.F., Delhay, J.M., and Zuber, N., Eds., Vol. 2, pp. 181-274, Hemisphere, Washington, D.C.

Hainoun, A., Hicken, E., and Wolters, J., 1996, "Modeling of Void Formation in the Subcooled Boiling Region in ATHLET Code to Simulate Flow Instability for Research Reactors," Nucl. Eng. Des., Vol. 167, pp. 175-191.

Inasaka, F., Nariyai, H., and Shimura, T., 1989, "Pressure Drops in Subcooled Flow Boiling in Narrow Tubes," Heat Transfer, Japanese Research, Vol. 18, pp. 70-82.

Ishii, M., 1976, "Study of Flow Instabilities in Two-Phase Mixtures," Argonne National Laboratory Report, ANL-76-23.

Johnston, B.S., 1989, "Subcooled Boiling of Downward Flow in a Vertical Annulus," ASME HTD-Vol. 109, pp. 149-156.

Kennedy, J.E., Roach, G.M., Dowling, M.F., Jeter, S.M., Ghiaasiaan, S.M., and Abdel-Khalik, S.I., 1997, "Onset of Flow Instability in Uniformly-Heated Microchannels," Georgia Institute of Technology Final Report, submitted to Westinghouse Savannah River Company.

Kroeger, P.G. and Zuber, N., 1968, "An Analysis of the Effects of Various Parameters on the Average Void Fractions in Subcooled Boiling," Int. J. Heat Mass Transfer, Vol. 11, pp. 211-233.

Lahey, R.T., and Moody, F.J., 1979, *The Thermal-Hydraulics of a Boiling Water Nuclear Reactor*, Second Edition, American Nuclear Society, LaGrange Park, IL.

Levy, S., 1967, "Forced Convection Subcooled Boiling: Prediction of Vapor Volumetric Fraction," *Int. J. Heat Mass Transfer*, Vol. 10, pp. 951-965.

McBeth, R.V., 1965-66, "An Appraisal of Forced Convection Burnout Data," *Proc. Inst. Mech. Eng.*, Vol. 180, pp. 47-48.

McBeth, R.V. and Thompson, B., 1964, "Boiling Water Heat Transfer Burnout in Uniformly Heated Round Tubes: A Compilation of World Data with Accurate Correlations," UKAE Report AEEW-R 356, Winfrith, England.

Pasamehmetoglu, K.O., Willcutt, G.J., Elson, J.S., and Siebe, D.A., 1998, "Thermal-Hydraulic Design of the APT Tungsten Neutron Source," submitted to Nuclear Systems Design and Analysis Group, Technology and Safety Assessment Division, Los Alamos National Laboratory, Los Alamos, New Mexico.

Peng, X.F. and Wang, B.X., 1993, "Forced Convection and Flow Boiling Heat Transfer for Liquid Flowing Through Microchannels," *Int. J. Heat Mass Transfer*, Vol. 36, pp. 3421-3427.

Roach, G.M., 1998, "Onset of Flow Instability and Critical Heat Flux in Uniformly-Heated Microchannels," Georgia Institute of Technology Masters Thesis.

Rogers, J.T., Salcudean, M., Abdullah, Z., McLeod, D., and Poirier, D., 1987, "The Onset of Significant Void in Up-Flow Boiling of Water at Low Pressure and Velocities," *Int. J. Heat Mass Transfer*, Vol. 30, pp. 2247-2260.

Saha, P. and Zuber, N., 1974, "Point of Net Vapor Generation and Vapor Void Fraction in Subcooled Boiling," *Proc. Fifth Int. Heat Transfer Conf.*, Tokyo, Japan.

Staub, F.W., 1968, "The Void Fraction in Subcooled Boiling: Prediction of the Initial Point of Net Vapor Generation," *J. Heat Transfer*, Vol. 90, pp. 151-157.

Stoddard, R.M., Blasick, A.M., Dowling, M.F., Abdel-Khalik, S.I., Ghiaasiaan, S.M., and Jeter, S.M., 2000, "OFI and CHF Database for APT Tungsten Target Annuli," Georgia Institute of Technology Final Report, submitted to General Atomics.

Thom, J.R.S., Walker, W.M., Fallon, T.A., and Reising, G.F.S., 1966, "Boiling in Subcooled Water During Flow in Tubes and Annuli," *Proc. Inst. Mech. Eng.*, 3C180.

Todreas, N.E. and Kazimi, M.S., 1990, *Nuclear Systems I*, Hemisphere, New York.

Unal, H.C., 1975, "Determination of the Initial Point of Net Vapor Generation in Flow Boiling Systems," *Int. J. Heat Mass Transfer*, Vol. 18, pp. 1095-1099.

Whittle, R.H. and Forgan, R., 1967, "A Correlation for the Minima in the Pressure Drop Versus Flow-Rate Curves for Subcooled Water Flowing in Narrow Heated Channels," *Nucl. Eng. Des.*, Vol. 6, pp. 89-99.

Yadigaroglu, G., 1981, "Two-Phase Flow Instabilities and Propagation Phenomena," *Thermohydraulics of Two-Phase Systems for Industrial Design and Nuclear Engineering*, J.M. Delhay, M. Giot, and M.L. Riethmuller, Eds., pp. 353-403, Hemisphere, Washington, D.C.